FINAL REPORT

ANALYSIS AND MODELING OF SUMMERTIME CONVECTIVE CLOUD AND PRECIPITATION STRUCTURE OVER THE SOUTHEASTERN UNITED STATES

NASA Grant NAG8-654

Kevin R. Knupp
Atmospheric Science and Remote Sensing Laboratory
Johnson Research Center
University of Alabama in Huntsville
Huntsville, AL 35899

ANALYSIS AND MODELING OF SUMMERTIME CONVECTIVE CLOUD AND PRECIPITATION STRUCTURE OVER THE SOUTHEASTERN UNITED STATES

FINAL REPORT

NASA Grant NAG8-654

Period of performance: 15 September 1987 - 31 December 1990

Kevin R. Knupp
Atmospheric Science and Remote Sensing Laboratory
Johnson Research Center
University of Alabama in Huntsville
Huntsville, AL 35899

REPORT SUMMARY

This work presents findings on the internal structure of two contrasting mesoscale convective systems observed during the COHMEX program conducted during June-July 1986. The analysis utilizes both GOES IR satellite data and other surface based data platforms, most notably Doppler radar. The two mesoscale convective systems evolved in relatively low-shear environments that typify the Southeast United States subtropical continental climatic regime during the summer months. Both systems exhibited relatively long lifetimes, but displayed appreciable spatial and temporal variability. The 13 July MCS was composed of intense convective elements and evolved to a classical squall line structure consisting of leading edge of deep convection flanked by a trailing stratiform region. In this case certain patterns in cloud top behavior were related to internal kinematic and precipitation structure. A sinking cloud top was observed in conjunction with the intensification and expansion of precipitation within the stratiform region. It was found that the temporal variability of cloud top was related to vertical motion patterns determined from VAD analyses, but the relation was by no means uniform. Another significant accomplishment in this case was a detailed documentation of the the reflectivity field evolution within the stratiform region.

The 15 July MCS exhibited a contrasting structure and evolution. While convective elements within this system were less vigorous, the amount of stratiform precipitation produced was large relative to the activity of deep convection. Deep convective elements in this case formed on the western boundary in a cyclic fashion at 3 h time intervals and then moved eastward relative to the system movement while weakening. The area of stratiform precipitation was substantial in this case, but the horizontal distribution was not uniform, exhibiting variations of 10 dBZ. Moreover, weak convection was embedded within the stratiform region. Mesoscale downdraft of 15-20 cm s^{-1} was common over the lowest 6-7 km throughout the period of measurements. Very weak mesoscale updraft of several cm s^{-1} magnitude was confined to the upper 2-3 km (7-10 km AGL) level of the stratiform region. A prominent inflow jet having a peak speed of 15 m s^{-1} near 2-3 km AGL was observed throughout. Unlike the sloping jet observed in the 13 July MCS, the 15 July jet was quasi-horizontal and located well below the melting level.

It is recommended that several items be addressed in future research activities to more fully understand small MCS charactereistics and their cloud top behavior. Cloud top patterns appear to have useful information, especially if the crystal habit at cold cloud top temperatures ($T < -50$ °C) of MCS stratiform regions is understood. There is a need to further understand the general characteristics of small MCSs and their importance on the global scale water/energy budget. For example, what is the characteristic size, lifetime and diurnal behavior of such systems in various regions of the world? Are small MCSs similar in structure to their larger squall line and MCC counterparts that exist elsewhere? It is believed that small MCSs contribute importantly to regional energy/hydrologic budgets and therefore require further examination.

ACKNOWLEDGMENTS

This research report describes work supported by NASA under grant NAG8-654. Much of the analysis software used to complete this work was provided by the National Center for Atmospheric Research (NCAR). Particular thanks is extended to Carl Mohr and Richard Oye, both of NCAR. NCAR is also recognized for the extensive data collection effort, during the COHMEX field effort, and the subsequent quality control of the radar and surface mesonet data used in this study. Mr. Steve Williams provided valuable assistance in the acquisition of GOES satellite data. Mr. Tim Rushing, Mr. Wallace Coker and Ms. Martha Helton provided assistance in the data analysis effort during the course of this study. A PC-McIDAS system, developed by the University of Wisconsin and supported by the Unidata program, was used in much of the satellite data analysis included herein.

TABLE OF CONTENTS

1. INTRODUCTION

This report summarizes the work completed under NASA Grant NAG8-654 for the period 15 September 1987 through 31 December 1990. The general scope of this work included an investigation of deep convective cloud systems that typify the summertime subtropical environment of northern Alabama. The major portion of the research effort included analysis of data acquired during the 1986 Cooperative Huntsville Meteorological Experiment (COHMEX), which consisted of the joint programs Satellite Precipitation and Cloud Experiment (SPACE) under NASA direction, the Microburst and Severe Thunderstorm (MIST) program under NSF sponsorship, and the FAA-Lincoln Laboratory Operational Weather Study (FLOWS), sponsored by the Federal Aviation Administration. This work relates closely to the SPACE component of COHMEX, one of the general goals of which was to further the understanding of the kinematic and precipitation structure of convective cloud systems (Dodge et al, 1986). Figure 1-1 (page 7 -- the figures in each section are located at the end of that section) shows the special observational platforms that were available under the SPACE/COHMEX program.

The original objectives of this investigation included studies of both isolated deep convection and of (small) mesoscale convective systems that are observed in the Southeast environment. In addition, it was proposed to include both observational and comparative numerical modeling studies of these characteristic cloud systems. Changes in scope were made during the course of this investigation to better accommodate both the manpower available and the data that was acquired. A greater emphasis was placed on determination of the internal structure of small mesoscale convective systems, and the relationship of internal dynamical and microphysical processes to the observed cloud top behavior as inferred from GOES IR (30 min) data. Because of the lack of quality graduate students[1], the numerical modeling component of this investigation did not progress as planned.

The major accomplishments of this investigation were as follows:

a) Considerable effort was devoted to analysis of the 13 July case, in which a mesoscale convective system was observed to form, evolve and dissipate over the SPACE network. The evolution of 3-D precipitation distribution and the association with the kinematics has been examined in detail. Furthermore,

---

1. The atmospheric science program at UAH was formally started in Fall, 1990. Prior to this time graduate students were available only from other acedemic units. Because graduate levels courses in atmospheric science were not originally available, it was difficult to provide the proper training to students who lacked general motivation for the discipline.

GOES IR data have been combined with the radar analysis to establish relationships between the internal precipitation/kinematic structure and the evolving cloud-top patterns. Details of this case are presented in Section 2.

b) A second MCS observed on 15 July was analyzed in a similar fashion. In this case a long-lived but relatively small MCS moved over the SPACE mesonet during the morning hours. This case was much less intense than that of 13 July, and some interesting differences in general behavior were observed. Details are given in Section 3.

c) A preliminary case study analysis was conducted on a series of convective events over the SPACE mesonet on 28-29 June. Time constraints did not allow further analysis of this event. General aspects of this case are summarized in Section 4.

Analysis of these three cases has defined some of the structural characteristics of small MCSs and the degree of similarity in 3-D structure and evolution to the larger-scale MCSs documented in both tropical and midlatitude regions. Detailed analysis of two MCS cases has shown considerable variability precipitation distribution and in kinematic structure and evolution. Such work is highly relevant to long-range NASA initiatives in the remote sensing of cloud properties and in scientific areas such as TRMM.

In addition, two ancillary studies were completed during the course of this work. In the first an investigation of attenuation of microwave radiation by rain was completed to promote analyses of the above cases. In the second case an investigation was initiated to take advantage of a particular opportunity. These two studies are defined below.

d) A detailed investigation of attenuation of C-band microwave radiation was conducted to enhance the analysis efforts under items (a) and (b) above. The NCAR CP-4 C-band radar provided the most complete areal radar coverage during the course of the COHMEX program. Because time changes in precipitation distribution (reflectivity factor) were a fundamental goal, corrections for attenuation were required to eliminate the artificial effects of attenuation. General details of this study are provided in Appendix A.

e) A study of automated classification of hydrometeor images was conducted with the assistance of V. Chandrasekar (at no cost to this project) and a graduate student (Electrical and Computer Engineering). After only one year an M.S. thesis detailing the technique of hydrometeor classification of images obtained from 2-D probes mounted on aircraft was finalized. This work is generalized in Section 5. The results of this work will likely be of potential benefit to the scientific objectives of NASA-sponsored TRMM and related programs.

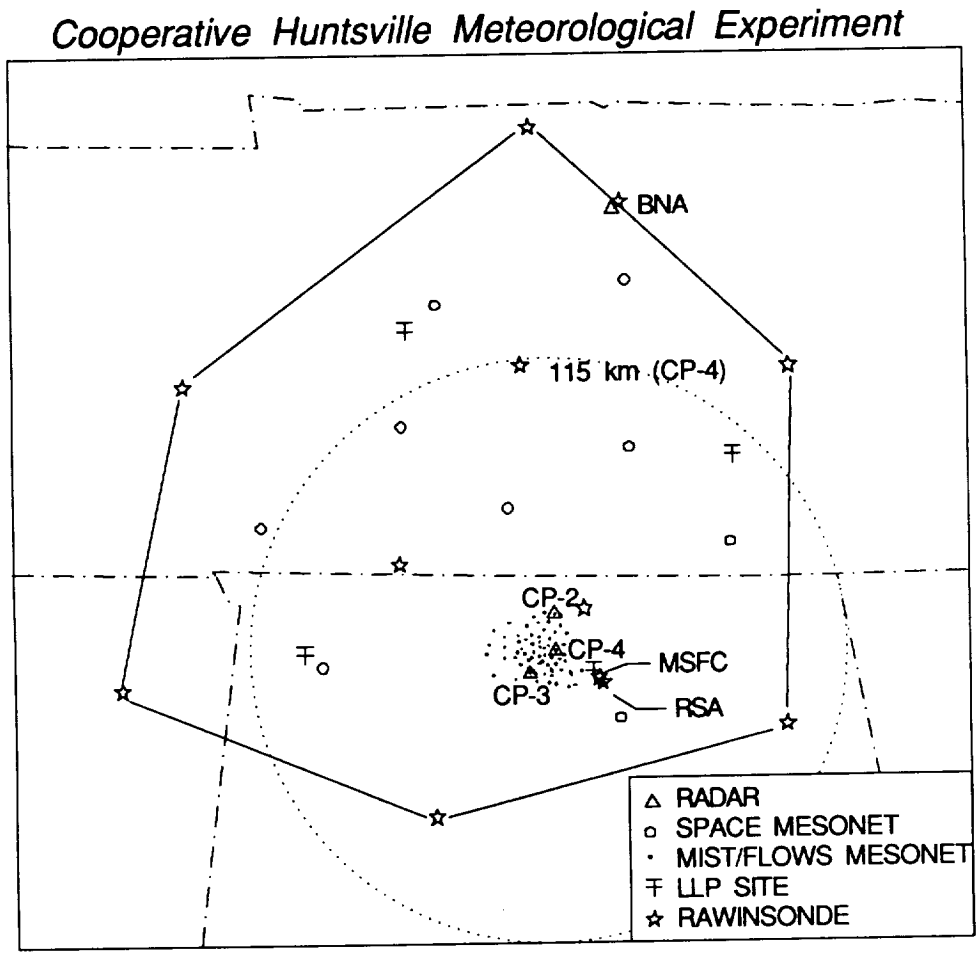

Figure 1-1. Special instrumentation employed for the Cooperative Huntsville Meteorological Experiment (COHMEX), conducted in June and July 1986. The MIST/FLOWS high density network in shown as a cluster of points in the vicinity of CP-4.

2. ANALYSIS OF THE 13 JULY MCS

The MCS observed on this day formed and evolved over the COHMEX network within the range of the Doppler radars. Thus, good documentation on the development and dissipation of this MCS is available. In many respects, the structural characteristics of this MCS resemble those of larger-scale MCSs in both tropical and midlatitude regions. Although the rawinsonde network was not operational on this day, serial soundings were acquired at 1200, 1800, 2000 and 2300 UTC from locations RSA and MSFC (see Fig. 1-1 for locations). The analysis incorporates RADAP data, Doppler radar data from CP-4, CP-2 and CP-3, surface data from both the SPACE and MIST mesonets, and GOES satellite. Special effort was made in this case to quantitatively combine GOES and IR and Doppler radar data to examine the MCS evolution.

Several goals have been defined for this case, including (1) a general description of the growth and structure (kinematic and precipitation) of the MCS observed on this day; (2) a detailed examination of the development of precipitation within the anvil region of the MCS; (3) a definition of the relationship between the cloud and mesoscale flows, with a focus on variability of deep convection, and the impact of deep convection on the MCS; and (4) remote sensing applications of this case. These objectives required considerable analysis of both cloud-scale flows (using multiple Doppler radar) and mesoscale flows. The following subsections summarize work conducted on both scales.

2.1 Synopsis

The development of the MCS was relatively rapid as demonstrated in the visible GOES images presented in Fig. 2-1. The VIS imagery show that formation of deep convection was associated with a comma cloud formation, apparently indicative of a short-wave disturbance not resolved by the NWS rawinsonde network. The first significant development of deep cumulus activity began near 1700 UTC (with particularly rapid expansion beginning near 1800), and the first echo (18 dBZ threshold) was observed in the RADAP data at 1730 UTC 80-120 km west-southwest of Nashville (BNA). Much of this development occurred within range of the CP-4 radar which began operations at 1645 UTC. Activity 80 km SW and 70 km ESE of CP-4 at 2001 UTC (Fig. 2-1a) later dissipated in favor of the cloud features north and northwest of CP-4. By 2000 UTC (Fig. 2-1a) the MCS was in a state of rapid expansion and consisted of an expanding anvil north of CP-2 and a developing E-W convective line immediately to the west. Two hours later at 2201 UTC (Fig. 2.1b) the MCS cloud shield had expanded considerably as additional components of the system formed. Details of this expansion are elucidated below.

Figure 2-2 presents two soundings close in time to the developing MCS. The location of the 2004 UTC sounding is shown in Fig. 2-1a. The MCS formed within an environment having appreciable low to middle level moisture (precipitable water values of ~50 mm) and appreciable instability (CAPE ~2500 J kg^{-1}). Environmental winds were primarily zonal, with a peak u (east-west) component of +10 m s^{-1} near 85 kPa and a minimum u of -5 m s^{-1} near 20 kPa. The east-west orientation of this MCS was thus parallel to the environmental shear vector. It should be noted that the instability of the environment, while not unusual, was on the high side (approximately the top 20%) for cases observed during the COHMEX program (e.g., see Williams et al, 1987).

This MCS generated high totals in both rainfall and cloud-to-ground lightning. Total rainfall amounts displayed in Fig. 2-3 were determined from all available raingage sites (special mesonet, TVA, NWS and observer) to determine spatial characteristics of total rainfall over both the SPACE mesonet and MIST mesonet. Peak point values are close to 50 mm, and a similar degree of spatial variability is apparent over both networks. The extreme variability over spatial scales of several km over the MIST/FLOWS network (Fig. 2-3) was produced by intense, transient deep convection between 2000 and 2100 UTC. Total cloud-to-ground (CG) lightning count patterns (Fig. 2-4) show a band extending from the western SPACE mesonet eastward to about 50 km east of the MIST/FLOW network. Several regions have peak densities exceeding 250 strikes per 125 km^2 (one grid box). The MCS total count was ~30,000 strikes. The basic structure of the CG distribution is largely replicated in the analysis of total rainfall. The CG information also illustrates the rapid MCS intensification, followed by rapid dissipation just behind the SW border of SPACE network.

Figs. 2-5, 2-6 and 2-7 summarize the RADAP and GOES IR history of this MCS. As stated above, first echo exceeding the 18 dBZ RADAP threshold at 0.5 deg elevation occurred at 1730 UTC. Prior to 1730, deep convective activity not related to the development of the MCS of interest formed east and southeast of CP-4 near 1600 UTC and dissipated shortly after 2000 UTC -- see Fig. 2.1a -- as the convective components within the expanding MCS to the northwest intensified. As shown in Fig. 2-5, the area of the MCS occupied by the 18 dBZ contour expanded linearly with time to a maximum of ~12,000 km^2 at 2300 UTC. The areal extent after this time is unknown since the system moved beyond the maximum range of 232 km. Also shown in the top panel of Fig. 2-5 is the area of 18 dBZ at 2.0 deg elevation, and the area within the 35 dBZ contour at 0.5 deg elevation. At the range involved here, the 2 deg scan intersects the system at middle levels (5-11 km), thus the 2 deg scan yields information on the precipitation distribution within the anvil region. Figure 2-5 indicates that the area of 18 dBZ at 2 deg exhibits a rather distinct inflection, increasing substantially just before 2100 UTC. Interestingly, this point of inflection is close in time to the peak in the area of 35 dBZ echo at 0.5 deg, which is a

good measure of the convective cloud activity. The lower panel of Fig. 2-5 shows a subjective estimate of the number of individual convective cores as determined from PPI plots of the type shown in Fig. 2-6. Since a 2.2 deg radar beam at 180 km range is 6.5 km in diameter, only the most substantial convective cores (either large single cores or closely packed aggregates of small cores) are are resolved at high reflectivity thresholds. This value thus yields a measure of the number of *major cores*. The peak occurs near 2040 UTC, which precedes the areal maximum of the 35 dBZ contour by 20 min. Identifiable mesoscale regions of deep convection that were observed during the MCS life cycle are labeled (A, B, and C) in Figs 2-6 and 2-8.

Finally, the minimum cloud top temperature determined from GOES IR data is presented in the lower panel of Fig. 2-5. The minimum temperature lags the number of convective cores, but coincides with the peak 35 dBZ area. Subsequent cloud top warming then occurs at a relatively slow rate. A similar type of behavior is found in the area of given cloud top temperature thresholds, discussed in following subsections.

The interpretation of the scenario suggested by Fig. 2-5 is the following. As the number of convective cores increased, a point is reached in which interactions, most notably mergers of convective elements and/or their associated outflows, take place. Outflow mergers were observed over the MIST/FLOWS mesonet between 2000 and 2100 UTC and were associated with the development of intense, transient deep convection (see Section 2.3.2). Merger events were also evident in the formative stages a the squall line component (B). There is evidence in this case that the merger process increased the overall upward flux of mass within the MCS, and that at some point this upward flux was of sufficient strength to generate a significant amount of precipitation within the anvil region.

The initial stages of the MCS were associated with very intense convective elements, some of which are described in detail below. Severe weather in the form of strong/damaging winds were common over south-central Tennessee and northern Alabama between 1900 and 2130 UTC. (Storm Data documents a number of damaging wind events involving toppling of trees and power lines). The Doppler radars (CP-2, CP-4 and FL-2) and surface mesonet collectively detected at total of 25 microbursts on this day, by far the most active day during COHMEX (Atkins and Wakimoto 1990). Thus, this event was similar to that of MCC formation, in which severe weather activity was found to be most prevalent during the initial stages (Maddox, 1980).

2.2 Precipitation distribution and cloud-top history

As stated above, one of the goals of this analysis effort was to document the four-dimensional behavior of precipitation within this MCS. Figures 2-7 and 2-8 provide a detailed overview picture of the cloud top and precipitation development over the 5 h period 1900 to 0100 UTC. This sequence begins ~90 min after first echo (within the MCS) and captures the intensification to late mature stages of the MCS. Both the IR and CP-4 radar sequences show a rapid areal expansion of the system between 2000 and 2300 UTC. (The VIS images at 2000 and 2200 UTC, Fig. 2-1, should be compared with the IR images at these times.) The major components (A,B, and C) noted in the previous section are also visible in the IR and CP-4 radar information. At 1900 UTC the 1.5 deg PPI scan from CP-4 shows scattered intense convective activity clustered into three primary regions. The cluster of cells NW of CP-4 is associated with the eventual core of the MCS. A second cluster/line SE of CP-4 defines the region of activity that formed earlier in advance of the MCS. This activity weakened with time as shown in Figs 2-8a-c. Finally, a limited region of intense convection WSW of CP-4 at 1900 appears to become an integral component of the MCS, forming the north-south oriented line (C) which adjoins the MCS by 2100 UTC (Fig. 2-8c) and attains a peak intensity about 1 h later at 2200 UTC (Fig. 2-8d). However, unlike the east-west line (B) west of CP-4, the north-south line C was not a long-lived feature and did not develop appreciable stratiform precipitation along its trailing edge.

Movement of each mesoscale component, in particular the southward motion of the east-west line B and the eastward advance of the north-south line C, produces a net cyclonic rotation of the system. Cyclonic vorticity was also observed directly on smaller scales, from the cloud scale to the cloud cluster scale. For example, several individual cloud systems, labeled as "CYC" in Figs. 2-8b,c, exhibited intense rotation at middle levels. In addition, a pronounced cyclonic rotation of a larger scale (~10 km) was observed at middle levels in association with the dissipation of intense but transient convective elements near CP-4 between 2100 and 2200 UTC. The residual echo associated with this circulation at 2158 UTC (Fig. 2-8d) is labeled "RES".

Turning now to the details of the MCS expansion, we first focus on the CP-4 low-level reflectivity patterns of Fig. 2-8b. This system first showed signs of organization at 2000 UTC, when MCS subcomponents A, B and C are evident. In addition, two general east-west lines of less intense convective cells are denoted as B' and B", the former of which formed along an outflow boundary associated with A. Line B" formed in advance of pre-existing outflow boundaries by unknown processes, perhaps boundary layer roles. Between 2000 and 2100 UTC component A weakened while B (whose distinct line components have merged) and C continued to expand. Also, an intermediate, short-lived but intense cluster of convective cells developed within 30 km range of CP-4

near 2100 UTC. Although these cells were extremely transient they left behind a prominent footprint in the IR signature, namely the cold tops of ~200 K which persisted near CP-4 even after significant low-level precipitation diminished (see Fig 2-7 b,c). Such patterns demonstrate one of the complications that arise in attempting to relate IR signatures to low-level precipitation. After 2200 cloud top temperatures continued to warm, while beneath the expanding anvil canopy stratiform precipitation exhibited significant expansion between 2200 and 0000 UTC. At 2350 UTC the MCS shows the classical structure consisting of a convective leading edge and a well-formed stratiform region with REF>30 dBZ, and a band of reduced REF in between. The expansion of precipitation is this case was thus coincident with a slow warming of anvil cloud top. In comparing Figs 2-7 and 2-8, it should also be pointed out that a significant extent of the northern portion of cold anvil had virtually no precipitation at the surface.[2]

The relation between cloud top and precipitation distribution within the east-west line (component B defined in Fig. 2-8) has been further quantified by examining north-south vertical sections of Z averaged over some east-west distance of the line. This particular region was selected because of good radar coverage of line feature B during the period of stratiform precipitation development. The motivation here is to define the formation of precipitation within the stratiform region and quantify the relation between the evolving cloud top surface and associated precipitation distributions below. The averaging domain for this analysis is shown in Fig. 2-8 (panels c-f) for times between 2100 and 0000 UTC. Averages of reflectivity factor where computed over the interval $-90<x<-20$ km (CP-4 coordinates), while radial velocity was averaged over a more limited domain of $-60<x<-40$ km. Reflectivity data were averaged in a linear sense according the the following:

a) Convert REF units from dBZ to Z [$Z = 10^{0.1*dBZ}$];
b) Average the linear Z units to obtain Z_{av} (only if dBZ>0);
c) Convert Z_{av} back to log units [$dBZ_{av} = 10 \log(Z_{av})$].

GOES IR data were averaged on a McIDAS system over the same horizontal domain as reflectivity. Approximate corrections for viewing angle projection of cloud top were applied (see footnote 2). A representative sounding (Fig. 2-2) was used to convert brightness temperature (assumed to be black body) to height. In this conversion, we computed θ_e values corresponding to maximum and minimum parcel temperatures arriving at a given temperature level near cloud top, and then computed an average θ_e. Height errors originat-

---

2. The GOES satellite viewing angle of cloud top features, located 14 km AGL and 35 deg latitude, produce a false northward shift of ~ 9 km in the apparent location due to the projection of cloud top onto the surface.

ing from the temperature-height conversion alone tend to maximize near the tropopause level and are generally less than several hundred meters. The resultant product is a series of north-south vertical planes displayed in Fig. 2-9.

The averages reveal the formation of a classical squall line structure, with a convective component on the leading edge (on the south side) and an expanding stratiform component along the trailing boundary. At the initial time of 2057 UTC two separate convective regions are apparent, and the stratiform precipitation is largely above the melting level. This dual convective core structure (at 2057 and at 2258) points to the potential importance of discrete propagation along the gust front produced by the more intense convective elements that comprise the second line (see Fig. 2-8 for horizontal mappings at 2 km). The fact that the average IR top lay below the average REF top indicates the presence of a few strong cells within the line. The averaging technique employed (i.e., averaging of linear Z_e units) emphasizes the presence of high reflectivity cores. As time progresses stratiform precipitation expanded both aloft and at the surface. The initial development of stratiform precipitation between 2100 and 2200 UTC is obscured by the presence of trailing convective activity (Fig. 2-8d and Figs. 2-9b,c) which inflates the average REF. The contamination produced by the convective component is eliminated below by deleting the contribution of convective cores to the average. By 2258 UTC a well developed stratiform region with a prominent radar bright band had become established. It is noteworthy that as the stratiform region emerged, the convective region weakened and widened in the north-south direction. The widening and weakening of the convective region is particularly pronounced between 2300 and 2350, as shown if Figs. 2-9 d-f. Such a behavior may be due to the fact the the squall line moved into a low-level environment that had likely been cooled by previously convective activity (i.e., component C in Fig. 2-8 and panels b1 and c1 of Fig. 2-9).

Fig. 2-9 also illustrates the time-dependent nature of the relation between cloud top and echo top (5 dBZ) within the stratiform region. Over the period 2058 to 2350 the distance increases from small values at 2058 to 1-2 km by 2350. This behavior is in contrast to the increasing vertical gradient in REF (between REF values of 5 and 20 dBZ). In the next section these cloud top / reflectivity patterns are related to inferred mesoscale vertical motions within the anvil.

2.3 Internal kinematic structure.

The evolving flows within the MCS have been examined from the mesoscale viewpoint through VAD analyses and compositing techniques, and from analysis of both single and multiple Doppler radar data. The following subsections are divided into discussion of primarily mesoscale flows and cloud scale flows.

2.3.1 Development and structure of mesoscale flows

Characteristics of mesoscale flows were determined from compositing techniques (as done in the previous section) applied to the radial velocity field of component B, and from VAD analysis of the region around CP-4. The paragraphs below outline some of the characteristics of the mesoscale horizontal and vertical flows that are of relevance.

Composite radial velocity analysis

The composited radial velocity patterns shown in right panels of Fig. 2-9 reveal a changing structure of component B that is as unsteady as the reflectivity fields. Between 2100 and 2200, a jet-like profile in the u velocity is seen to emerge at middle levels within the convective region. At higher levels in advance of the convective region, flow is directed in the opposite direction from east to west. The patterns during this initial period also suggest the development of a negative vorticity across the convective region at middle levels (by 2157 UTC -- Fig. 2-9c2) which appears to expand and weaken after by 2258 UTC and after. The presence of a secondary minimum in radial velocity within the anvil region at 2258 points to the development of the rear inflow jet which apparently occurred in response to the development of stratiform precipitation. Further details on this inflow jet are provided below. Comparison of flow magnitudes during the last hour of observation (Fig. 2-9d2-f2) show that all flows weakened with time as the system entered the dissipating stage. Such a decline closely paralleled that seen in Z_e and illustrates that this particular system was distinctly unsteady from both a microphysical and kinematic viewpoint.

VAD analysis

VAD analyses were completed for 20 individual volume scans acquired by CP-4 as the MCS *evolved* and moved over the the radar. It is emphasized at the onset that the MCS did not come close to achieving a stationary (steady) state. In fact, it appears that temporal changes in structure are comparable to changes by horizontal advection for this system. Because maximum elevations were limited to either 15° or 18.5°, the EVAD technique described by Srivastava et al (1986) was not attempted here. A conventional VAD analysis (based on the work of Browning and Wexler, 1968) was completed using software acquired from NCAR. This software is based on fitting (in a least squares sense) a sinusoidal curve of the following form to the VAD data:

$$V_r(az) = C0 + C1\sin(az) + C2\cos(az) + C3\sin(2az) + C4\cos(2az).$$

In addition, the following parameters were used in the analysis:

- The primary range was 40 km; additional ranges of 35, 45 and 48 km were used to fill gaps.
- The terminal fall speed is assumed to depend only on Z_e according to the formula $V_T = AZ_e^B \exp[(0.1z)^{1/2}]$, where A=0.4 and B=0.2 above the melting level (4.0 km AGL) and A=3.0 and B=0.1 above the melting level.
- Filtering was applied on 2 km of data in the radial direction.
- Objective editing was done to eliminate points greater than 1.5 standard deviation from the fitted curve.

Additional subjective editing and inspection of raw data fields, was expended in producing accurate VAD-derived quantities, which include average Z_e, divergence, and horizontal wind. Vertical motion (w), obtained from downward integration of the divergence field, has been constrained to a zero boundary condition at both the surface and estimated cloud top (obtained from the GOES IR data).

Results of the VAD analysis from 20 individual volume scans, covering the 2120- 2350 time period (with a 40 min gap in between) are presented in Fig. 2-10. The 40 min gap between 2200 and 2243 provides a separation in the analysis from an initial convective regime, to a stratiform regime after 2243 UTC. This VAD analysis samples the central portion of the general anvil shield associated with the MCS as shown in Fig. 2-7. Although the VAD domain overlaps a small portion of the averaging domain of convective line B, results from the VAD domain will not in general apply to that of the B domain in view of the contrasting evolution seen in each region. For example, the VAD region experienced a brief episode of intense convection near 2100 UTC, which was following by a sudden absence of deep convection, and the appearance of stratiform precipitation. In contrast, the B region, as demonstrated in previous sections, experienced a more steady period of propagating deep convection in the form of a squall line. However, there is some evidence that the mesoscale updraft in each domain is similarly located toward the rear of the system.

The initial portion of the VAD analysis covers the latter stages of deep convection within the VAD region. Although REF peaks at low levels near 2.5 km, there is no evidence of a radar bright band as there is for the stratiform regime. The fields of divergence appear to be a scaled-down version of profiles that typify deep convection. Convergence is dominant within the lower middle levels, and divergence is weakly evident at low levels and prominent at high levels. The vertical motion profile is thus dominated by updraft which initially exceeded 75 cm s^{-1} near the 9 km level. Such a value is appreciable in view of

the large radius used (40 km) in the analysis. The horizontal velocity fields displayed in panels c and d represent perturbations from the ambient values and are defined as

$$V_i' = V_{VAD} - V_o,$$

where V_i' represents one of the horizontal wind components u' or v', V_{VAD} represents the wind component determined from the VAD analysis, and V_o represents the ambient wind components determined from the (unperturbed) 1800 UTC Redstone sounding (Fig. 2-2). It is likely that the environmental winds V_o exhibited considerable evolution after 1800 UTC. Although the absolute values may not be valid, the nature of the perturbation values are probably satisfactory. The system appears to have rearranged the momentum field by decreasing u momentum at middle levels, and increasing u momentum at lower and upper levels.

In the stratiform region, a distinct bright band is apparent, and the divergence profile differs from that of the initial period. Convergence is significant at middle levels, showing an increasing tendency with time. The standard mesoscale updraft/downdraft couplet is analyzed here, although the patterns differ in relative location and magnitude from those documented in larger systems. For example, the updraft/downdraft interface is located near 6-7 km, well above the melting level location (4.5 km) that is often the case (e.g., Rutledge et al, 1988). Peak downdraft is analyzed near 4 km and is located just above the level of the rear inflow jet (depicted in the v' field of Fig. 2-10d) which is shown to increase over the analysis period. Further details of the inflow jet are given in vertical sections presented below. The mesoscale updraft magnitude ranges from very low values (<5 cm s^{-1}) at 2300, increasing to ~ 14 cm s^{-1} by 2350 UTC. Even the latter values are considerably less than those observed at 2130 UTC, and those summarized in Rutledge et al (1988).

The incorporation of satellite information as an upper boundary condition with VAD analysis techniques offers great potential for comprehensive analysis of MCSs. Such information can be used to define cloud top height and the vertical motion of cloud top. The former was utilized in this study and is especially valuable in cases where the distance between echo top (~ 0 dBZ or any other appropriate threshold) and cloud top is large. In Section 2.2 above it was noted that this distance increased with time from approximately several hundred meters initially to ~ 2 km as the stratiform region matured and expanded horizontally. The upper velocity boundary is a more difficult problem since an estimate of the terminal fall speed of small ice crystals at cloud top is required.[3] Thus, a knowledge of ice crystal habit and nucleation characteristics

---

3. We should note here that the characteritics of cloud top microphysical processes, and the microphysical behavior above ~ 8 km altitude, are generally unknown due to the absence of *in situ*

is required, but such information is generally lacking at temperatures in the -60 to -75 °C range. Ice crystal fall speeds are probably on the order of 20 cm s^{-1} (A. Heymsfield, private communication), which generally exceeds the mesoscale updraft/downdraft magnitude within the upper 2 km of most MCSs.

In order to further understand the behavior at cloud top, the average IR brightness temperature was calculated over the circular region of 40 km radius used in the VAD analysis. Shown in Fig. 2-11, this average temperature quantity shows smooth variations over a 4 h time period. The initial temperature decrease (signifying a rising cloud top) is followed by a more prolonged temperature increase (downward motion of cloud top) at 2200 UTC. Although the initial rise in cloud top from 2100 to 2200 can be related to the 50-75 cm s^{-1} mesoscale updraft diagnosed form the VAD analysis (Fig. 2-10), the tendency in the subsequent decent of cloud top, which was gradual between 2200 and 2300 and more rapid after 2300, is not mirrored in the upper-level vertical motion tendency of the VAD analysis. For instance, w is very weak between 2240 and 2300 UTC even though cloud top descends at a slow rate, while near 2350 w is more significant in the presence of a greater rate of warming at cloud top. In fact, the inferred 22 cm s^{-1} rate after 2300, at a time when the system is weakening, may be reflective of zero vertical motion at cloud top. In view of the previous discussion, it may not necessarily be valid to relate this T tendency to vertical motion tendency, since particle habits (and hence fall speeds) could change significantly during the transformation from convective to stratiform regimes.

If cloud top particle motion is assumed to be uniform downward at ~20 cm s^{-1}, as suggested in Fig. 2-11, then an estimate of cloud-top motion can be obtained from the difference in IR measurements from two times. Such a calculation was done on the IR averages over the same domain, $-90<x<-20$, as was done for REF in Section 2-2, over the 2300 to 0000 UTC period. The average temperature change over this domain is shown in Fig. 2-12 (top panel) and is compared with the average REF analysis and corresponding cloud top distribution (bottom panel) at 2350 UTC. There are appreciable horizontal variations in this difference, and the region of inferred updraft and downdraft (at cloud top) is consistent with the VAD analyses presented above. In particular, downward motion is indicated at cloud top over the transition region, or reflectivity trough (i.e., the relative minimum in REF at low levels), and ascent at cloud top is shown over the rear portion of the stratiform region slightly north of the center of the enhanced Z_e in the bright-band region. This also corresponds to a relative peak in the IR-determined height of the St anvil cloud. It is recognized that temperature changes over such a long period may not be valid

---

measurements.

in view of the nonsteady nature of this MCS, but it illustrates that such a calculation may have quantitative value if appropriate time and space scales are selected.

Analysis of north-south vertical sections

Some of the features resolved in the previous analyses can be clarified through inspection of vertical north-south sections passing through CP-4. The location of these sections has been indicated on a number of previous figures. These sections were obtained via interpolation of volume scan data (the same as used in the VAD analyses) to a 3-D grid and then forming vertical cuts in the north-south direction through the CP-4 radar location. These products therefore contain far less detail than actual RHIs.

Figure 2-13 presents analysis of REF and V_r (which is approximately the v horizontal wind component) at 2130, 2258 and 2350 UTC. Superimposed on each panel are individual profiles (Z or *w*) taken from the VAD analysis. At 2130 UTC (Figs 2-13a,b) deep convection is located very near CP-4, and significant upward motion is shown in the *w* profile of panel b. At this time, the mean position of the convective cores of mesoscale component B (mostly west of this plane) is near y=-25. Cells located near y=-75 (Fig. 2-13a) are associated with the north-south convective line (mesoscale component C) shown in Figs. 2-8c,d. Within the anvil region north of CP-4 the developing rear inflow jet is shown and has a peak inflow speed of -12 m s^{-1}. Significant outflow at higher levels exists within the anvil above the midlevel inflow jet. This outflow weakens with time as shown in panels b,d, and f, while the inflow jet intensifies and protrudes well into the MCS by 2350 UTC. At both 2258 and 2350 UTC this jet enters the system near the 7 km level at y=75 and gradually descends to low levels near the convective region while accelerating to speeds of >12 m s^{-1} after having passed through 100-150 km of the MCS. Mesoscale downdraft shown in the profiles of panels d and f are consistent with the location of this descending current. Such a structure is quite similar to that found in larger squall line systems that exist in higher-shear environments (Smull and Houze 1988). This study thus documents the development (time-dependent nature of the low-level jet).

When and where did the low-level jet develop in this case? For component B, the jet was well established by 2130 UTC, but its formation time and previous history is unknown. An inflow jet showing similar structure existed earlier at 2006 UTC within the stratiform region of component A. The CP-2 RHI in Fig. 2-14 illustrates the inflow jet within this component and its apparent interaction with the very intense convective element located at near range. The relative location of this RHI is indicated in Figs. 2-1, 2-4, 2-7 and 2-8. The peak speed within this jet (which is not the same feature as in the line) is approximately 15 m s^{-1}, and a similar sloping (descending along the flow) struc-

ture is evident here. Noteworthy here is that the jet was fully developed 2.5 h after echoes associated with A first formed and ~1 h after stratiform precipitation was observed in the RADAP data.

2.3.2 General structure and evolution of the deep convective components

The evolution and structure of an MCS is closely related to the general, time-dependent characteristics (mass fluxes in updraft, downdraft, precipitation processes, etc) of deep convection. The time series of Fig. 2-3 points to a close relation between deep convective activity (35 dBZ, 0.5 deg elevation) and generation of precipitation within the anvil region (18 dBZ, 2.0 deg elevation). What physical processes determine this relationship? Two of the more obvious mechanisms that have been considered (e.g., Yanai et al 1973) include:

a) direct detrainment of cloud material and residual buoyancy within the updraft outflow. This effect is most pronounced within the most vigorous clouds. For instance, Figs. 2-14 and 2-15 show RHI scans (Z and V_r through the cores of two particularly vigorous clouds during the period in which deep convection was most intense. Each cloud system exhibits high Z_e (~60 dBZ), high echo top and appreciable upper level divergence.

b) static detrainment of cloud and buoyancy from weaker cloud systems that exhibit less significant upper level divergence. The term static here refers to the greater tendency of such cloud systems to simply leave behind their residual material as they dissipate.

A broad spectrum of convective cloud intensities (cloud tops ranging from 8 to 17 km AGL) was observed within the relatively unstable environment of the 13 July MCS. Only a relatively small fraction of the total attained very intense levels; two of these are shown in Figs. 2-14 and 2-15.[4] In both cases the radial velocity patterns indicate appreciable radial divergence across the updraft region at high levels. In Fig. 2-14 the total differential is 50-60 m s^{-1} at a height of 13 km and indicate updrafts ~30 m s^{-1} or greater. Both RHIs also show appreciable outflow speeds within the anvil region further removed from the convective core. After the peak in overall convective intensity at 2100 UTC, the intensity, size and longevity of cloud systems declined in a manner consistent with that portrayed in Figs. 2-8 and 2-9. In Fig. 2-16 a CP-4 RHI at 2347 UTC shows a relatively weak convective core exhibiting a very small radial velocity differential at 100 km range. This plane also captures a dissipating but more intense

---

4.
The variability in deep convection observed in this case is quite striking. In fact, *it is hypothesized that the varibility in deep convection within the MCS of the low-shear subtropical environement is greater than within the MCSs of the Great Plains environment.* Such an hypothesis has important implications to both spatial and temporal sampling issues of concern to TRMM.

core at 80 km range having appreciable divergence (15 m s^{-1}) aloft. This picture emphasizes the need to understand cloud characteristics and their relationship to mesoscale flows in which they are embedded, over the entire life cycle of deep convection, something that has not been fully addressed here. Of particular importance are details (microphysical and kinematic) of cloud weakening/dissipation as a function of cloud intensity, etc., and the relation to the observed distribution of Z_e and mesoscale flows within the stratiform region.

2.4 Development of stratiform precipitation

In the previous sections the appearance and expansion of the stratiform precipitation region was described. The temporal and spatial characteristics of this expansion were highlighted in the RADAP analyses (Figs 2-3 and 2-4), the CP-4 horizontal (PPI) sections, and in the averaged vertical section analysis (Figs. 2-8 and 2-9). In this section a further quantification of the evolution of the stratiform region will be presented. This discussion will be separated into two time periods, one near the development of stratiform precipitation (2130-2148 UTC) and the other centered on the early mature structure of stratiform precipitation (2258-2335 UTC). Time differencing of Z_e between two times is used to calculate rates of Z_e growth. Corrections for attenuation, which have been applied here (Appendix A), are therefore important in this calculation.

The initial development of stratiform precipitation can be detailed more accurately by examining a subregion of that used in the REF composites of Fig. 2-9. The motivation is to eliminate the contribution of REF from the trailing convective cells (see Fig 2-8c for location) during the 2130-2148 time period when stratiform precipitation was expanding at middle levels and settling to low levels. The modified composite sections shown in Fig. 2-17 indicate an *in situ* intensification and horizontal/vertical transport of REF over this 18 min period. The time difference in REF, i.e.,

$$DIFF = Z_{av}(2148) - Z_{av}(2130)$$

is presented in Fig. 2-18 to quantify the magnitude of the local intensification and transport.[5] A vertical profile plot of the average values of this difference over the y interval indicated in Fig. 2-18 is shown in Fig. 2-19a. Relatively high DIFF values of 5-10 dBZ are analyzed in a horizontal layer centered at a height

---

5. For an accurate calculation of the difference, a good estimate of attenuation is needed since CP-4 was viewing this region along the convective line as shown in Fig. 2-8. Of particular importance at during this time period is the presence of relatively intense precipitation just to the west of CP-4. This correction was applied here and elsewhere to all CP-4 data. Appendix A elucidates some of the details of this calculation.

near 4 km, just below the melting level. A second peak located at middle levels near (y,z)=(50,9) results from northward horizontal transport in the anvil outflow. Differences much less than zero for $y<0$ are due to the southward advection of the convective region. We note here that there is considerable structure in the patterns of negative difference which are apparently indicative of highly transient features in the convective region.

We now focus our attention on the central portion of the stratiform region and examine the average values here (Fig. 2-19a). Positive values in the average DIFF are located within the $3<z<11$ km layer. The peak of 7 dBZ results from downward settling of hydrometeors and the time tendency from formation of a radar bright band as the particles fall below the melting level. The increase in DIFF above the melting levels is most likely due to aggregation within the temperature layer $263 \leq T \leq 273$ K (Yeh et al, 1986). The increase in Z_e between 6 and 11 km is is possibly due to growth of ice crystals by vapor deposition and riming, which has been observed to occur within stratiform regions containing mesoscale updraft (Yeh et al 1986). The negative values in DIFF above 11 km, which occur in the presence of Z_e in the range 0-10 dBZ, can be expained as a net descent of ice crystals. Much of the increase in Z_e over this 18 min period occurs locally by several microphysical effects and is not simply a direct transport of hydrometeors from the convective region.

There is obviously a need to associate the kinematics and other radar measurements observed here with in situ measurements of hydrometeors, as has been done in Yeh et al (1986), Churchill and Houze (1984) and Willis and Heymsfield (1989).

For comparison, a similar difference calculation was completed for the 2258-2335 period, which represents a more advanced stage of stratiform region development. The stratiform region was still expanding and intensifying at this time. The average Z_e sections used in this difference are those appearing in Fig. 2-9, panels d1 and e1. Vertical profiles of Z_e and DIFF, averaged over the y domain, are presented in Fig. 2-19b. At this time the bright brand, although well established, is undergoing further intensification. The DIFF profile is positive at 1-2 dBZ between 1 and 8 km height, and strongly negative at 11 km. The negative feature is due to settling of hydrometeors as in the earlier period, except this settling appears to be more pronounced during this time interval. In Section 2.2 it was observed that cloud top also exhibited more pronounce sinking during this period. Once again, growth of precipitation is seen between the melting layer and 9.5 km height. Thus, as the stratiform region expanded and intensified (i.e., increasing stratiform precipitation rate at the surface), cloud top was sinking. At this time the VAD analysis presented above showed a strengthening of the mesoscale updraft.

One item of relevance here concerns the fraction of stratiform precipitation, relative to the total, measured at the surface. Direct measurement from recording raingage sites over the southern portion of the SPACE mesonet (Fig. 2-3b) reveals total stratiform precipitation of 2-4 mm (average 3 mm), which represents 22% of the total precipitation (average of 13.5 mm for sites 1, 2, 11 and 13). This fraction is less than that estimated from larger MCSs which average 30-40% (Johnson and Hamilton 1988).

2.5 MCS dissipation

The previous sections have described characteristics of this MCS from initiation to the late mature stage, spanning the 6 h time period 1800 to 0000 UTC. The MCS continued to weaken after 0000 UTC as individual convective cores weakened. In fact, the demise of this MCS after 0000 UTC was quite impressive. The total rainfall amounts displayed in Fig. 2-3 show an appreciable north-south gradient in rainfall and lightning counts near the south border of the SPACE network. The secondary peak near the bottom of the figure in central Alabama is attributed to secondary MCS development to the south as shown in Fig. 2-21. In fact, as the original MCS weakened, secondary MCS development occurred to the northwest, northeast and south. The southernmost MCS in Fig. 2-21 is comparable in size to that of the original MCS. This pattern of unorganized regeneration (no preferred flank) is broadly similar to that observed on much smaller scales for individual multicellular Cb systems observed under low-shear conditions. As shown in Fig. 2-22, the environment north of the MCS at 0000 UTC 14 July was even more unstable than the environment over northern Alabama at 1800 and 2004 (Compare Fig. 2-22 with Fig. 2-2).

2.6 Discussion

The observations from this case are synthesized as follows. The observed intensification and expansion of precipitation within the trailing anvil region of a component of this MCS (the east-west line B) occurred in association with a prominent mesoscale updraft of 50-70 cm s^{-1} magnitude within the region immediately to the east of the line. The stratiform precipitation development was most rapid near the time of maximum activity of deep convection. Much of this precipitation growth appears to have been generated within the anvil region, as opposed to being transported directly from the region of active deep convection. As the stratiform region further evolved to a structure exhibiting a prominent bright band, both the cloud top and radar top (roughly the 0 dBZ contour) descended in the presence of weak mesoscale updraft just below cloud top. While the vertical gradient of reflectivity factor increased during this process, the distance between the IR cloud top and the 0 dBZ level increased by a factor of 3 (800 to 2400 m) over a 2 h period. Although several of these observations warrant further study, one item of particular interest concerns the cloud

top behavior. How does the observed warming at cloud top (in the presence of upward motion ~2 km below) relate to the actual vertical motion of the top boundary? Such a question has important implications on the nucleation and habit of ice crystals near cloud top in the temperature range -60 to -75 °C.

2.5 Summary

The MCS in this case formed in a relatively unstable environment having relatively weak flow. Cloud formation patterns were suggestive of synoptic scale forcing which focused initial convection over south-central Tennessee. Initial echo was observed at 1730 UTC, and the system dissipated by ~0100 UTC after having been active for 7.5 h. The lifetime and size of this MCS were thus 25-50% that of the nocturnal MCS prevalent over the Great Plains. As in the Great Plains MCC scenario, deep convection was most intense and severe during the formative stages of this MCS. Severe weather in the form of damaging winds and copious lightning were common. The system rapidly expanded via new generation along individual and intersecting outflow boundaries. A large expanding anvil shield with associated stratiform precipitation was apparent by 2100 UTC, 3.5 h after initiation. The system reached maturity between 2300 and 0000 UTC, roughly 7 h after first echo and then dissipated very rapidly after attaining the mature state. The mature stage was characterized by a convective leading edge and a trailing stratiform region 50-100 km wide. The major axis of the system was oriented parallel to the tropospheric wind shear vector. Because the mature stage was short-lived, the fraction of precipitation produced by the stratiform region was lower (~20%) than that of larger systems documented in the literature. The system consisted of three primary subcomponents, each which exhibited different structural properties. This system was distinctly nonsteady during its life cycle. VAD analyses of vertical motion showed a dominance of initial mesoscale updraft (and rising cloud top) associated with intensification and expansion of stratiform precipitation. A variable pattern in generally weak (4-15 cm s^{-1}) mesoscale updraft activity and a more pronounced descent of cloud top marked the onset of the mature stage. A mesoscale downdraft of 30-40 cm s^{-1} magnitude was associated with a middle level, downward sloping, rear inflow jet. In contrast to the unsteady nature of the mesoscale updraft, the mesoscale downdraft was more steady and prominent throughout the mature stage. The mesoscale downdraft was deeper in this case (6.5 km - extending 2 km above the melting level) than in other documented cases. Precipitation was observed to grow appreciably within the stratiform region. In association with the intensification and expansion of stratiform precipitation, cloud top was observed to fall at a rate of ~20 cm s^{-1}.

The next section describes the structure of smaller and less intense MCS that displayed a number of difference from the one considered here.

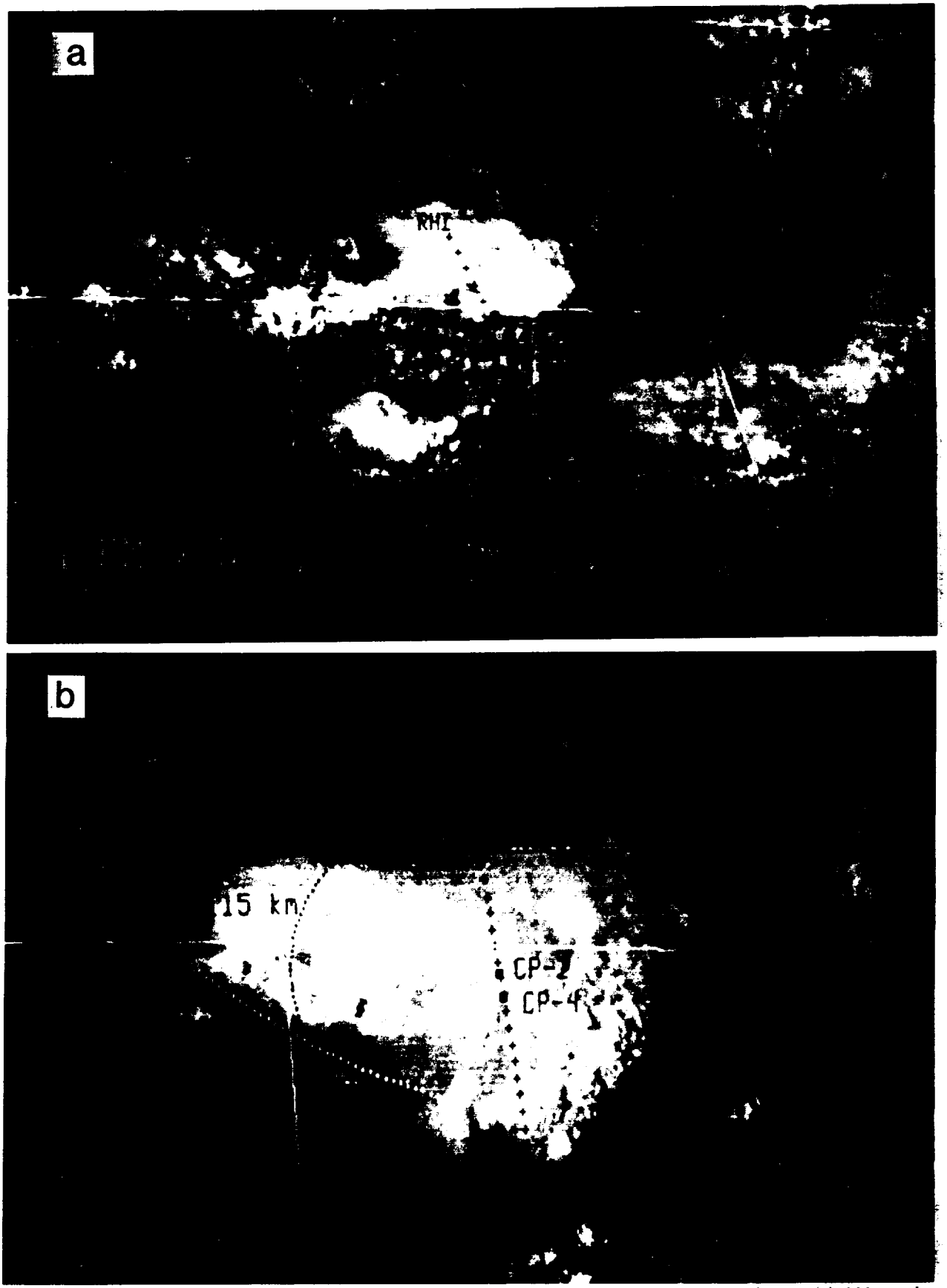

Figure 2-1. GOES visible satellite images (1 km resolution) over the COHMEX region at (a) 2001 and (b) 2201 UTC 13 July 1986. The locations of the CP-2 and CP-4 radars are indicated in both panels. Also shown are maximum ranges of CP-4 (115 km) and of the Nashville (BNA) RADAP data (240 km). An additional location, S, labeled in panel (a) refers to the sounding taken at 2004 UTC. Vertical sections presented in later figures are denoted by the +'s, which are spaced at 10 km intervals.

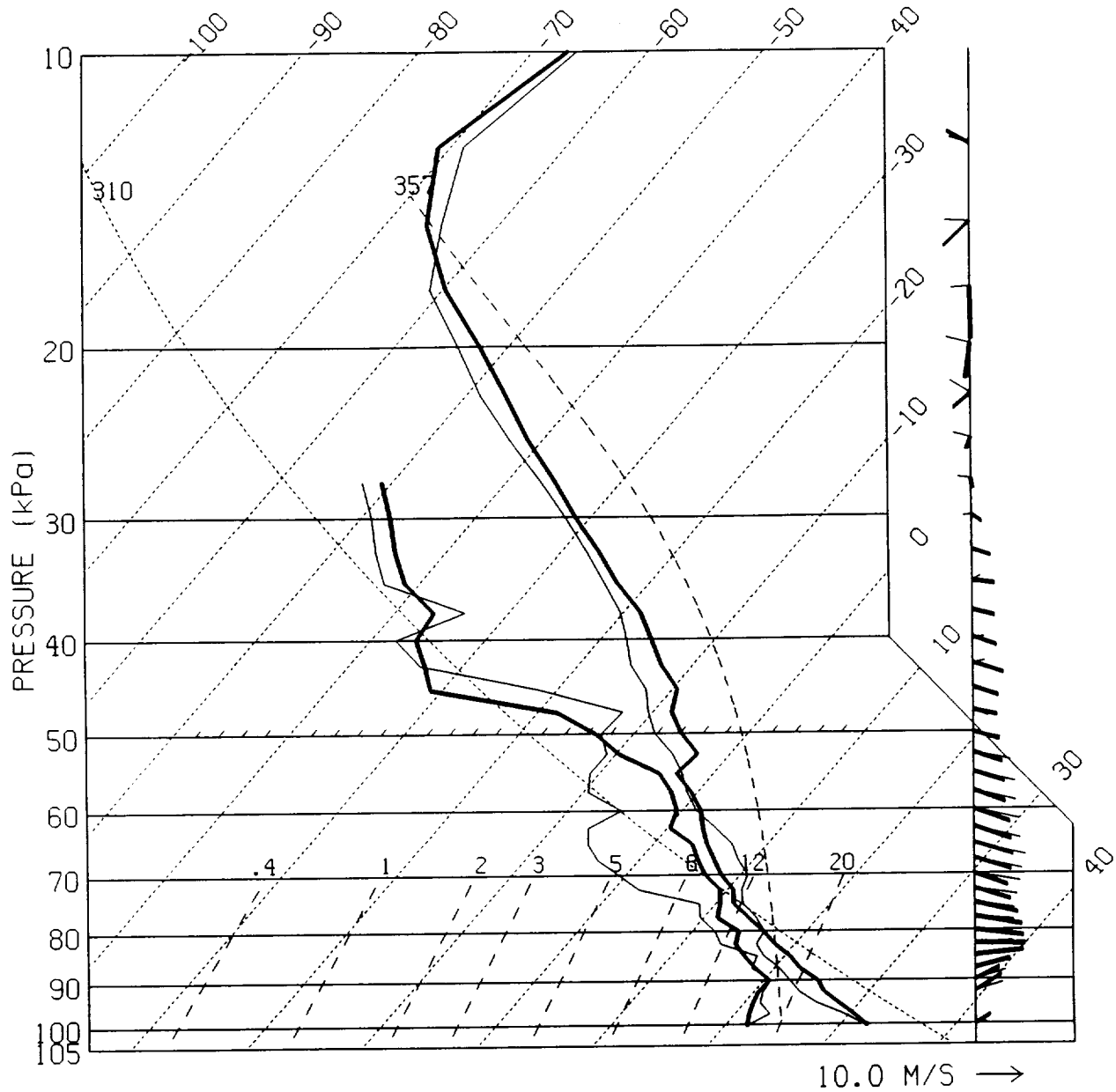

Figure 2-2. Soundings, plotted on a skew-T, log P diagram, taken from location RSA at 1800 UTC (thin lines) and from MSFC at 2004 UTC (thick lines). See Fig. 2-1 for the location of the 2004 sounding relative to the MCS, and Fig. 1-1 for relative locations of RSA and MSFC. The dashed curved line is a saturated adiabat having (0_e = 357 K) computed from average surface conditions and defines the temperature profile of a parcel ascending unmixed from cloud base. The dotted line labeled 310 (deg K) is a reference dry adiabat. The psuedo vectors on the right side indicate winds, plotted in conventional fashion. For example, low-level winds are westerly, and peak in a jet-like fashion at about 10 m s^{-1} near 84 kPa.

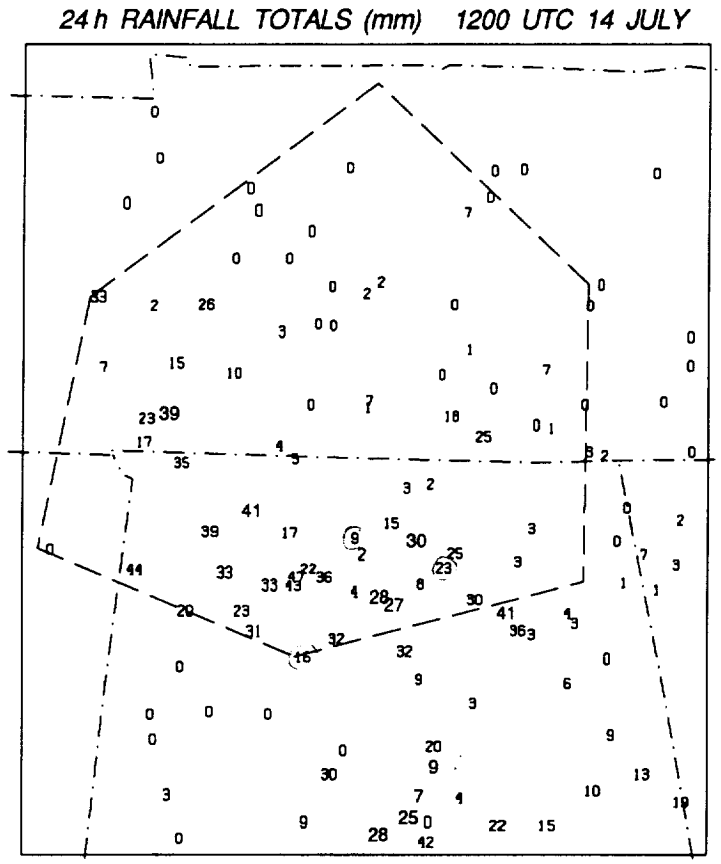

Figure 2-3a. Rainfall totals over a 24 h time period (1200 UTC 13 July to 1200 UTC 14 July 1986). The data set includes special experimental mesonet sites (PAM, FAM, NAM - all plotted in Figure 1-1), all TVA raingage sites (ADAS and PSO), all NWS sites, and Alabama volunteer observer sites. These rainfall totals include contributions from the primary MCS under study, in addition to (a) a secondary, smaller MCS that traversed the western portion of this region; and (b) secondary development along the southern limit of this domain. Rainfall totals exhibit considerable variability not only on this scale, but also on the scale if the MIST/FLOWS network defined in Fig. 1-1.

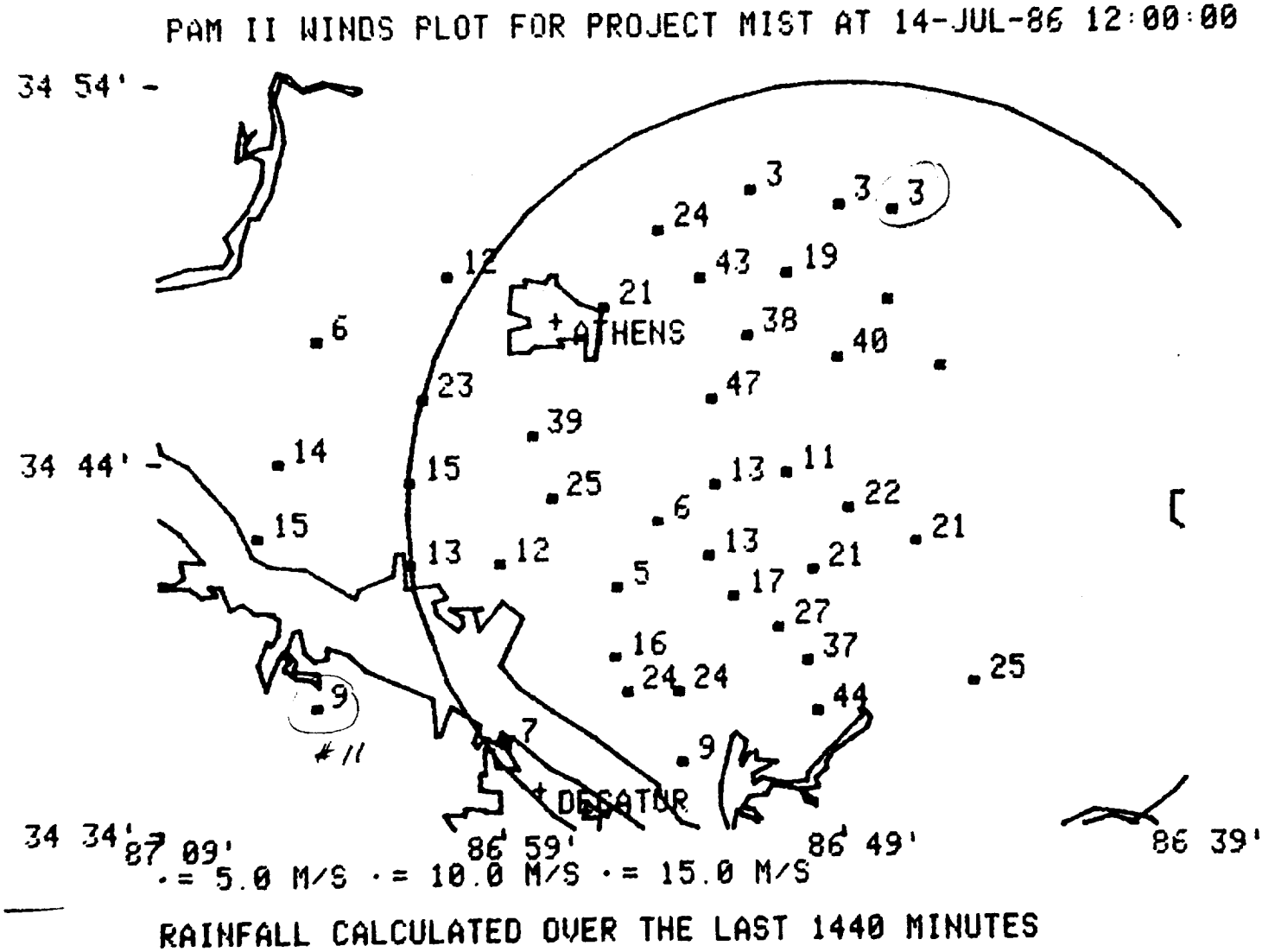

Figure 2-3b. Rainfall totals (24 h values, 1200 UTC 13 July to 1200 UTC 14 July) in mm over the MIST network of PAM stations.

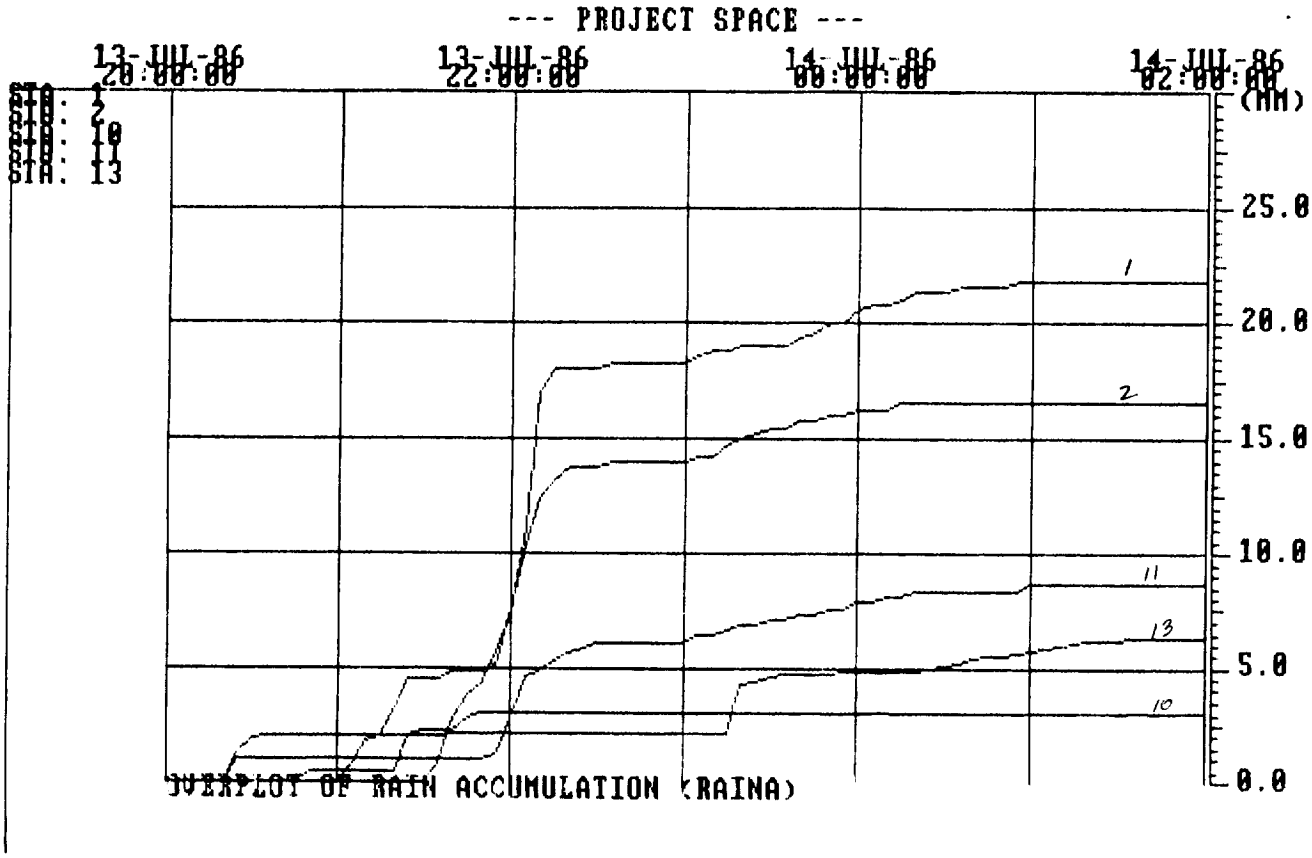

Figure 2-3c. Time series of rainfall accumulation from 4 sites (1, 2, 11 and 13) over the south-central portion of the SPACE network. Site 11 is located over the SW corner of the MIST newtork. These sites are circled in Fig. 2-3a.

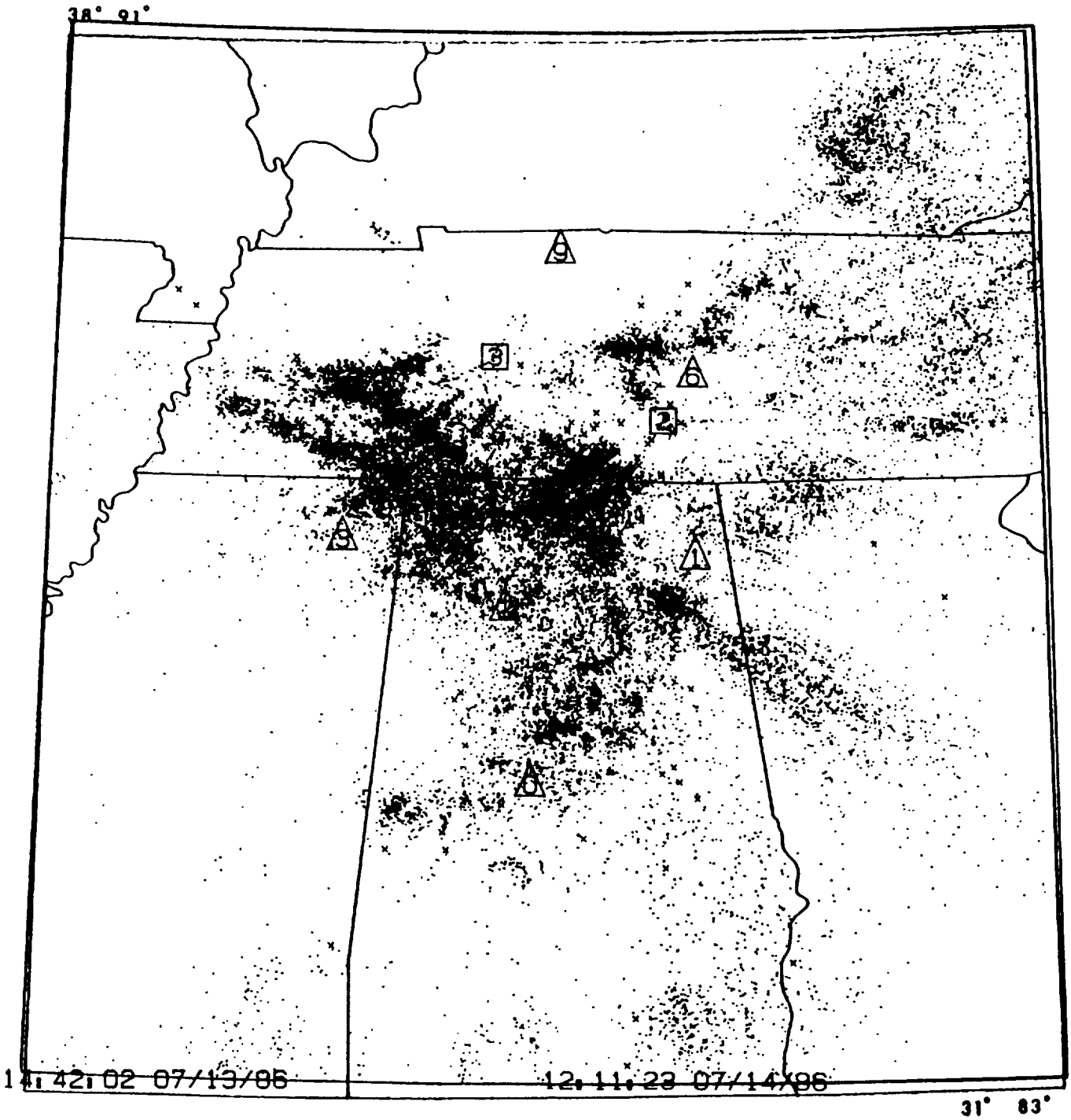

Figure 2-4. Total counts of cloud-to-ground lightning flashes over the time period 1442 UTC 13 July to 1211 UTC UTC 14 July 1986. Dots indicate negative flashes (negative charge transferred to the ground) and x's indicate positive flashes.

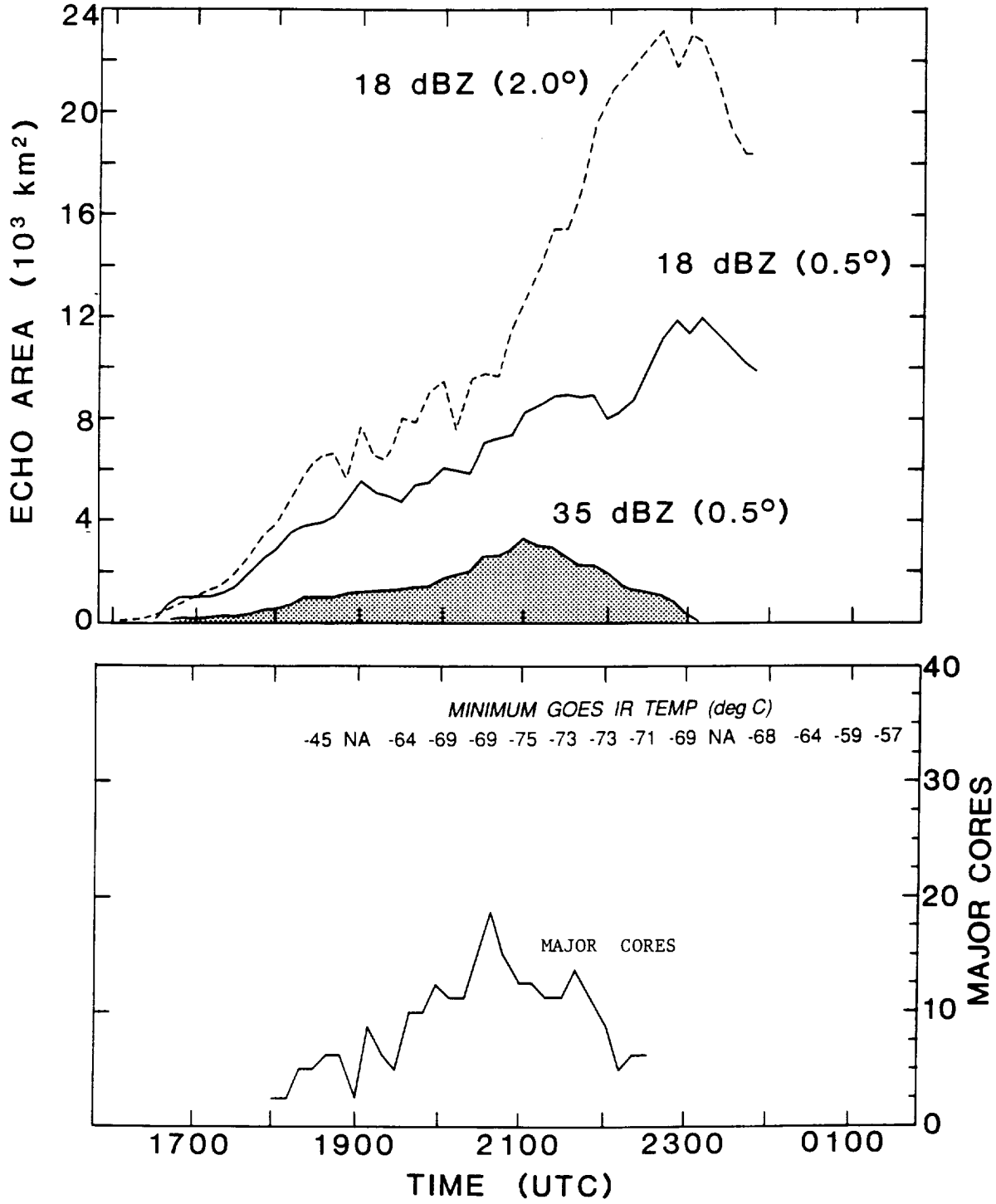

Figure 2-5. Time series plot of quantities derived from RADAP data. The top panel includes the areas of specific reflectivity (18, 35 dBZ) thresholds at the elevations given (0.5 or 2.0 deg). The lower panel presents an estimate of the number of major convective cores (i.e., those that are resolvable at the horizontal scales of >6 km), determined subjectively from inspection of PPI plots (e.g., see Fig. 2-4) at an elevation of 0.5 deg. The minimum GOES IR temperature (pixel value) within the MCS is also listed in the lower panel.

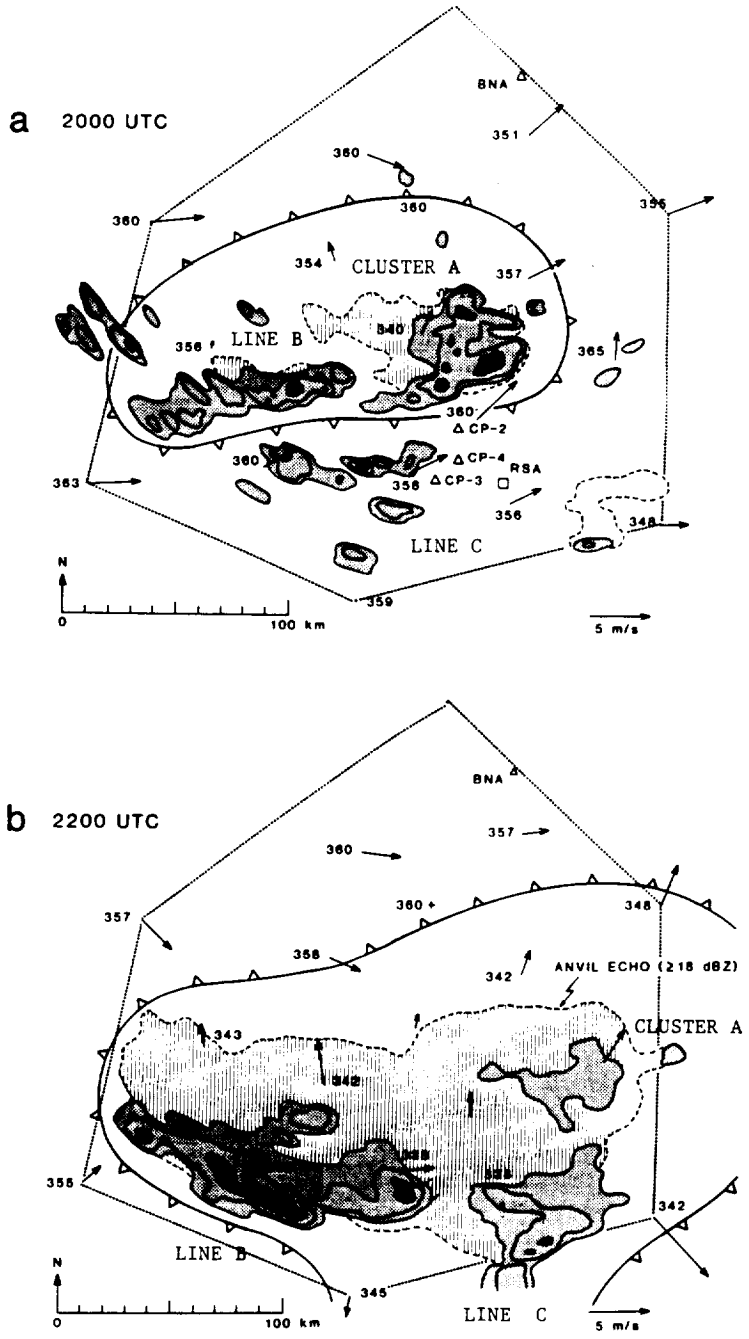

Figure 2-6. PPI plots of RADAP data from the Nashville WSR-57 radar (BNA). The stippled region depicts patterns from the 0.5 deg scan, with contours drawn at 18, 30, and 43 dBZ. Vertical hatching represents the 18 dBZ contour from the 2.0 deg scan, which intersects, at the range involved, the MCS at about the 5-11 km level. (It should be noted that the horizontal and vertical dimension of the radar sample volume at 170 km range for a 2.2 deg beam is about 6.5 km.) Identifiable mesoscale components are labeled A,B, and C. Surface wind data are plotted in vector form, and numbers refer to equivalent potential temperature (K). The barbed lines in each panel refer the the low-level outflow boundary, which expands with time. Time series data from individual sites were used to help determine the boundary location.

Figure 2-7 (on the following 3 pages). Color-enhanced analyses of GOES infrared satellite images for one-hour time intervals. The color enhancement is defined at the bottom of panel (a). Additional contours are drawn at 4 K intervals to define details at low temperatures. Circles of constant radii plotted in the panels define the range limit of CP-4 (115 km) and the average range of the CP-4 VAD analyses (40 km). Also shown are locations of CP-4 (4), CP-2 (2), individual sounding locations (S), and locations of vertical cross sections (lines of +'s which have a 10 km spacing).

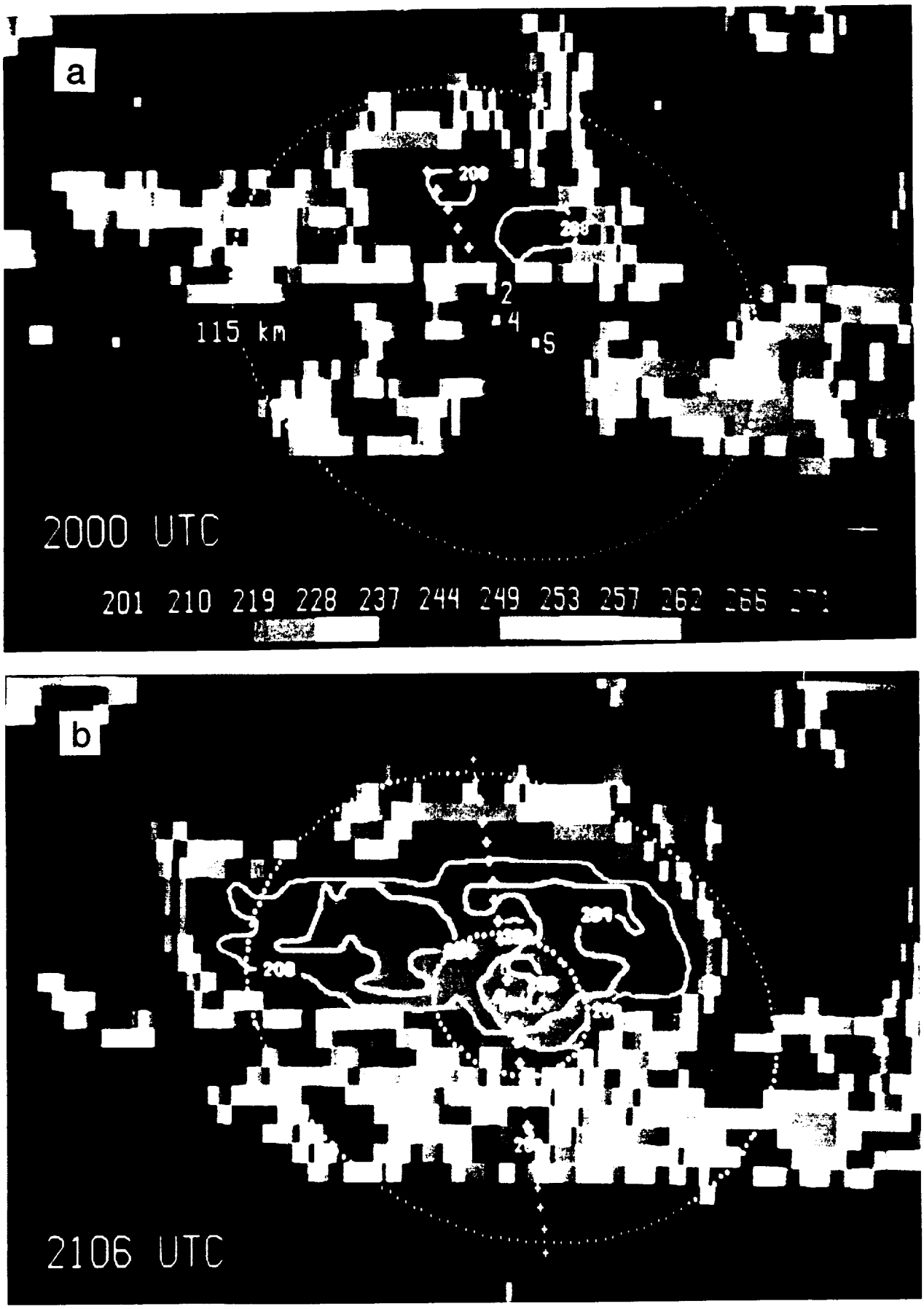

Figure 2-7 continued.

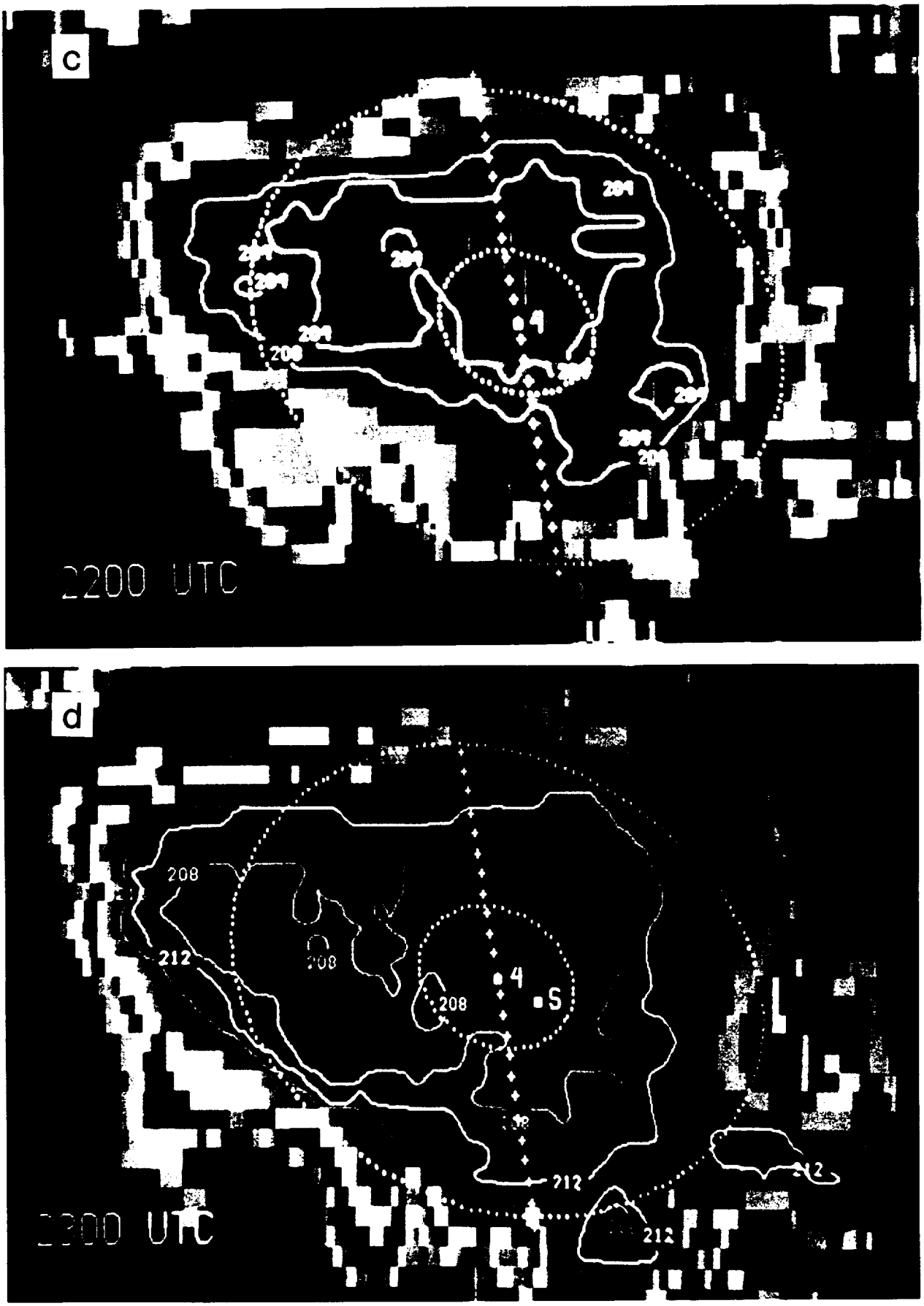

Figure 2-7 continued.

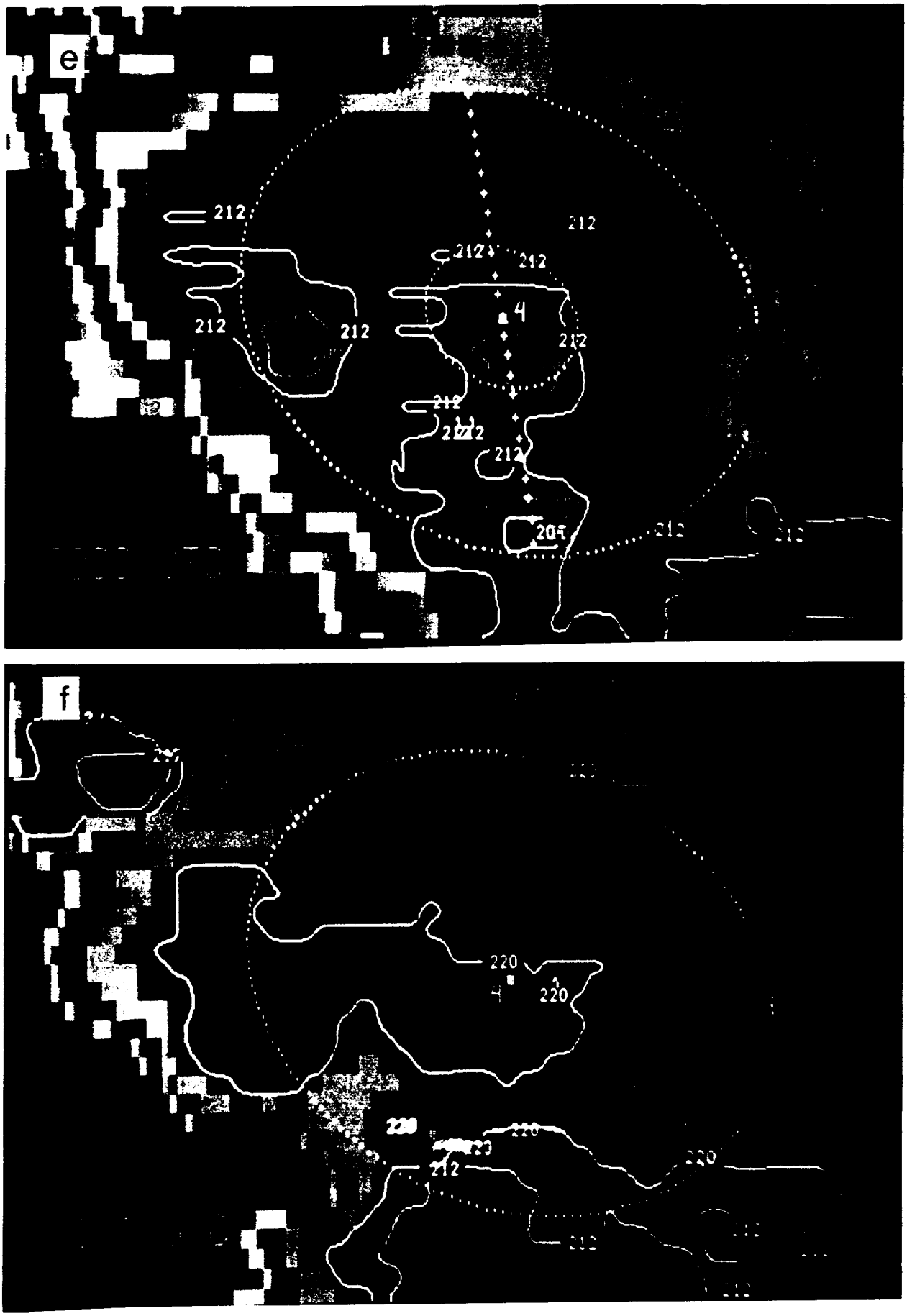

Figure 2-7 continued.

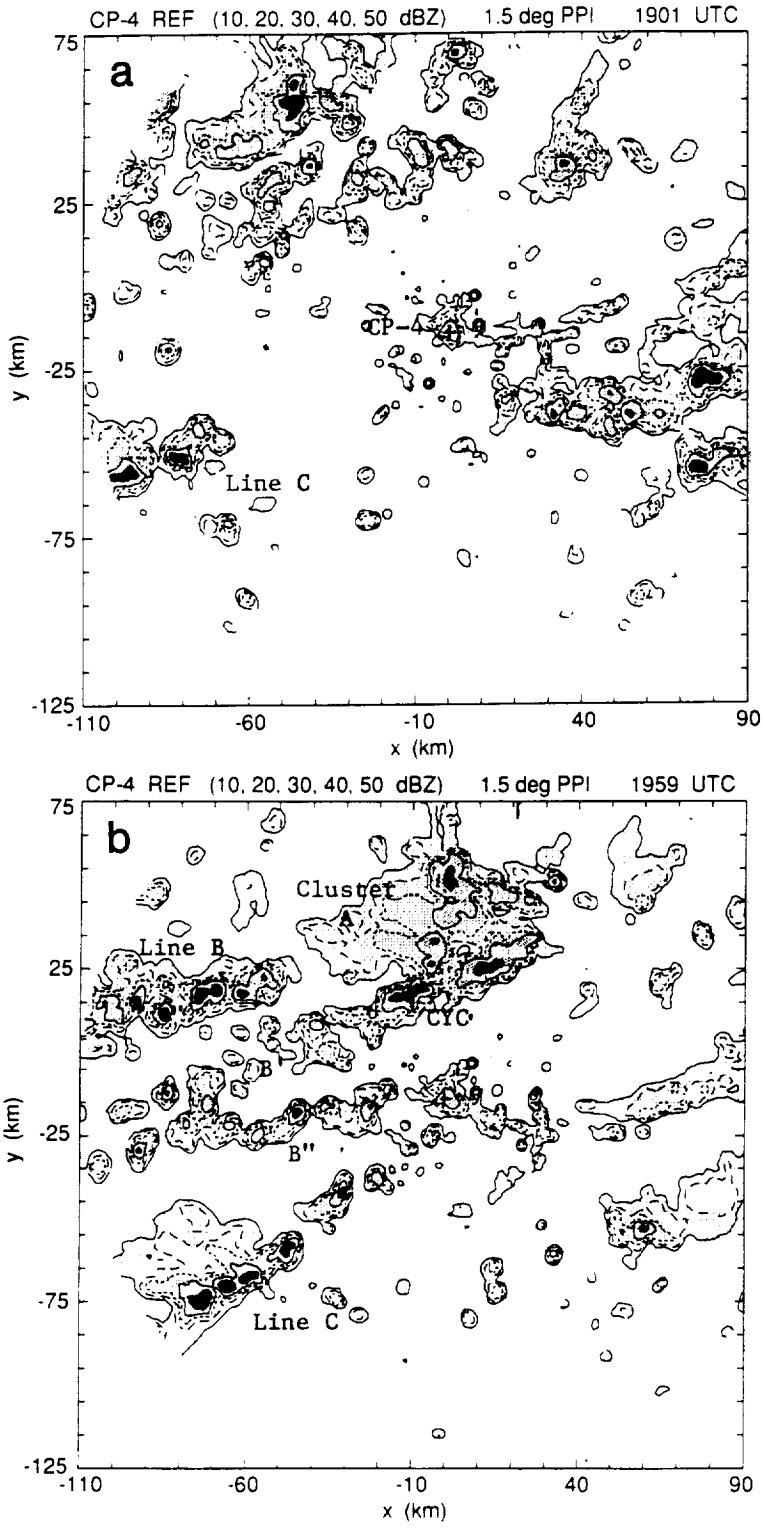

Figure 2-8. Horizontal distribution of reflectivity factor from CP-4 from 1.5 deg PPI scans (panels a and b) and from CAPPIs at 2 km (panels c-f) at approximate 1 h intervals for the period 1900 - 0000 UTC. In all panels REF is contoured at 10 dBZ intervals from 10 to 50 dBZ. In panels c-f the CP-4 VAD analysis domain is defined by the 40 km radius circle (CP-4 is located at the center), and the x interval over which composite patterns were constructed (Z_c and V_r) are indicated. In all panels an estimated correction for attenuation has been made. See Appendix A for details.

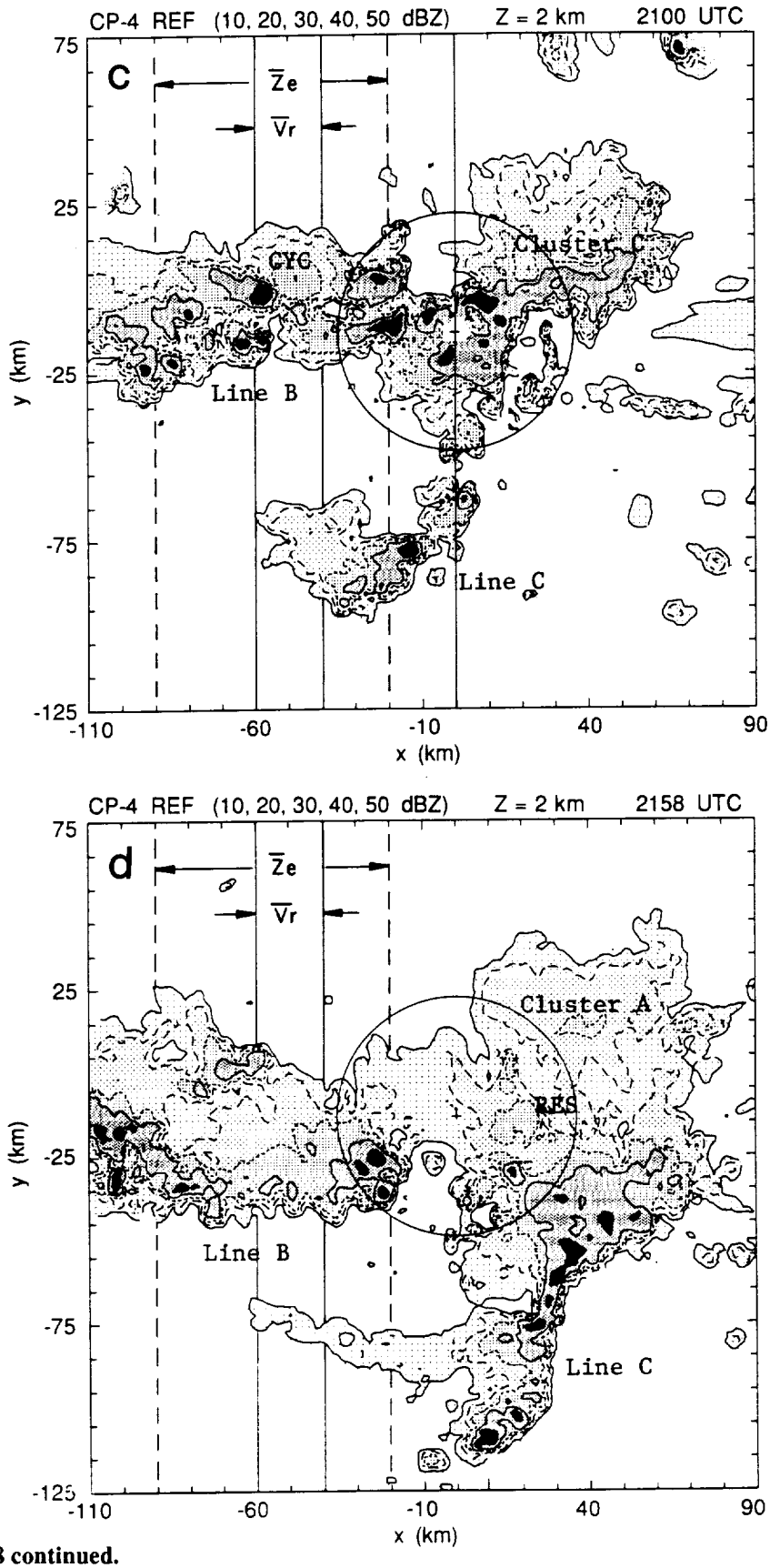

Figure 2-8 continued.

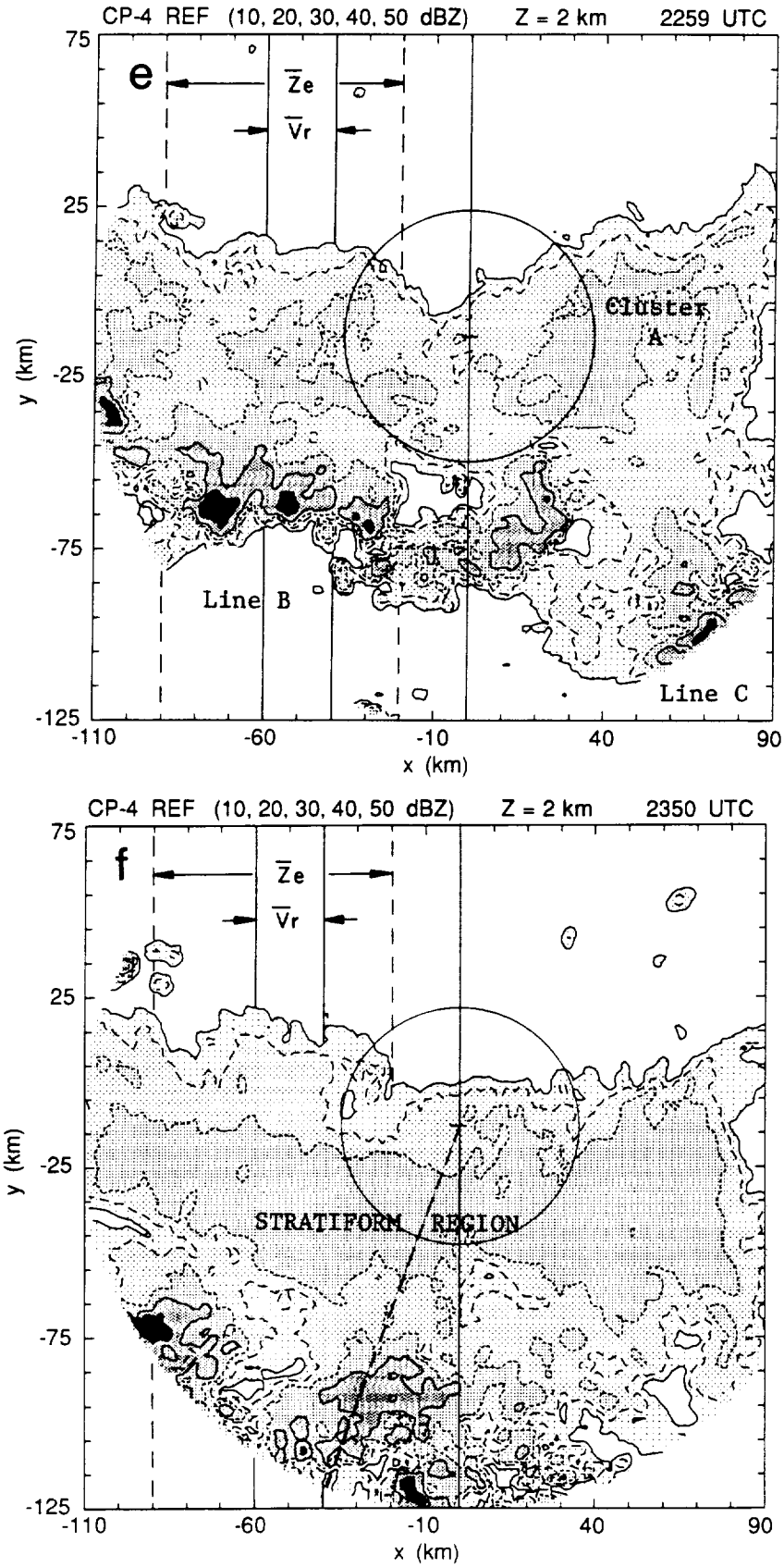

Figure 2-8 continued.

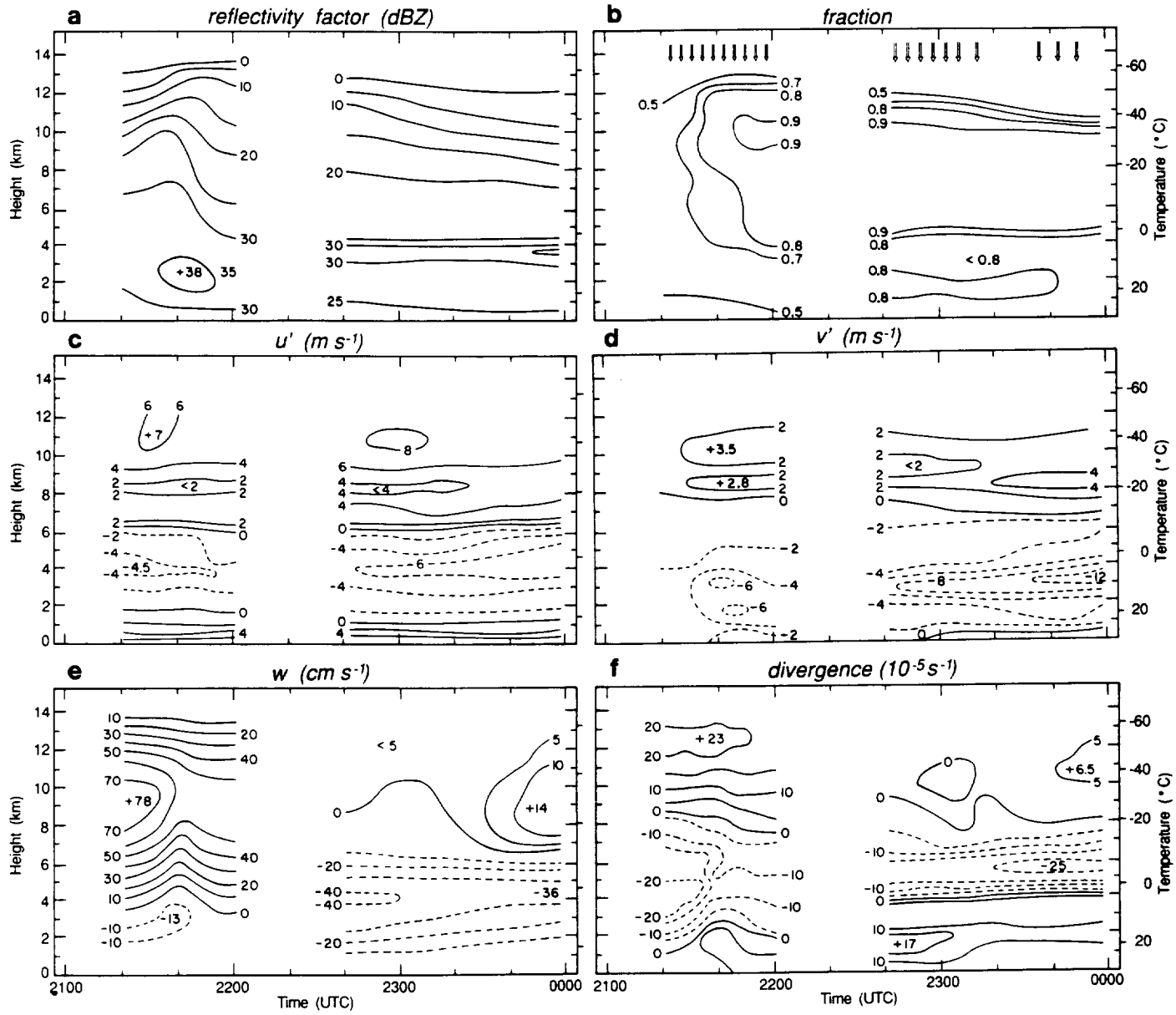

Figure 2-10. Time vs. height section of peak parameters obtained from the CP-4 VAD analysis over the circular domain (40 km circle) shown in Figures 2-7 and 2-8. The arrows in panel b indicate the time of individual VAD analyses, and the fraction is defined as the number of points within a given circle that have a refelctivity value greater that 0 dBZ. The horizontal velocity parameters u' and v' are departures from the base state, defined as $u' = u_{VAD} - u_o$, where the zero subscript denotes the ambient value determined from the 1800 UTC rawinsonde.

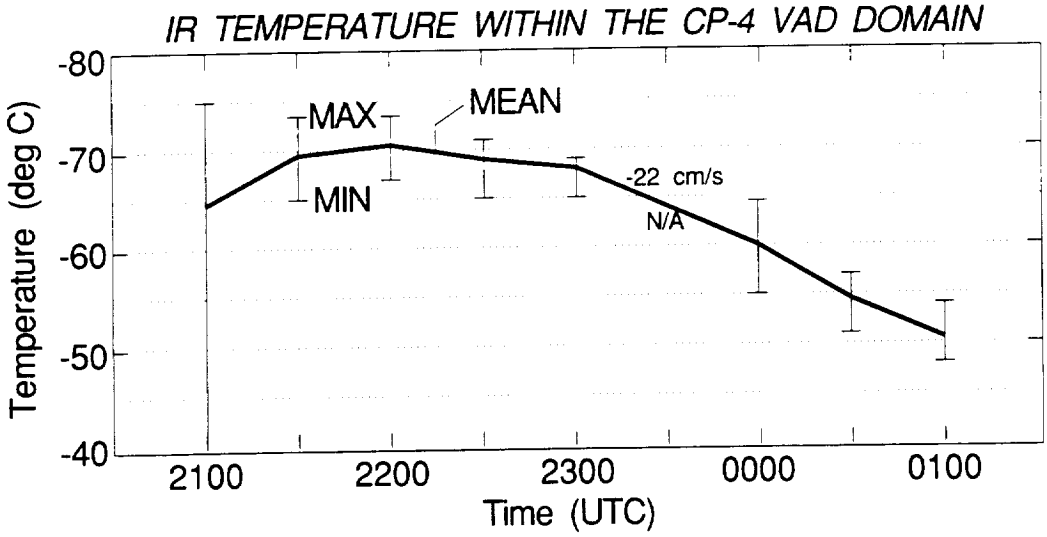

Figure 2-11. Time series of GOES IR temperature averaged over the CP-4 VAD domain of 40 km radius. The bold solid line indicates the areal average brightness temperature, and the vertical bars represent the range of temperature values over the circle. The initial value at 2100 UTC shows that a portion of the domain was not covered by anvil cloud.

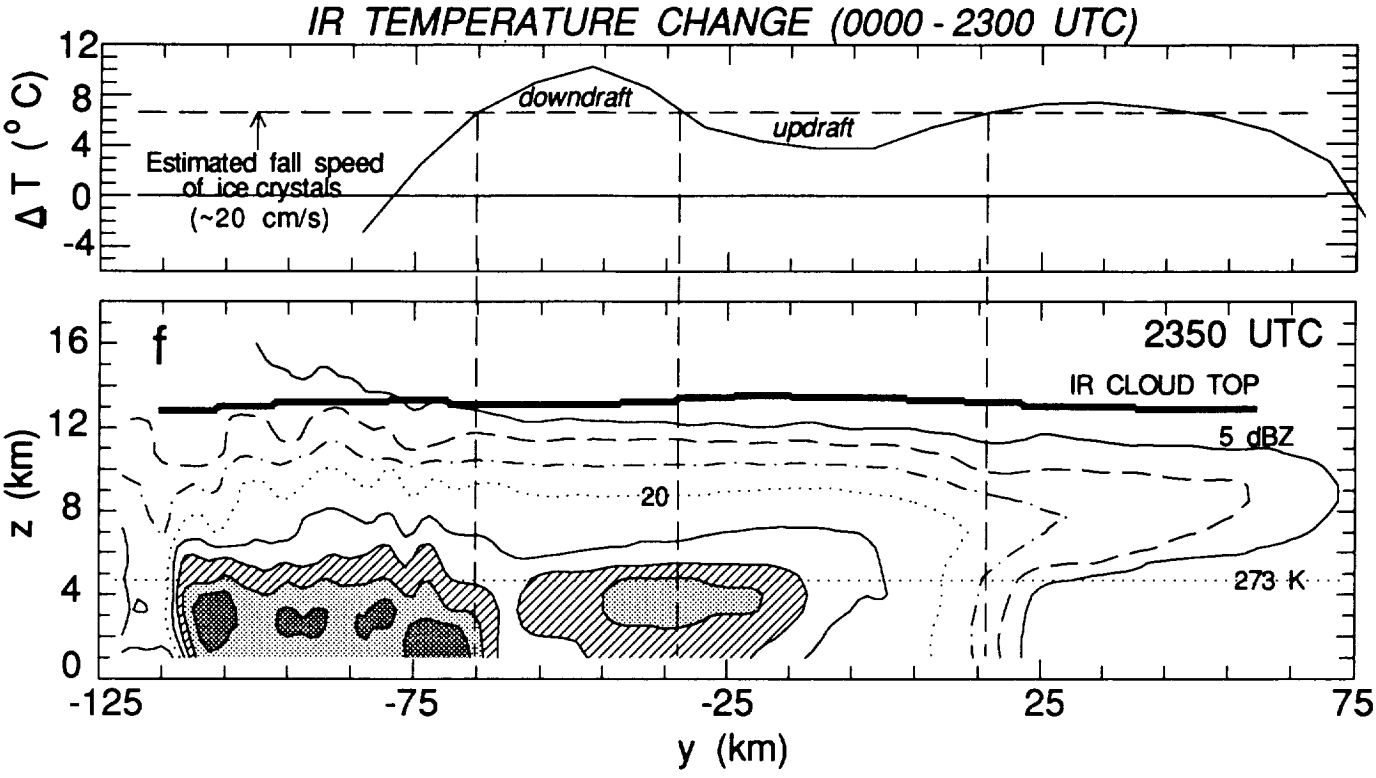

Figure 2-12. Change in IR brightness temperature over the Z_e composite domain defined in Fig. 2-8 over the one hour period from 2300 to 0000 UTC. The bottom panel is the 2350 analysis duplicated from Fig. 2-9f1. The horizontal dashed line in the top panel is the warming rate corresponding to a cloud-top descent of 20 cm s^{-1}. Values greater or less than 20 cm s^{-1} are inferred to be possible region of mesoscale downdraft and updraft, respectively.

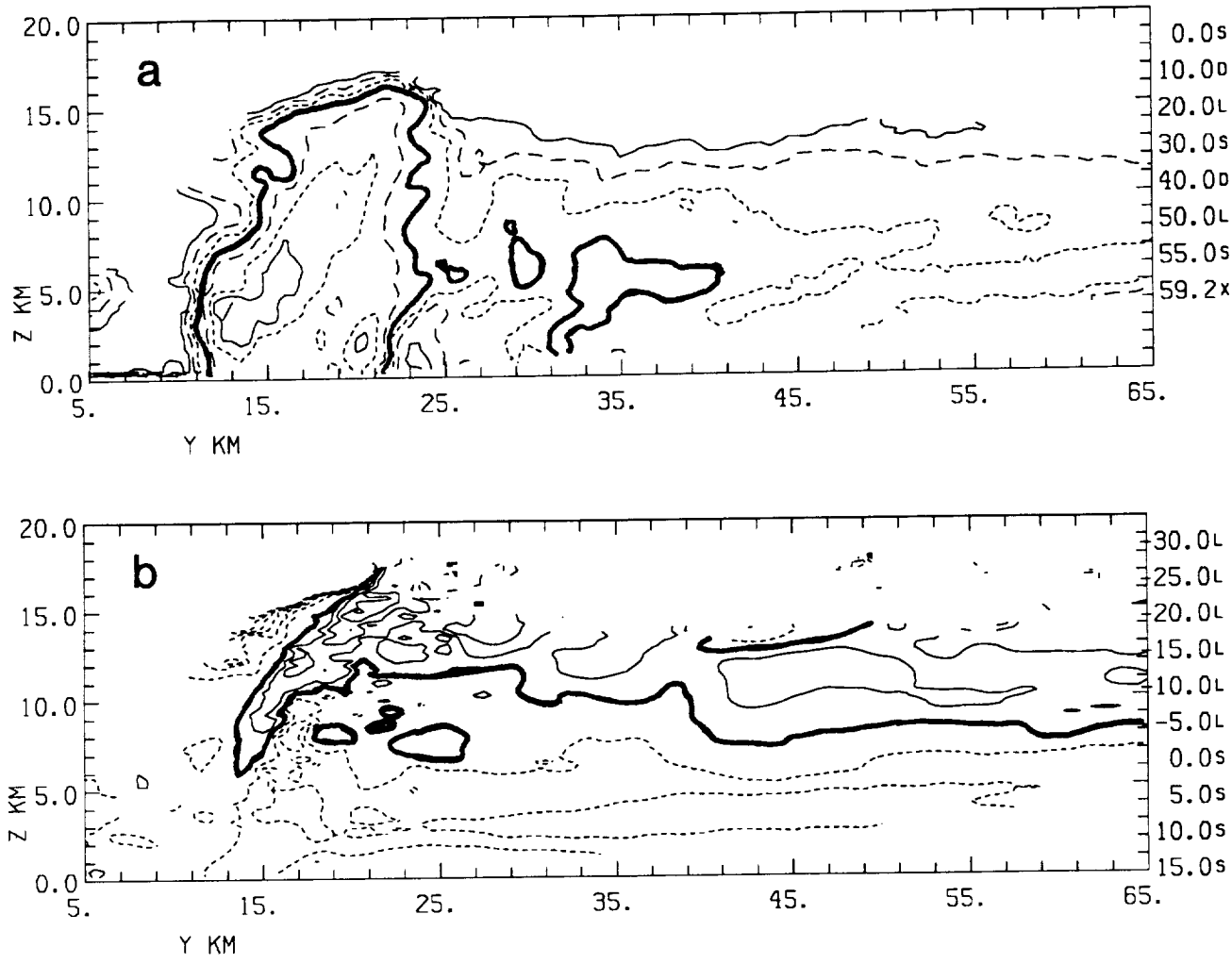

Figure 2-14. CP-2 RHI through an intense convective core at 2006 UTC. (a) Reflectivity factor contour as indicated on the far right. The 30 dBZ contour is bold. (b) Radial velocity contoured every 5 m s^{-1}, with dashed lines indicating negative values. The bold line is 0 m s^{-1}. The relative location of this RHI is indicated in Figs. 2-1, 2-4, 2-7 and 2-8.

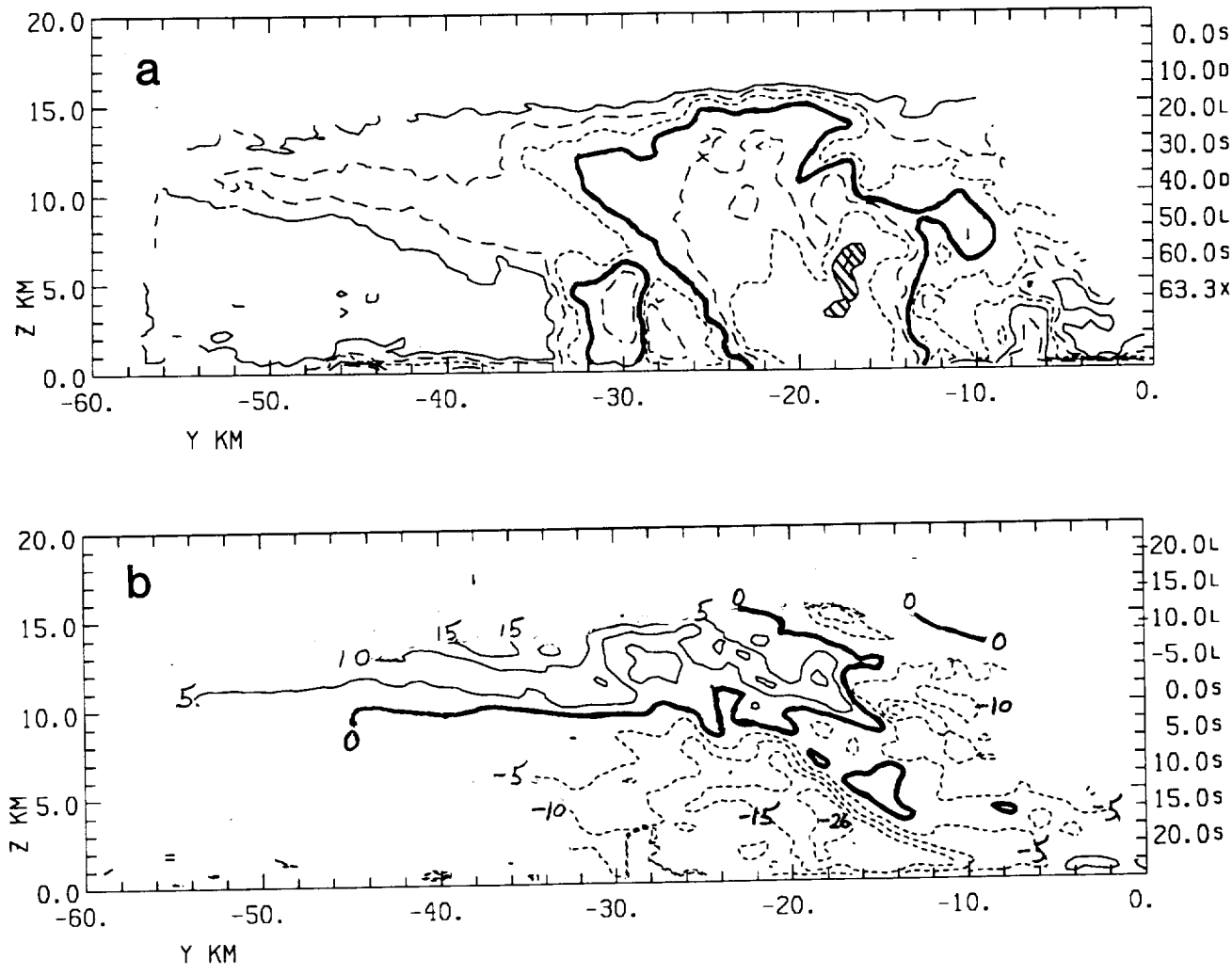

Figure 2-15. Same as Fig. 2-14, except for 2106 UTC. The location of this RHI is indicated in Fig. 2-8.

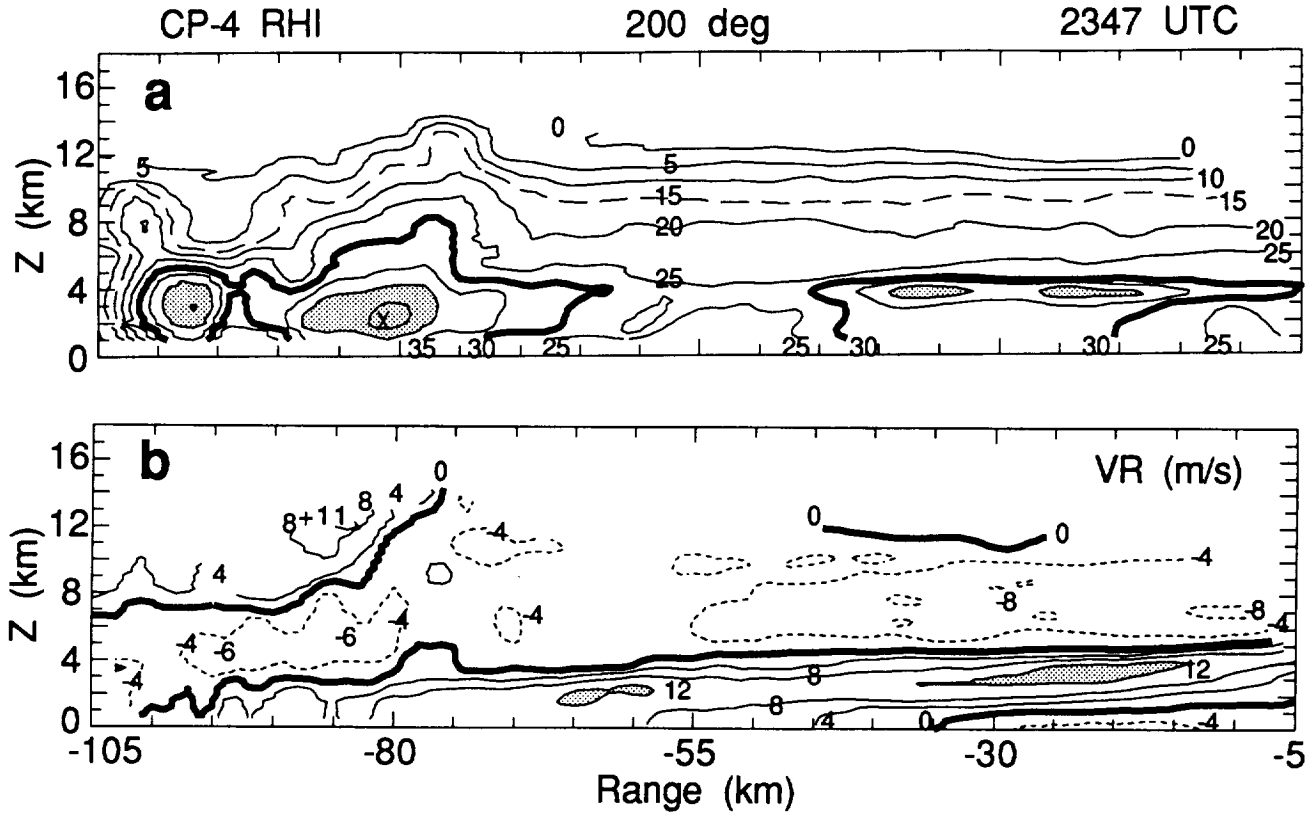

Figure 2-16. CP-4 RHI at 2347 UTC through a portion of the stratiform region and a dissipating region of deep convection. The location of this profile is shown in Fig. 2-8f. (a) Reflectivity factor contoured every 5 dBZ beginning at 0 dBZ. REF>40 dBZ is stippled. (b) Radial velocity contoured every 4 m s^{-1}. Dashed lines are negative values (approaching the radar), and the bold line is zero velocity. Stippling denotes V_r exceeding 12 m s^{-1}.

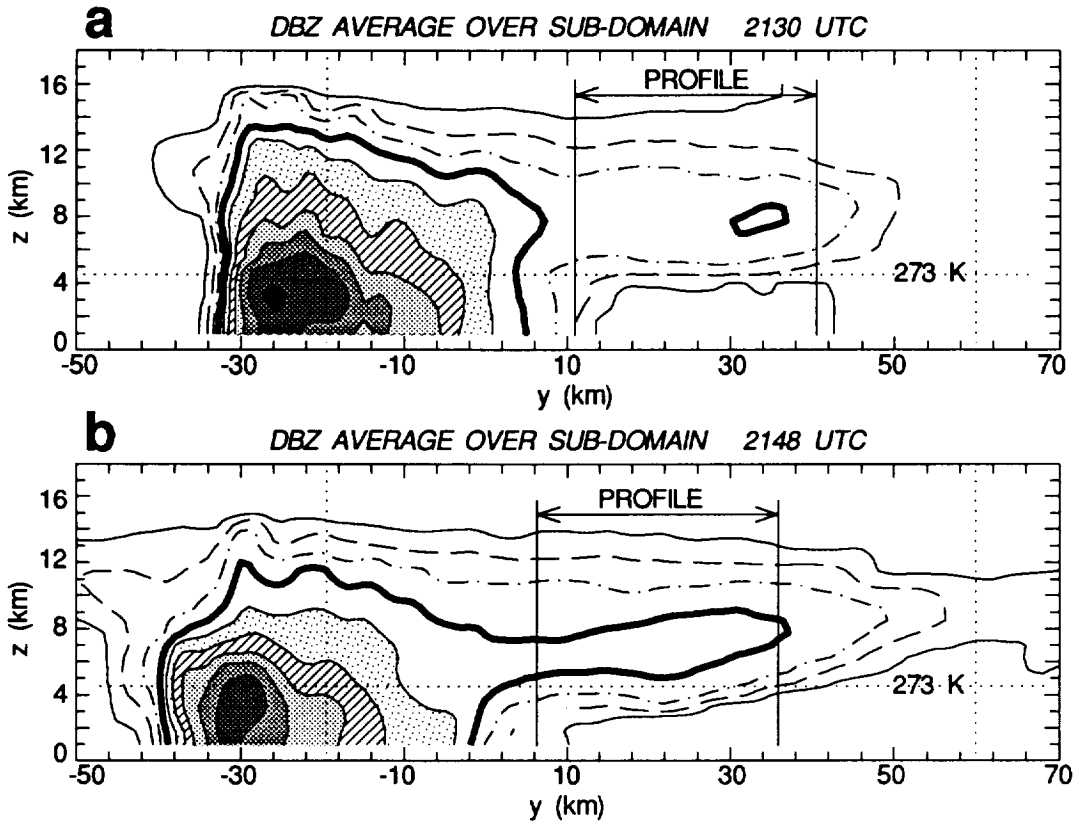

Figure 2-17. Composite reflectivity patterns as in Figure 2-9. Contours are drawn every 5 dBZ beginning at 5 dBZ. These averages apply to a more limited domain as shown in Fig. 2-8. The vertical dotted lines represent the horizontal domain of the difference calculation of Fig. 2-18. Vertical profiles averaged over the x interval shown in each panel are shown in Fig. 2-18.

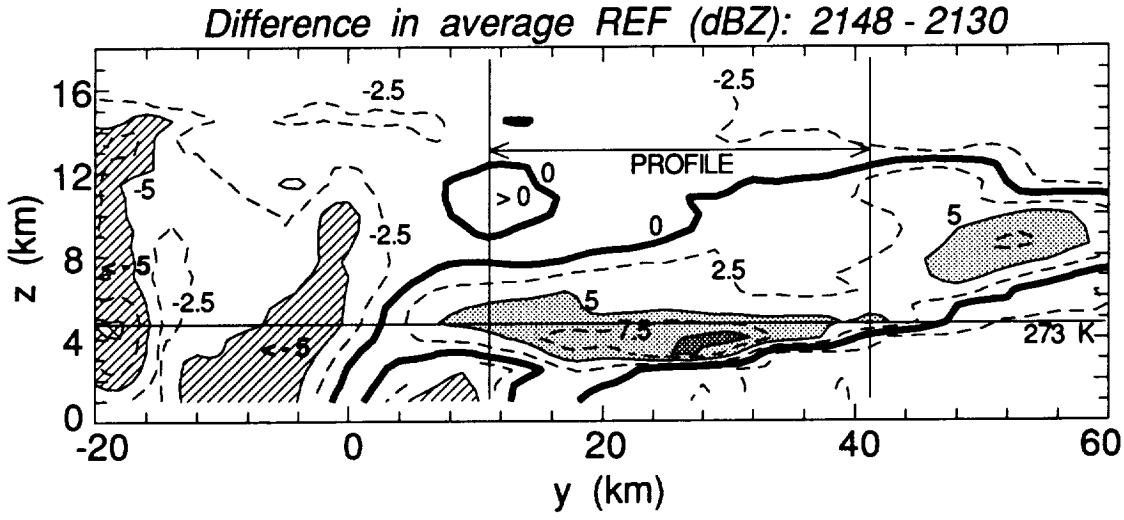

Figure 2-18. Difference field, obtained by subtracting the composite reflectivity of 2148 UTC from that obtained at 2130 UTC (Fig. 2-17), accounting for mean motion of the system. A vertical profile within the y interval labeled as 'Profile' is displayed in Fig. 2-19a. Bold lines represent values of zero difference.

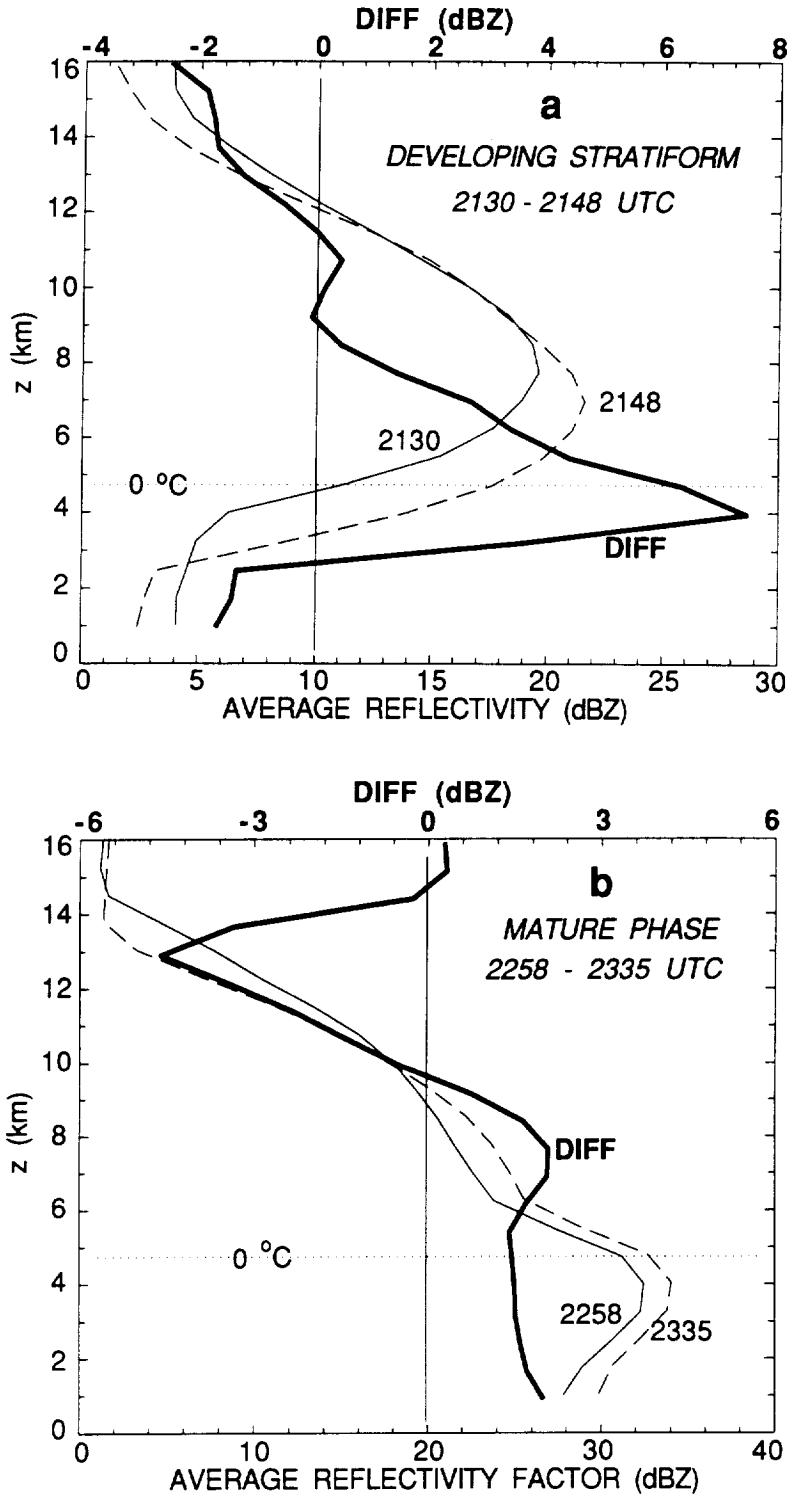

Figure 2-19. Vertical profiles of average reflectivity factor for individual times (obtained over the regions labeled 'PROFILE' in Figs. 2-9, 2-17, 2-18 and 2-20, and their difference, for the time pairs shown in Figs 2-xx.

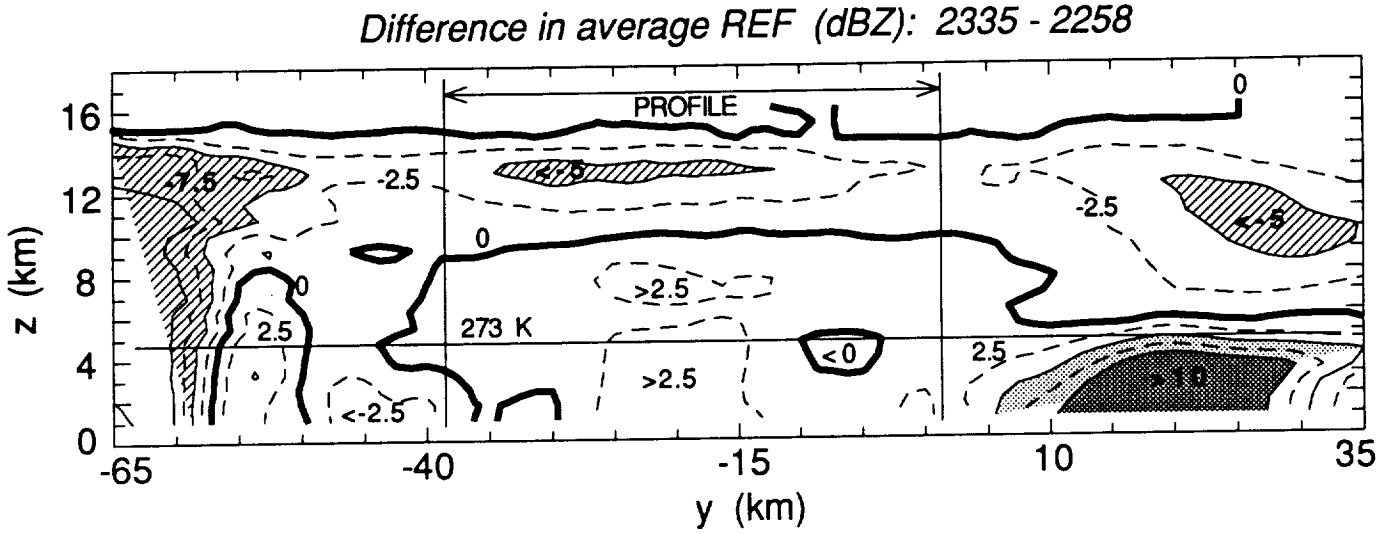

Figure 2-20. Difference field, as in Fig. 2-18, for the 2258-2335 period. The composite cross sections for these times are shown in Fig. 2-9d1,e1. A vertical profile of values within this region indicated by 'domain' is given in Fig. 2-19b.

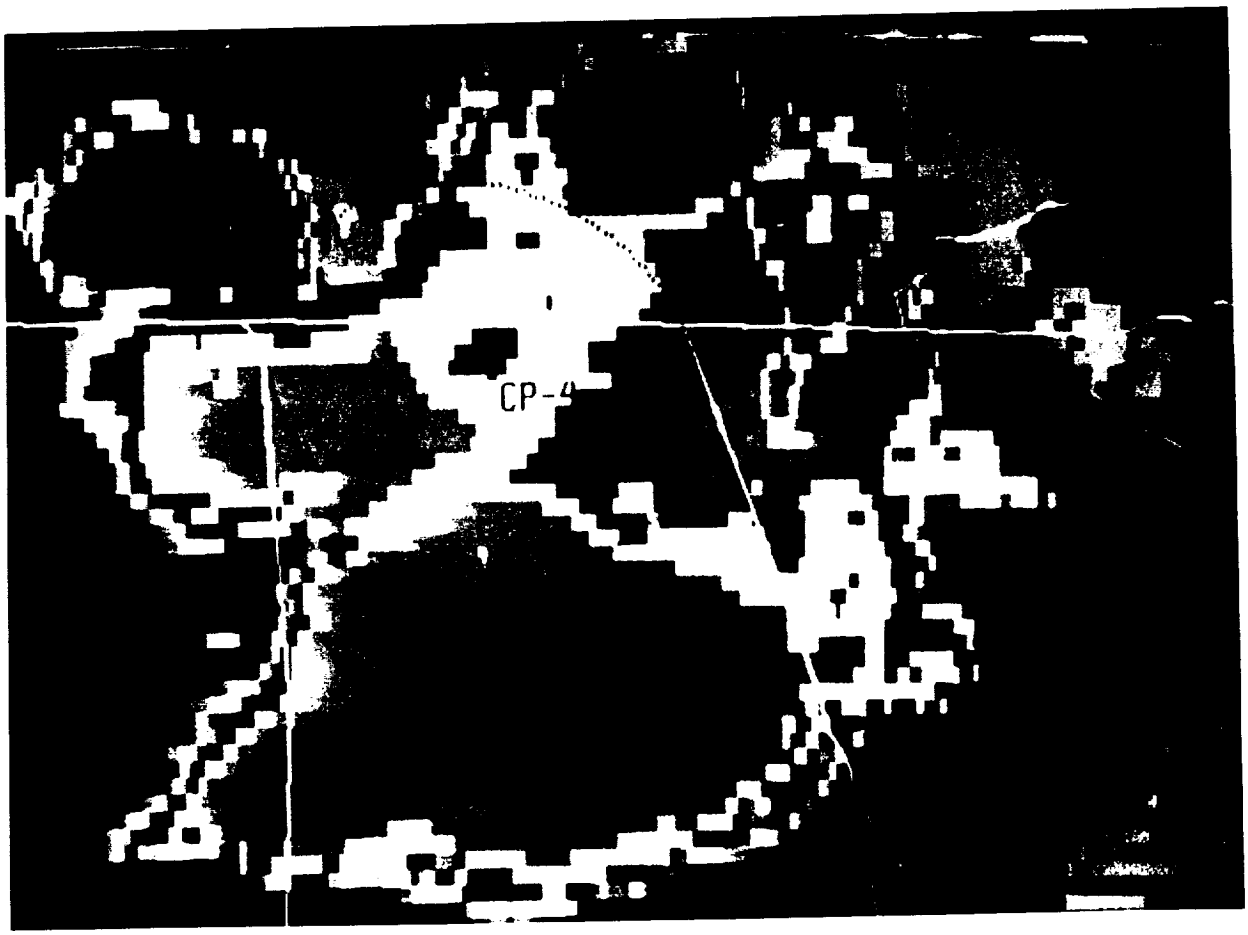

Figure 2-21. GOES IR image at 0200 UTC 14 July 1986. The color enhancement is the same as in Fig. 2-7. The original MCS that intensified over CP-4 has weakened, while three other regions of MCS activity have developed along the south, northeast and northwest flanks of the original MCS.

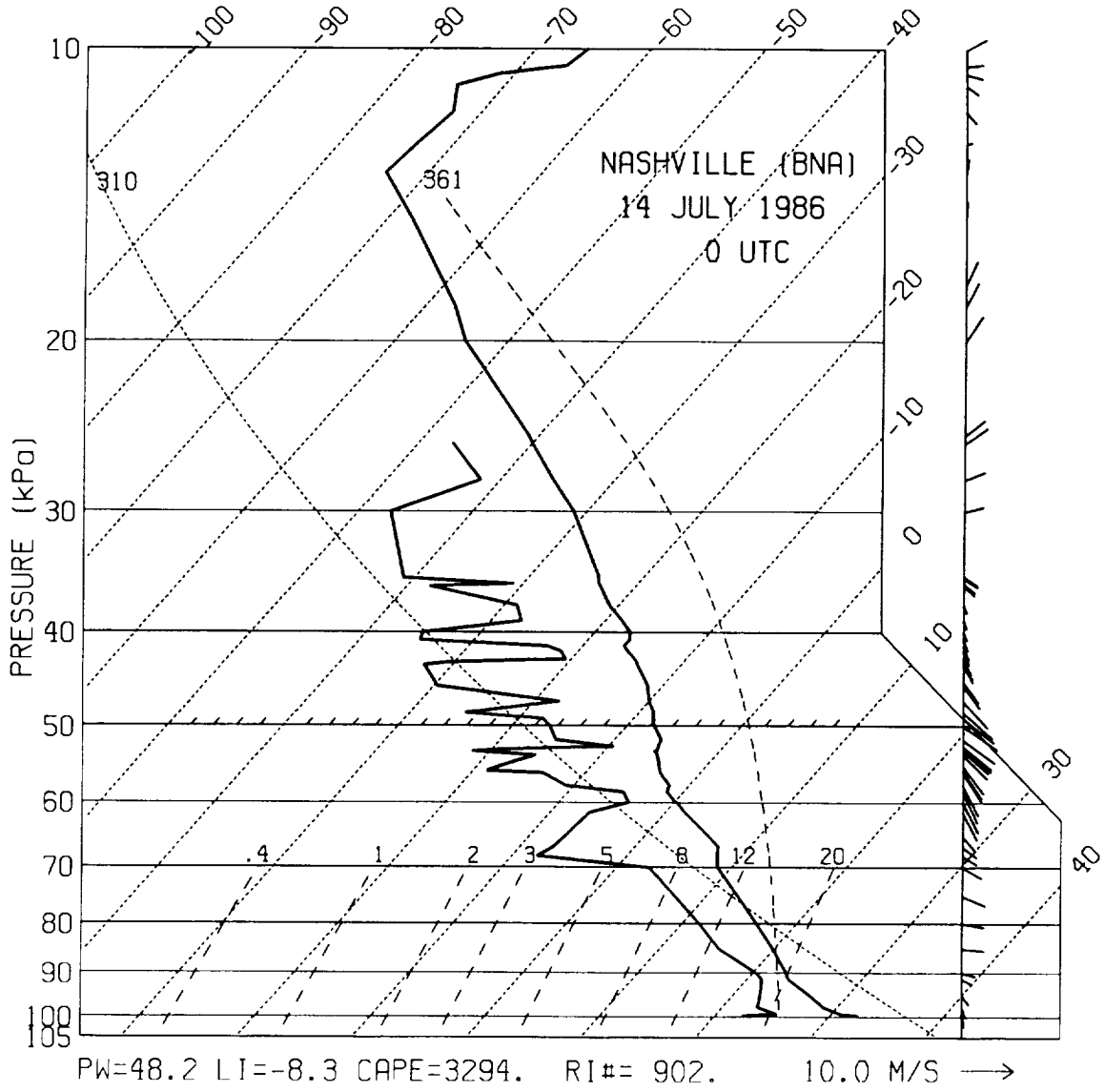

Figure 2-22. NWS sounding from Nashville (BNA) at 0000 UTC 14 July 1986. See Fig. 2-4 for location.

3. ANALYSIS OF THE 15 JULY MCS

The MCS observed in this case exhibited a number of characteristics different from that of 13 July. The system was unusual in that it formed near 0900 UTC (~0230 LST) 15 July and dissipated near 2100 UTC (~1430 LST), which is a complete reversal of climatological patterns of deep convection (including systems that exhibit mesoscale organization) for the summer months in the Southeast. Moreover, the system attained an unusually long lifetime of 12 h (4 h more than the 13 July MCS) despite its small horizontal dimension of ~100 km. At maturity the MCS was quasi-circular in shape, and the stratiform region was located to the left (with respect to system motion) of the convective region. The convective components in this case were much less vigorous than in the 13 July case. A comprehensive analysis, utilizing conventional single Doppler radar analyses, analysis of multiparameter (CP-2) data, network sounding and surface data and GOES satellite data is presented to characterize the internal kinematic and precipitation structure of this system.

3.1 Environment and MCS synopsis

Figure 3-1 summarizes the GOES IR view of the cloud field evolution over the Southeast region during the pre-initiation through mature phases of the MCS. The MCS of interest in this study formed adjacent to a previous larger-scale MCS which had dissipated over Kentucky at ~0700 UTC. This system is shown in its latter stage at 0600 in Fig. 3-1a. By 0900 a new region of cold cloud top, representing the initiation of the MCS of this study, is labeled as "NEW" in Fig. 3-1b. This MCS then continued to expand through 1500 UTC as illustrated in Figs. 3-1c,d. Thus, this system formed near the southern flank of a previous MCS which underwent rapid dissipation. In fact, during the 0600-1500 UTC time period, the background cloud field over the region experienced considerable dissipation. The MCS attained a peak intensity during the 1500-1700 period, and slowly weakened thereafter, dissipating completely by 2100 UTC. Figure 3-2 shows a finer-scale sequence of the IR characteristics during the latter portion (1600-1800 UTC) of the mature phase. This sequence portrays the evolution of the third and final convective region (M3) observed within this MCS during its life cycle. The previous two components M1 and M2 are shown in Fig. 3-1. Structural details during the 1600-1800 time period are presented in Sections 3.2-3.5.

A representative sounding which characterizes the environment of the developing MCS is shown in Fig. 3-3a. This environment is moist from the surface to above 50 kPa, with integrated precipitable water values of ~51 mm. Although this sounding is moderately unstable as indicated by CAPE values of ~1700 J kg^{-1}, the intensity of convection within the system was generally weak to moderate. Section 3.5 describes some of the observed deep convective cloud

structures within M3. Both the environmental tropospheric winds and the vertical wind shear were generally small with the exception of the region at the top of the nocturnal inversion where a weak jet of 5.5 m s^{-1} from 290 deg is observed. This particular wind profile appears to have played a key role in dictating the relative location of deep convection within the system, which occurred primarily along the western flank of the system. A subtle low-level jet was also noted in the 13 July case.

Surface features at 1200 UTC over the COHMEX surface mesonet (20 surface stations distributed within the polygon shown in Fig. 1-1) display relatively little structure as the surface was largely decoupled from the free atmosphere. The most pronounced signal was weak divergence associated with the area of precipitation. The air mass over the mesonet was nearly saturated at 21 ^{o}C.

The general distribution of precipitation within the MCS at 2 h intervals is shown in Fig. 3-4. The first echo associated with the MCS of interest was observed at 0900 UTC, and areal expansion of both the low-level radar echo and cold cloud top occurred from 1000 to 1600 UTC (Figs. 3-1 and 3-4). Stratiform precipitation distributed between the convective elements had become significant by 1200 UTC (Fig. 3-4b). During the mature MCS stages (1400-1800 UTC), the most intense convective elements show a preference for the western portion of the MCS, and stratiform precipitation was prevalent over the eastern portion. However, more detailed patterns from the CP-4 analysis, shown below, illustrate that weaker convection occurred on other flanks as well. A reflectivity envelope, presented in Fig. 3-5 was obtained from the 10 min RADAP data. This product further illustrates the observed periodic behavior of intense convection within the western flank. Individual clusters of deep convection were observed to form at 3 h time intervals at 1000, 1300 and 1600 UTC and are labeled as M1, M2 and M3. The most substantial of the three was M2. These pulsations provided prominent signatures in the GOES IR data as shown in Figs. 3-1c,d and 3-2. Each development took place along the MCS western flank and then moved eastward in a system-relative sense as the cloud top pattern warmed. The trajectory of the cold cloud top was directed ~40 deg to the left of the trajectory of high reflectivity in response to the increased ambient westerly flow aloft (Fig. 3.3a). This scenario is illustrated in Fig. 3-1 for the first two mesoscale features labeled M1 and M2. Between 1200 and 1500 UTC M1 is observed to weaken while M2 evolves from its initial appearance at 1300 a fully-developed state by 1500 UTC as shown in Fig. 3-1d. During the warming phase at cloud top, all three components were associated with stratiform precipitation within and below the coldest cloud top region of the system. A similar scenario is indicated in Fig. 3-2 for M3. Further details of this evolution for M2 and M3 are presented in Sections 3.3-3.5

Cloud-to-ground lightning activity (Fig. 3-6) was generally low relative to the total precipitation produced (S. Goodman, personal communication). The CG patterns shown in Fig. 3-6 start at 1233 UTC and therefore miss most of the M1 life cycle. The patterns show a general north-south oriented swath ~50 km wide with cellular patterns, produced largely by deep convective components within M1, M2, and M3 embedded within the general swath. The cluster of points over the west-central portion of the network corresponds to M2. These patterns show a relatively high density of negative CG flashes, followed by a number of positive CG flashes. Cluster M3 is represented in the CG data by the (lower density of) points just east of DF 4 (the box containing the 4 in Fig. 3-6). The relative variation in CG density between M2 and M3 is thus greater in the CG signatures than in the REF swath signatures of Fig. 3-5. The precipitation output from this MCS was not well-sampled because of its small size. Precipitation totals shown in Fig. 3-7 display appreciable variability. Only two sites were directly affected by convective cores, while the others recorded primarily stratiform precipitation in amounts up to ~10 mm. Locally high values over the eastern portion of the MCS were produced by relatively weak deep convection observed within the eastern flank of the MCS. Other precipitation amounts recorded east of the reflectivity swath were produced by transient cloud systems associated with, but not directly adjoined to the MCS. Rainfall over the MIST network shown in Fig 3-8 displays considerable variability (3-14 mm) in a region considered to be part of the stratiform region. The stratiform contribution is thus more significant, in both absolute amount and relative contribution, than in the 13 July MCS.

The MCS attained a peak areal coverage of cold cloud top temperature (<221 K) of ~1000 km^2 at 1400 UTC in association with convective region M2. The maximum area occupied by the 241 K (-32 °C) isotherm was ~6700 km^2 at 1500 UTC, less than 10% the area of an MCC as defined by Maddox (1980). The peak area within the 18 dBZ contour at 0.5 deg elevation also occurred at 1500 UTC. Peak reflectivity factor and minimum cloud top temperature measured by RADAP and GOES IR were 50 dBZ and 214 K, respectively. In the next section a detailed examination of the internal system structure associated with components M2 and M3 during the 1600-1810 UTC period are presented.

3.2 General precipitation and kinematic structure

Single Doppler analyses conducted during the mature to dissipating phases (1600 to 1830 UTC) of the system show both similarities and differences to the larger MCC and squall line systems documented in the literature. The intensity of the deep convective components was generally weak, the areal coverage of deep convective components was relatively low at ~20% and the location relative to the stratiform portion, although generally within the western portion of the system, lacked a systematic relative orientation. At times convective cells were located along the far eastern portion of the MCS. For example, Figure 3-9

shows patterns of reflectivity factor (Z_e) at the 2 km AGL level at 1604 UTC, near the time of M3 emergence. Although the most intense convective echoes are associated with component M3, located near (x,y)=(-65,20), the high resolution patterns in the CP-4 data reveal other less intense convective cores near the southern and northeastern boundaries of the MCS. Such embedded rainshower structures are probably responsible for the small-scale variability in precipitation over the MIST network. The interior stratiform region shows spatial variability in cells having relatively high peak reflectivity of 45 dBZ. There are two other regions of precipitation detached from the main body of the MCS, one located to the east and the other immediately to the north. The radial velocity field shows a relatively laminar flow pattern. Even the convective region associated with M3 is relatively benign kinematically at this level.

Component M3 maintains intense values of Z_e 27 min later at 1631 UTC (Fig. 3-10, note that this presentation is at 3 km instead of 2 km AGL)), but the other weak convective features present near the NE border at 1604 are less substantial, a trend that continued through 1657 UTC. Radial velocity patterns at the 3 km level show a region of significant inflow over the northern portion of the MCS. The structure of the inflow jet is further elucidated in vertical sections presented below. A secondary peak in radial inflow is associated with the convective region M3. This accentuated flow appears to directly associated with the inflow feeding the updrafts of M3. A broadly similar distribution of Z_e is seen in region of M3 at 1701 (Fig. 3-11), but the relative location of this group has shifted further southward and additional weak cells have formed along the NW system flank. Weak detached cellular echoes trailing the MCS are also visible along the N edge of the analysis domain. In fact the trailing region of the MCS contains abundant low to middle level cloud material, only a small fraction of which produces precipitation. The horizontal extent of this trailing cloud field is indicated in the IR images of Fig. 3-2 and the GOES visible images at 1630 and 1800 UTC (Fig. 3-13). These clouds exhibit top temperatures ranging between 260 and 280 K in the presence of relatively high reflectance in the visible. The REF distribution within stratiform region in the vicinity of CP-4 has decreased 5-10 dBZ from peak values of 40-45 dBZ at 1604 to values of 30-35 dBZ at 1658 UTC. It is also noteworthy that the stratiform region exhibits an evolving cellular pattern on scales of 10's of km. For example, two regions of enhanced stratiform precipitation (labeled S1 and S2 in Fig 3-10) can be identified at 1631 UTC, but not at adjacent times of 1604 (Fig. 3-9) and 1701 UTC (Fig. 3-11).

By 1810 UTC, the late mature stage, echoes associated with M3 have weakened further and have moved in a system-relative sense to the SW border (Fig. 3-12). Such a relative movement over the the period of observations (1604 to 1810 UTC) suggests a net cyclonic rotation of the MCS. A similar pattern of rotation is also suggested in the visible GOES images during the dissipating stages after 1800 UTC (not shown). Echo intensities within the stratiform region again exhibit isolated patches exceeding 35 dBZ. Radial velocity patterns at 1810

UTC (Fig. 3-12b) have become even more stratified and uniform than observed earlier. At earlier times more structure in velocity was seen in association with the convective region along the western flank.

3.3 Characteristics of the stratiform region

Some detailed characteristics of the stratiform region were determined through VAD analysis and analysis of high resolution RHI scans acquired by CP-2 and CP-4.

3.3.1 Mesoscale flows from the VAD analyses

Characteristics of the stratiform region surrounding the CP-4 radar were determined from VAD analyses during the 1604-1830 time period. The VAD analysis parameters for this case were identical to those of the 13 July case with the exception of the radii used. The principle radius was 20 km as shown in Figs. 3-2, 3-11 and 3-12. Supplemental radii of 16, 24 and 28 km were used to obtain higher vertical resolution throughout the depth of the stratiform region. GOES IR data were used to estimate stratiform cloud top height. Analyses from two times, 1655 and 1810 UTC, are presented here. The available elevations were 0.5, 1.0, 3.0, 5.0, 7.0 and 15 deg for the 1655 analysis; and 0.5, 1.0, 2.0, 3.0, 4.0, 5.0, 6.5, 8.0, 9.5, 11.0, 12.5, 14.0, 15.5, 17.0 and 18.5 deg for the 1810 analysis.

In general the stratiform region over the eastern portion of the MCS exhibited downward motion throughout much of the cloud depth, typically from the 6-7 km level to the surface. The stratiform region cloud top over CP-4 was generally 9-10 km AGL. Only the uppermost portion exhibited very weak ascent on the order of several cm s^{-1}. The 1655 UTC analysis presented in Fig. 3-14 was acquired over the east-central portion of the stratiform region, centered 45 km east of the convective region M3 (see Figs. 3-2 and 3-11 for relative location). The REF profile peaks at 3.5 km and decreases linearly to near zero a 8 km.[6] Below 3.5 km REF is nearly constant at 24-25 dBZ. The profile of divergence is highly structured and shows strong variability and an oscillating behavior over the lower half of the region. Relatively strong divergence (18×10^{-5} s^{-1}) located near the surface decreases rapidly and transforms to convergence within the 1.2-2.7 km layer. A second deeper layer of convergence ($\sim 10^{-4}$ s^{-1}) is located between 3.5 and 7 km. Only weak divergence is analyzed over the upper portion of the stratiform region. (The magnitude and depth of this divergence is uncertain due to poor VAD sampling at higher levels -- see previous paragraph). Mesoscale downdraft dominates the region and exhibits a double-peaked minimum of -17

---

6. Note that REF is an average of individual points about the VAD circle. In cases where a horizontal gradient exists, such as at 1655 UTC, REF will exhibit appreciable variation. Also, at least 50% of the total points around the circle are required for an estimate.

cm s^{-1} at 1.5 km and -15 cm s^{-1} at 3.75 km. The upper 2-3 km of the region shows very weak ascent peaking at 4 cm s^{-1}. The horizontal wind profiles reveal the presence of the inflow jet discussed in the following subsection. While the *u* profile is uniform at 2.5-3.0 m s^{-1}, the *v* component exhibits appreciable variation with a jet-like maximum of 10 m s^{-1} near 1.75 km.

The 1810 VAD analysis shown in Fig. 3-15 sampled the northern portion of the stratiform region. At this time the bright band is more prominent at 30 dBZ near 4 km (0.5 km below the 0 °C level). While the profile of divergence is qualitatively similar to that at 1655 UTC, the heights of the maxima in convergence are higher at 2.5 and 6.5 km, respectively. Secondary regions of divergence are seen at heights of 4.5 and 8 km. Two regions of mesoscale downdraft are analyzed, one near 1.5 km (18 cm s^{-1}), similar to the magnitude and location analyzed at 1655, and a secondary peak near 5.5 km (11 cm s^{-1}). Mesocale updraft over the upper 2 km is again very small. The *u* wind profile shows more variability (-3 to +4 m s^{-1}) than at 1655. Such a profile is suggestive of low-level and upper-level outflow from the system core, and middle level inflow into the convective region from the stratiform region. The *v* wind profile shows the same jet-like structure present earlier, but the peak is stronger at 12 m s^{-1} and occurs at a slightly higher level of 2.25 km, as opposed to 1.75 km at 1655 UTC. Thus, the jet appears to display only a very gradual downward slope, much less than that observed in the 13 July case.

In summary, the mesoscale patterns observed within the stratiform region of this case differ from those observed in other MCSs, including the 13 July system. The stratiform region is dominated by mesoscale downdraft exhibiting a double maximum value over the lowest 6-7 km. Only the upper 2 km exhibits very weak mesoscale updraft. In this case the mesoscale updraft/downdraft interface is located well above the 0 °C level. Also, the inflow jet was quasi-horizontal unlike the tilted structure observed in most other cases. Such patterns are substantially different from measurements taken in the stratiform region of larger-scale convective systems (e.g., Rutledge et al, 1988). Further details of the inflow jet are described next.

3.3.2 The inflow jet

Throughout the 1600-1810 UTC period a low-level inflow jet located within the stratiform region was observed within the 2-3 km level. This feature is apparent in the V_r displays of Figs. 3-9 - 3-12. A vertical section through this jet, obtained from a CP-4 RHI at 330 deg azimuth is presented in Fig. 3-14. The 330 deg RHI was used here since no other RHI scans were acquired at greater azimuth. Maximum speeds measured within the jet (including samples from other times) were 13-15 m s^{-1}, and the jet location was far below a well developed bright band within the stratiform region. The perturbation of the wind within this jet feature is somewhere in the range 5-10 m s^{-1} depending on what is assumed

for environmental winds. The special soundings released around (SW, NW, and within - see Fig. 3-9 for locations) the MCS between 1700 and 1800 all show a jet-like profile whose speed peaks between 2.5 and 3.5 km AGL. The St. Joseph sounding (5) represents the airflow just upwind of the precipitation filled volume of the MCS. The peak v wind component at this location is 11.0 m s^{-1} at 3.0 km AGL. In view of this sounding location to the NW, this data point provides additional structure on the sloping nature of the inflow jet. The Redstone (RSA) sounding sampled the stratiform region 22 km SE of CP-4. Its wind profile, which peaks at 10 m s^{-1} at 2.8 km AGL km, is consistent with the CP-4 VAD analysis. In examining the CP-4 measurements alone (Fig. 3-14), there is some acceleration of the flow (3-4 m s^{-1}) in the streamwise direction as the jet approaches higher Z_e within the stratiform region. Further into the stratiform region near CP-4 the jet decelerates and broadens in the vertical.

There are two atypical characteristics of the inflow jet observed here that differ from inflow jets observed in other MCSs. The first feature is the quasi-horizontal orientation, much unlike the slanted structure observed in the 13 July MCS and others documented in the literature. Such an orientation likely has important implications of the thermodynamics and dynamics of this system that are not understood. The second characteristic is the relatively low height of the jet axis, 2-3 km AGL, which is ~2 km below the melting level. In addition, the inflow jet did not appear to directly interact with the convective region of this MCS, due to the relative orientation of the convective and stratiform regions, as was the case for the 13 July MCS and other cases documented in the literature (e.g., Smull and Houze 1988).

3.4 Kinematic structure of the convective region M3

As noted in Section 3.1, the MCS life cycle was strongly dominated by three mesoscale regions of deep convection, M1, M2 and M3, that appeared along the western system flank at relatively uniform 3 h time intervals. The final component M3 evolved during the period of Doppler radar observations and is described here. From the satellite perspective shown in Fig. 3-2, M3 was first apparent at 1600 UTC, achieved a fully-developed state by 1700 and began to weaken by 1800 UTC. The pattern for all three components was to form and intensify along the western flank and then drift eastward while weakening. Thus, during the latter stage stratiform precipitation was associated with the warming cloud top. For example M3 was apparent at 1604 as a relatively intense cell group located near (x,y)=(-65,10) in Fig. 3-9a. As M3 expanded from the satellite perspective, additional cells were observed in the radar presentations at 1631 (Fig. 3-10a), 1658 (Fig. 3-11a) and at 1810 UTC (Fig. 3-12a). Throughout this period the general alignment of cells was NW to SE. Vertical structure information obtained from high resolution RHI scans at three times, 1639, 1701 and 1757 is presented in the following.

At 1639 UTC the CP-4 RHI scan at 285 deg azimuth (Fig. 3-17) sampled the core region of M3. This scan shows a discrete jump in echo top from 8-9 km AGL within the stratiform region at near range, to 13 km within the anvil of M3 which was ~30 km wide. Two major cells appear in this scan. The far cell at R=-70 km represents new growth and displays weak divergence in V_r of several m s^{-1} within the 6-9 km layer. Its inferred updraft/downdraft magnitudes are weak, probably on the order of 5 m s^{-1}. In contrast, the deeper core located near R=-55 shows appreciable convergence at middle levels (2-8 km AGL) and divergence at upper levels (9-13 km). The total divergence in V_r is ~15 m s^{-1} over 11 km horizontal distance. Only very weak divergence is shown over the lowest 1 km. Thus, the updraft at this time was at least moderate in intensity (~15 m s^{-1}). The total velocity differential across the M3 anvil region is 15 m s^{-1} (similar to that of the single intense convective component alone) over a distance of 30 km. The adjacent stratiform region exhibits a highly uniform flow structure, which was a striking characteristic of the stratiform region throughout the period of observation. However, patterns in Z_e show horizontal variations at all levels and bumps in the echo top of the stratiform region. One interesting feature that appears within the upper portion of the stratiform to convective region transition region is a zone of positive V_r at z=6 km, R=40 km. Such a structure also appears in the 1701 UTC CP-2 scan discussed below.

The CP-2 RHI scan along 235 deg azimuth at 1710 UTC (Fig. 3-18) reveals a similar and slightly more vigorous structure. As in the CP-4 RHI through M3, the intense echo core located at far range (R=-65) is kinematically weak despite the high measured Z_e. The main core at R=-50, however, shows appreciable divergence at high levels and convergence at middle levels, similar to that at 1639. The V_r difference over the upper region is ~20 m s^{-1} over 35 km distance. Most of this is accomplished by the primary core located at R=50 km. Only weak divergence was measured at low levels. This particular scan shows a prominent inflow (negative V_r) located within the 0.5-2.5 AGL layer near R=-70 km. At very low levels near the surface, weak outflow (positive V_r) from system downdrafts is apparent. A similar pronounced inflow layer is apparent in the CP-4 scan (Fig. 3-17) near R=-75. Thus, this region appears to have been favorable for growth of new convection and explains the development of major convective features observed along the western boundary.

At 1757 UTC the latter mature stage structure of M3 is captured in the CP-2 RHI along 208 deg azimuth shown in Fig. 3-19. Now located on the SW flank of the MCS, M3 remains a kinematically active feature, but has experienced a decrease in intensity from that at 1710. The 0 dBZ echo top has descended by 1.5 km to 11.5 km, and the velocity differential across the core at upper levels is ~11 m s^{-1} over 20 km distance, about half that at 1710. With the appearance of enhanced Z_e around the melting level at R=-65, the general structure shows signs of becoming more stratiform in nature. Only very weak new growth is apparent at greater ranges. One important difference is the inferred closer interac-

tion between the convective zone M3 and the inflow jet (visible in the stratiform region) which is encroaching M3 at this time. Thus, one important consequence of the change in relative location of M3 is a significant change in the wind shear profile experienced by deep convection. Whether the increased shear participated in the weakening of the system requires numerical simulation in addition to the observations presented here. It is interesting that the system continued to slowly decline in intensity after this time in view of the fact that the afternoon hours are typically most favorable for deep convection in the Southeast. Greater static stability at low levels, as indicated in the 1720 UTC Double Springs sounding (location 2 in Fig. 3-2) located just outside the precipitation region near the SW edge of the MCS, probably assisted in the dissipation process.

3.5 CP-2 multiparameter analysis

Multiparameter measurements from CP-2 revealed a highly variable structure in Z_{DR} within both the convective and stratiform regions of the MCS. In this section we will examine inferred microphysical characteristics of convective and stratiform components of the MCS at 1701 and 1757 UTC.

The RHI along 235 deg azimuth at 1701 UTC (Fig. 3-18) samples both stratiform and convective (M3) regions of the mature MCS. There are patterns displayed here that were measured at other times and locations within the MCS. The intense convective component within M3 at R=50 has relatively low Z_{DR} values, between 1 and 2 dB, within the liquid portion at low levels. Above the melting layer relatively low Z_{DR} values <0.3 dB are co-located with the core of Z_e, indicative of graupel growing within moderate updraft. (The V_r patterns indicate that this is a region of moderate updraft.) This pattern is one which was apparently sustained over the life cycle of M3. Another feature associated with this convective core is the 15 km wide zone of high Z_{DR} (peak >1.5 dB) adjacent to this core at (R,z)=(-40,7). This also was a persistent feature and appears to have been closely associated with the shear layer produced by outflow from the thunderstorm anvil above and a narrow swath of flow into the convective region from the stratiform region below (labeled "IF" in Fig. 3-18c).

The convective core near R=-65 in Fig. 3-18b exhibits relatively high Z_{DR} approaching 3 dB. Again Z_{DR} decreases significantly above the melting level. In combining this information with the V_r data in Fig. 3-18c we infer that graupel growth is again active within this core whose updraft extends to about 8 km. However, above 5 km Z_e is less than 25 dBZ. Thus, it appears that the collision-coalescence growth process is producing a large fraction of precipitation over the lower 4 km of this cloud.

The stratiform region at R<35 shows a more consistent structure. Variations in Z_{DR} are related to variations in particle size and associated values of Z_e. Peak Z_{DR} values of 1-1.5 dB just below 4.0 km AGL bring out the melting layer.

Above the level of melting, Z_{DR} decreases to a relative minimum in the range 0.3-0.6 dB between 4.5 and 6.0 km AGL. This may indicate the presence of aggregrates which would tend to tumble and therefore produce low Z_{Dr}. Above 6 km to near echo top, Z_{DR} values are greater at 0.6-1.0 dB, perhaps indicative of oriented pristine ice crystals. According the the VAD analysis, this region was experiencing very weak upward motion which would promote supersaturation and ice crystal growth by vapor deposition.

The RHI analysis presented in Fig. 3-19 samples the M3 region at 1757. This plane intersects (a) new but weak growth at far range; (b) a weakening major convective element, representing the major component of M3, at intermediate range; and (c) the stratiform region at near range. The stratiform region in this case exhibits a more non-uniform structure in both Z_e and Z_{DR} (Fig. 5a,b). Vertical profiles within the stratiform region at 33.5 km range are shown in Fig. 3-20c. A bright band is located near the 4 km level (the 0° C level is at 4.4 km). Enhanced values of Z_{DR} occur in association with enhanced Z_e. A secondary peak in Z_{DR} (1.5 dB) is also present near 6.7 km height (T = -14 °C). As shown in Fig. 3-19b, this region of enhanced Z_{DR} is confined to a region ~10 km wide. Such patches were observed throughout the period of CP-2 measurements (including the 1701 analysis, Fig. 3-18b) and are similar in some respects to Z_{DR} observations made in stratiform clouds (e.g., Bader et al, 1987).

At other locations within convective cores much different profiles of Z_{DR} are seen in Fig. 3-19a,b. For example, the profile within the core of an old convective element (Fig. 3-20b) shows a relative minimum value in Z_{DR} 1 km above the 273 K level, which is capped by nearly uniform values of ~1 dB from 7 to 10 km. The radial velocity patterns in Fig. 3-19c suggest a pattern of weak updraft (several m s^{-1} or less) within the upper half of this domain, and weak downdraft over the lower portion. Thus, the Z_{DR} profile may suggest a systematic fallout of precipitation from the cloud, with graupel providing the low Z_{DR} values and oriented plate-like crystals producing the higher values above 7 km.

Finally, a region of new precipitation growth within kinematically-weak cumuli (echo top ~6km and updraft on the order of several m s^{-1}, as inferred from the radial velocity patterns in Fig. 3-20a) is suggested by the measurements at 81.5 km range. This growth is located directly above an outflow boundary as indicated in the profile of radial velocity (Fig. 3-20a) Here, relatively high Z_{DR} values peaking just above 3 dB are located within relatively weak ZE of 15-20 dBZ. Such values are similar to measurements described by Illingworth (1988) and suggest a small number of large raindrops whose growth was accomplished by the collision-coalescence process.

3.6 Summary

The following items summarize the features observed within this atypical MCS:

a) The MCS formed during the early morning hours and dissipated by midafternoon, a characteristic which appears atypical of deep convection over the Southeast.

b) The MCS existed for ~12 hr and attained a maximum horizontal dimension (of precipitation) of 120 km.

c) Much of the precipitation was stratiform (the fraction relative to the total was not computed), and the distribution of total and stratiform was variable.

d) Over the life cycle of this system, deep convection was not a substantial feature. Individual convective elements were generally weak to moderate in intensity. One key question which arises in this regard is: Was the convective activity sufficient to account for the flux of vapor and precipitation into the stratiform region, or was external forcing acting to help promote the stratiform precipitation?

e) The stratiform region was located to the left, with respect to motion, of the convective region, as apposed to the trailing orientation in the 13 July case (and typical squall line cases documented in the literature).

f) The stratiform region was dominated by mesoscale downdraft, peaking at 15-20 cm s^{-1} magnitude, over the lower 6-7 km. Only the upper 2-3 km of the region displayed weak mesoscale updraft of several cm s^{-1} magnitude. The height of the updraft/downdraft boundary was large in this case and was ~2 km above the melting layer. Such an observation would have a significant impact of estimated profiles of latent heating.

g) The precipitation characteristics (size, habit/orientation) within both the convective and stratiform regions showed appreciable variability.

h) The inflow jet observed here was quite quasi-horizontal in orientation. A total height variation of no more than 1 km was observed over a horizontal distance of 125 km. The jet was also located at a low level of 2-3 km, 1.5-2.0 km below the melting level.

Item (a) is thought to be unusual for small MCSs that characterize the Southeast during the midsummer months (based on our own informal observations). Items (f) and (h) represent characteristics that deviate from the normal observed structure of all MCSs.

Figure 3-1 (on the following two pages). Regional GOES IR images at 0600, 0900, 1200 and 1500 UTC. The Nashville (BNA) WSR-57 RADAP maximum range of 240 km and the COHMEX observational network are shown. Brightness temperature is gray shaded at the following levels (K): interior black, $T<217$ K; white, $T<237$; light gray, $237<T<250$; medium gray, $250<T<260$; dark gray, $260<T<270$. An additional contour is drawn at 230 K in each panel. In panel c, the location of the 1200 UTC BNA sounding is shown.

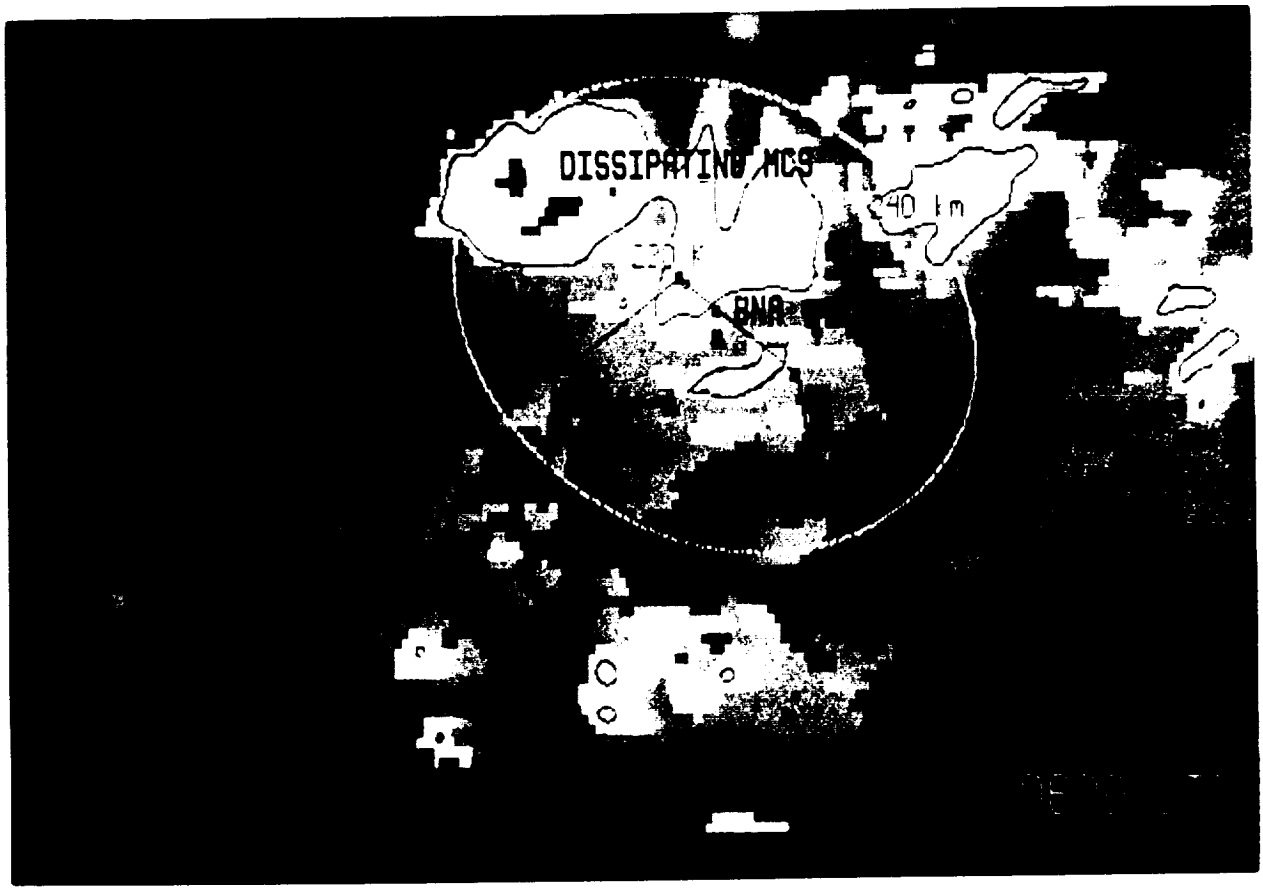
DISSIPATING MCS
240 km
BNA

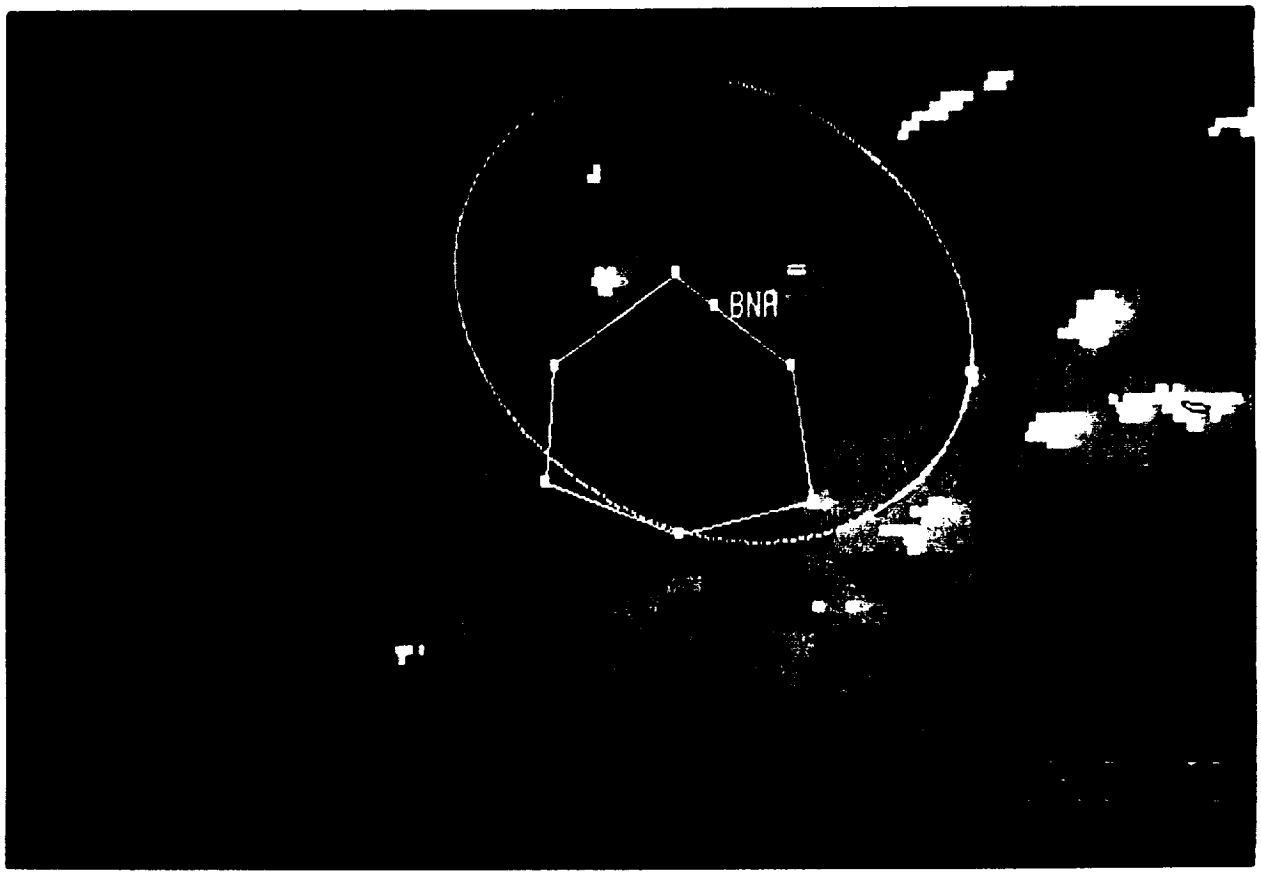
BNA

Figure 3-2 (on the following two pages). GOES IR images at 1600, 1630, 1700 and 1800 UTC. CP-4 range markers at 115 km (maximum range) and 20 km (the VAD analysis range) are shown. Other dotted lines drawn in panels *b* and *c* refer to RHI scans from CP-2. Brightness temperature is gray shaded at the following levels (K): white, $T<237$; light gray, $237<T<250$; medium gray, $250<T<260$; dark gray, $260<T<270$. Additional contours are drawn at 240, 230 and 220 K. In panel *c*, locations of soundings taken between 1715 and 1815 UTC are shown.

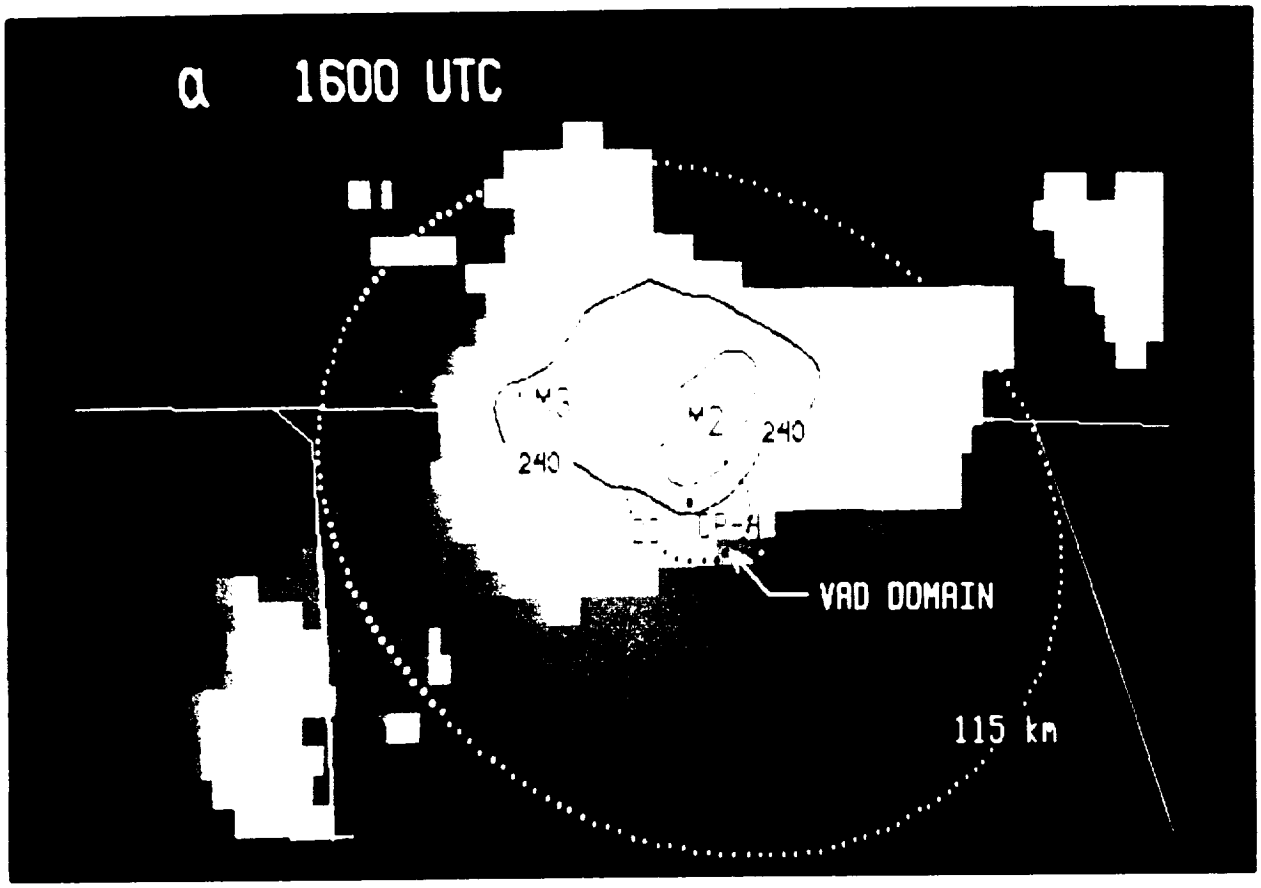
a 1600 UTC
M2
240
240
CP-4
VAD DOMAIN
115 km

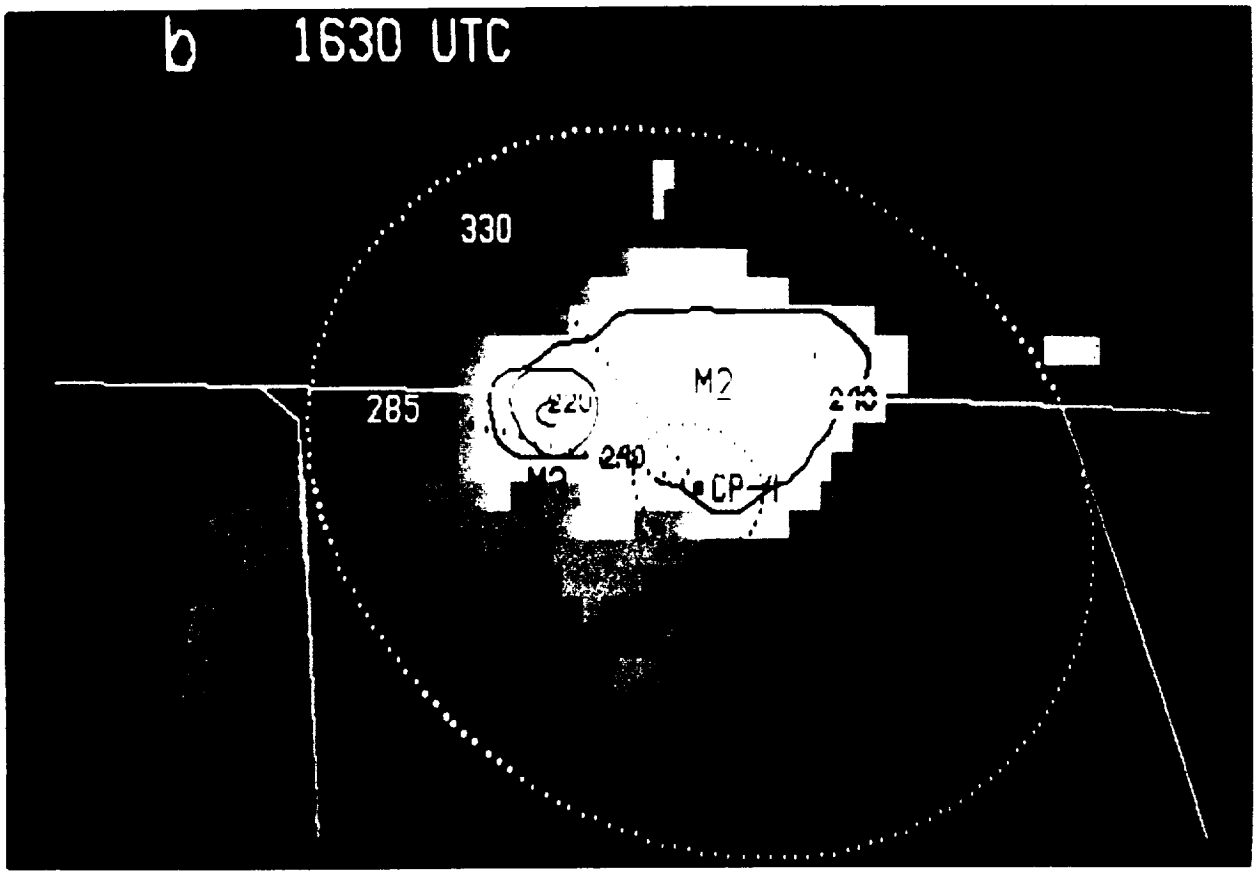
b 1630 UTC
330
285
M2
240
CP-4

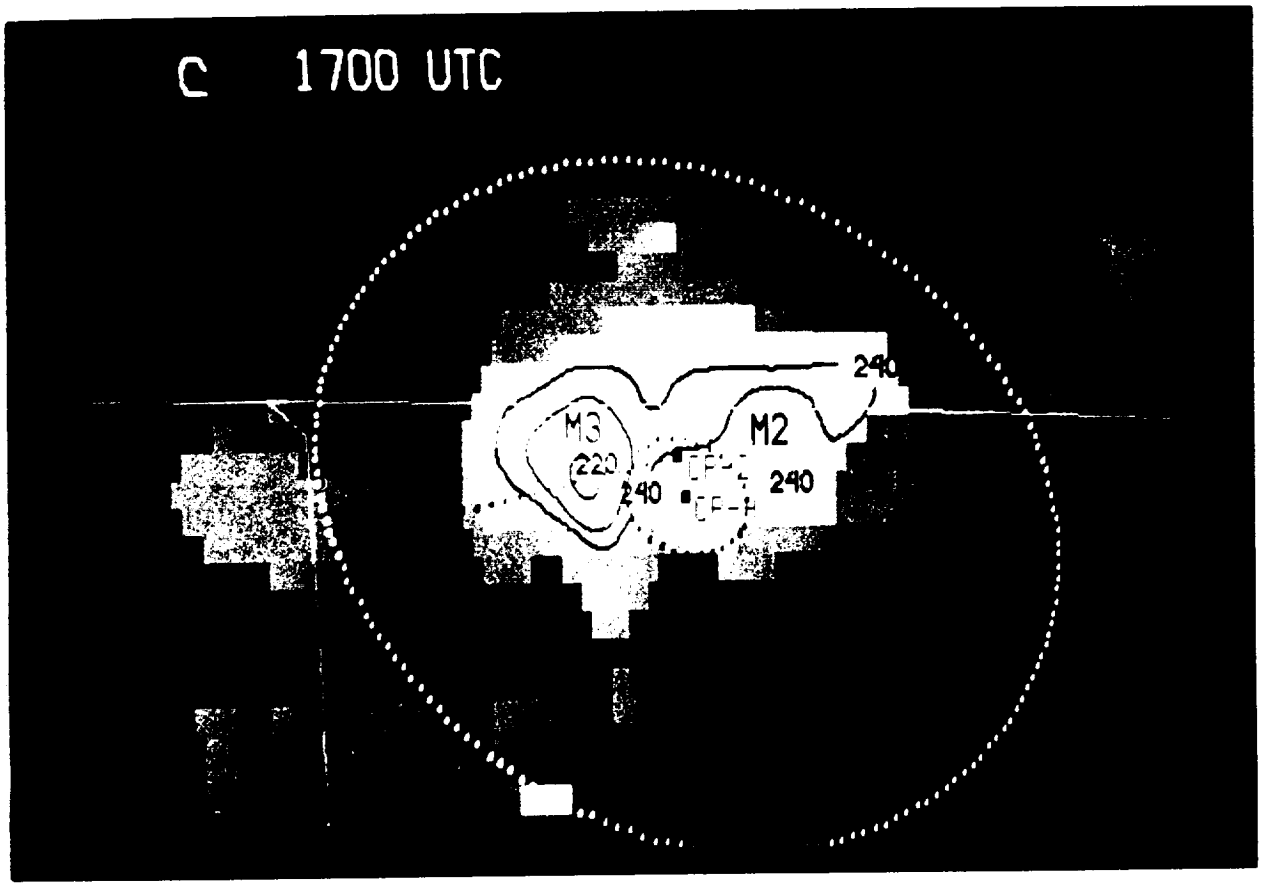
c 1700 UTC
M3
220
240
M2
240
240

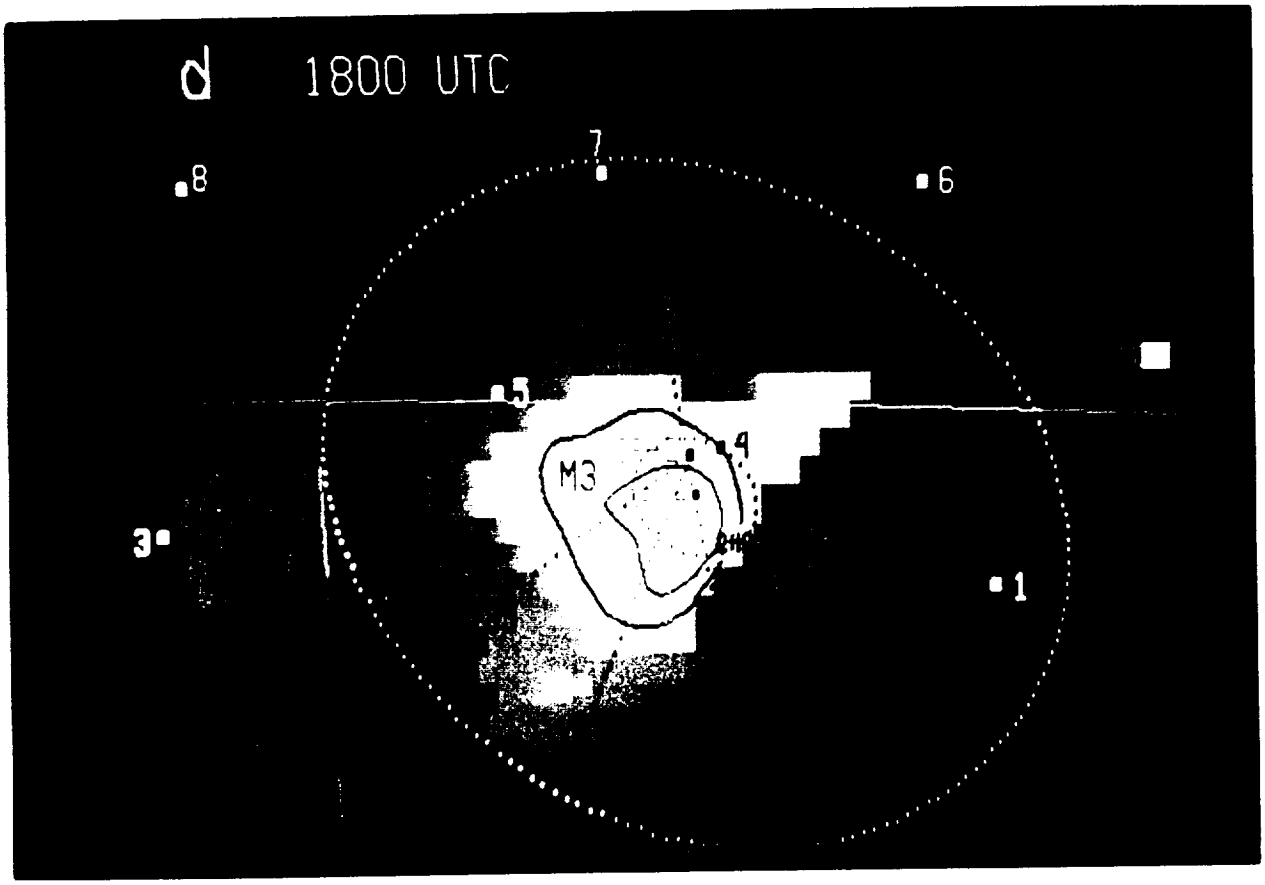
d 1800 UTC
7
8
6
5
4
M3
3
1

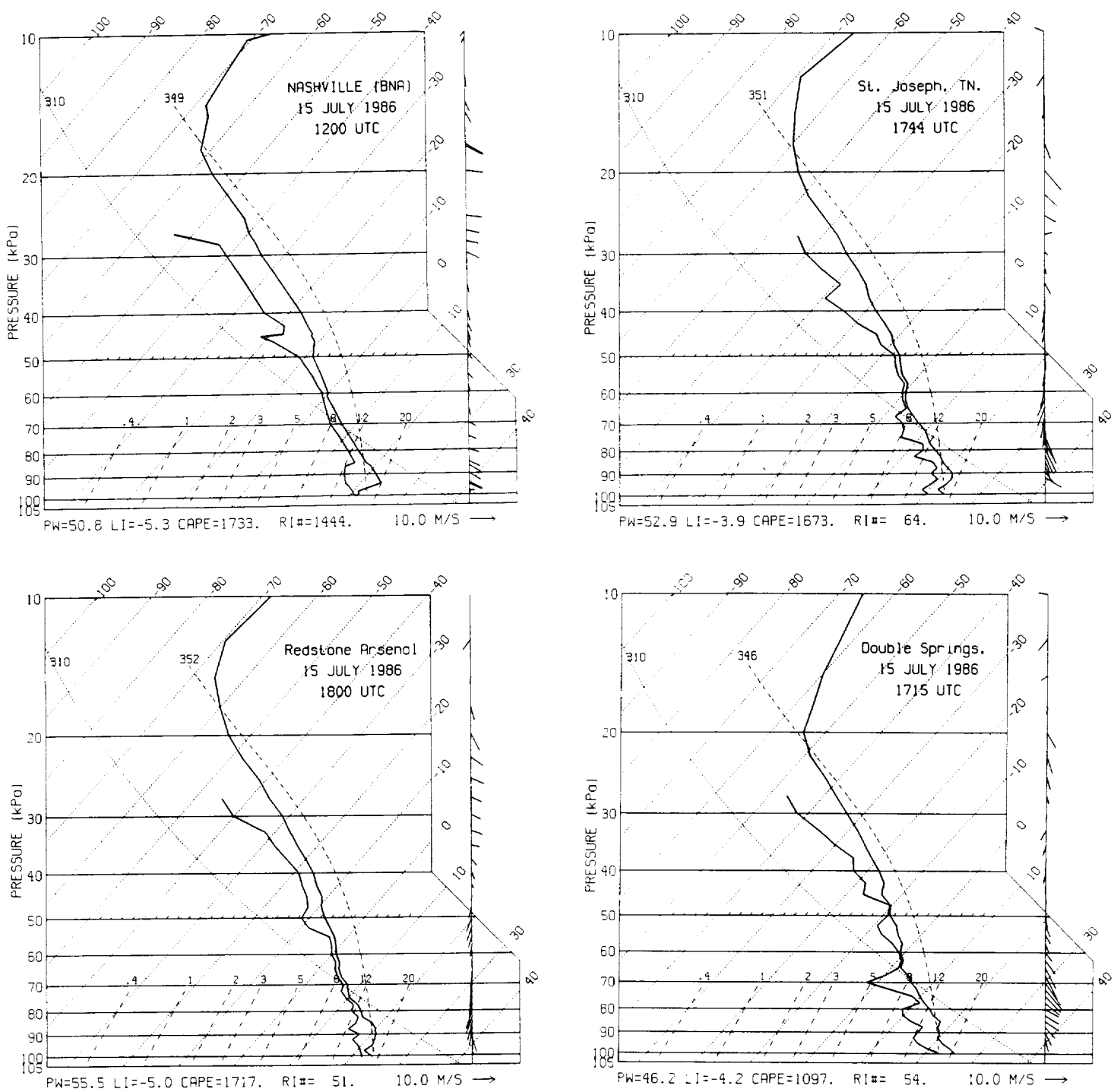

Figure 3-3. Rawinsonde soundings, plotted on skew-T ln p diagrams, which sample the undisturbed environment of the MCS (a), and which sample the near (disturbed) environment of the MCS (b-d). (a) NWS sounding taken at 1200 UTC from Nashville (BNA), approximately 100 km to the NE of the MCS. The relative location is shown in Fig. 3-1. (b) Special sounding released at 1744 UTC along the NW edge of the MCS, denoted as location "5" in Fig. 3-9. (c) Special sounding released within the eastern portion of the stratiform precipitation region at 1800 UTC, denoted as location "RSA" in Fig. 3-9. (d) Special sounding released near the SW edge of the MCS at 1720 UTC, denoted as location "2" in Fig. 3-9.

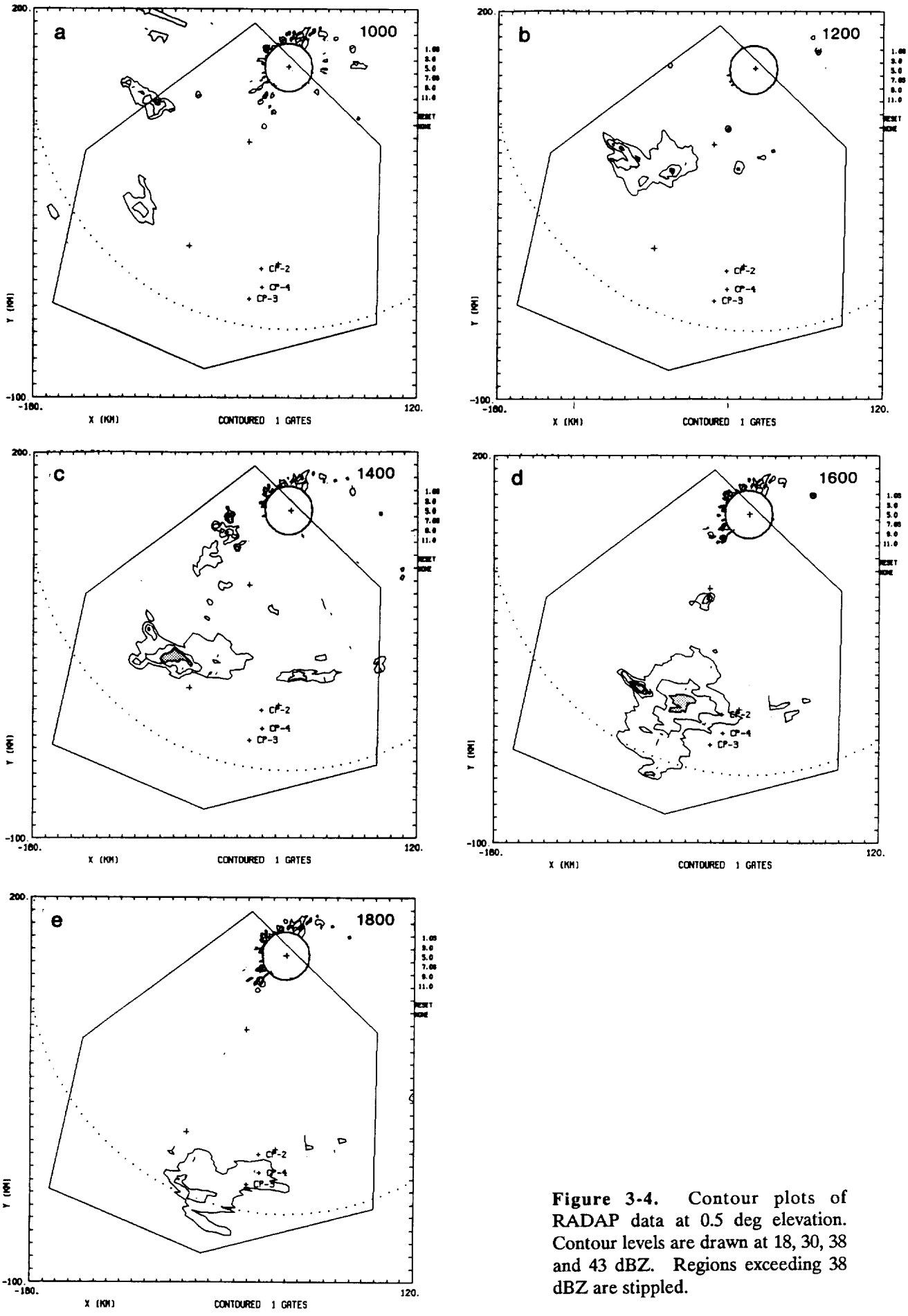

Figure 3-4. Contour plots of RADAP data at 0.5 deg elevation. Contour levels are drawn at 18, 30, 38 and 43 dBZ. Regions exceeding 38 dBZ are stippled.

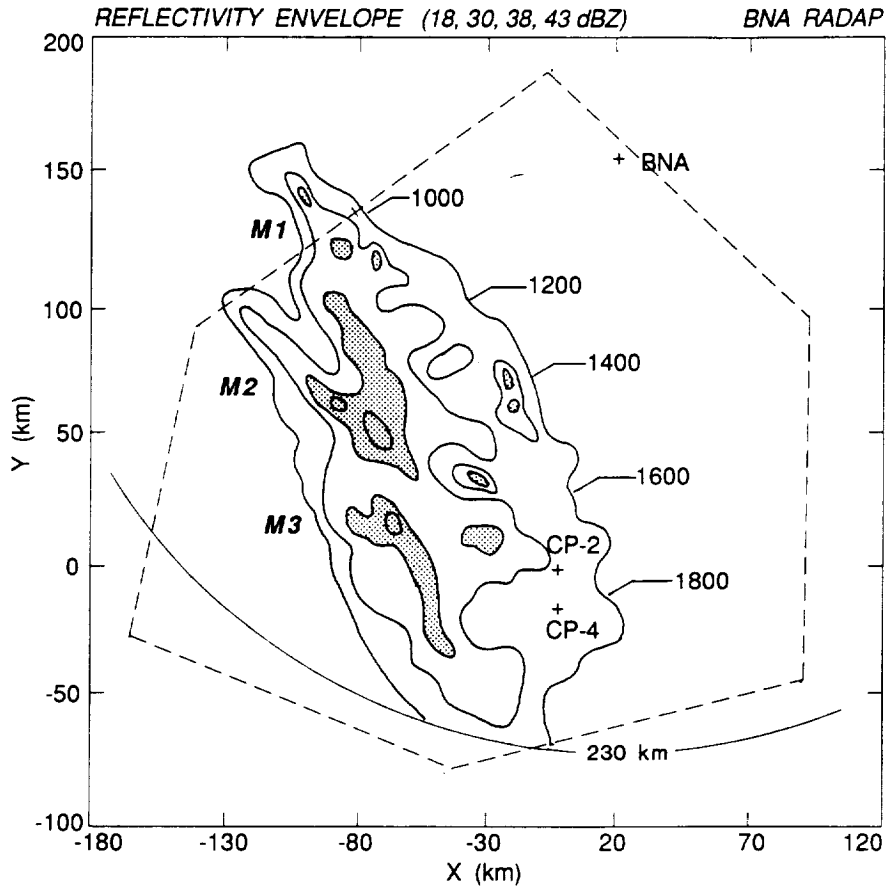

Figure 3-5. Envelope of reflectivity factor obtained from the 0.5 deg PPI of the Nashville (BNA) RADAP. Values exceeding 38 dBZ are shaded. The approximate system central axis, normal to system motion, is labeled in UTC. First echo was observed at 0900, and the final echo was observed by CP-4 at 2100 UTC, when the system was beyond the maximum range of 232 km.

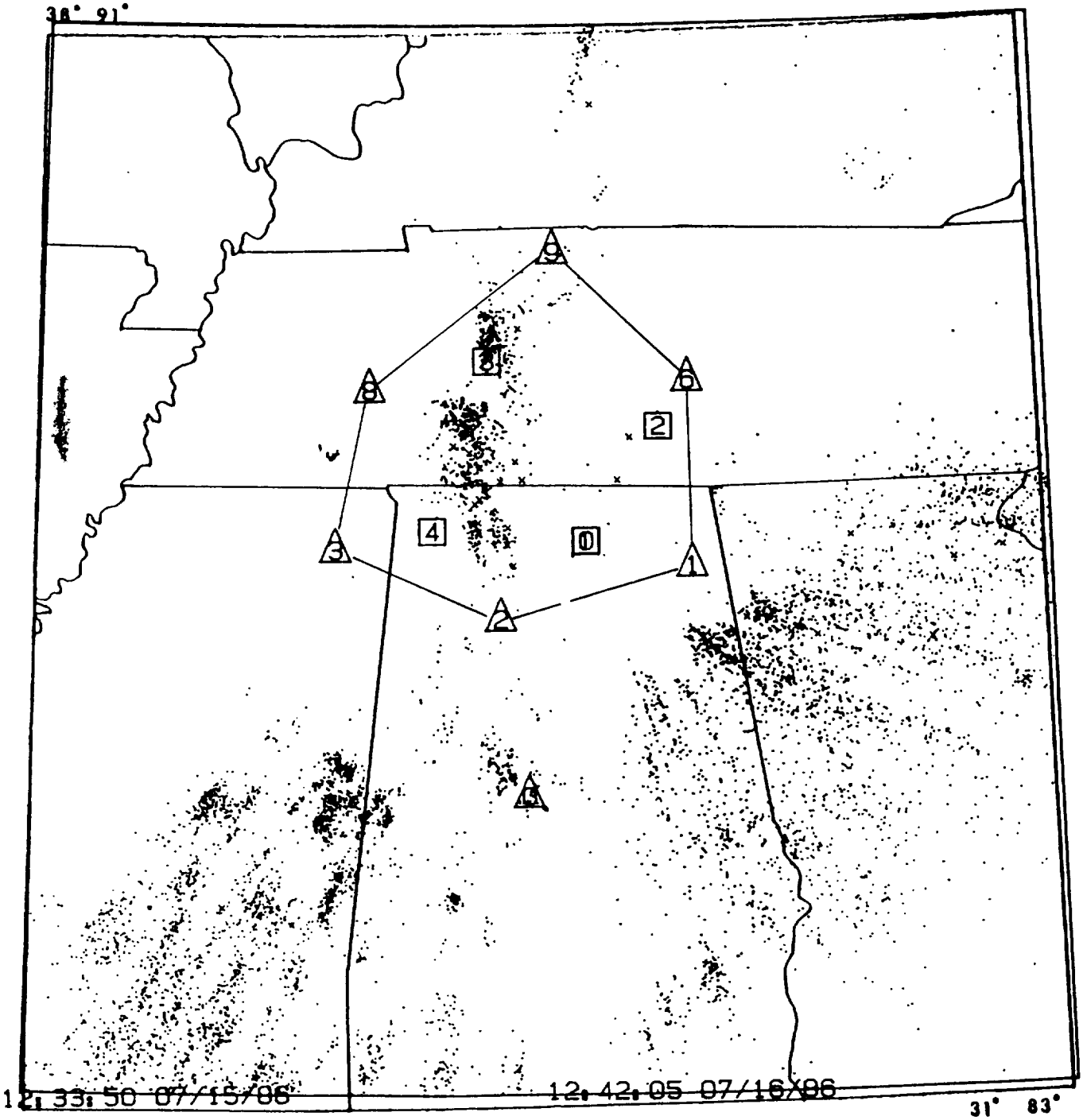

Figure 3-6. Total lightning counts during the period 1233 UTC 15 July to 1242 UTC 16 July 1986. Dots represent negative flashes and "x" symbols denote positive flashes.

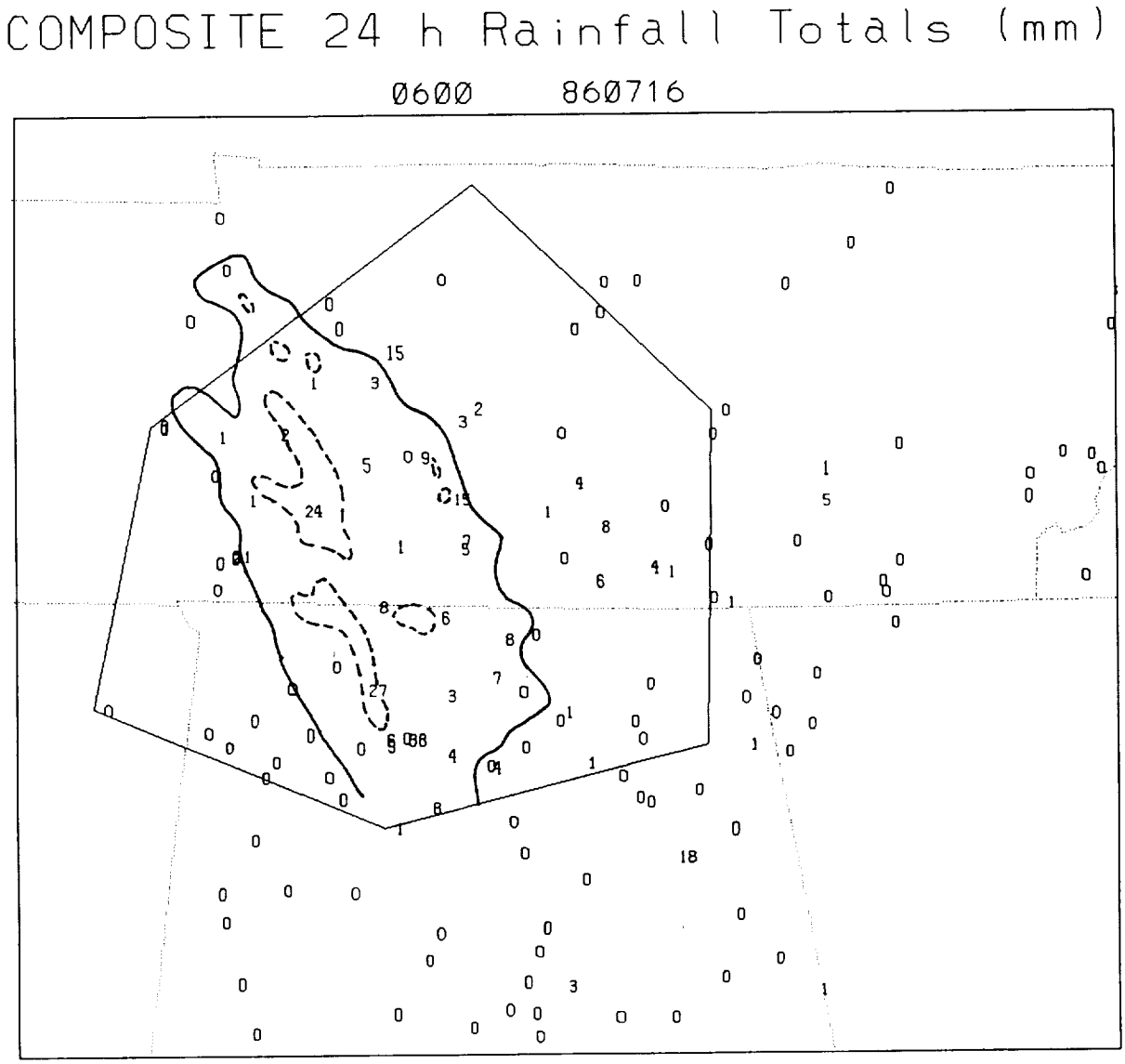

Figure 3-7. Total precipitation amounts (as in Fig. 2-3) for the 24 h period ending 1200 UTC 16 July. During this period the MCS of interest was the only cloud system to precipitate over the region. Selected contours from the reflectivity envelope analysis of Fig. 3-1 are superimposed as the solid (18 dBZ) and dashed (38 dBZ) lines.

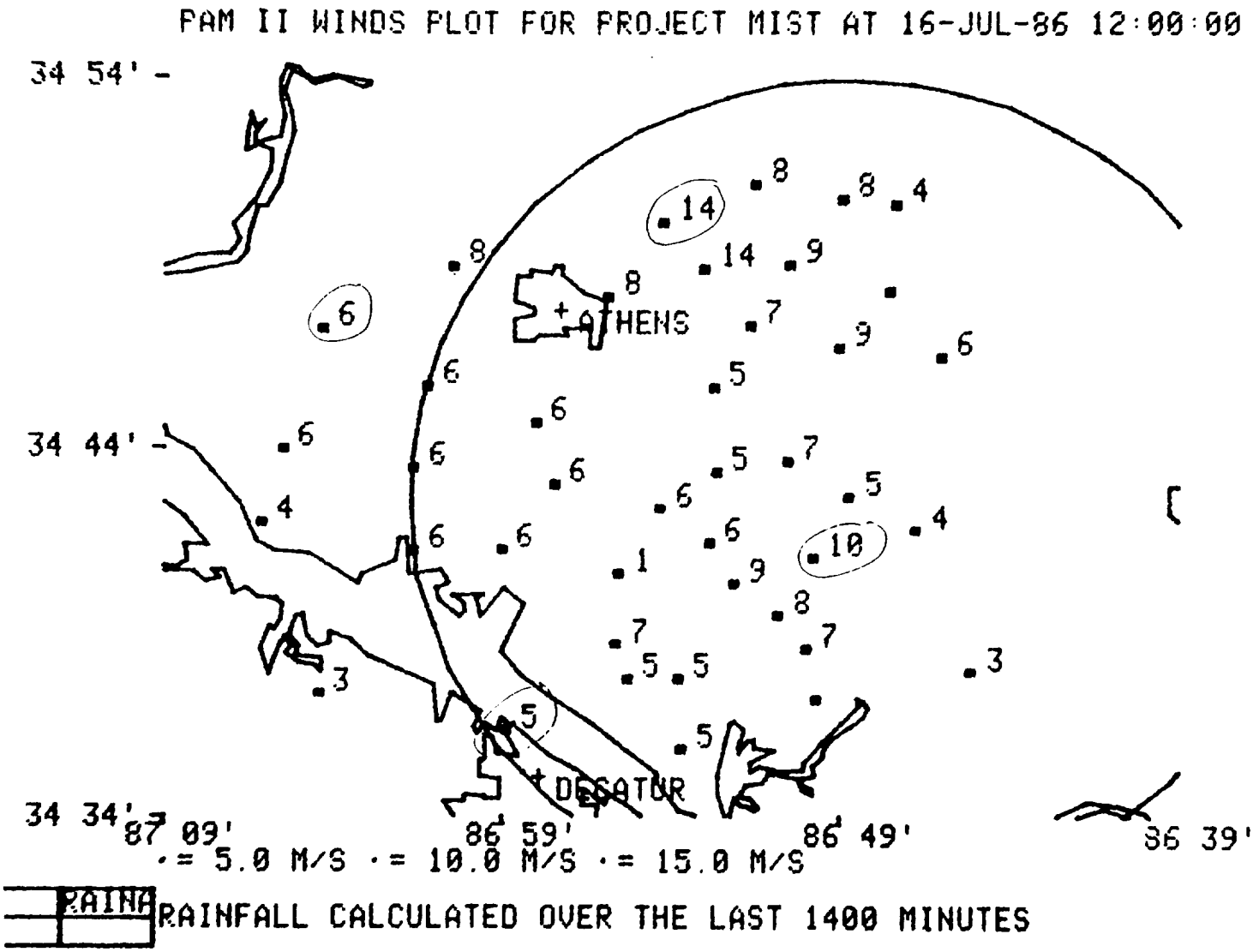

Figure 3-8. Total precipitation amounts (mm) from PAM stations over the MIST network. See Fig. 1-1 for relative location.

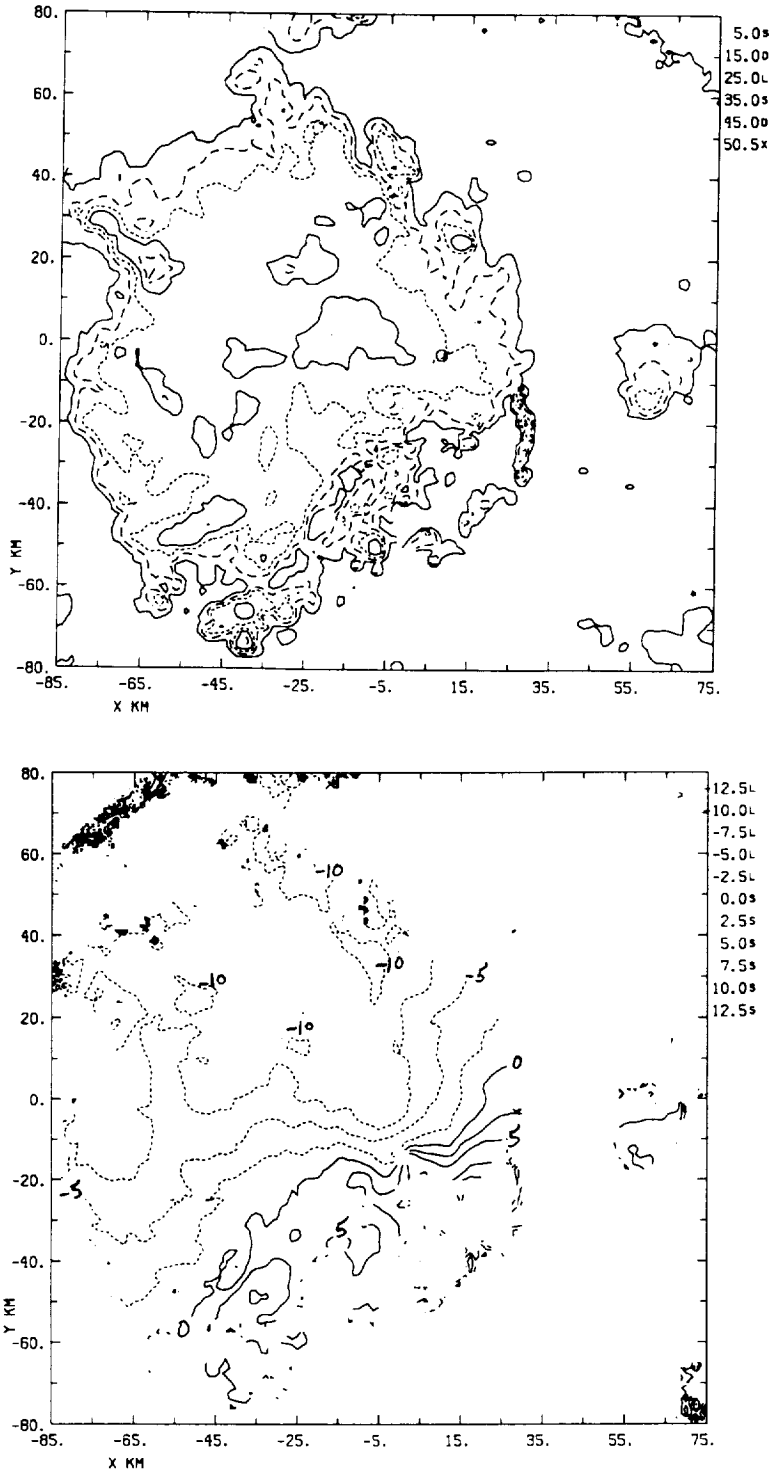

Figure 3-9. Analysis of CP-4 (a) reflectivity factor and (b) radial velocity at the 2 km level at 1604 UTC. Reflectivity is contoured every 10 dBZ beginning at 5 dBZ, and radial velocity is contoured every 2.5 m s^{-1}.

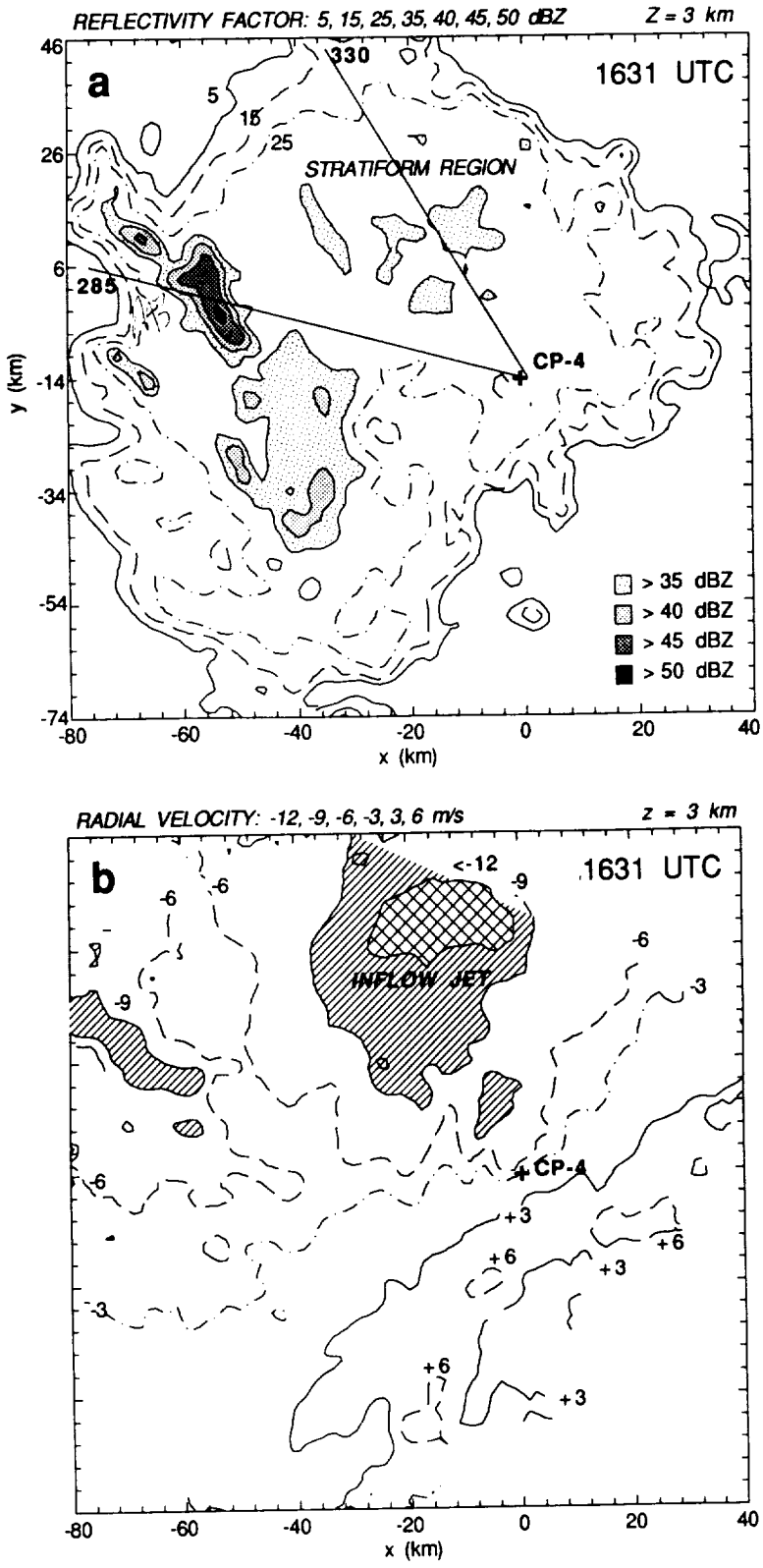

Figure 3-10. As in Fig. 3-8, except for 1631 UTC. CP-4 RHI scan locations (labeled in deg azimuth) at 1639 are shown.

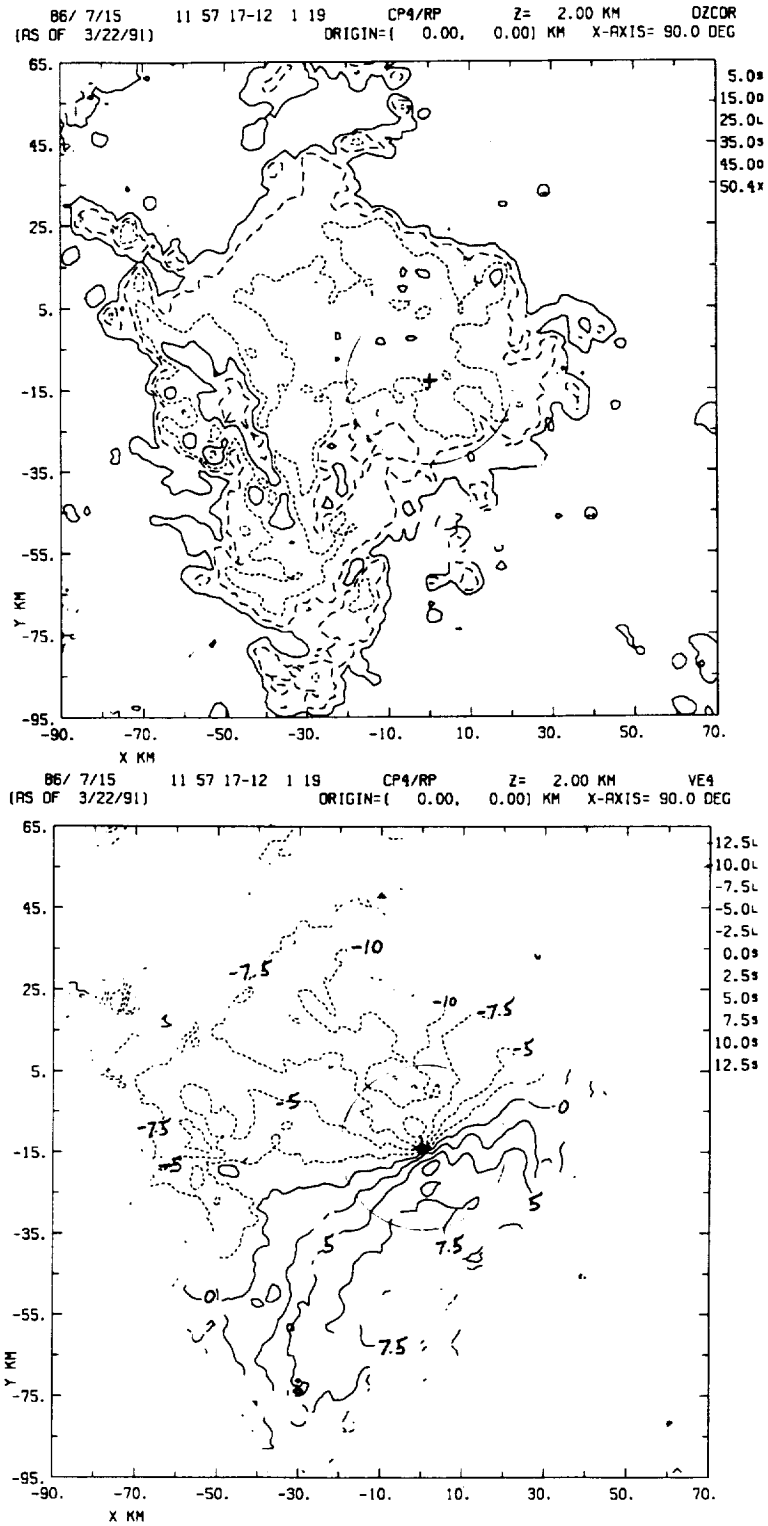

Figure 3-11. As in Fig. 3-8, except for 1658 UTC. CP-2 RHI scan locations at 1701 UTC are shown.

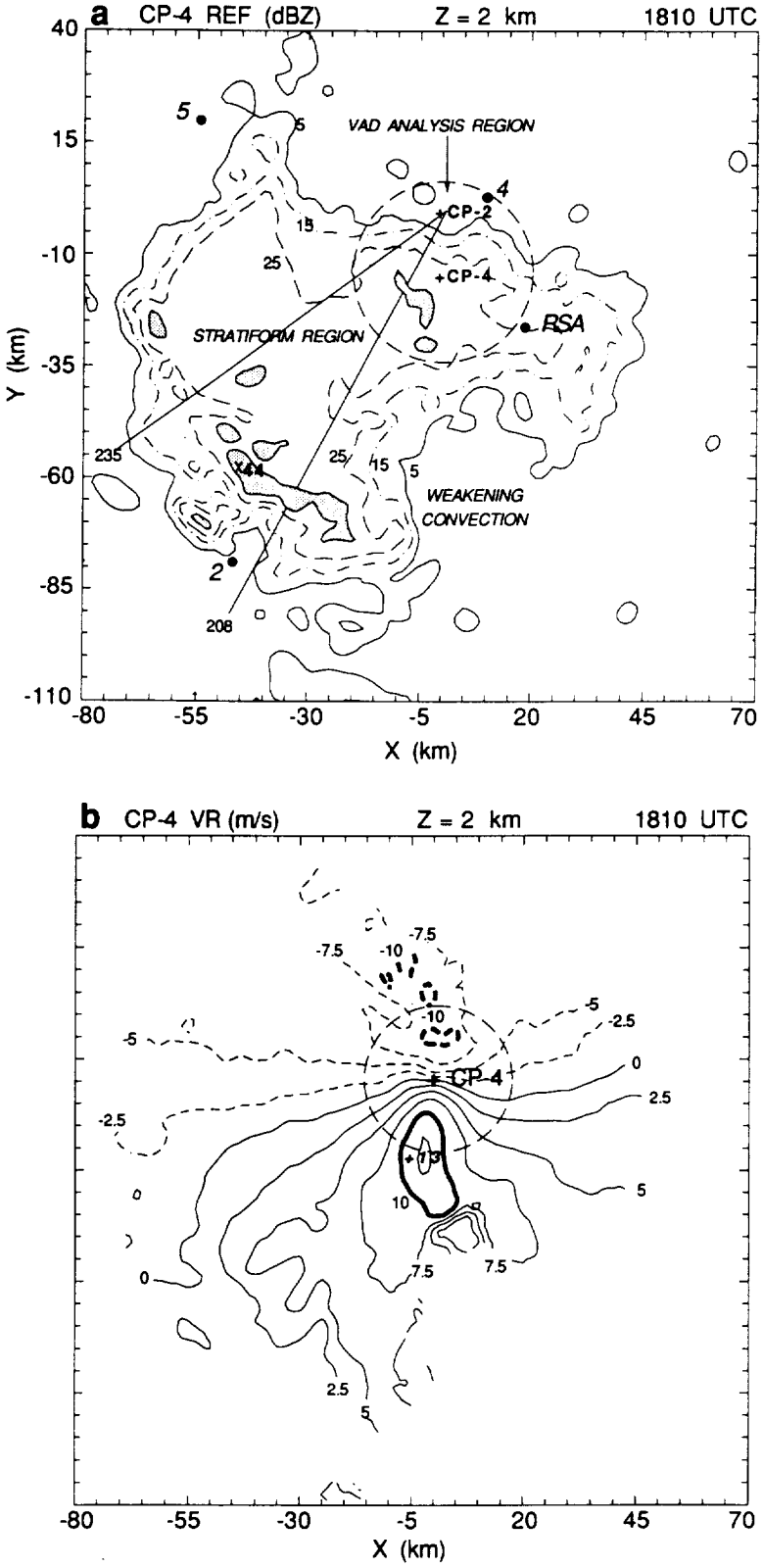

Figure 3-12. As in Fig. 3-8, except for 1810 UTC. Sounding locations (2, 4, 5 and RSA) and locations of CP-2 RHI scans near 1757 UTC are indicated in panel a. At this time the MCS is in a state of decline.

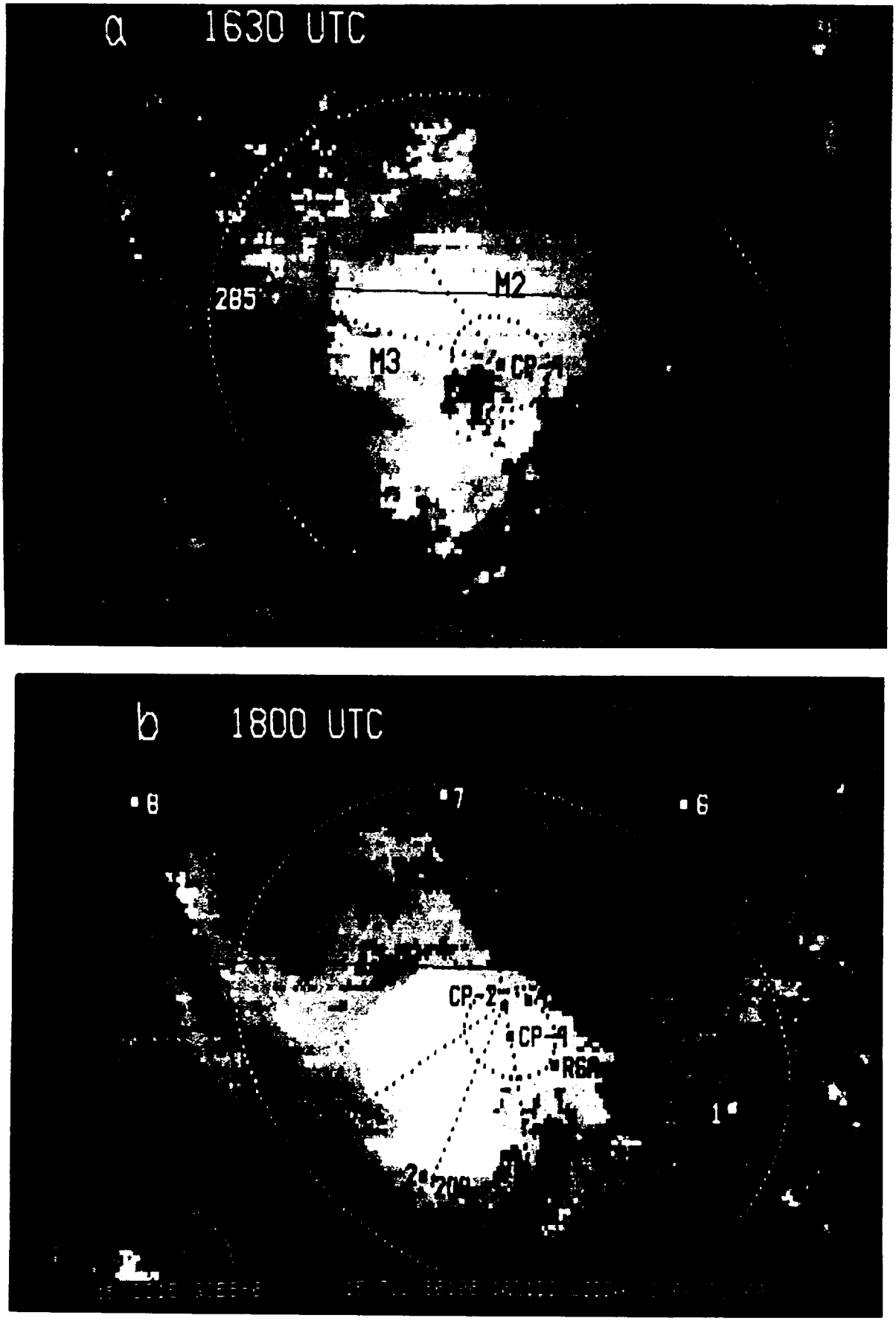

Figure 3-13. GOES visible imagery at 1630 and 1800 UTC. The labeling is the same as that for Fig. 3-2.

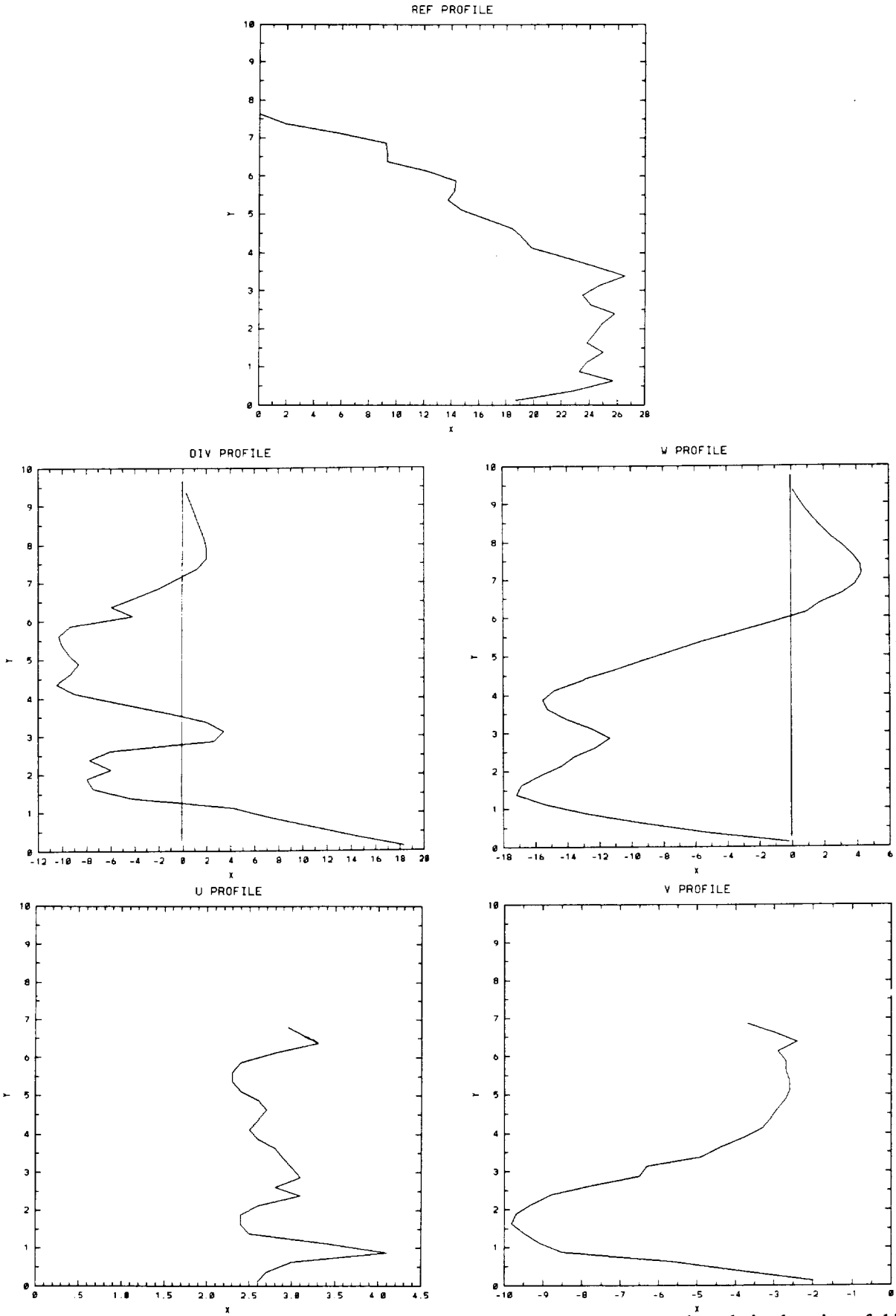

Figure 3-14. Quantities derived from the CP-4 VAD analysis at 1655 UTC. The relative location of this region is shown in Figs. 3-2c and 3-11. Ranges of 16, 20, 24 and 28 km were used to obtain high vertical resolution.

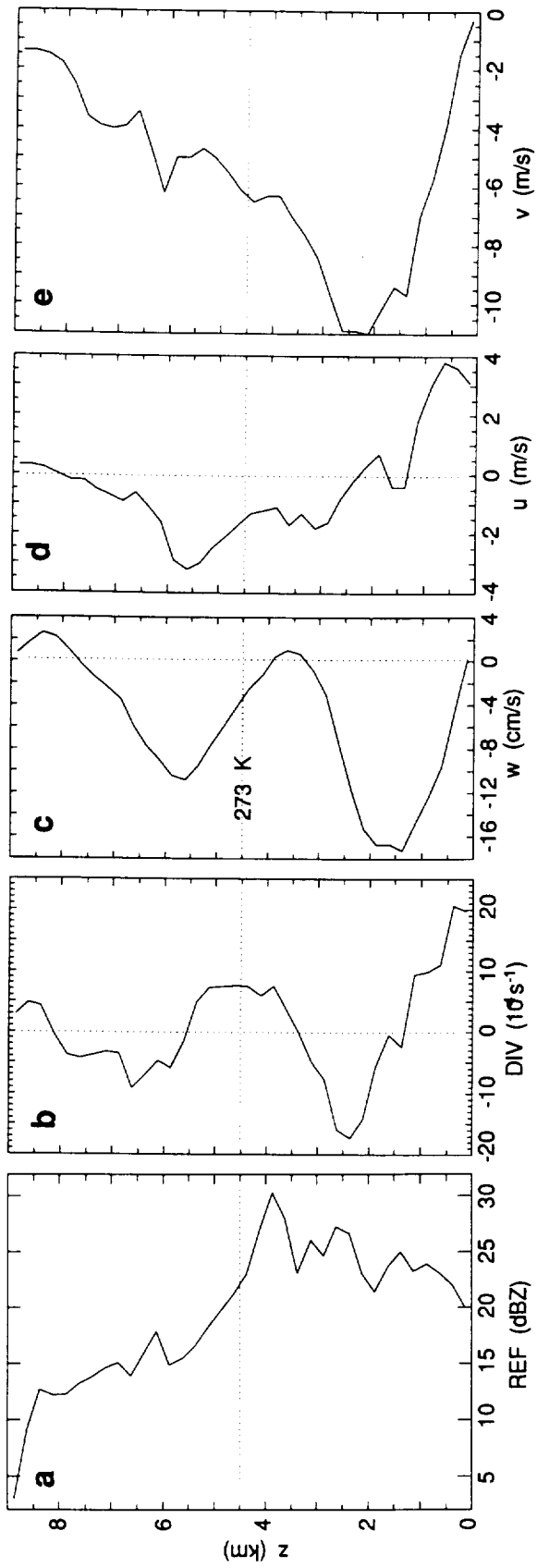

Figure 3-15. VAD analysis as in Fig. 3-14 except for 1810 UTC. The relative location of the VAD domain is shown in Fig. 3-2d, 3-12 and 3-13b.

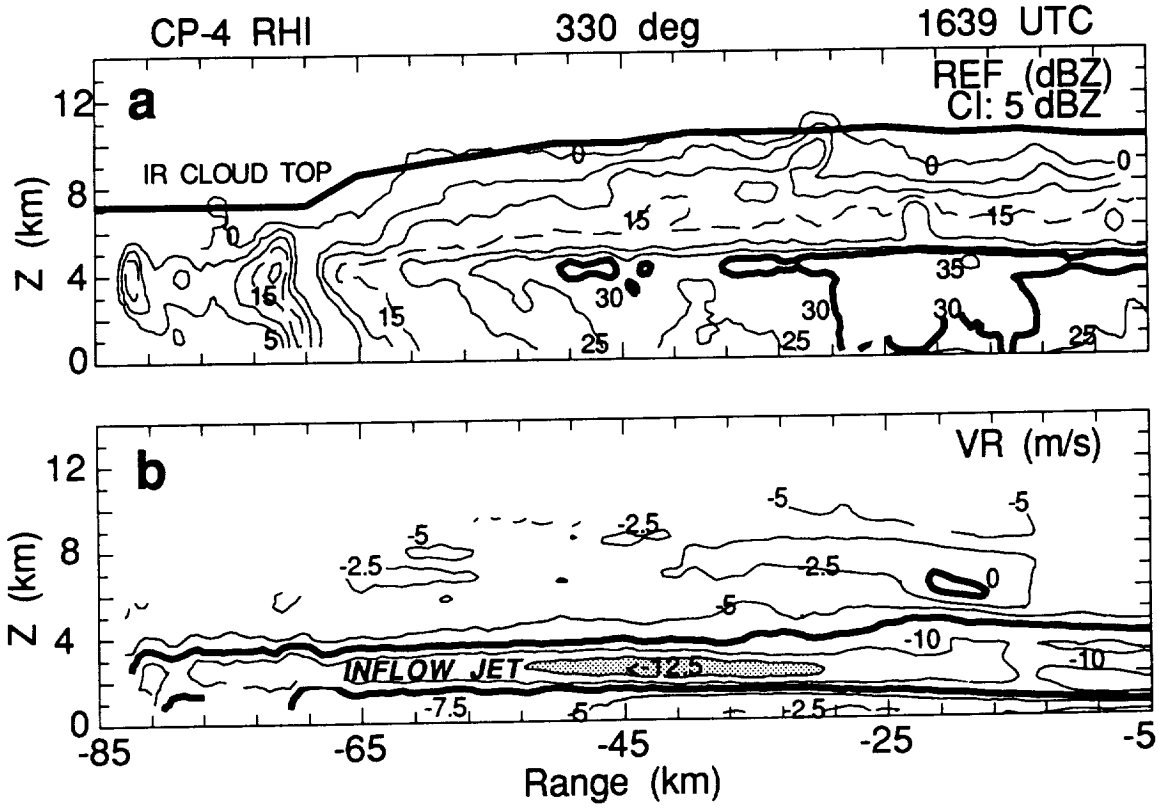

Figure 3-16. CP-4 RHI scan at 330 deg azimuth, at 1639 UTC (see Figs. 3-2b and 3-9 for location), showing the structure of the MCS inflow jet. (a) Reflectivity factor drawn every 5 dBZ beginning at 0 dBZ. The solid line is 30 dBZ. The IR-derived cloud top is also shown as a solid line near the 0 dBZ echo top. (b) Radial velocity contoured every 2.5 m s^{-1}. Thick solid lines are drawn at 0 and -7.5 m s^{-1}, and values less than 12.5 m s^{-1} are stippled. This jet is quasi-horizontal unlike that of the 13 July MCS.

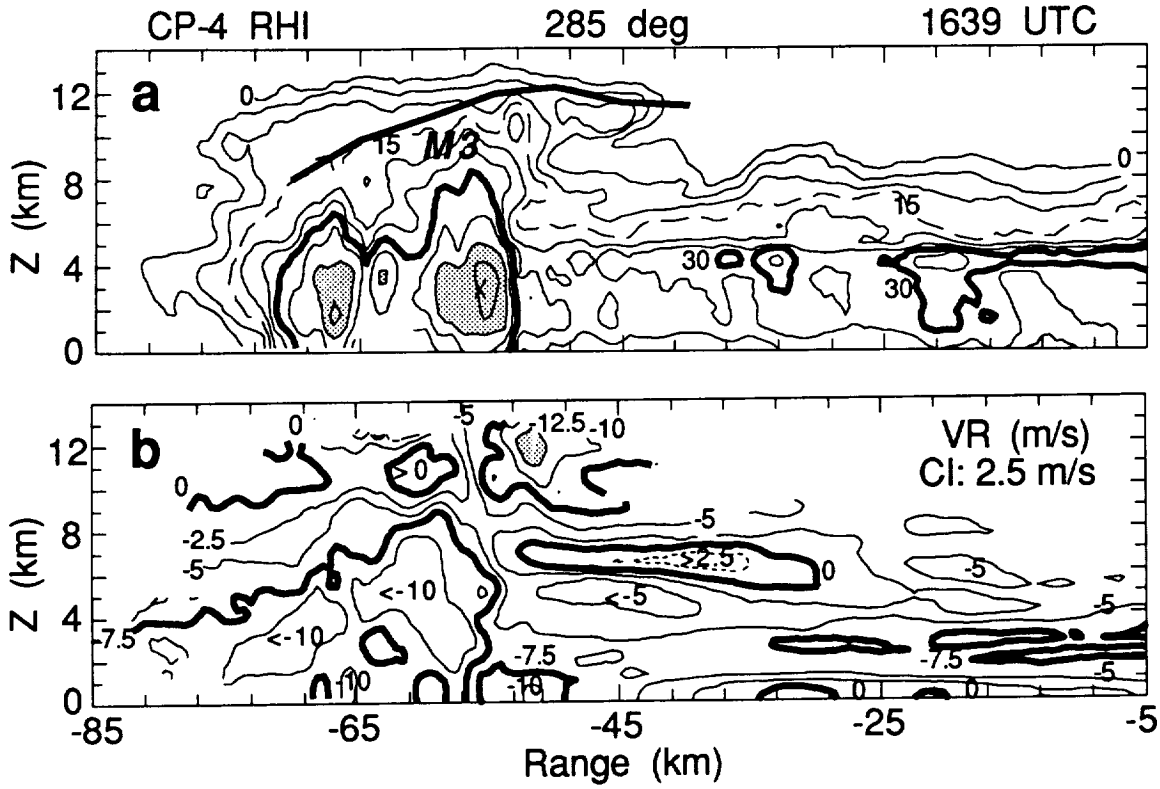

Figure 3-17. CP-4 RHI scan through mesoscale convective region C at 285 deg azimuth, at 1639 UTC (see Figs. 3-2b and 3-9 for location). (a) Reflectivity factor drawn every 5 dBZ beginning at 0 dBZ. The solid line is 30 dBZ. Values exceeding 40 dBZ are stippled. (b) Radial velocity contoured every 2.5 m s^{-1}. Thick solid lines are drawn at 0 and -7.5 m s^{-1}, and values less than 12.5 m s^{-1} are stippled.

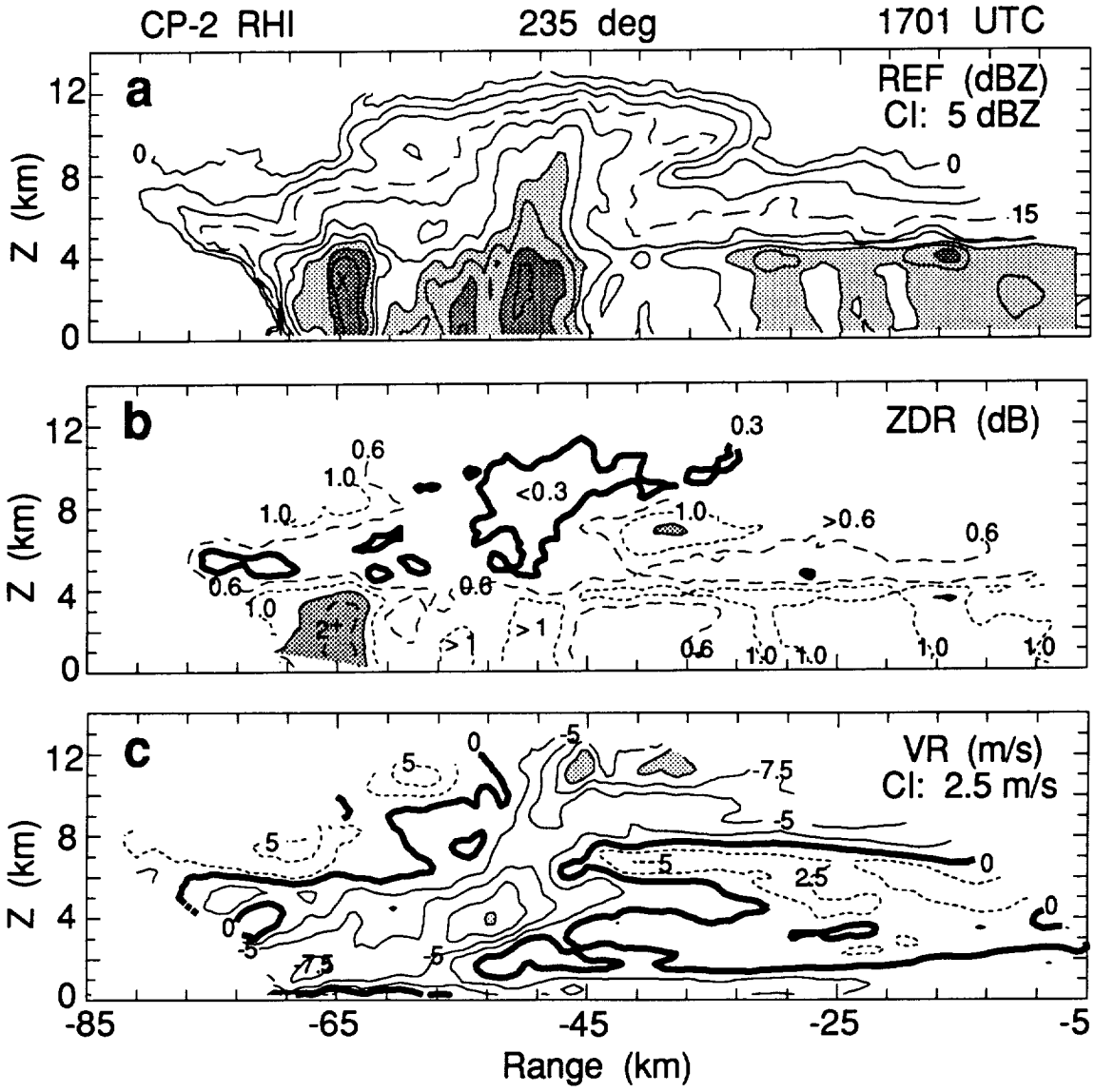

Figure 3-18. CP-2 RHI along 235 deg azimuth at 1701 UTC. The relative location of this RHI is shown in Fig. 3-2c and 3-11.

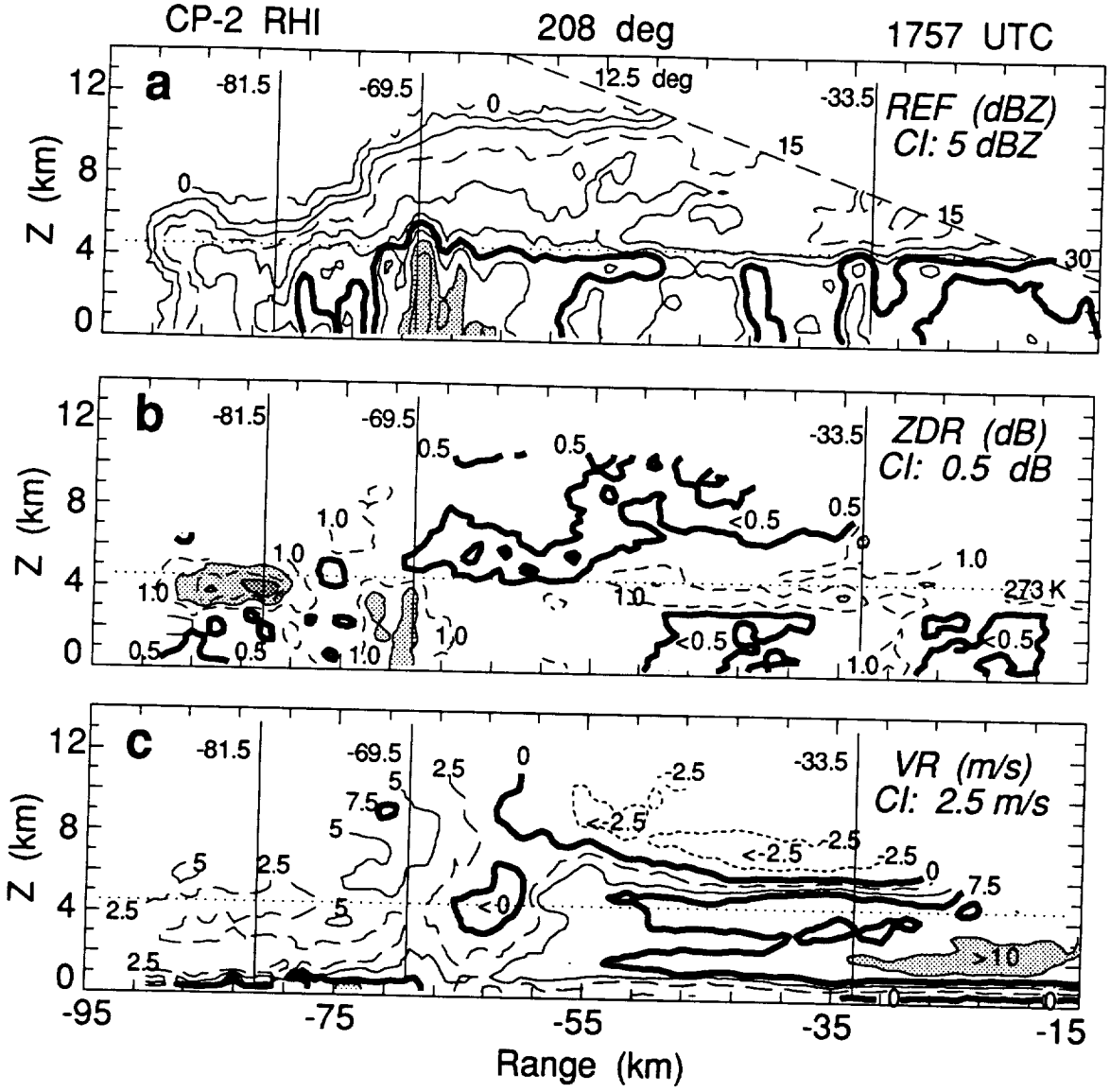

Figure 3-19. CP-2 RHI scan at 208 deg azimuth at 1757 UTC. The relative location of this scan is indicated in Figs. 3-2d and 3-12. (a) Reflectivity factor drawn every 5 dBZ, beginning at 0. The thick line is 30 dBZ and shading depicts REF>40 dBZ. (b) Z_{DR} drawn every 0.5 dB, beginning at 0.5 dB. The thick line is 0.5 dB and shading depicts Z_{DR}>1.5. (c) Radial velocity drawn every 2.5 m s^{-1}. The solid lines are drawn at 0 and 7.5 m s^{-1}, values exceeding 10 m s^{-1} are shaded. The dotted horizontal line in each panel indicates the environmental 0 °C level. Vertical solid lines show the location of profiles displayed in Fig. 6.

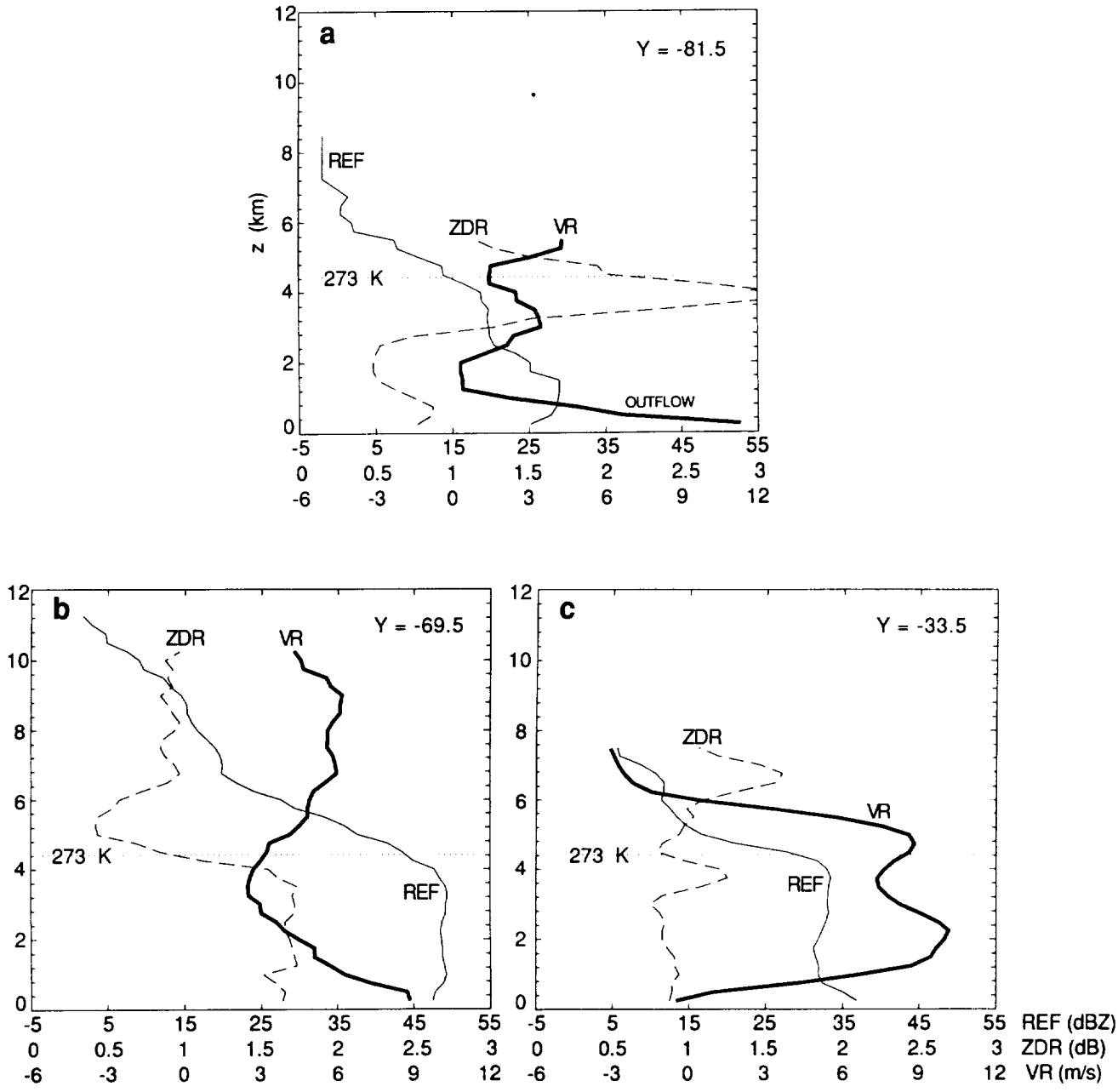

Figure 3-20. Vertical profiles of Z_e, Z_{DR} and VR at ranges of (as shown in Fig. 3-19) (a) 81.5, (b) 69.5 and (c) 33.5 km from CP-2.

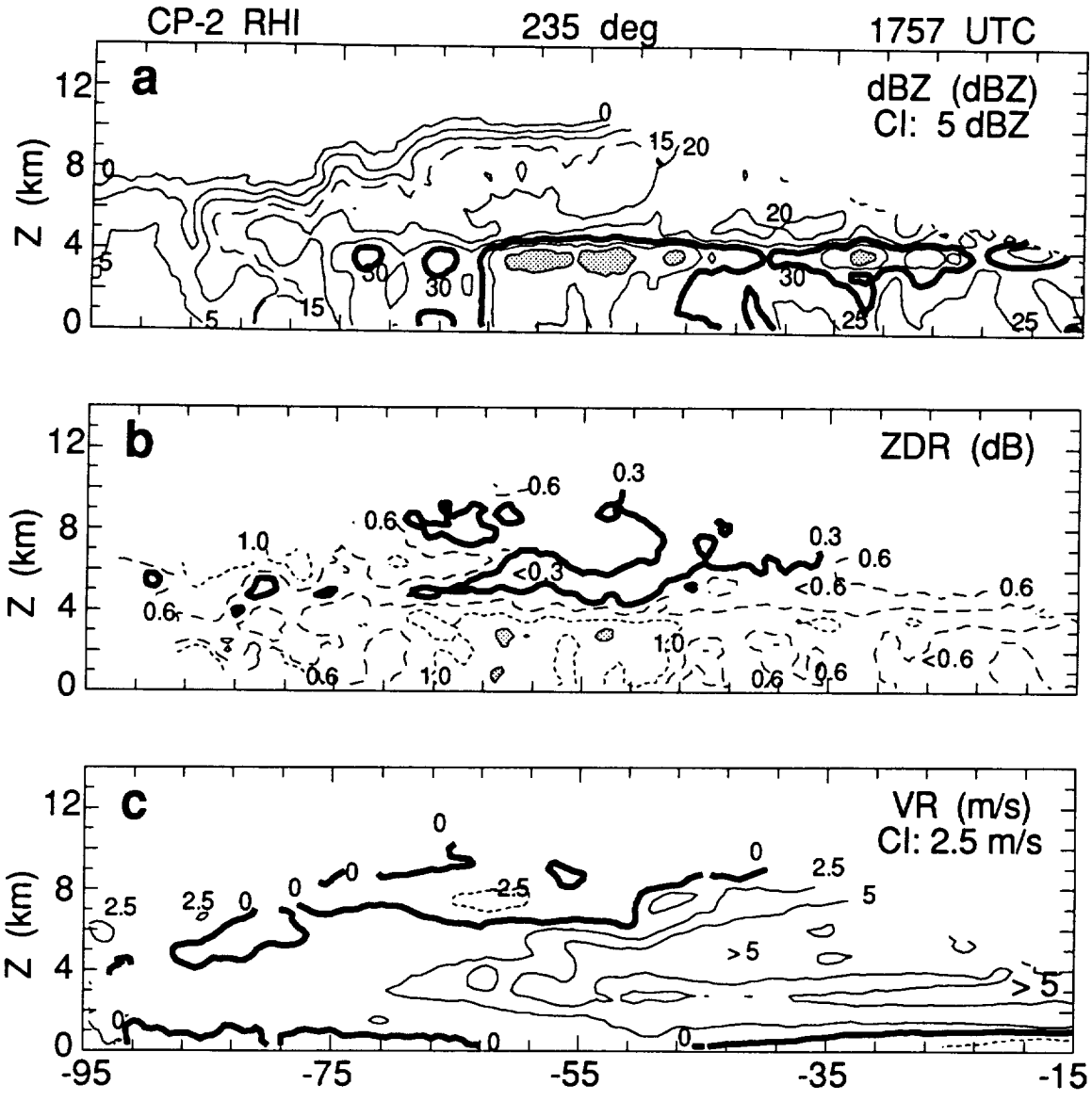

Figure 3-21. CP-2 RHI scan at 235 deg azimuth at 1757. The relative location of this scan is indicated in Figs. 3-2d and 3-12.

4. ANALYSIS OF THE 28 JUNE MCS

A preliminary analysis of this interesting MCS was conducted at the start of this project, but was not pursued further due to lack of time. In this case a very short-lived MCS evolved over the central SPACE mesonet in association with a large-scale short-wave trough which had merged earlier in the day with the residual circulation of Hurricane Bonnie. This tropical influence thus produced an environment that was thus quite moist from the surface to 500 mb. Precipitable water values were high at ~55 mm, and CAPE values over the SPACE mesonet were variable at 1000-2000 J kg^{-1}. Initial echos within the small MCS in this case formed around 2200 UTC 28 June and dissipated by ~0400 UTC 29 June. The maximum horizontal dimension was about 80 km. Figure 4-1 shows the system at a stage (0025 UTC 29 June) when individual convective cores were most intense. At this time a line of 4 intense convective elements is located near the central portion of the domain. Weaker convective cells are located to the south, and a stratiform region about 40 wide and 70 km long exists to the north and northeast. Remnants of a previous MCS are located along the far western portion of the domain. This system produced locally heavy rainfall in the vicinity of the convective cores. Measured Z_e decreased appreciably above the melting level, yielding a profile that is similar to those observed in tropical regions (e.g., Szoke *et al* 1986). The radial velocity structure of this system was suggestive of an organized inflow along the southern flank of the system, that tilted upward and to the north over an outflow at lower levels.

In summary, this system is yet another example of a particular precipitation and kinematic organization that small MCSs may assume. An extensive set of CP-2 data were acquired on this system. Analysis of these data would provide the basis for an excellent observational study of precipitation distribution and type, and the relation to flow structure, with an MCS exhibiting some tropical-like qualities.

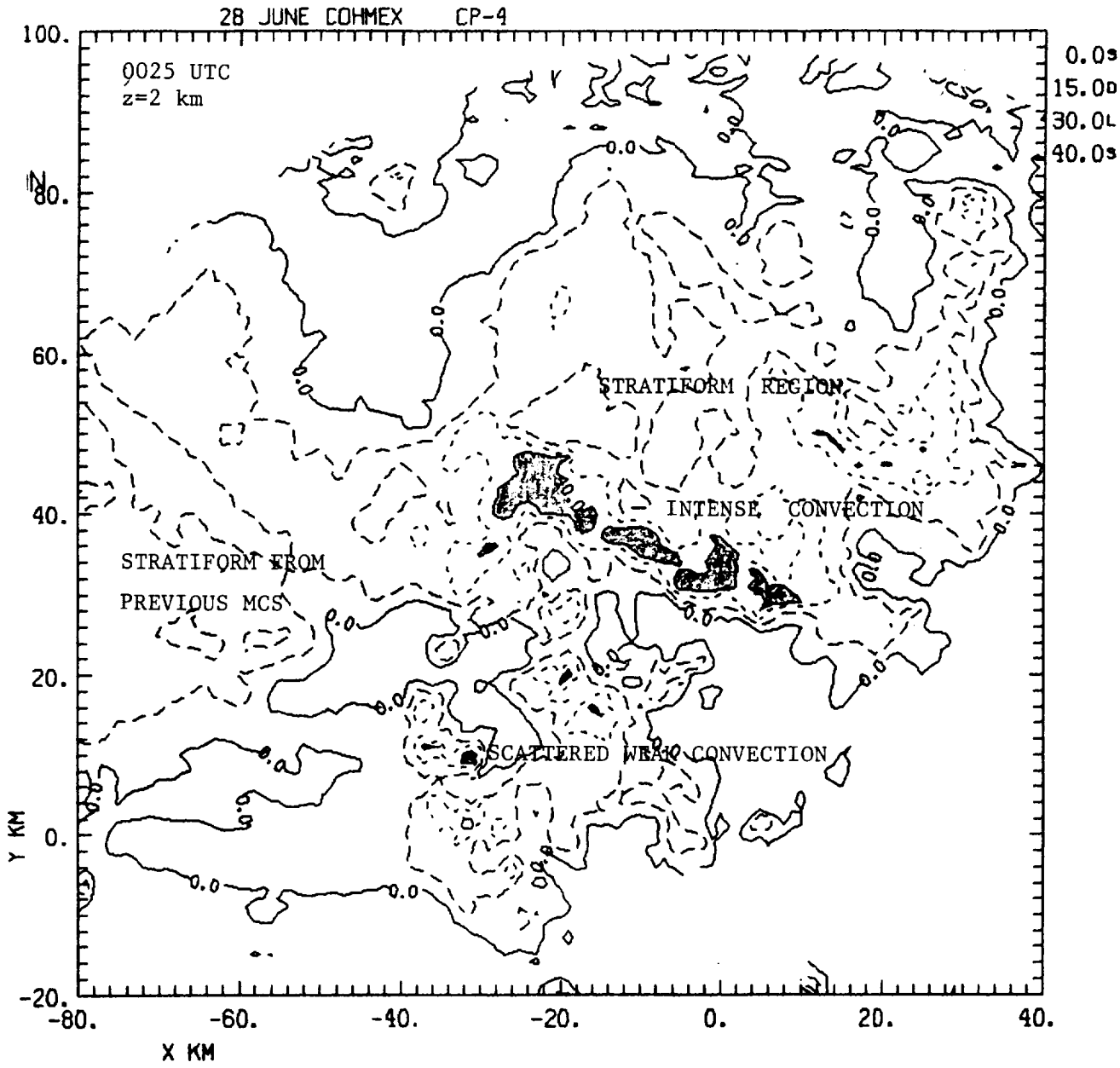

Figure 4-1. CP-4 horizontal section of Z_e at 2 km AGL. The values have not been corrected for attenuation and CP-4 bias, and so are 2-5 dBZ too low. Contours are drawn at 0, 15, 30 and 40 dBZ, with values exceeding 40 dBZ shaded. Features referred to in the text are labeled.

5. AUTOMATED HYDROMETEOR CLASSIFICATION

Although this work was not originally proposed, an opportunity existed to complete this study within a short time frame. The work summarized here is taken from the M.S. Thesis of Mr. M.T. Gururajarao, who completed this work within one year under the direction of V. Chandrasekar and K. Knupp. Such work is of fundamental importance to the microwave remote sensing of cloud top and precipitation, since the signal received by satellite is highly dependent upon microphysical characteristics of both liquid and ice phase hydrometeors. The objective of this study was to attempt to automate the classification (shape, particle type, etc.) and to quantify large populations (in terms of size distributions) of images acquired from two-dimensional probes (2D-C, 2D-P) mounted on aircraft. Analysis of such data has in the past involved considerable manual (subjective) effort. Although some previous work has been done in automatic classification using computer algorithms, there is the need for improved techniques.

Under this research effort, it was attempted to extract the contour of a raw binary image acquired from a PMS device (the image is basically a cross-sectional shadow) and then estimate size and shape parameters (axis ratio, canting angle), the size distribution, and differentiate the various particle types using Fourier and moment descriptors. Contour and radial Fourier analysis was performed on the images to obtain parameters to determine the shape and size of the particle. The analysis was completed on both idealized images (for test purposes) and on actual data. Data were obtained from the 1983 Maypole experiment in Colorado and from measurements of ice-phase hydrometeors (graupel, snow, and pristine ice crystals) particles in Germany. To illustrate, Fig. 5-1 shows two example of actual images of ice particles along with their corresponding fourier descriptor (FD) spectrum, which is used to classify images. Different particles in general have relatively unique FD spectra which allow accurate classification. Fig. 5-2 illustrates the results for a raindrop and a graupel particle using the moment descriptor (MD) method. The ability of the FD technique to accurately classify particles is summarized in Table 5-1 (Maypole and Germany data). The three columns shown include a visual classification (subjective), the automatic FD classification, and the statistical classification technique of Holroyd (1987). Within the framework of this somewhat limited data sample, it is obvious that the FD technique is quite accurate. Another capability of the moment technique is computation of size distributions of the particle data. Fig. 5-3 shows a size distribution plot for the Maypole data (the precipitation probe measures particles greater than ~2 mm diameter. Here we see an approximate exponential distribution over the range of particle sizes 2-7 mm.

In summary, this study has shown that utilization of FD and MD techniques to estimate hydrometeor habit, size and canting angle are more accurate that other methods developed in that past. This work appears to have considerable potential for future studies whose aim is to quantify the microphysical composition of clouds.

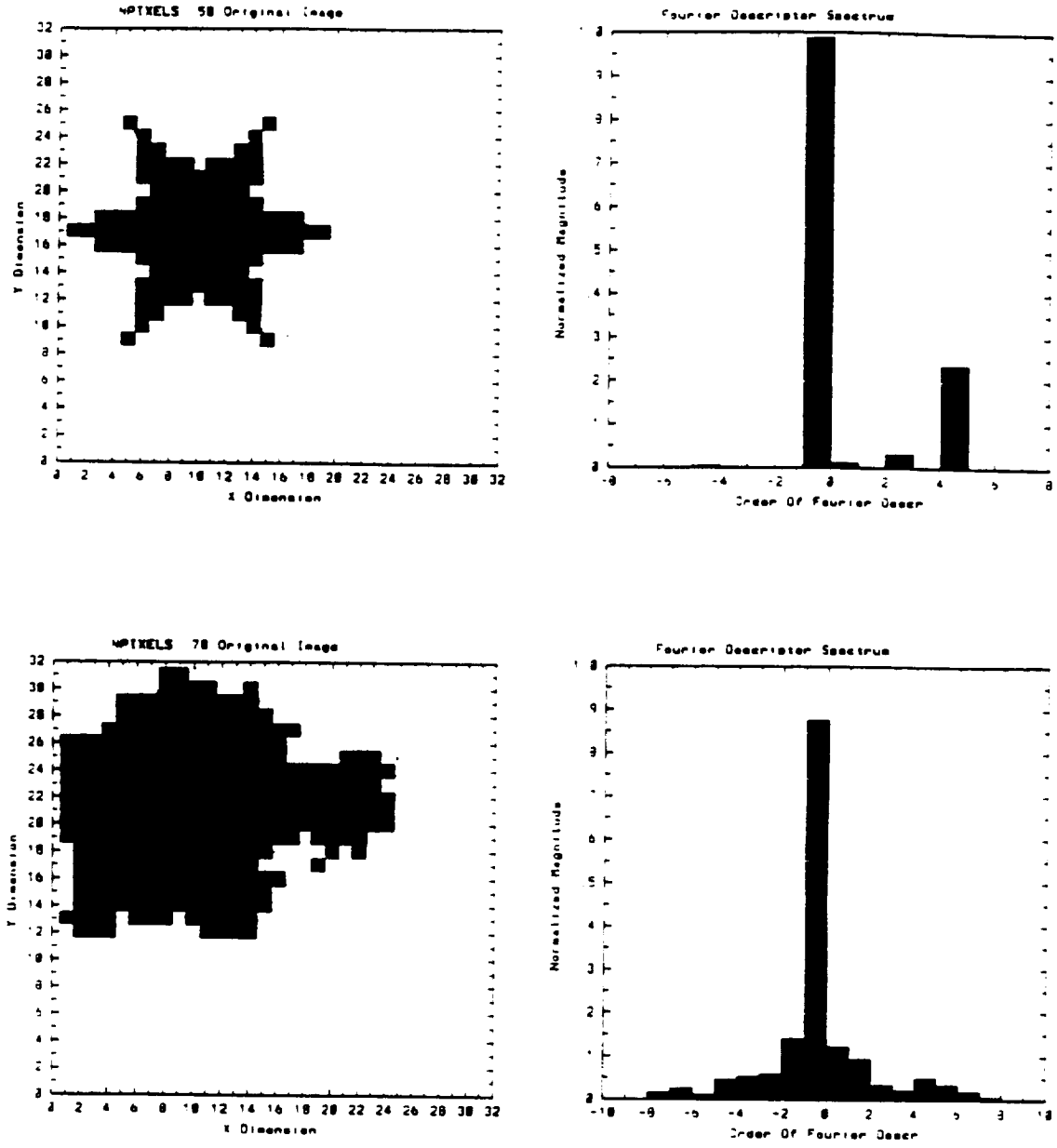

Figure 5-1. (a) Image of a synthetic stellar ice crystal and its FD spectrum and (b) image (from real data) of an aggregrate and its FD spectrum. Note that the FD spectra show of each show substantial differences. It is this signature that is used to distinguish among particle types.

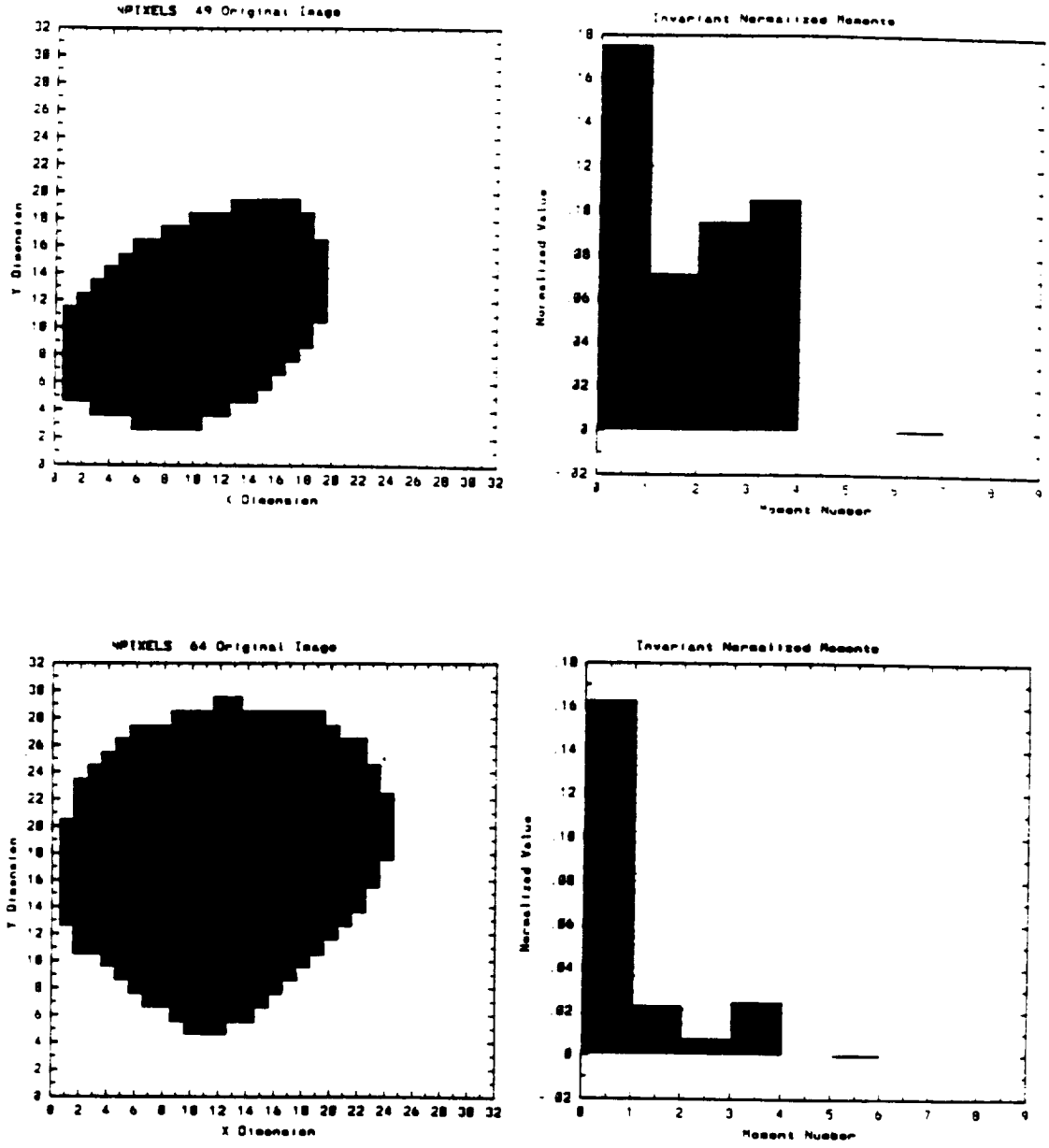

Figure 5-2. (a) Image of a raindrop and the corresponding distribution of its seven moment desriptors (MD). (b) Image of a conical graupel particle and its seven MDs.

"Maypole" images

Hydrometeor Class	Visual classification (%)	Automatic FD classification (%)	Automatic statistical class (%)
Tiny	2	2	-
Linear	-	-	5
Oriented	-	-	-
Aggregates	2	4	2
Graupels	7	6	6
Spherical	22	18	30
Irregular	9	8	-
Dendrite	-	-	-
Hexagonal	-	-	-
Raindrop	58	62	56

1000 "Germany" images

Hydrometeor Class	Visual classification (%)	Automatic FD classification (%)	Automatic statistical class (%)
Tiny	11	13	5
Linear	2	2	9
Oriented	3	3	1
Aggregates	42	48	15
Graupels	1	1	40
Spherical	-	1	15
Irregular	13	8	-
Dendrite	20	22	5
Hexagonal	1	-	10
Raindrop	7	6	-

Table 5-1. Comparison of results of visual, automatic FD, and the automatic technique of Holroyd (1987) for Maypole data (top) and for Germany data (bottom).

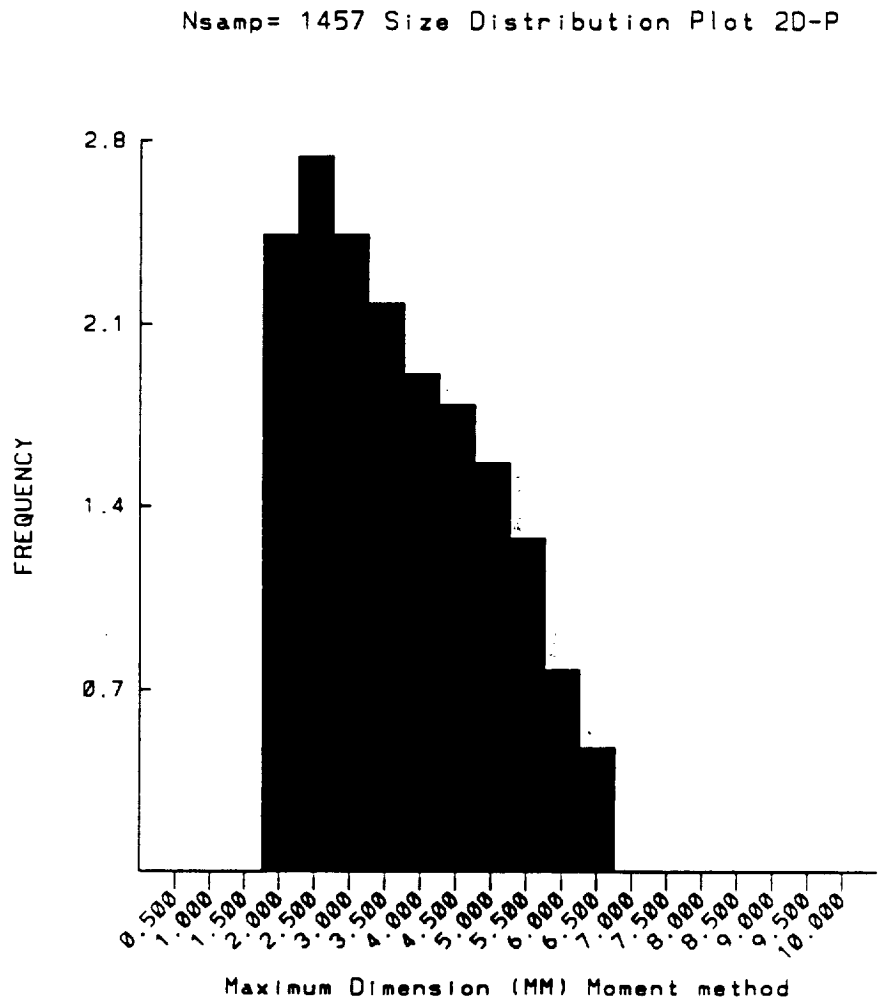

Figure 5-3. Example of a size distribution plot of raindrops, obtained using the moment method (MM), applied to data collected by a 2D-P probe from the Maypole experiment.

6. SUMMARY AND RECOMMENDATIONS

6.1 Basic findings

This work has examined details on the internal structure of two contrasting mesoscale convective systems observed during the COHMEX program in June-July 1986. These systems evolved in relatively low-shear environments of the Southeast (a subtropical continental climatic regime). Both systems exhibited relatively long lifetimes and displayed a large degree and temporal variability. The 13 July MCS was composed of intense convective elements and evolved to a classical squall line structure consisting of leading edge of deep convection flanked by a trailing stratiform region. Details of both deep convective components and the stratiform component were presented. The most notable findings in this case the relation between cloud top and internal kinematic and precipitation structure. It was demonstrated that intensification of reflectivity within the stratiform region occurred in situ. A sinking cloud top was observed in conjunction with the intensification and expansion of precipitation within the stratiform region. It was found that the temporal variability of cloud top was related to vertical motion patterns determined from VAD analyses, but the relation was by no means uniform.

The 15 July MCS exhibited a contrasting structure and evolution. Convective elements within this system were less vigorous and yet the amount of stratiform precipitation produced was large relative to the activity of deep convection. Deep convective elements in this case form on the western boundary in a cyclic fashion at 3 h time intervals and then moved eastward relative to the system movement while weakening. While area of stratiform precipitation was substantial in this case, the horizontal distribution was not uniform, but exhibited variations of 10 dBZ. Moreover, embedded weak convection was embedded with the stratiform region. Mesoscale downdraft of 15-20 cm s^{-1} was common over the lowest 6-7 km throughout the period of measurements. Very weak mesoscale updraft of several cm s^{-1} magnitude was confined to the upper 2-3 km (7-10 km AGL) level of the stratiform region. An prominent inflow jet having a peak speed of 15 m s^{-1} near 2-3 km AGL was observed throughout. Unlike the sloping jet observed in the 13 July MCS, the 15 July jet was quasi-horizontal and located well below the melting level.

Other ancillary work included a preliminary study of the 28 June MCS which exhibited a tropical-like structure and shorter lifetime. Also work on objective categorization of hydrometeors was completed within a one-year time frame.

6.2 Recommendations for further research

It is recommended that the following items be addressed in future research activities:

1) Acquire measurements of ice crystal habit at cold cloud top temperatures ($T<-50\ ^{o}C$) of MCS stratiform regions. Such measurements would establish a range of values of ice crystal fall speeds that would assist in the estimation of cloud top vertical motion and subsequent integration with VAD analyses.

2) Establish the significance of cloud top vertical motion and the relation to internal cloud kinematic (e.g., vertical motion) and precipitation processes.

3) All characteristics (e.g., vertical transports, microphysical processes, entrainment/detrainment) of deep convective components require detailed understanding during the *complete* life cycle of evolving MCSs. Cloud-scale processes initiate the mesoscale response within MCSs and relate closely to the structure of mesoscale updrafts, downdrafts and associated horizontal flows. Many of the cloud details and cloud-scale / mesoscale relationships are not well understood. For example, characteristics of convective cloud dissipation have not been quantified in previous studies.

4) There exists a need to further understand the general characteristics of small MCSs and their importance on the global scale water/energy budget. For example, what is the characteristic size, lifetime and diurnal behavior of such systems in various regions of the world? Are small MCSs similar in structure to their larger squall line and MCC counterparts that exist elsewhere?

It is believed that small MCSs contribute importantly to regional energy/hydrologic budgets and therefore require further examination.

REFERENCES

Atkins, N.T., and R.M. Wakimoto, 1990: Forecasting wet microburst activity over the Southeastern U.S. Preprints, 16th Conf. Severe Local Storms, Kananaskis Park, Canada, AMS, 607-612.

Bader, M.J., S.A. Clough and G.P. Cox, 1987: Aircraft and dual-polarization observations of hydrometeors in light stratiform precipitation. *Quart. J. Roy. Meteor. Soc.*, **113**, 491-515.

Browning K.A., and R. Wexler, 1968: The determination of kinematic properties of a wind field using Doppler radar. *J. Appl. Meteor.*, **7**,

Chong, M.P., P. Amayenc, G. Scialom, and J. Testud, 1987: A tropical squall line observed during the COPT 1981 experiment in west Africa. Part I: Kinematic structure inferred from dual-Doppler radar data. *Mon. Wea. Rev.*, **115**, 670-694.

Churchill, D.D., and R.A. Houze, Jr., 1984: Mesoscale updraft magnitude and cloud ice content deduced from the ice budget of the stratiform region of a tropical cloud cluster. *J. Atmos. Sci.*, **41**, 1717-1725.

Hildebrand, P.H., 1978: Iterative correction for attenuation of 5 cm radar in rain. *J. Appl. Meteor.*, **17**, 508-514.

Holroyd, E.W. III, 1987: Some techniques and used of 2D-C habit classification software for snow particles. *J. Atmos. Oceanic Tech.*, **4**, 498-511.

Illingworth, A.J., 1988: The formation of rain in convective clouds. *Nature*, **336**, 754-756.

Johnson, R.H., and P.J. Hamilton, 1988: The relationship of surface pressure features to the precipitation and airflow structure of an intense mid-latitude squall line. *Mon. Wea. Rev.*, **116**, 1444-1472.

Maddox, R.A., 1980: Mesoscale convective complexes. *Bull. Amer. Meteor. Soc.*, **61**, 1374-1387.

Miller, L.J., C.G. Mohr and A.J. Weinheimer, 1986: The simple rectification to Cartesian space of folded velocities from Doppler radar observations. *J. Atmos. Oceanic Tech.*, **3**, 162-174.

Mohr, C.G, L.J. Miller, R.L. Vaughan and H.W. Frank, 1986: The merger of mesoscale data sets into a common Cartesian format for efficient and systematic analyses. *J. Atmos. Oceanic Tech.*, **3**, 143-161.

Rutledge, S.A., R.A. Houze, M.I. Biggerstaff and T. Matejka, 1988: The Oklahoma-Kansas mesoscale convective system of 10-11 June 1985: Precipitation structure and singe-Doppler radar analysis. *Mon. Wea. Rev.*, **116**, 1409-1430.

Smull, B.F., and R.A. Houze, 1987: Rear inflow in squall lines with trailing stratiform precipitation. *Mon. Wea. Rev.*, **115**, 2869-2889.

Szoke, E.J., E.J. Zipser and D.P. Jorgensen, 1986: A radar study of convective cells in mesoscale convective systems in GATE. Part I: Vertical profile statistics and comparison with hurricanes. *J. Atmos. Sci.*, **43**, 182-197.

Srivastava, R.C., T.J. Matejka, and T.J. Lorello, 1986: Doppler radar study of the trailing anvil region associated with a squall line. *J. Atmos. Sci.*, **43**, 356-377.

Willis, P.T., and A.J. Heymsfield, 1989: Structure of the melting layer in mesoscale convective system stratiform precipitation. *J. Atmos. Sci.*, **46**, 2008-2025.

Yanai, M., S. Esbensen, and J. Chu, 1973: Determination of bulk properties of tropical cloud clusters form large-scale heat and moisture budget. *J. Atmos. Sci.*, **30**, 611-627.

Yeh J.-D., M.A. Fortune, and W.R. Cotton, 1986: Microphysics of the stratified precipitation region of a mesoscale convective system. *Conf. on Cloud Phys. and 23rd Radar Meteor.*, Snowmass, Colo., AMS, J151-J154.

APPENDIX A: Attenuation analysis

The radar analysis conducted on the 13 July case study described above indicated very early in this work that attenuation at 5.5 cm wavelength (C-band) can be substantial in heavily precipitating (primarily rain) mesoscale systems. The motivation for this attenuation work was to attempt to correct for attenuation so that quantitative calculations on echo growth rates in the stratiform region of the 13 July MCS cloud be accomplished. A great deal of effort has been expended in order to quantify the C-band attenuation as accurately as possible.

The procedure followed is an interative technique outlined by Hildebrand (1978), in which estimated attenuation, based on the measured reflectivity, is computed and then added to the measured reflectivity in an interative fashion. Provided that the radar is calibrated perfectly, and that detailed information on the spatial distribution of temperature is known, and that that total attenuation is not "great", one can compensate for attenuation.

In this work, we have used the formula included in Hildebrand (1978), assuming a Marshall-Palmer raindrop distribution. Attenuation computations were applied to the raw data within the REORDER program obtained from Richard Oye of NCAR. In applying this technique, we have installed the following criteria on raw reflectivity data:

1) no more than 4 iterations are applied,

2) 54 dBZ (corresponding to a rainfall rate of ~100 mm h^{-1}) represents a ceiling used to estimate the attenuation constant for a given pass,

3) the attenuation increment for a given iteration cannot exceed 5.0 dB.

These threshold values were determined through a number of sensitivity runs in which all of the above parameters were varied individually. Comparison with CP-2 reflectivity factor (assuming the the S-band is not attenuated) showed that the above values were optimum. When the total attenuation along a give path becomes large (>10 dB), then values greater than those defined above tended to produce an excessive correction.

Figures A-1 and A-2 show an example of attenuation fields computed using CP-4 radar data at a time when attenuation was particularly significant (in excess of 21 dB) along a line of intense convective cells. In Fig. A-1, spatial patterns of C-band attenuation are shown along with patterns of S and C-band reflectivity. The peak in estimated attenuation is ~11 dB at the 2 km level, and is underestimated in portions of the domain by up to 5-10 dB. Excessive attenuation is especially apparent along the profile line indicated in Fig. A-2. The total values here approach 20 dB, as estimated from the difference between S- and C-band reflectivity factor. Two-way attenuation values in the X-band, which can be calculated directed from the CP-2 radar (which has both X and S band capability) exceeds 50 dB in the vicinity of the cluster of intense cores located near (x,y) = (-30,-25).

Additional work on characteristics of attenuation in the precipitation environment (primarily rain only) of mesocale systems is in progress and will be submitted as a paper in the near future to the *Journal of Atmospheric and Oceanic Technology*.

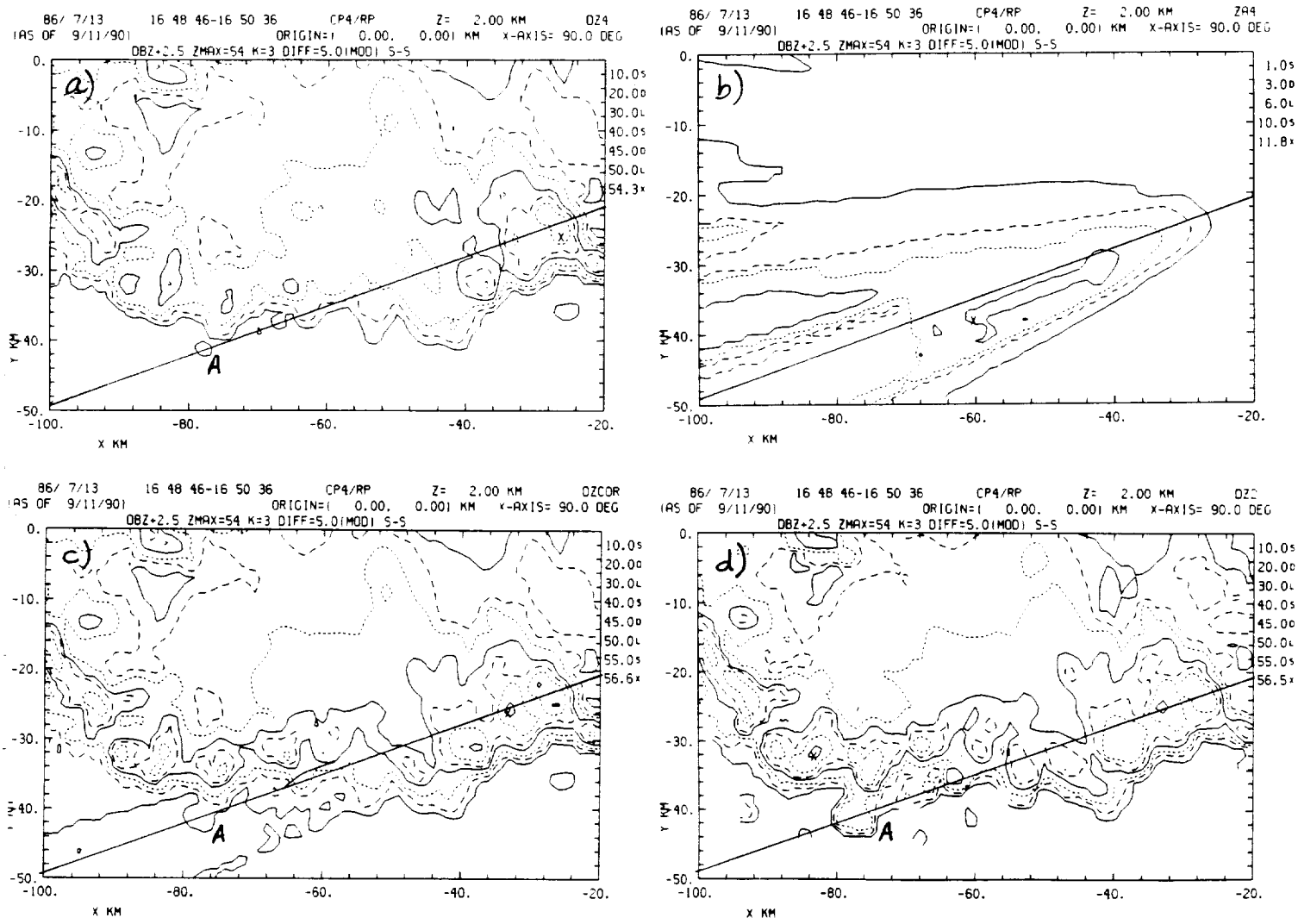

Figure A-1. Horizontal plots of (a) uncorrected CP-4 C-band reflectivity factor, (b) estimated C-band attenuation based on the C-band reflectivity, (c) corrected C-band reflectivity factor (the sum of a and b), and (d) CP-2 S-band reflectivity factor which experiences very little attenuation. CP-4 is located at coordinates (x,y) = (0.4,-14.1).

Figure A-2 (following page). Profiles of quantities interpolated along the radial from CP-4 shown in Fig. 2. The profiles include (a) uncorrected CP-4 C-band reflectivity factor, (b) CP-4 reflectivity with estimated attenuation added, (c) CP-2 S-band reflectivity factor, (d) Z_{DR} from CP-2, (e) estimate of two-way attenuation (dB) from CP-4, and (f) calculated difference between S-band and C-band reflectivity. The latter panel shows that measured attenuation approaches 20 dB along this path, and is about double that estimated in panel (e). In particular, note that the peak reflectivity factor for the cell labeled "A" in all panels and in Fig. 2 is underestimated by 18 dBZ.

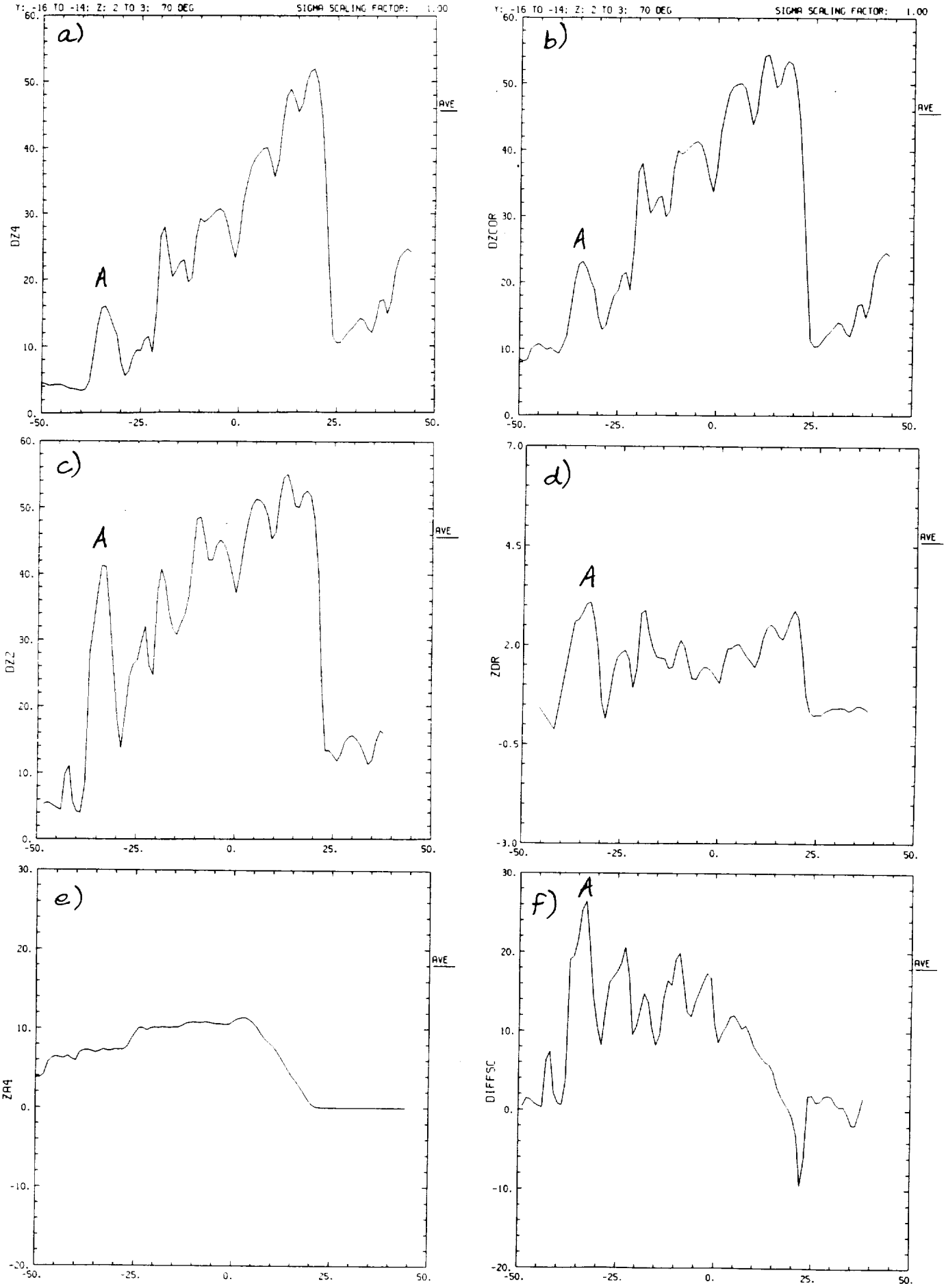
Y: -16 TO -14; Z: 2 TO 3: 70 DEG
SIGMA SCALING FACTOR: 1.00
a)
b)
c)
d)
e)
f)
A
AVE
DZ4
DZCOR
DZ2
ZDR
ZA4
DIFFSC

Appendix B: Publications

The following list defines those publications that have appeared in conference proceedings under the sponsorship of this NASA grant. These include, in order of appearance:

Knupp, K.R., and S.F. Williams, 1988: Multiscale analysis of a sustained precipitation event. Preprints, *15th Conf. on Severe Local Storms*, AMS, 452-455.

Knupp, K.R., 1988: Observational analysis of mesoscale convective system growth and structure. Preprints, *10th International Cloud Physics Conference*, Bad Homburg, FRG.

Knupp, K.R., 1989: Observed structural variability of deep moist convection with a mesoscale convective system. Preprints, *24th Conference on Radar Meteorology*, AMS, Tallahassee,467-470.

Knupp, K.R., 1990: Radar observations of precipitation growth and evolution within the anvil region of a MCS. Preprints, *Conf. on Cloud Physics*, San Franciso, AMS, 607-612.

Knupp, K.R., 1991: Kinematic and Precipitation Structure of a Small, Long-Lived Mesoscale Convective System. Preprints, *25th International Conference on Radar Meteorology*, Paris.

Copies of these papers are included on the following pages. In addition, the thesis below was supported under this grant:

Gururajarao, M.J., 1990: Image Processing Techniques to Analyze Random Hydrometeor Images. M.S. Thesis, The University of Alabama in Huntsville, 128 pp.

Finally, the following manuscripts to be submitted as formal publications were based on this support. Each paper represents either an extension of the above conference papers, thesis, or the material presented in this report, and will be submitted to the journals indicated:

Knupp, K.R., and S. Goodman, 1991: Development and Evolution of Mesoscale Flows and Precipitation within a MCS. To be submitted to *J. Atmos Sci.*

Knupp, K.R., 1991: Kinematic and Precipitation Structure of a Small, Long-Lived Mesoscale Convective System. To be submitted to *Mon. Wea. Rev.*

Knupp, K.R., and V. Chandrasekar, 1991: Estimation and measurement of C-band attenuation in heavy rain environments. Manuscript in preparation, to be submitted to *J. Oceanic Atmos. Tech.*

Chandrasekar, V., and M. Gururajarao, 1991: Image processing techniques to analyse 2-D PMS images of ice crystals. Manuscript in preparation, to be submitted to *J. Oceanic Atmos. Tech.*

Chandrasekar, V., and M. Gururajarao, 1991: Pattern recognition techniques to classify ice crystal habit types. Manuscript in preparation, to be submitted to *J. Oceanic Atmos. Tech.*

MULTISCALE ANALYSIS OF A SUSTAINED PRECIPITATION EVENT

Kevin R. Knupp and Steven F. Williams

Atmospheric Science and Remote Sensing Laboratory
Johnson Research Center
University of Alabama in Huntsville
Huntsville, Alabama 35899

1. INTRODUCTION

Forecasting of deep convection in general remains a challenging problem. This problem can be viewed as a parameterization in which large-scale (> 100 km) variables or conditions are used to infer processes which are organized on the cloud or small mesoscale (2-20 km). The way in which low-level convergence is organized on small scales is only beginning to be understood and defined (e.g., Wilson and Schrieber, 1986). In many cases, cloud-scale convergence is a culmination of interaction between several scales of motion (Purdom, 1982).

In this paper, analyses of special experimental mesoscale data are used to infer the mechanisms of deep convection initiation for a particular case study of 28-29 June 1986. In this case, scattered to widespread deep convection remained over the region of northern Alabama to central Tennessee for 24 consecutive hours. The mesoscale environment was complicated and involved the merger of Hurricane Bonnie remnants with a preexisting midlatitude short-wave trough. This case is also interesting because the most intense convection occurred prior to and near dawn, a time atypical for this region during the summertime (Wallace, 1975).

The experimental data were collected during a two-month field program -' the Satellite Precipitation and Cloud Experiment (SPACE) - conducted in conjunction with the Microburst and Severe Thunderstorm program (MIST) during June and July of 1986. Special data sets used herein include meso-beta-scale rawinsonde data (collected at 3 h intervals from 1500 UTC 28 June to 0300 UTC 29 June), surface mesonet data, RADAP data from Nashville WSR-57 radar and GOES 30 min images. A description of the experimental platforms and weather conditions is given in Williams et al (1987). Figure 1 shows the distribution of instrumentation over the SPACE mesonet.

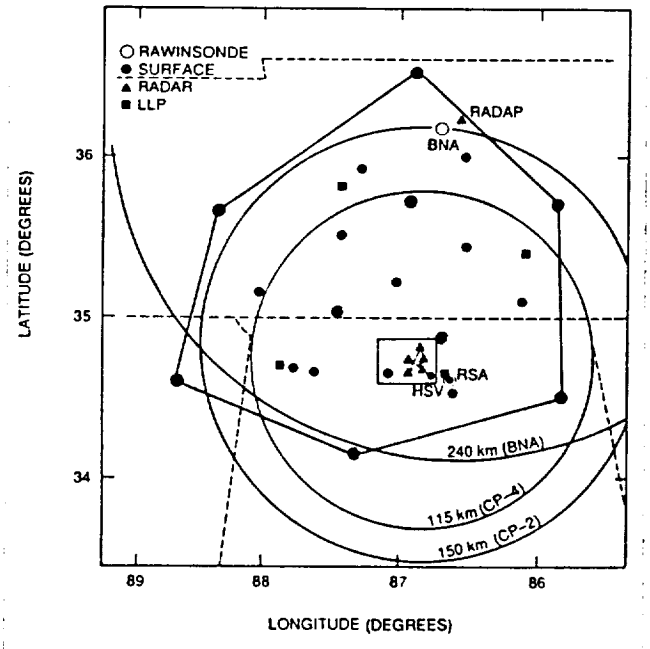

Figure 1. Mesoscale observational platforms available during the Satellite Precipitation and Cloud Experiment (SPACE) in June and July of 1986.

2. SYNOPTIC-SCALE OVERVIEW

The regional synoptic scale on 1200 UTC 28 June was characterized by relatively low shear and high levels of moisture throughout the troposphere. High moisture values were provided by the cloud and moisture remnants of Hurricane Bonnie, which attained hurricane strength on 25 June before impacting the extreme southeast corner of Texas near 1200 UTG 26 June. By 28 June, the distinct surface low pressure region had disappeared, although a cyclonic circulation was analyzed at 1-4 km AGL during the morning and early afternoon hours over the SPACE mesnonet.

The mesoscale environment was further complicated by a weak but prominent short-wave trough which began to interact with the residual hurricane circulation by 1200 UTC 27 June. By 1200 UTC 28 June, the two entities had merged into a single trough located just to the west of the SPACE mesonet. This trough moved slowly over the mesonet during the next 24 hours. Moisture values were high during the afternoon hours on 28 June, with tropospheric precipitable water generally greater than 50 mm (about 170% normal) over the region. Because of abundant middle level and convective cloudiness, surface temperatures remained relatively cool (25-30 deg C) over the region.

3. MESOSCALE ANALYSES

Three precipitation events were observed over the SPACE mesonet during a 24 h period beginning on 1200 UTC 28 June:

a) Weak rain showers moved into the western mesonet during the morning hours of 28 June, but dissipated by noon. These showers appeared to be directly linked to the residual cloudiness of Bonnie. This general cloud field dissipated during the afternoon hours.

b) Late afternoon deep convection formed around 2100 UTC over western and central Tennessee along the axis of a lower-tropospheric trough as depicted in Fig. 2. This convective activity dissipated after 0300 UTC 29 June as the trough axis passed east of the network.

c) Early morning deep convection reintensified over the central mesonet beginning around 0700 UTC 29 June. This activity developed unexpectedly and appeared to maximize around 1200 UTC.

The latter two events are analyzed in further detail in the following subsections.

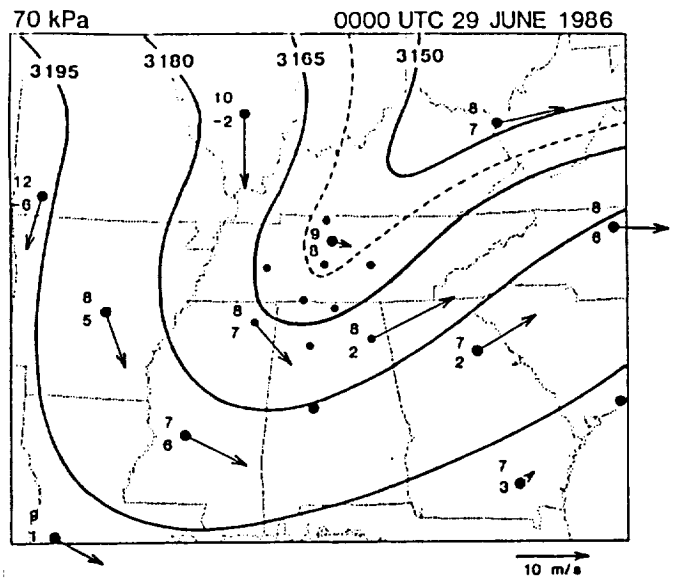

Figure 2. Regional-scale 700 mb analysis at 0000 UTC 29 June 1986, incorporating both synoptic-scale radiosonde stations (large dots) and SPACE mesoscale stations (small dots). Temperature and dewpoint are plotted in deg C.

3.1 Evening convective activity

Because of abundant cloudiness over the region, deep convection was slow in developing during the afternoon hours. Scattered showers formed over the northwestern mesonet around 2000 UTC and intensified thereafter. Beginning at 2100 UTC, strong thunderstorms developed over the western mesonet near the trough axis. The central mesonet experienced deep convection from 2200 UTC 28 June to 0300 UTC 29 June. Figure 3 illustrates the distribution of precipitation and the relationship to tropospheric flow patterns. Cool outflow air is analyzed over much of the mesonet near the precipitation (Fig. 3a). Flow patterns at 85 kPa (and at 70 kPa - not shown) reveal that the deep convection formed along the trough axis where mesoscale vertical motion appears to have maximized. The 50 kPa level flow (Fig. 3c) was generally less coherent at this time and at other analyzed times during the day. Divergent flows over the central mesonet dominated the upper level flow patterns at this time (Fig. 3d).

The deep convection that formed around 2300 UTC (Fig. 3) did so in a relatively narrow region of the central mesonet where greatest static instability was analyzed. Greatest instability lay along a line from the southwest corner of the mesonet through the central mesonet. A sounding released from St. Joseph displayed in Fig. 4 (location shown in Fig. 3) shows a lifted index of about -5 (water loading is excluded and would be significant here) and abundant moisture throughout the lower troposphere. Deep convection over the central mesonet intensified until ~0100 UTC, declining thereafter and dissipating by 0400 UTC. Fig. 5a portrays a GOES IR image at 0100 UTC. The 0300 UTC radiosondes indicate that this area of convection moved into a region of greater static stability, apparently marginal to support deep convection.

The system structure at 0100 UTC consisted of a cluster of convective cells about 60 km in diameter, completely merged at low refectivity. Fig. 5a shows a GOES IR image near this time. Doppler radar displays indicated a net cyclonic rotation in the entire mesoscale precipitation area, as well is in some of the individual intense convective cores. The system appeared to produce a well-defined outflow (as indicated in the radial velocity patterns). Thus, it appeared in real time that convection would continue for some time. The fact that convective intensity declined after 0100 UTC can be attributed to storm translation into a region of greater static stability as discussed above.

Assuming that one had knowledge of the spatial and temporal variations in stability, in addition to the structure of the lower-tropospheric trough and the decline in convective intensity, one would have probably forecast only lingering showers for the remainder of the evening. As we shall see in the following section, this forecast would have been incorrect.

3.2 Early morning activity

The early morning activity refers to the development of a 200 km long convective line over the east-central mesonet beginning near 0700 and lasting past 1300 UTC. Fig. 5c shows a GOES IR image of the mature system at 1300 UTC.

Events during the time interval 0300-1200 UTC 29 June were more poorly defined due to termination of mesoscale rawinsonde releases after 0300. In addition, little could be gleaned from the surface mesonet because the cool and nearly saturated surface air was essentially decoupled from air above ~500 m AGL. The only soundings available after 0300 UTC include one 0600 release from the BNA NWS site (see Fig. 1 for relative location). This 0600 UTC sounding indicated a trough passage around 0300 and some decrease in static stability due to cooling of ~2 deg C at middle levels at 0600 UTC. Inspection of the 0300 mesoscale soundings indicate an eastward progression of somewhat drier and more stable air produced within mesoscale downdrafts associated with the stratiform precipitation shown over the western mesonet at 0000 UTC (Fig. 3a.). For example, the St. Joseph 0300 sounding displayed a relatively stable structure within this mesoscale downdraft air. The observed low-level winds at 0300 would have placed this relatively stable air over the east-central mesonet by 0800 UTC.

The only hint of impending convection was suggested in GOES IR images over the 0500-0900 UTC time period. At 0500 an accentuated narrow band of clouds, oriented SW-NE, had formed over the NW corner of the mesonet. From 0600 to 0700, accentuated cloudiness translated southeastward to the central mesonet, but a more cellular structure had replaced the banded structure (see Fig. 5b). At 0800, the band reformed in striking fashion over the southeast-central mesonet, maintaining the same SW-NE orientation present at 0500. Expansion of cold cloud tops continued from 0800 to 1300 (see Fig. 5c for the structure at 1300). This scenario suggests that a band of upward motion translated uniformly over the mesonet, triggering convection only where static instability was sufficient. Individual network soundings from the 0300 release display subtle horizontal variations in low-level static stability that apparently were important. These differences qualitatively explain the relative variations in subsequent cloud intensity over the mesonet. The most unstable air (at 0300 UTC) resided over the southeast-central mesonet where convective intensity was greatest 6-9 h later.

4. FORECASTING IMPLICATIONS

One generally anticipates that forecast accuracy will increase as the spatial and temporal sampling interval decrease. Thunderstorm forecasting is essentially a problem in cloud initiation in which we ask the question: *By what mechanisms are deep convective clouds generated, and how do these mechansims relate to variables that are measured by satellite, radar, radiosonde or surface instrumentation?* As in any forecasting application, two ingredients are necessary: (1) knowledge of mesoscale and cloud scale processes, and (2) the ability to measure the necessary parameters on appropriate spatial and temporal scales. Despite the special instrumentation available

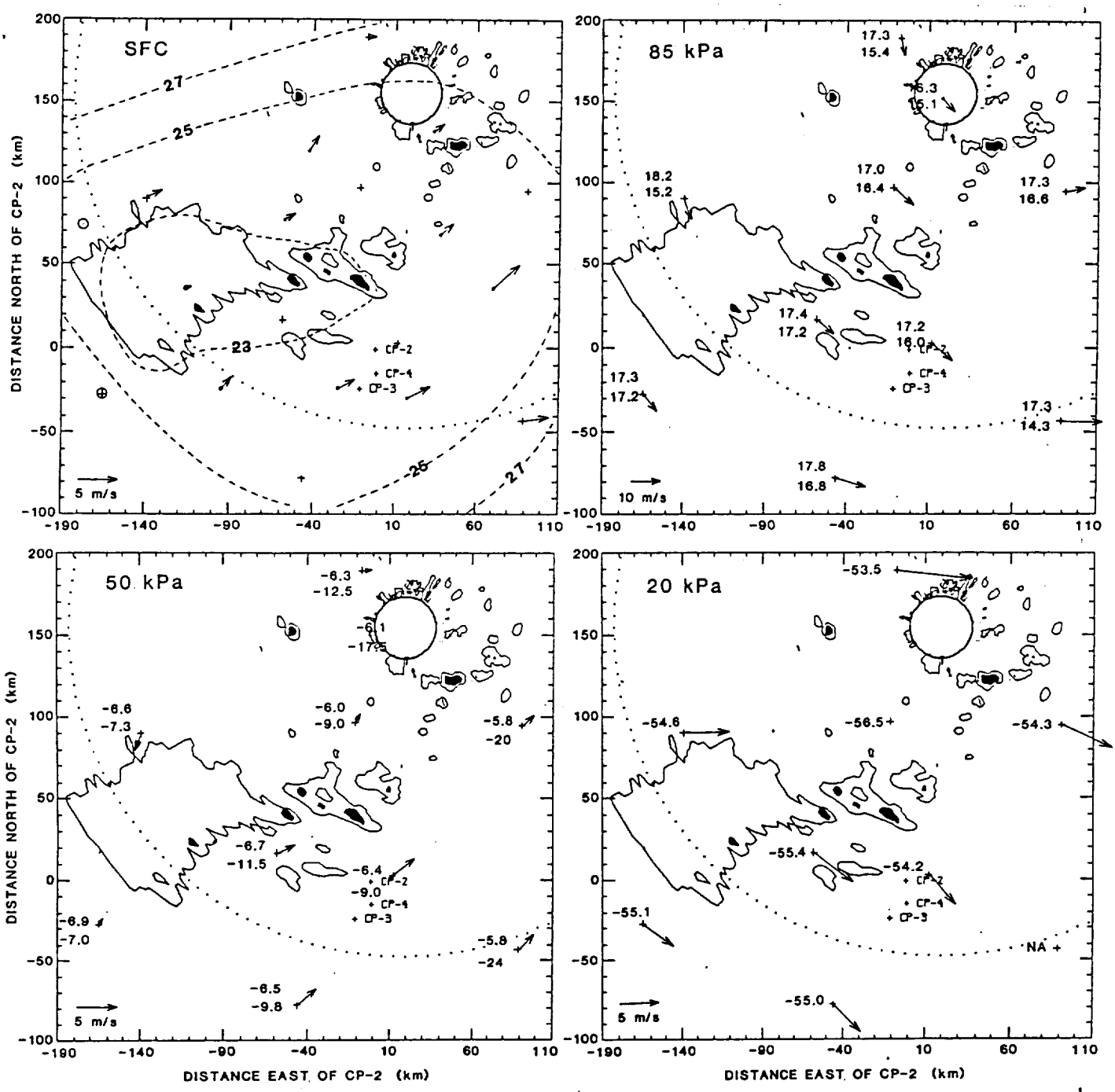

Figure 3. Mesoscale analysis at 0000 UTC 29 June over the SPACE mesonet: (a) surface, (b) 85 kPa, (c) 50 kPa, and (d) 20 kPa. Temperature and dewpoint are plotted in deg C in all panels. All panels show reflectivity factor obtained from the Nashville (BNA) RADAP data. The line represents the 18 dBZ contour, and black regions denote convective cores > 38 dBZ. The dotted line is the BNA range marker of 185 km.

for this preliminary study, neither of the two above conditions was completely satisfied. First, the "disturbance" that initiated the early morning convection was not resolved by previous rawinsonde analyses, and was inferred only qualitatively by satellite images. Moreover, it appeared to occur to the rear of the major trough depicted in Fig. 2. Second, it is surmised that the rawinsonde station spacing was marginal at best in this case. Significant variations at scales smaller than 100 km and 3 h in time transpired in this case. It seems probable that the mesoscale outflow generated 8 h earlier (near 0000 UTC 29 June) by previous convection contributed to the generation of this system, but the data are insufficient to provide specific characteristics of the outflow.

5. SUMMARY

This preliminary study has described mesoscale features associated with two distinct mesoscale precipitation events, separated in time by ~10 h, that occurred over the same region. The first event took place during the late afternoon to early evening hours along a lower tropospheric trough. This event could be explained (but only generally) with a preliminary follow-up analysis. The second event appeared to take place to the rear of the trough during the following morning

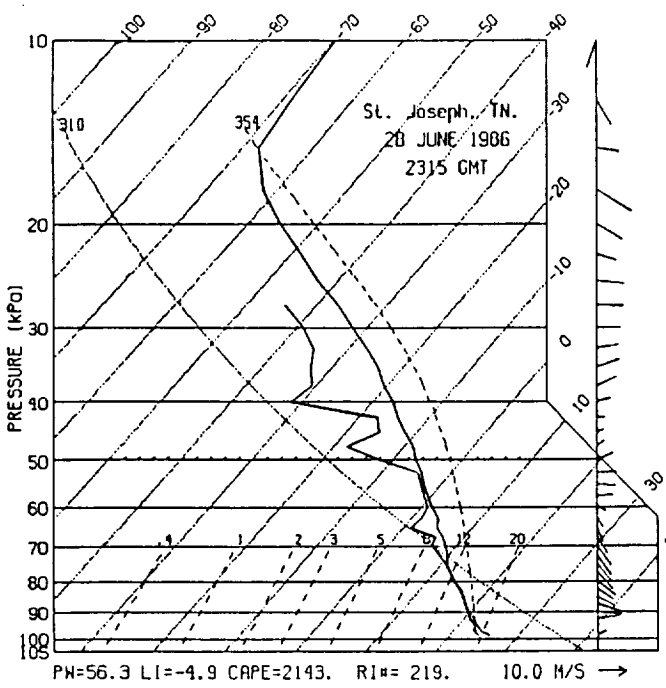

Figure 4. Skew T, ln p plot of a sounding released at 2315 UTC 28 June from St. Joseph (see Fig. 3 for location indicated as STJ).

hours, at a time when convection over this region is least likely. A preliminary analysis of this event could not explain its general behavior, partly because soundings were lacking, partly because the surface was decoupled from air aloft, and partly because the system appeared to result from interactions of processes occuring on different scales. In both cases, mesoscale horizontal variations in static stability profiles, particularly at low levels, appear to have been important.

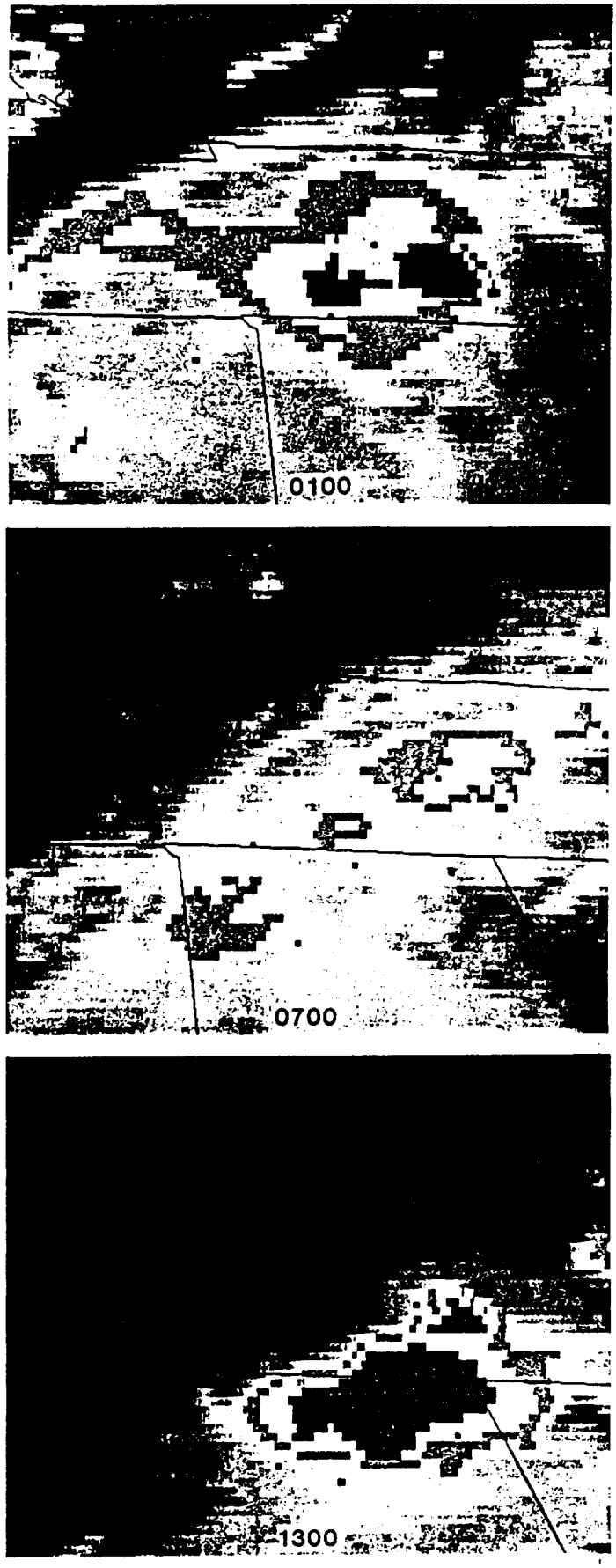

Figure 5. GOES infrared satellite images at (a) 0100 UTC, (b) 0700 UTC, and (c) 1300 UTC 29 June. A MB enhancement has been applied to highlight regions of thunderstorm anvil.

6. ACKNOWLEDGEMENTS

This research was sponsored by the National Aeronautics and Space Administration under Grant NAG8-654.

7. REFERENCES

Purdom, J.F.W., 1982: Subjective interpretations of geostationary satellite data for nowcasting. *Nowcasting*. K. Browning, Ed., Academic Press, 149-166.

Wallace, J.M., 1975: Diurnal variations in precipitation and thunderstorm frequency over the conterminous United States. *Mon. Wea. Rev.* 103, 406-419.

Williams, S.F., H.M. Goodman, K.R. Knupp, and J.E. Arnold, 1987: SPACE/COHMEX Data Inventory Document. NASA TM-4006, Marshall Space Flight Center, AL, 480 pp.

Wilson, J.W., and W.E. Schreiber, 1986: Initiation of convective storms at radar-observed boundary-layer convergence lines. *Mon. Wea. Rev.*, 114, 2516-2536.

10th International Cloud Physics Conference
15-20 August, 1988, Bad Homburg, FRG

OBSERVATIONAL ANALYSIS OF MESOSCALE CONVECTIVE SYSTEM GROWTH AND STRUCTURE

Kevin R. Knupp
Atmospheric Science and Remote Sensing Laboratory, Johnson Research Center
University of Alabama in Huntsville
Huntsville, Alabama 35899 USA

1. INTRODUCTION

Deep convection is often organized into mesoscale clusters ranging in horizontal dimension from less than 20 km to greater than 200 km. In some cases, the mesoscale cluster (referred to herein as a mesoscale convective system or MCS) may be composed of convective cores flanked by stratiform anvil. Such systems can vary in size from ~100 km scale (e.g., Knupp and Cotton, 1987) to ~500 km scale (Maddox, 1980). Although spatial and temporal scales may differ between large and small MCS's, a great deal of similarity in cloud and mesoscale flows appears to exist in some cases. The manner in which the mesoscale flows (e.g., mesoscale ascent within the anvil and mesoscale descent below the anvil) evolves remains abiguous. Moreover, the mechanisms which contribute to the formation of the mesoscale updraft are not completely understood. In this paper, we will consider two hypothesized mechanisms which contribute to mesoscale updraft and associated precipitation formation, namely: (1) detrainment of buoyant air from convective towers, and (2) hydrostatic response to heating associated with deep convection. These two hypotheses are examined with reference to a particular case study in which detailed and comprehensive observations were made over the life cycle of the system.

2. DATA

The upscale development of this system is documented with several observational platforms which were implemented during the Satellite Precipitation and Cloud Experiment (SPACE), conducted over northern Alabama and central Tennessee during June and July, 1986. In this preliminary study, we will consider RADAP data acquired from a WSR-57 radar located at Nashville (BNA), data from two C-band Doppler radars (CP-3 and CP-4), special surface mesonet data (20 stations), and conventional GOES visible and IR imagery acquired at 30 min intervals. Instrument locations are shown in a later figure (Fig. 3a). The RADAP data were collected every 2 deg in azimuth and elevation, at approximately 120-230 km range. Thus, these data depict only major convective cores due to the 4-8 km beam size and azimuthal sample spacing at the ranges involved. Higher spatial and temporal resolution data (reflectivity factor and radial velocity) were available from CP-3 and CP-4.

3. ANALYSIS

3.1 OVERVIEW OF THE MCS DEVELOPMENT

The MCS of interest evolved in a relatively unstable, low-shear environment as shown by the representative sounding in Fig. 1. (The sounding location is indicate by *RSA* in Fig. 3a.) Deep convection formed in a mesoscale cluster by early afternoon in response to large-scale lifting associated with a subtle short-wave trough. At maturity some 4-5 h after first echo, the MCS consisted of an east-west line of broken convective cells (oriented parallel to the shear vector), flanked to the north by a region of stratiform precipitation ~80 km wide. The net MCS motion from north to south (perpendicular to the mean flow) was accomplished primarily by propagation along a mesoscale outflow. Individual cells moved with the mean flow along the major axis of the system.

A time series overview of some MCS characteristics is presented in Fig. 2. First echo (at an 18 dBZ threshold) was observed near 1730 UTC (1130 LST) over the west-central portion of the mesonet, although weak to moderately-intense echoes were observed earlier (1600-2000 UTC) over the southeastern portion of the network. The system exhibited a relatively uniform expansion and intensification from first echo until ~2100 UTC, when maximum echo intensity was recorded in the RADAP data. Surface outflow air was first apparent near 1830 UTC, but low-valued θ_e outflow air was not recorded until ~1930. The surface outflow air continued to expand in area after 1930 and appeared to aid importantly in development of subsequent convection.

Incipient anvil associated with the MCS deep convection first appeared in the visible GEOS satellite imagry at 1900 UTC. As shown in Fig. 3, the anvil exhibited significant expansion from 2000 to 2200 UTC. The visible anvil expanded from ~7,000 km^2 at 2000 to ~36,000 km^2 at 2300. The distribution of precipitation during the MCS developing stages is also shown in the RADAP data (left panels) of Fig. 3. During the early MCS stages (1800-2000), convective echoes appeared as distinct entities, not significantly merged with neighboring cells. By 2000 UTC, cell merger was more prominent as a convective line appeared (labeled A in Fig. 3). Over the next 3 h, this convective line (which was acutally a subset of the MCS) expanded, eventually evolving to the early mature structure shown in Fig. 3b. During the 2 h time interval from 2000 to 2200 UTC, precipitation within the anvil displayed both expansion and an increase in intensity (see Figs. 2 and 3). Development of precipitation within the anvil thus lagged formation of the uniform anvil cloud top by roughly one hour.

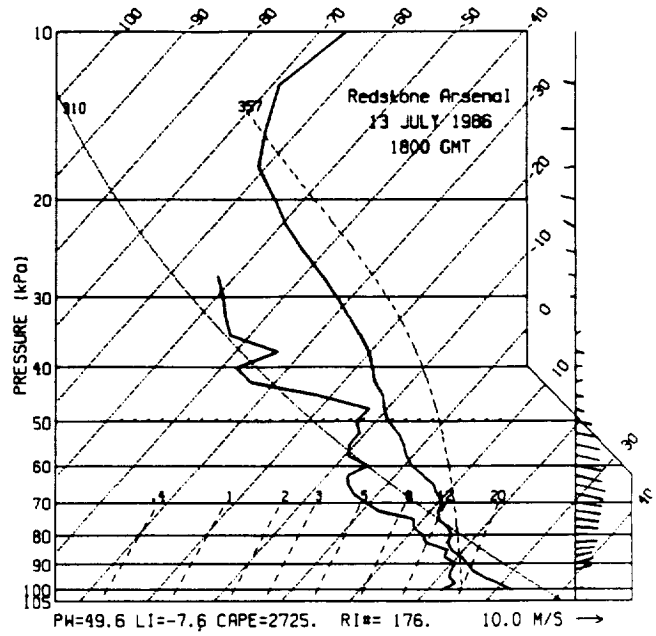

Figure 1. Rawinsonde sounding for 1800 UTC 13 July 1986, plotted on a skew-T, ln diagram. The sounding location is from point RSA shown in Fig. 3a.

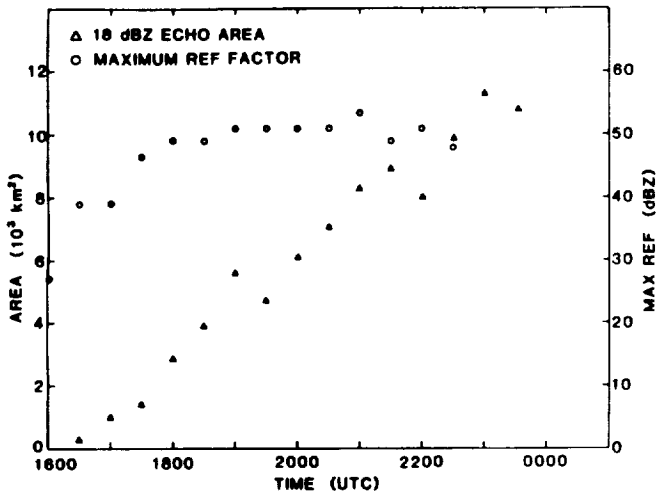

Figure 2. Time series plot of MCS echo area (reflectivity factor > 18 dBZ) and maximum reflectivity factor obtained from the RADAP data. The MCS moved beyond maximum range starting ~2300 UTC, so values beyond this time are underestimated.

3.2 CHARACTERISTICS OF THE ANVIL EXPANSION

The formation of the anvil and its associated mesoscale updraft and precipitation is examined in further detail with the aid of higher-resolution Doppler radar data. Figure 4 presents analyses of reflectivity factor at the 8 km level (which intersect the lower portion of the mature anvil) at two times (2100 and 2200 UTC), between which development of precipitation within the anvil was most rapid. The vertical sections in Fig. 4 display a significant development of precipitation within that anvil during this time period. Such expansion was accomplished by the following mechanisms:

(1) discrete propagation of new cells along the leading (left) edge of the system (see Fig 4a);

(2) development of convection behind the leading edge, as shown in Fig. 4b;

(3) apparent development or intensification of a mesoscale updraft and assoicated divergence within the anvil.

Mechanisms (1) and (2) would supposedly act to provide condensate to the anvil region via (a) detrainment within the upper portion of convective-scale updrafts, and/or (b) incorporation of decaying convective cells into the anvil region through relative motion.

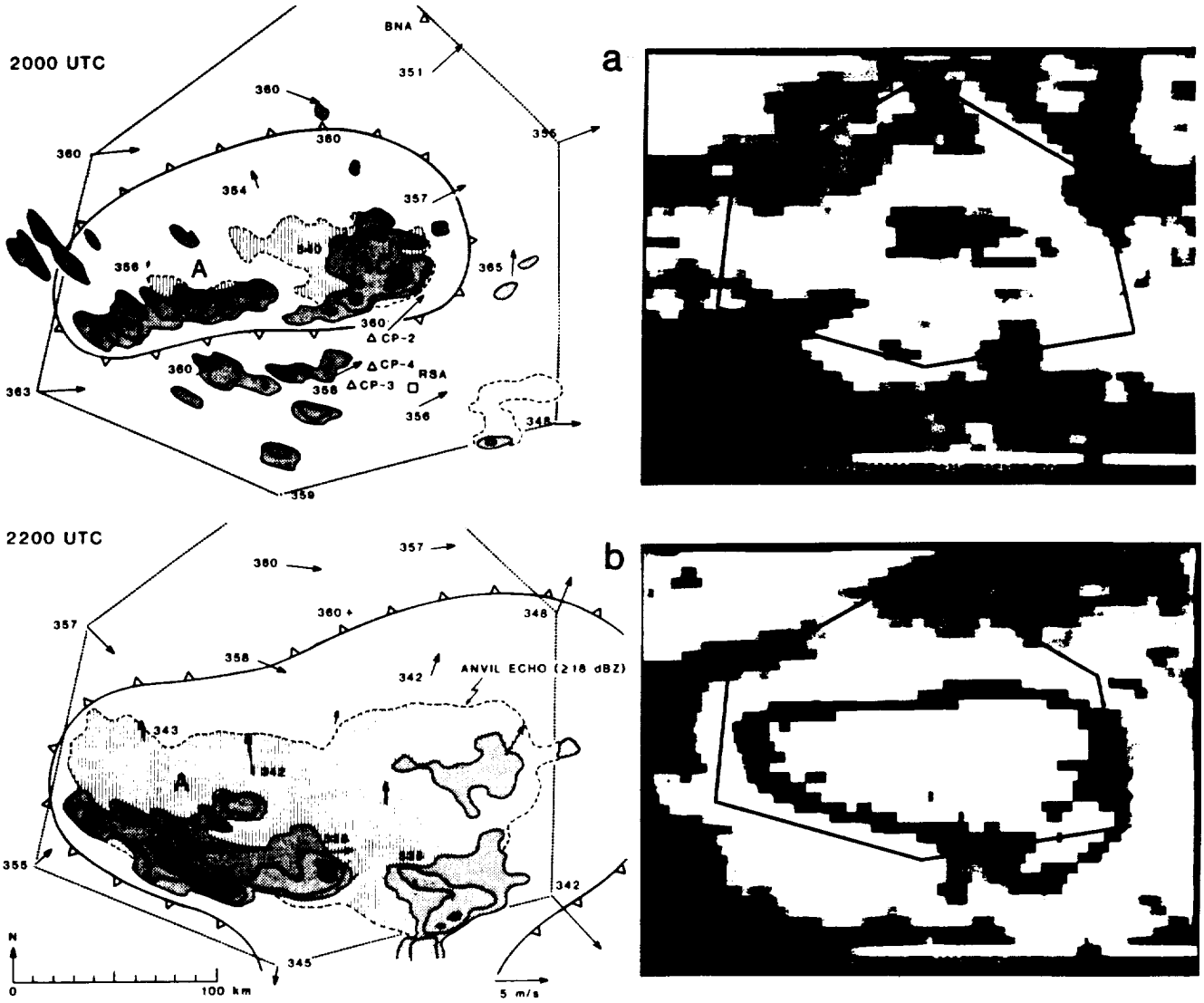

Figure 3. RADAP-derived echo patterns and GOES IR images during the MCS developing stages at 2000 and 2200 UTC. On the left panels, surface mesonet data (wind vectors and θ_e in deg K) are also plotted. Refectivity factor is contoured at 18, 30 and 43 dBZ. Stippling denotes Z > 18 and solid black refers to Z > 43 dBZ. Vertical hatching depicts reflectivity factor > 18 dBZ on the 2 deg elevation scan, which intersects the MCS at about the 10 km level. The right panels are GEOS IR images, with a MB enhancement applied to highlight the anvil region.

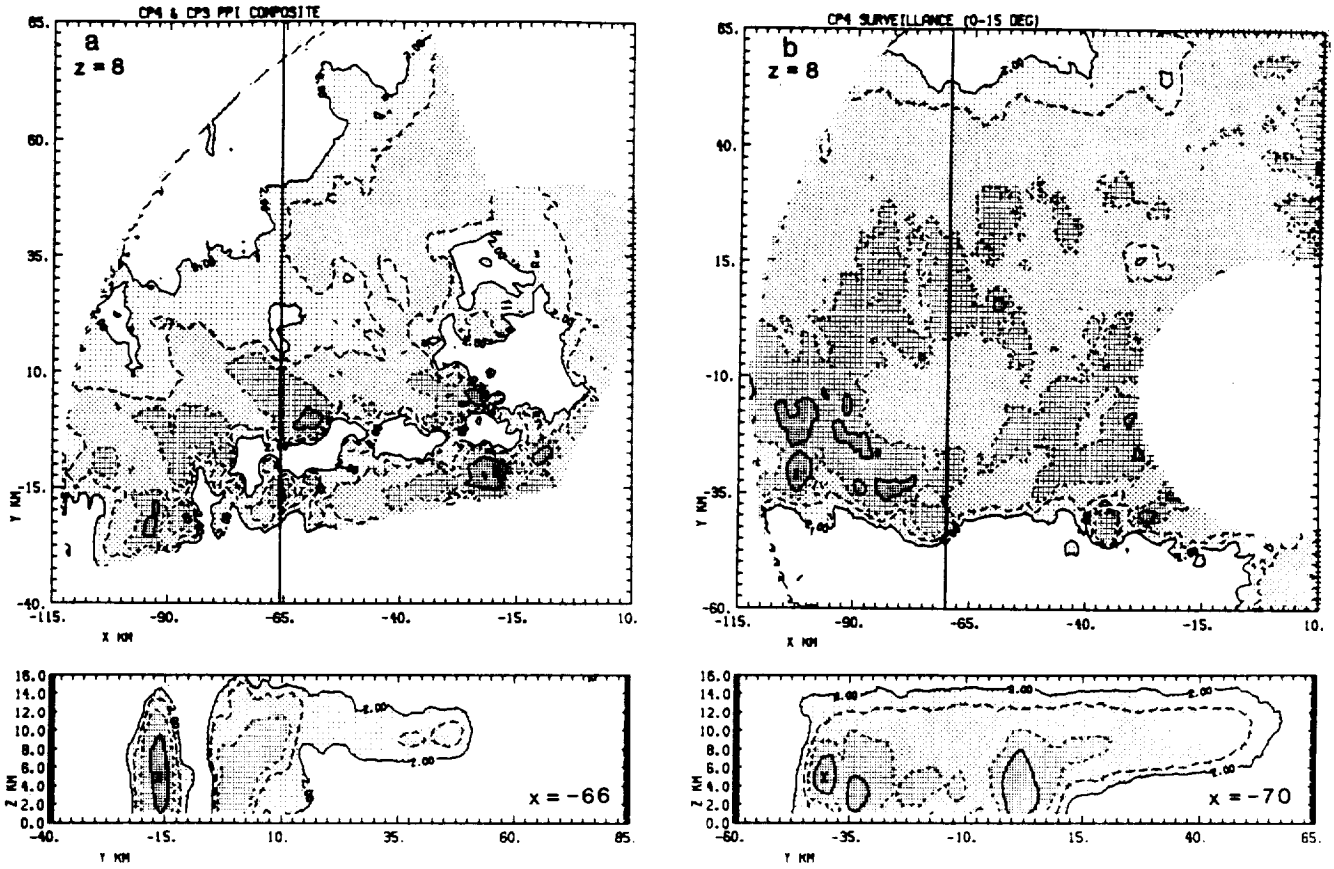

Figure 4. Patterns of C-band reflectivity factor from CP-4 at the 8 km level (top panels) and along a north-south vertical section (bottom panels) along the line indicated in the top panels. Contours are drawn at 2, 10, 20 and 35 dBZ.

Development of precipitation within the mesoscale anvil (beginning near 2100 UTC) closely followed the occurrence of deepest and most intense convective cells. For example, in Fig. 4a, convective cells with tops to ~17 km MSL were analyzed near coordinates (-17,-15). However, it is interesting to note that these intense convective cells did not exhibit any systematic horizontal transport of precipitation from the convective core within the diverging upper-level updraft (i.e., well-defined precipitation anvils were not apparent). This lack of transport may be related to the short lifetime (10-20 min) and small size (~ 5 km diameter) of individual convective cells observed within this MCS.

Mesoscale divergence within the anvil region of the maturing MCS produced a perturbation velocity normal to the major axis of the system. Analysis of the Doppler velocity data indicate that the magnitude of this perturbation was in the range 5-10 m s^{-1} between 2100 and 2200 UTC. Local rawinsonde data (Fig. 1) indicate that the ambient environmental wind component normal to the major axis was near zero. The result of the perturbation wind above the 8 km level was to provide a front-to-rear ground-relative flow of condensate from the leading edge to the stratiform region. Consequently, stratiform precipitation was observed to advance northward from the MCS convective zone from ~2200 UTC (the time of Fig. 4b) to 0000 UTC. Rainfall rates within this stratiform region were 2-3 mm h^{-1}.

The 5-10 m s^{-1} magnitude of the front-to-rear flow component is insuffient to account for the appearance of the deep anvil displayed in Fig. 3b. Much of this precipitation appears to have developed locally.

4. SUMMARY AND DISCUSSION

This case study has revealed some of the time dependent characteristics of precipitation within an evolving MCS. Extensive stratiform precipitation did not appear at the surface until ~4.5 h after first echoes appeared. The development of the mesoscale cloud anvil preceded the development of significant precipitation (reflectivity factor greater than 5 dBZ) within the anvil by ~ one hour. Precipitation development within the anvil could not be accounted for directly by advection of precipitation from convective cores. Rather, it appears that much of the anvil precipitation developed locally, possibly as the mesoscale updraft intensified. This preliminary finding differs from the results of Rutledge and Houze (1987), who determined that precipitation within the stratiform region of an intense squall line system originated from convective cores. They did infer that significant precipitation growth took place within the mesoscale updraft.

Development of anvil precipitation in this case corresponded to maximum observed intensity of convective cells, suggesting perhaps that the intensity of convection plays a key role in the development of the mesoscale updraft. The results of this preliminary analysis do not unambiguously reveal the source of the mesoscale updraft. However, the relatively spontaneous apprearance of stratiform precipitation within the anvil region does support the hypothesis that the mesoscale updraft is a hydrostatic response to convective-induced heating. Further analyses are planned to further diagnose the temporal beviour of both convective-scale and mesoscale motions within this MCS.

5. ACKNOWLEDGEMENTS

This research was sponsored by the National Aeronautics and Space Administration under grant NAG8-654

6. REFERENCES

Knupp, K.R., and W.R. Cotton, 1987: Internal structure of a small mesoscale convective system. *Mon. Wea. Rev.*, **115**, 629-645.

Maddox, R.A., 1980: Mesoscale convective complexes. *Bull. Amer. Meteor. Soc.*, **61**, 1374-1387.

Rutledge, S.A., and R.A. Houze, 1987: A diagnostic modeling study of the trailing stratiform region of a midlatitude squall line. *J. Atmos. Sci.*, **44**, 2640-2656.

24th Conference on Radar Meteorology
27-31 March 1989, Tallahassee, Florida

OBSERVED STRUCTURAL VARIABILITY OF DEEP MOIST CONVECTION WITHIN A MESOSCALE CONVECTIVE SYSTEM

Kevin R. Knupp
Atmospheric Science and Remote Sensing Laboratory
Johnson Research Center
University of Alabama in Huntsville
Huntsville, AL 35899

1. INTRODUCTION

This particular study is part of a more general long-term investigation which has the following goal: to document the observed structure, and variability in structure, of deep precipitating convection within low-shear environments that typify the Southeast during summer months. Detailed observations indicate that, on a given day within a relatively homogeneous environment, deep convection can assume a wide variety of structures (e.g., cloud diameter, cloud top, precipitation intensity, and kinematic characteristics). Such variability may be hypothesized to result from variations in the magnitude of convergence within the atmospheric boundary layer, including low-level variability in thermodynamic variables. This is the general hypothesis under consideration in this long-term investigation. One primary objective is to ascertain the parameters which influence storm characteristics.

This paper presents some radar observations of convective cloud structure within and around a developing mesoscale convective system (MCS) which attained an eventual horizontal dimension of approximately 100 by 200 km. The major focus is to compare cloud structure within a cluster of clouds removed from the developing MCS, with clouds existing along a large-scale outflow boundary within the MCS. Longer-term objectives on this particular case will relate convective cloud structure and transports to the evolutionary pattern of mesoscale flows and precipitation distribution within the MCS. Although the results reported here are based principally on multiple Doppler radar analyses, a three dimensional cloud model will be used as a complementary tool in future work.

2. GENERAL MCS STRUCTURE AND EVOLUTION

The MCS of interest developed over south-central Tennessee and northern Alabama on 13 July 1986. A host of special observational platforms, set up under the general Cooperative Huntsville Meteorological Experiment (COHMEX), acquired detailed measurements within the MCS. The mature MCS was composed of a 200 km long east-west broken line of convective cells, flanked to the north by a region of stratiform precipitation up to 100 km wide. Initial echoes within the MCS appeared 4-5 h prior to the mature MCS phase. Individual convective cells were most intense just prior to the development of stratiform precipitation. The period of study in this paper spans the MCS developing phase, prior to the appearance of widespread precipitation within the mesoscale anvil.

Figure 1 portrays the development of this system from about one hour after first echo (1820 UTC, Fig. 1a) to about the time of observed maximum reflectivity factor within individual convective cores (2030 UTC, Fig. 1c), after which expansion of the mesoscale anvil was most rapid (see Knupp, 1988). At 1820 UTC (Fig. 1a) two regions of deep convection existed: (1) a group cells associated with the developing MCS located ~100 km to the northwest of the Doppler radars, and (2) a smaller cluster of cells located 20-50 km to the southeast. By 1940 UTC (Fig. 1b) the southeast cluster had weakened while convective cores within the intensifying MCS to the northwest exhibited a significant increase in peak reflectivity and area. At 2030 UTC intense convective cells assumed an east-west linear configuration along a vigorous mesoscale outflow boundary (Fig. 1c). Convective cores along the outflow boundary at 1940 and at 2030 exhibited much higher echo top heights (up to 17 km) and greater volume of high reflectivity factor. On this day, maximum reflectivity was found to exhibit only a very weak dependence on observed echo tops within the range 10-17 km.

As the MCS evolved, the environment to the south of the MCS displayed significant changes with time. One site within the network acquired soundings on this day (location shown in Fig. 1b), and two of these (1800 and 2000 UTC) are displayed in Fig. 2. These two soundings correspond closely in time to Figs. 1a and 1b. As the MCS approached the sounding site, the environment was cooled and moistened at lower middle levels and warmed at upper levels. Thus a weak stabilization was imposed, but cloud vigor was observed increase despite the stabilization. The wind profile was correspondingly modified slightly, but shows a similar negative shear structure (the shear vector being directed from east to west) over much of the troposphere above the ~10 m s^{-1} maximum near 85 kPa. Such a change in environmental winds would supposedly influence storm structure to some degree, but for the sake of simplicity, it will be assumed here that this change alone exerted a relatively minor influence on storm structure. This supposition will be tested in the future with a three-dimensional cloud model.

3. OBSERVED CLOUD STRUCTURES

In the following subsections the similarities and differences in the structure of three individual cloud systems will be examined. These systems are labeled as A, B and C in Fig. 1.

3.1 Cloud System A

The relative location of this cloud, located within the cluster of cells to the southeast, is shown in Fig. 1a. Convective cores within this cluster developed about one hour before their counterparts within the eventual MCS to the northwest. The quasi-linear orientation of the cloud elements was roughly along the mean wind (and the shear vector). In most cases, new cells formed along the western border of the system and moved downwind (east). The majority of convective cores (generally unicellular and short-lived) within this group displayed echo tops less than ~11 km, with two exceptions being cloud system A (~12 km) and a larger cloud system to its southeast, shown also in Fig 1a. This latter system developed echo tops to near 13-14 km. System A exhibited first echo near 1800 UTC and attained a maximum reflectivity factor of 65 dBZ at 1820. This was the most vigorous cell of about 6 that developed within effective dual Doppler radar range. It was the only precipitating cloud system to exhibit a well-defined radial divergence (~10 m s^{-1} over a ~3 km radial distance) within the downdraft near the surface, about 20 min after first echo. Analysis of maximum reflectivity factor in time-height section format suggests that cloud updrafts maximized 5-10 min prior to this analysis time of 1824 UTC. The cloud then weakened after formation of the low-level downdraft and was kinematically weak after 1835 UTC.

A three-dimensional depiction of the 40 dBZ reflectivity factor surface at 1823 UTC (Fig. 3) reveals a general downshear tilt of the core. Much weaker precipitating convection is located to the east (downwind). As shown in the Doppler analysis in Fig. 4, the most significant updrafts throughout the depth of the cloud at this time are located in the northern portion of the cloud at 4 km. Vertical cross sections through the precipitation core (not shown) indicate that weak downdrafts (several m s^{-1}) dominate the lower 4 km, while updrafts of 10-15 m s^{-1} are analyzed above 4 km. The kinematics at this time (as well as time-height section of radar reflectivity factor not presented) thus portray a weakening cloud system whose lifetime was about 40 min. The cloud can be categorized as unicellular, although weak secondary

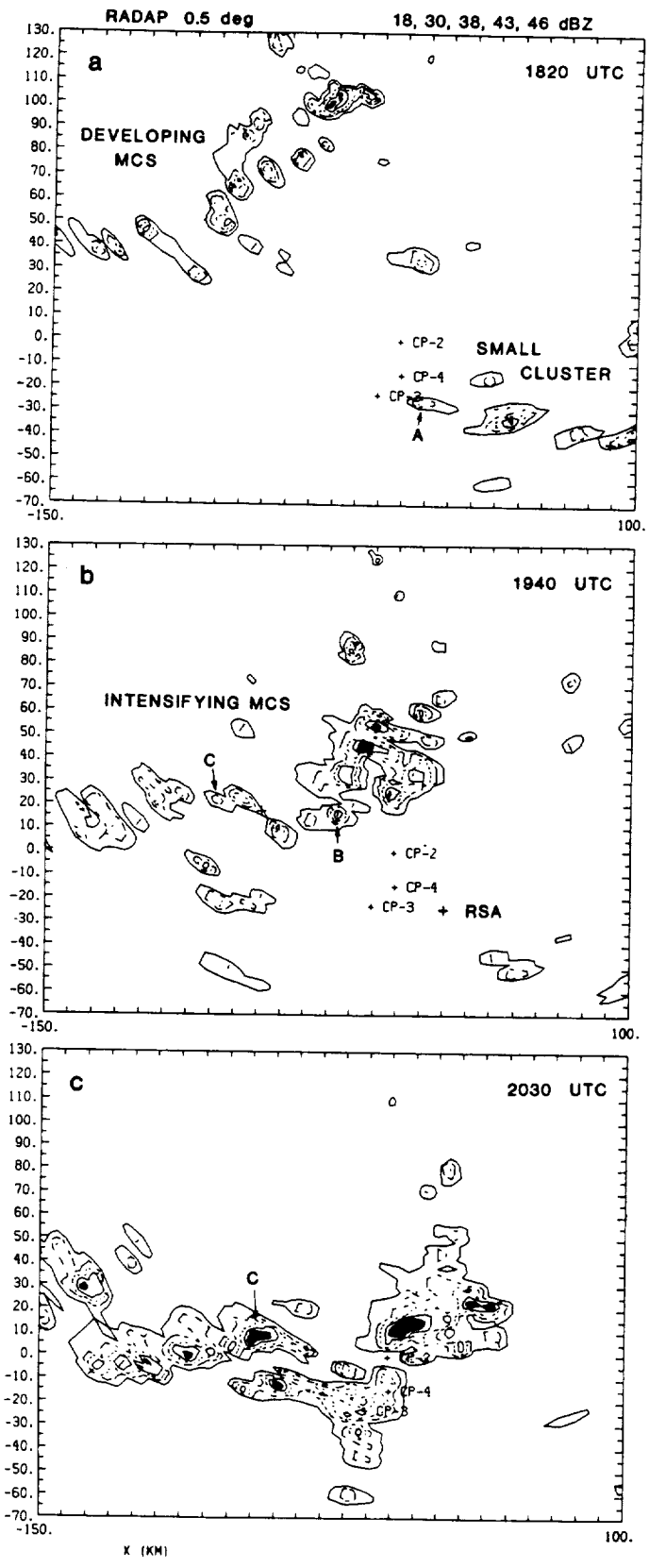

Figure 1. RADAP data from Nashville, located about 180 km north of CP-2. Contours correspond to 18, 30, 38, 43 and 46 dBZ. Reflectivity factor greater than 46 dBZ is shaded black. Echo distributions are shown at (a) 1820 UTC, ~1.5 h after first echo; (b) 1940 UTC; and (c) 2030 UTC, just before the maximum observed intensity and area of convective cores. Locations of Doppler radars (CP-2, CP-3 and CP-4) and the RSA rawinsonde location (data plotted in Fig. 2) are denoted.

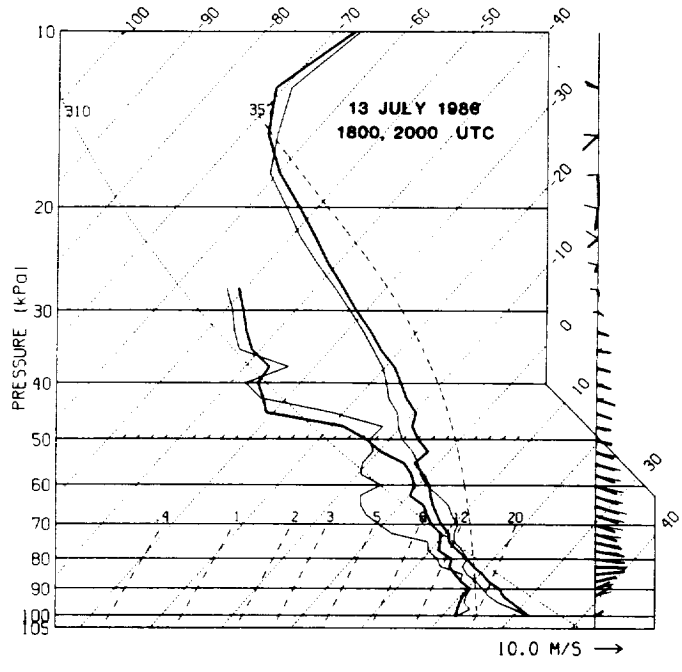

Figure 2. Soundings from location RSA (Fig. 1b) at 1800 UTC (thin lines) and at 2000 UTC (thick lines). Wind lines on the right are ground-relative vectors whose tails are located at the vertical line.

updraft and precipitation development did occur (as shown in Fig. 4) after the primary updraft impulse. The structure and scenario of cloud A appears to typify the structure of other deep precipitating convective clouds located within this cluster.

3.2 Cloud System B

Cloud B appeared ~1.5 h after cloud A along the front edge of the intensifying MCS. As shown in Fig. 1b, an east-west line of cells extends westward from a relatively intense cluster 30 km north of CP-2. Analysis of surface data indicates that a mesoscale outflow boundary was influential in the initiation of B, as well as cells in its vicinity. Thus the environment of B differed from that of A, not only in the magnitude and nature of the low-level forcing, but also in differences in the thermodynamic and wind profiles above the ABL (as indicated by the pair of soundings in Fig. 2).

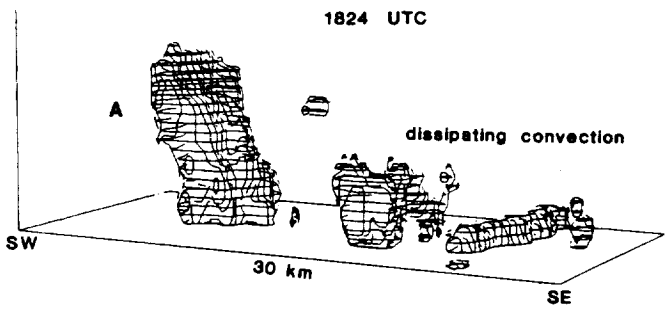

Figure 3. Three-dimensional depiction of the 40 dBZ reflectivity factor surface (from CP-2, S-band) at 1824 UTC (cloud system A). The z axis is located in the southwest corner of the 30 by 15 km domain. The relative location of this cloud is shown in Fig. 1. Vertical lines are drawn every 0.5 km, and horizontal lines every 0.25 km. The surface extends to 9.5 km height.

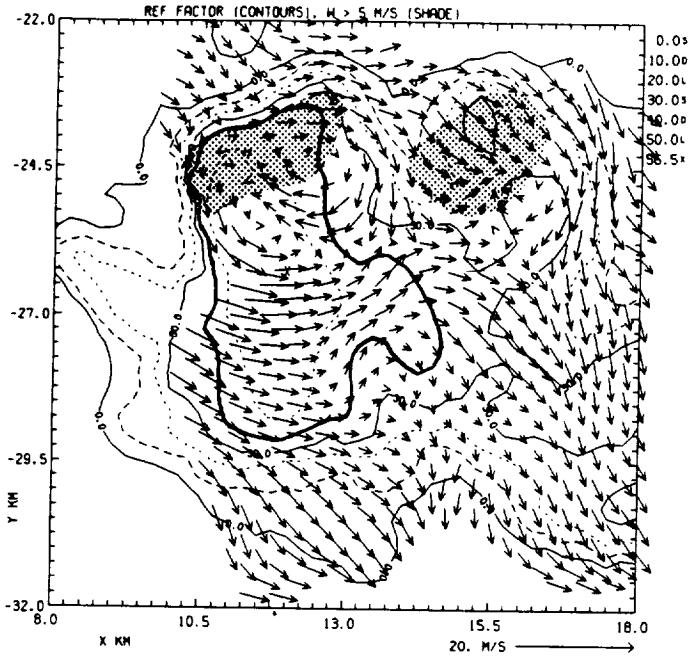

Figure 4. Approximate cell-relative flow within cloud A at 4 km AGL, obtained from a dual Doppler analysis (CP-2, CP-3) at 1824. Reflectivity factor (CP-2) is contoured every 10 dBZ, beginning at 0 dBZ. The 40 dBZ contour is highlighted. Regions of updraft > 5 m s^{-1} are stippled. Vertical motions were obtained by downward integration of mass divergence, with variational constraints applied to the lowest boundary.

The general structure of B is shown in Fig. 5, a three-dimensional surface of 40 dBZ reflectivity factor as in Fig. 3. This view indicates a multicellular (multiple turret) structure in the reflectivity field. A vertical cross section through the low-level precipitation core appears in Fig. 6. Both similarities and differences can be seen between the structure of this cloud and the structure of cloud A in Fig. 3. The analysis of each corresponds within 3 min to the appearance of the low-level downdraft (divergence in radial velocity) near the surface. Both exhibit a similar downshear tilt of the 40 dBZ core, and both display a prevalence of updrafts at upper levels, particularly within the northern cloud sector. Cloud B, however, was generally more vigorous than A, having updrafts and downdrafts about twice the magnitude (Fig. 7a). The u momentum within the core of B also differs from that of A (Fig. 7b), suggesting a probable difference in the momentum of the environment (greater than that indicated in the soundings of Fig. 2) as well as dynamical differences associated with the environmental differences. At the time of the analysis of Figs. 5 and 6, cloud B was growing explosively along its northern flank (see Fig. 5) where secondary cell development occurred (the vertical section in Fig. 6 cuts through this secondary updraft only at high levels). Subsequent echo tops within the secondary cells reached 15-16 km. Such intense secondary cell development did not appear in cloud A.

3.3 Cloud System C

Strongest individual convective cell cores displayed increased intensities (higher echo tops and greater horizontal dimension) and longer lifetimes as the MCS attained peak intensity between 2030 and 2100 UTC. Figure 1c shows several particularly large cells within the MCS, one of which is displayed in three-dimensional form in Fig. 8. This cloud system formed along the mesoscale outflow boundary at approximately 1930 UTC. At the analysis time of 2018 UTC, the outflow boundary was located about 20 km to the south of C. The general structure of C can be categorized as organized multicellular, with new cell development occurring in the southeast flank. (Recall that clouds A and B developed secondary cells within their northeast sectors.) The echo top within this relatively large complex, which had an apparent active lifetime greater than one hour, reached ~16 km at this time (Fig. 7c).

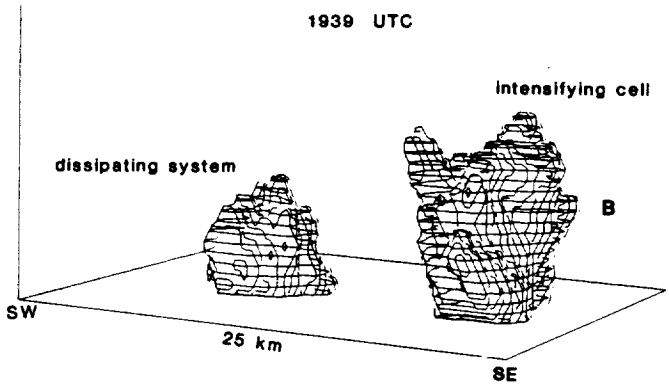

Figure 5. As in Figure 3, except for cloud system B at 1939 UTC. The surface extends to 9 km height, and the horizontal domain is 25 by 20 km.

Single Doppler radar patterns from CP-4 reveal significant upper-level divergence near the core of the system. Clouds at this stage of MCS development were therefore more intense, developed to greater heights and had longer lifetimes.

In general, the most vigorous clouds observed between 2000 and 2100 UTC formed near the mesoscale outflow boundary and were particularly vigorous when individual outflow appeared to interact with the mesoscale outflow. Some persistent cells such as C maintained a relatively high intensity even though the initiating outflow boundary advanced southward at ~ 10 m s^{-1} relative to the eastward-advancing cells.

Of interest is the fact the maximum reflectivity factor within this cloud is comparable to that of clouds A and B (see Fig. 7c). Such a behavior verifies the lack of a strong relationship between maximum echo top (for tops greater than 8-10 km) and maximum reflectivity factor in this case. Such a behavior is duplicated on other days and is a consequence of the relatively efficient warm rain process.

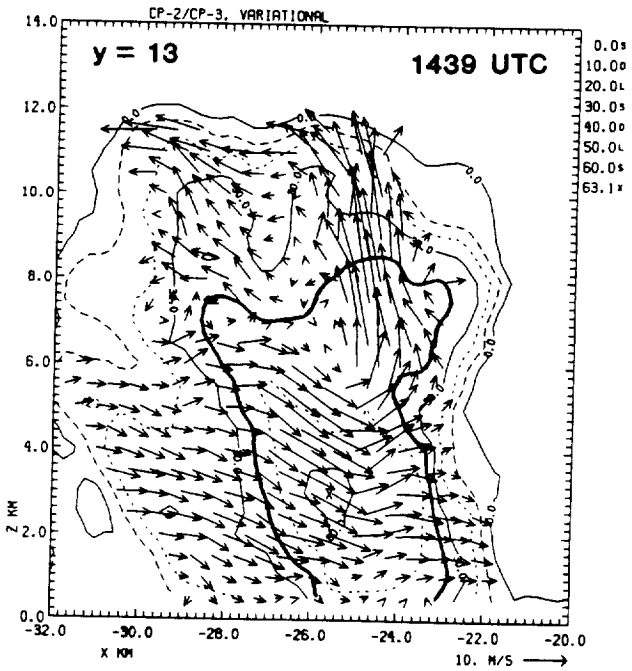

Figure 6. Cell relative flow along a vertical east-west plane within cloud system B at 1939, obtained from a CP-2/CP-3 dual Doppler analysis. The location of this vertical section is near the center of the 40 dBZ reflectivity surface in Figure 5. The 40 dBZ contour (CP-2) is highlighted.

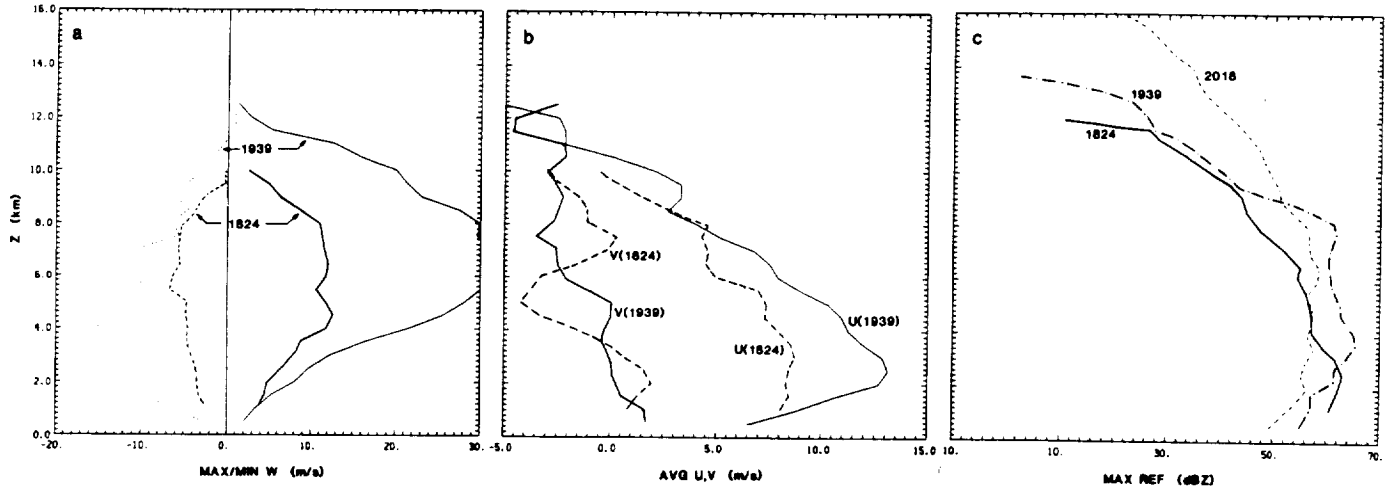

Figure 7. Vertical profiles of quantities for cloud systems A, B and C. (a) Maximum and minimum vertical motion (m s^{-1}, the magnitudes for B are probably overestimated). (b) Average ground-relative u and v (m s^{-1}) within the 20 dBZ echo volume. (c) Maximum reflectivity factor (dBZ), obtained from CP-2 (S-band) in A and B, and from CP-4 (C-band) in C.

4. SUMMARY

This analysis has highlighted some similarities and differences in deep precipitating clouds within and outside of a developing mesoscale convective system. Similarities in cloud structure include (1) a downshear tilt of the cloud precipitation core, and (2) generation of new cells toward the direction of cloud motion and parallel to the major axis of the cloud line. One systematic difference in the behavior of the three clouds examined was longevity and intensity. Cloud A (outside the MCS) was weak, short-lived and basically unicellular. In contrast clouds B and C were more intense and exhibited a tendency to propagate (i.e., they exhibited development of intense secondary cells). Such a contrast in behavior appears to be related in part to interactions between individual cloud downdraft outflows and the mesoscale outflow boundary.

The behavior of deep convection documented here has been observed qualitatively (Purdom and Marcus 1982) and simulated to some extent with numerical cloud models. For instance, Tripoli and Cotton (1980) demonstrated that cloud vigor is influenced by the magnitude of convergence within the ABL. It was found that deep convection of greater intensity occurred in response to increasing the magnitude of low-level convergence, localized to the cloud scale. In other related numerical studies, Droegemeier and Wilhelmson (1985) studied the nature of forcing along intersecting outflow boundaries. The results of such studies demonstrate the dependence of storm structure on low-level forcing, particularly for the case of low-magnitude environmental wind shear. Such forcing requires comprehensive study in order to fully understand cloud processes within environments having low shear.

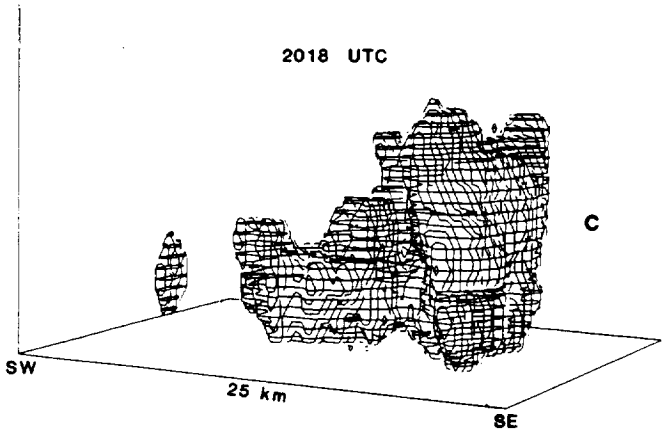

Figure 8. As in Figure 3, except for cloud system C at 2019 UTC. Reflectivity data were obtained from CP-4 (C-band). The surface extends to 12 km height, and the horizontal domain is 25 by 20 km.

Since the development of mesoscale anvil circulations within MCS's is intimately connected to cloud-scale processes, a detailed understanding of cloud kinematics and transport processes is needed. In this case, the mesoscale anvil developed rapidly once deep convection reach intense levels (15-17 km tops). Clouds did not attain such intensity (core size) until 4-5 h after first echo, apparently due to the requirement of a complex ABL. Additional analyses of other individual cloud systems within this MCS will be carried out so that cloud structures throughout the life cycle of the MCS can be defined and related to the mesoscale circulations. Preliminary results suggest that convective cloud intensity weakened, in a manner following the scenario presented in the numerical work of Rotunno *et al* (1988), as the MCS later developed fully-mature structure consisting of a convective line and a region of trailing stratiform precipitation.

ACKNOWLEDGMENTS

This research was funded by the National Aeronautics and Space Administration under grant NAG8-654, and by the National Science Foundation under grant ATM-8800606. Much of the radar analysis effort utilized the SPRINT and CEDRIC radar processing software developed at the National Center for Atmospheric Research (NCAR) by L.J. Miller and C. Mohr. NCAR also provided the VAX/VMS based graphics software used in this study. Mr. James W. Coker provided programming assistance.

REFERENCES

Droegemeier, K.K., and R.B. Wilhelmson, 1985: Three-dimensional numerical modeling of convection produced by interacting thunderstrom outflows. Part I: Control simulation and low-level moisture variations. *J. Atmos. Sci.*, **42**, 2381-2403.

Knupp, K.R., 1988: Observational analysis of mesoscale convective system growth and structure. Preprints, *10th International Cloud Physics Conf.*, Bad Homburg, FRG.

Purdom, J.F.W., and K. Marcus, 1982: Thunderstorm trigger mechanisms over the Southeast United States. Preprints, *12th Conf. Severe Local Storms*, San Antonio, Amer. Meteor. Soc., 487-488.

Rotunno, R., J.B. Klemp, and M.L. Weisman, 1988: A theory for strong, long-lived squall lines. *J. Atmos. Sci.*, **45**, 463-485.

Tripoli, G.J., and W.R. Cotton, 1980: A numerical investigation of several factors contributing to the observed variable intensity of deep convection over South Florida. *J. Appl. Meteor.*, **19**, 1037-1063.

Conference on Cloud Physics
July 23-27, 1990
San Francisco, CA

RADAR OBSERVATIONS OF PRECIPITATION GROWTH AND EVOLUTION WITHIN THE ANVIL REGION OF A MCS

Kevin R. Knupp
Atmospheric Science and Remote Sensing Laboratory, Johnson Research Center
University of Alabama in Huntsville
Huntsville, AL 35899

1. INTRODUCTION

This paper presents Doppler radar observations of the growth and evolution of precipitation (reflectivity factor) and associated mesoscale motions within the anvil region of an evolving mesoscale convective system (MCS). The MCS of interest (13 July 1986) was observed during the Cooperative Huntsville Meteorological Experiment (COHMEX), conducted over northern Alabama and central Tennessee during June and July, 1986. During the latter stages of the ~8 h lifetime of this MCS, an extensive region of stratiform precipitation was observed. The focus of the paper concerns the initial appearance and subsequent evolution of precipitation within the stratiform region of the MCS, and the relation to the mesoscale flows that are observed within the system.

2. ANALYSIS METHODOLOGY

The COHMEX program supported a number of experimental platforms, including five Doppler radars, surface and upper-air mesonets and three aircraft. This study primarily utilizes the NCAR CP-4 radar, which was operated in a surveillance mode more than any other Doppler during COHMEX. As the MCS evolved to a structure consisting of convective and stratiform regions, CP-4 was used to collect an full-volume scans, from which VAD and 3-D reflectivity factor analyses were completed.

Because a C-band radar such as CP-4 is subject to appreciable attenuation by heavy precipitation, such as was common within the 13 July MCS, corrections for attenuation are required for quantitative analysis of reflectivity. In this study, the attenuation formula given in Hildebrand (1978) were used. To be specific, one-way attenuation calculations were determined from the formula given below, which assume a Marshall-Palmer distribution:

$$K_a = (0.0045-0.00085T')R^{(0.980+0.020T')} \quad (R\leq 10),$$

$$K_a = (0.0030-0.00070T')R^{(1.155+0.065T')} \quad (R>10),$$

where R is rainfall rate in mm h^{-1} and the temperature parameter $T'=(T/10)+1.0$.

When applied to the measured CP-4 reflectivity fields, total two-way attenuation values of several dB were commonly produced by intense convective cores Extreme values of 10 dB were produced under conditions in which the CP-4 viewing geometry was oriented along a line of convective cores.

VAD analyses were completed for 20 volume scans acquired by CP-4 as the MCS moved over the the radar. Because maximum elevations were limited to either 15° or 18.5°, the EVAD technique described by Srivastava et al (1986) was not attempted here. A conventional VAD analysis was completed using software acquired from NCAR. A great deal of effort, in terms of editing and inspection of raw data fields, was expended in producing accurate VAD-derived quantities. Vertical motion, obtained from integration of the divergence field, has been constrained to a zero boundary condition at both the surface and estimated cloud top (obtained from the GOES IR data).

3. OVERVIEW DESCRIPTION OF THE MCS

The MCS formed within an environment having appreciable low to middle level moisture (precipitable water values of ~50 mm) and appreciable instability (CAPE ~2500 J kg^{-1}). Environmental winds were primarily zonal, with a peak u component of +10 m s^{-1} near 85 kPa and a minimum u component of -5 m s^{-1} near 20 kPa. At its mature state, the MCS was composed of an east-west line of convective cells flanked to the north by an extensive area of stratiform precipitation. The system orientation was thus parallel to the environmental wind shear vector.

Much of the MCS was in viewing range of CP-4 during the eight-hour lifetime of this system. Figure 1 illustrates the evolving IR patterns at cloud top during the time period (2100 to 0000 UTC) in which precipitation within the anvil was observed to form and expand to an area of ~20,000 km^2 (220 km by 80 km) at 0000 UTC 14 July. The expansion of precipitation within the anvil (at middle levels of ~8 km) was most rapid just after the time of maximum convective activity near 2100 UTC. Note that the anvil cloud top was descending (temperature increasing) during this period.

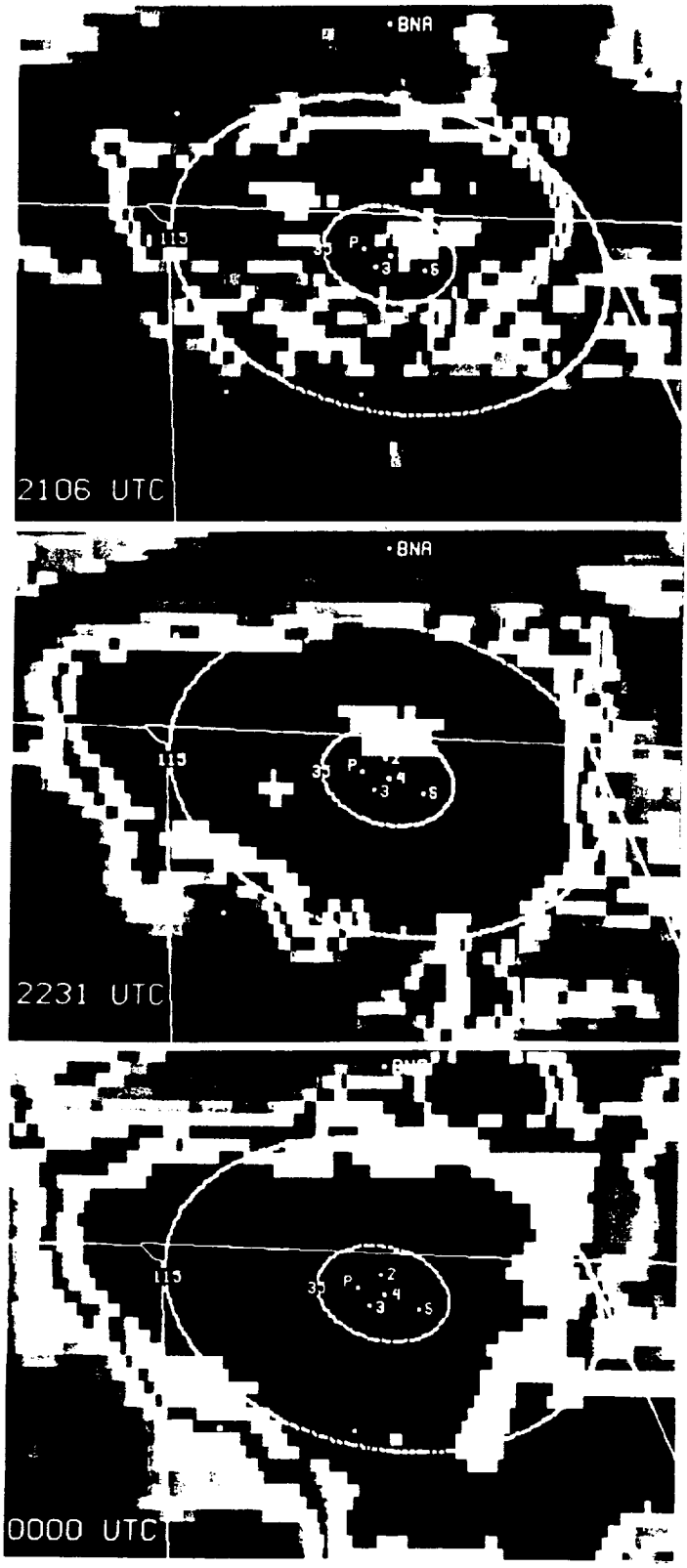

Figure 1. GOES IR images at 2106 and 2231 UTC (13 July 1986) and 0000 UTC (14 July). An MB enhancement has been applied. The location of CP-4 is denoted as "4". CP-4 range rings of 35 and 115 km represent the region of VAD analysis and maximum range, respectively. (a) At 2106 individual convective cells have attained peak intensity, and stratiform precipitation is beginning to form and expand at middle to upper levels. (b) By 2231 deep convection has subsided in intensity and is confined to the southern periphery of the anvil shield. Stratiform precipitation is beginning to appear at the surface, and mesoscale updraft values up to 60 cm s^{-1} are analyzed at upper levels within the 35 range ring. (c) By 0000 active convection has nearly disappeared, and the stratiform precipitation has attained a maximum area. Even though cloud top has warmed, upward motion of 10-15 cm s^{-1} exists at upper levels over CP-4.

Figure 2 illustrates the reflectivity field at low and middle levels, obtained from the WSR-57 RADAP-equipped radar at Nashville (BNA). The lower level data was obtained from the 0.5° scan, which which spans the 1.2 to 5.4 km AGL depth (assuming a 2° beam width and a mean range of 160 km). The middle level patterns, indicated by the vertical hatching in Fig. 2, were analyzed from the 2.0° scan, which spans the height interval 5.2 to 11.2 km. At this time, much of the anvil precipitation (as shown by the 18 dBZ contour in Fig. 2) is still aloft and in the process of descending to the surface. It is at this time that VAD analyses presented below are available.

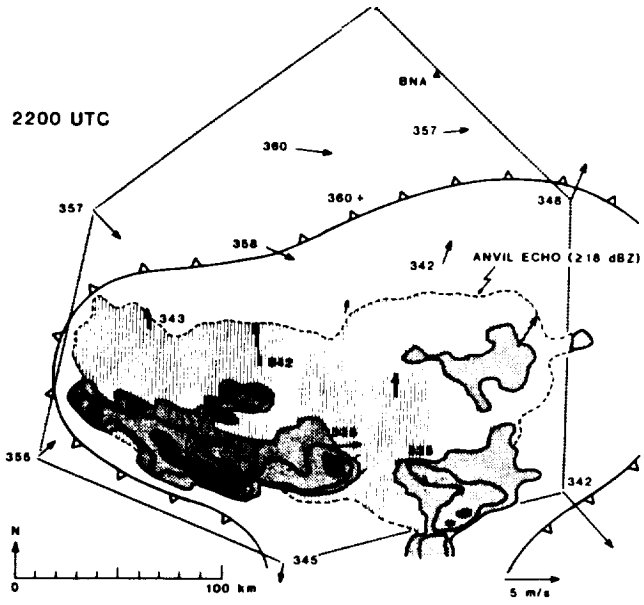

Figure 2. Patterns of reflectivity factor obtained from analysis of RADAP data collected by the WSR-57 radar located at Nashville (BNA). The 0.5°scan is stippled and contours are drawn at 18, 30 and 43 dBZ. The 18 dBZ contour from the 2.0°scan is hatched and shows the distribution of precipitation within the anvil.

Finer-scale precipitation structures obtained from the CP-4 radar are presented in Fig. 3. Correction for estimated attenuation has been made here. At this time the stratiform region has expanded to a distance of 60-70 km behind the convective line. Radial velocity patterns within the vertical plane, approximately normal to the MCS major axis and passing through CP-4 (not shown), reveal a descending inflow jet of 10 m s^{-1} magnitude (ground relative) entering the system at the trailing edge, and descending to low levels near the convective line. Airflow parallel to the major axis of this system is more substantial, in the range 8-12 m s^{-1}. In response to this flow, the translational motion of individual cells (as well as hydrometeor transport throughout the system) is primarily from the west. With the exclusion of this latter property, this MCS exhibits many of the general kinematic and precipitation features observed elsewhere, including the High Plains (Smull and Houze 1986) and the tropics (Chong et al 1988).

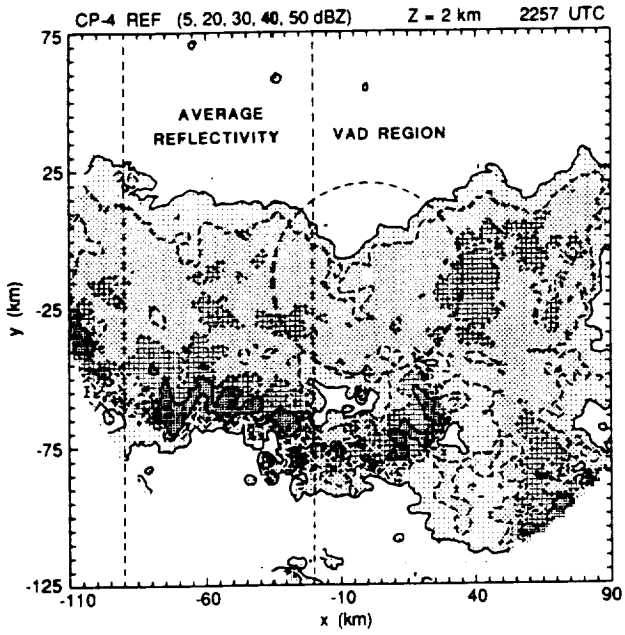

Figure 3. Patterns of reflectivity factor from CP-4, shown at 2 km MSL.

4. DEVELOPMENT AND EVOLUTION OF MESOSCALE FLOWS AND PRECIPITATION

4.1 Mesoscale flow patterns

VAD analyses from all full-volume scans between 2122 and 2353 UTC are presented in Fig. 4. This analysis is separated into two contiguous blocks, the first (2122-2156 UTC) coinciding with the rapid anvil expansion, just after the time of the maximum activity of deep convection. The second block (2243-2353 UTC) coincides with a significant decrease in intensity of deep convection (along the leading edge) and the appearance of stratiform precipitation within the anvil region.

At the start of the VAD analysis, dissipating convective cores were present inside the VAD analysis area. Within two hours prior to this time, intense convective cells, some of which exhibited reflectivity factor to 60 dBZ, tops to 16 km, and updrafts up to 30 m s^{-1} (estimated from a dual Doppler analysis) were observed within 35 km (the primary VAD circle) of CP-4. In Fig. 4, reflectivity factor shows a peak value at low levels. Vertical motion in excess of 50 cm s^{-1} (Fig. 4e) and relatively strong divergence is analyzed at upper levels. Convergence occurs throughout a relatively deep depth from 2 km to 8 km. Only relatively weak downdraft is analyzed, even though convective-scale downdrafts were prominent ($\sim$10 m s^{-1}) within some of the intense cells within the VAD circle just before 2122 UTC. Patterns in perturbation horizontal velocity (u' and v', Fig 4c and 4d, respectively) signify inflow at middle to low levels and outflow at upper levels. These perturbation values were computed as the difference between the VAD horizontal winds (i.e., the "system" winds) and the ambient wind measured by a rawinsonde release at 1800 UTC. The environmental winds were generally zonal throughout the troposphere, ranging from a maximum of 10 m s^{-1} near 85 kPa to -5 m s^{-1} at 20 kPa.

The second VAD block (2243-2348 UTC) corresponds to stratiform conditions over CP-4. Contours of all quantities are thus quasi-horizontal. A radar bright band appears in the analysis of Fig. 4a and shows a slow increase in intensity with time to just over 35 dBZ at the last VAD analysis time (2353 UTC). While u' is approximately constant, v' decreases uniformly to -12 m s^{-1} as the inflow jet entering the system from the north becomes established. A convergence maximum centered near 5.5 km also increases slightly, while divergence below 4 km decreases, and divergence above 7.5 km increases. Between 2240 and 2330 UTC the mesoscale updraft is very weak (< 5 cm s^{-1}) but increases to over 10 cm s^{-1} by 2348 UTC. It is unknown whether these changes are temporal or spatial (translational) in nature. It is interesting that both cloud top and reflectivity factor (Fig. 4a) descend throughout this period (2243 to 2348 UTC) even though vertical motion at cloud top is positive.

4.2 Reflectivity analyses

One of the objectives of this study is to determine the origin and evolution of precipitation within the stratiform region of this MCS. The evolution of the average vertical structure over the 2057-2348 UTC time period is portrayed in Fig. 5. The analysis utilizes vertical sections of reflectivity factor, averaged over the x=-90 to x=-20 interval as shown in Fig. 3. These sections were generated from volume scans over an x-axis interval thought to maximize the vertical resolution of the analysis. Because the SPRINT program (Mohr et al,) was used to generate this product, Z values have not been corrected for effects of attenuation unless time differencing was employed, as is the case below for Fig. 6.

Figure 5a shows the prevalence of echoes associated with a dual convective core region and the emergence of precipitation (i.e., the 5 dBZ contour) within the anvil of the growing MCS. Discrete propagation of convective elements, which was most prominent near this time, is responsible for the dual-turreted structure in Fig. 5a. During the subsequent three hours the convective line continued to propagate discretely southward (to the left in Fig. 5) while the stratiform precipitation region expanded and intensified. At both 2157 and 2257 UTC, the leading edge consisted of a single line. The east-west averages show an increasing Z within the convective region by virtue of increasing coverage. The maximum observed intensity of echoes during this period ac-

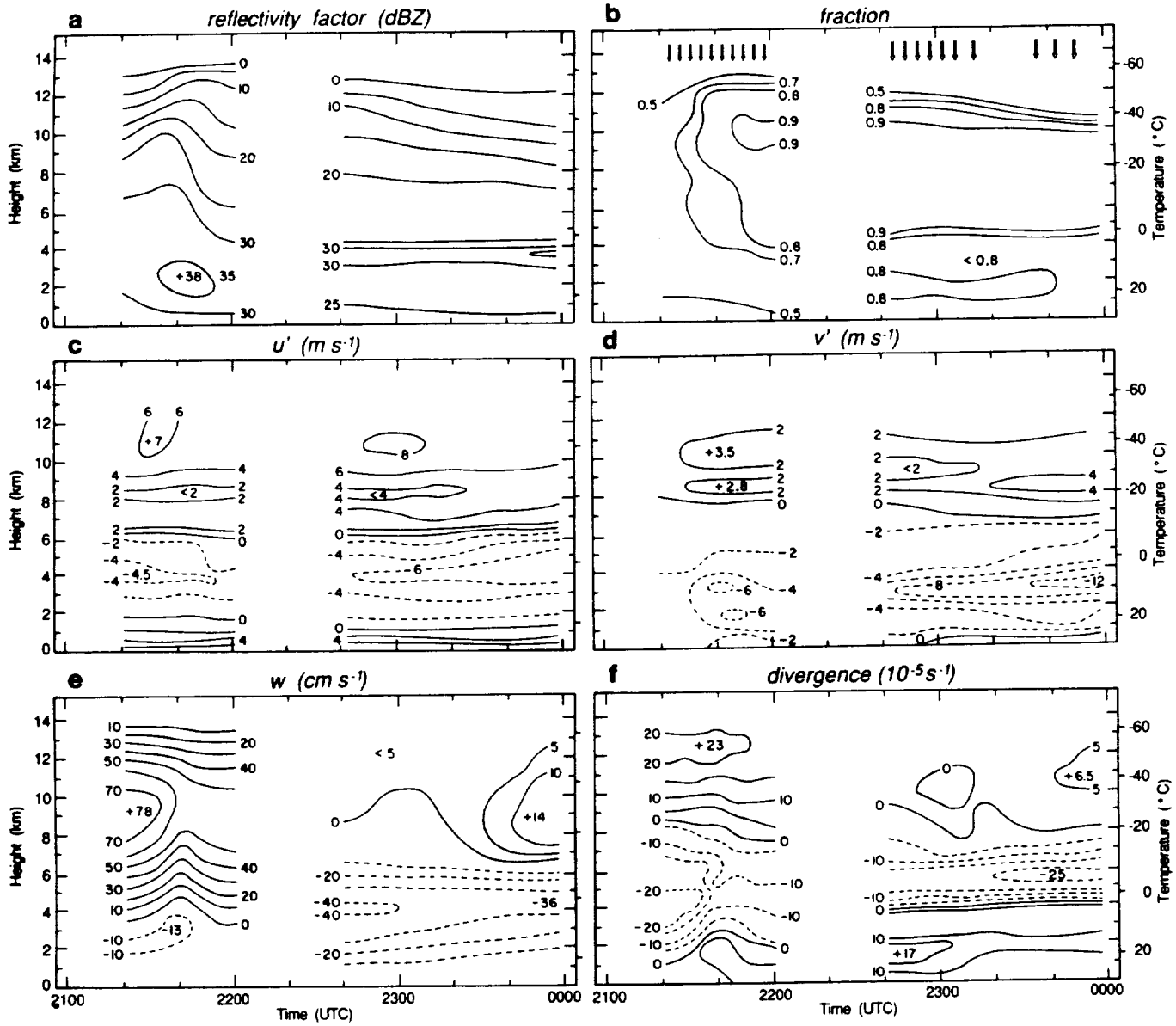

Figure 4. VAD analyses obtained from CP-4 volume scans, within the 35 km circle shown in Figs. 1 and 3. The "fraction" field in panel (b) refers to the fraction of good data points within a particular circle. Arrows in (b) denote times of volume scans. The u' and v' fields in (c) and (d) were obtained by subtracting the VAD winds from environmental sounding values.

tually decreased. By 2348 convective echoes were quite weak and no longer organized in a linear fashion, as shown in Fig. 5d. Throughout this period, precipitation within the stratiform region increased in both intensity and coverage. By 2257 a well-defined bright-band was analyzed (Fig. 5c) and remained prominent in the 2348 analysis (the last available time).

Before proceeding with more quantitative calculations on the echo growth, it is instructive to relate the reflectivity structures to the VAD analyses presented in the previous section. In making these comparisons, recall that the location of CP-4 is at y=-15 and centered 55 km east of the averaging box used to produce Fig. 5. (See Fig. 3 for the location of each analysis region.) At 2157 (after the maximum intensity of convection), the VAD analysis in Fig. 4e shows a prevalence of mesoscale updraft, peaking near 50 cm s^{-1} at upper levels. The emergence of the bright band in Fig. 5c at 2257 is associated with a maximum of mesoscale downdraft of 40 cm s^{-1}, and only very weak mesoscale updraft above about 9 km. Finally, at 2348 the mesoscale updraft has re-intensified to 14 cm s^{-1} in a location just north of the bright band. In spite of the fact that mesoscale updraft persists through the period 2157 to 2348, it is noteworthy that the 0 dBZ contour descended throughout at an equivalent speed of 37.5 cm s^{-1} (49 cm s^{-1} from 2257 to 2348). In association with the sinking of the hydrometeor field, an increasing vertical gradient in Z is observed. For example, the average gradient between 0 and 15 dBZ is 4.1 dBZ km^{-1} at 2157 and 6.0 dBZ km^{-1} at 2348.

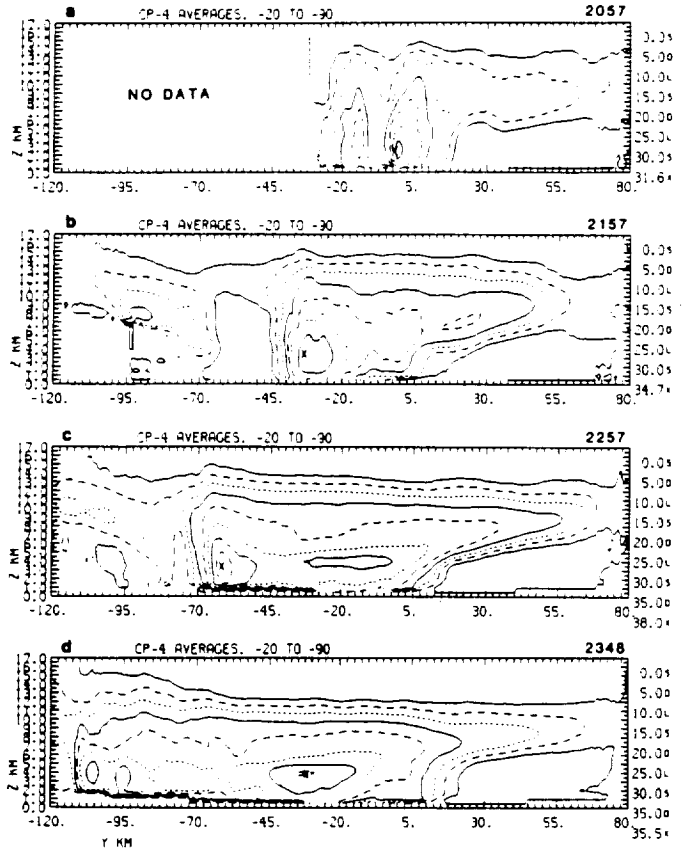

Figure 5. Vertical north-south sections of reflectivity factor, averaged over the east-west distance from x=-90 to x=-20, relative to CP-4. See Fig. 3 for the relative location of this averaging box. Contours are drawn every 5 dBZ, beginning at 0 dBZ.

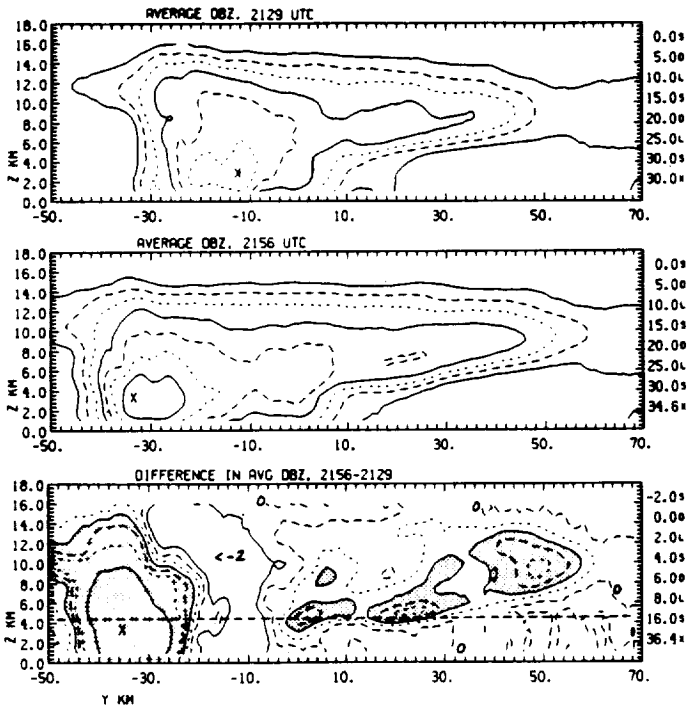

Figure 6. Vertical north-south sections of east-west averaged reflectivity factor at 2129 (top) and 2156 (middle), and their time difference (2156-2129 UTC, bottom). The averages for 2129 and 2156 were computed as in Fig. 5. Contours are defined at the right; the stippled region in the bottom panel highlights a difference >4 dBZ.

The behavior of the anvil shield (cloud top) is similar. Between 2300 and 0000, an equivalent sinking rate of 23 cm s^{-1} was inferred from the observed IR temperature increase (205.3 to 213.5 K), averaged over the VAD circle centered on CP-4 (Fig. 1). Such a value is presumably close to the terminal fall speed of ice crystals at this altitude, provided that w=0 at cloud top. It is interesting to note that the distance between the IR inferred cloud top and the radar cloud top of 0 dBZ within the VAD circle (Fig. 4a) increases with time. At 2157 the separation is 800 m, at 2257 it is 1600 m, and by 2348 the distance has increased to 2400 m. This behavior is in contrast to the increasing gradient in reflectivity factor from 2257 to 2348.

As demonstrated in Fig. 5, the expansion and intensification of Z within the anvil region was most rapid between 2057 and 2257. The growth of precipitation within the anvil during the initial expansion (i.e., from 2129 to 2156 UTC) was quantified by subtracting east-west averages (as in Fig. 5) of Z for two times, 2129 and 2156 UTC. The averages for each time are presented in Fig. 6 along with the time difference field. The absolute maximum (36.4 dBZ) located near y=-35 is produced by the southward movement (8 m s^{-1}) of the convective line. Another secondary maximum of >8 dBZ, located at (y,z)=(50,10), is due primarily to advection (via anvil outflow to the north) of hydrometeors. Although the v wind component is ambiguous from the vantage point of CP-4, it can be estimated from CP-4 data within the vertical plane passing through CP-4. These data indicate an anvil outflow speed of 4 m s^{-1} (ground relative) centered at 10 km, and a developing midlevel inflow jet of 8 m s^{-1} at 4-6 km AGL. Thus, advection of hydrometeors exhibits appreciable horizontal variation within the north-south plane.

Within the interior portion of the anvil region of Fig. 6, a local increase in reflectivity factor, generally >4 dBZ, is located along a line extending from (y,z) coordinates of (0,4.5) to (50,10.0). Because the slope of this maximum is nearly identical to that of the vertical gradient in dBZ at 2156 (the middle panel in Fig. 6), it is likely that this maximum is produced primarily by the downward settling of precipitation particles, i.e., vertical advection. Increases due to in situ growth are smaller, peaking around 4-5 dBZ at 8 km AGL near y=6 and y=30, and are positive throughout most of the anvil region. Nearly all of the increase in Z takes place above the 0 °C level, which is 4.5 km AGL (denoted by the dashed line in Fig. 6). Thus, the bright-band effect can account for the observed Z increase only in the ?-4.5 km AGL layer.

5. DISCUSSION

The observations from this case are synthesized as follows. The observed growth of precipitation within the trailing anvil region of an MCS occurred in association with a prominent mesoscale updraft of 50-70 cm s^{-1} magnitude. Much of this precipitation appears to have been generated within the anvil region, as opposed to being transported directly from the region of active deep convection. As the stratiform region further evolved to a structure exhibiting a prominent bright band, both the cloud top and radar top (roughly the 0 dBZ contour) descended in the presence of weak mesoscale updraft just below cloud top. While the vertical gradient of reflectivity factor increased during this process, the distance between the IR cloud top and the 0 dBZ level increased by a factor of 3 (800 to 2400 m) over a 2 h period. Although several of these observations warrant further study, one item of particular interest concerns the cloud top behavior. How does the observed warming at cloud top (in the presence of upward motion ~2 km below) relate to the actual vertical motion of the top boundary? Such a question has important implications on the nucleation and habit of ice crystals near cloud top in the temperature range -60 to -75 °C.

ACKNOWLEDGMENTS

This research effort was supported by NASA under grant NAG8-654. Much of the analysis software used herein was provided by the National Center for Atmospheric Research (NCAR). Particular thanks is extended to Carl Mohr and Richard Oye, both of NCAR. NCAR is also recognized for the extensive data collection effort, during the COHMEX field effort, and the subsequent quality control of the radar and surface mesonet data used in this study.

REFERENCES

Chong, M.P., P. Amayenc, G. Scialom, and J. Testud, 1987: A tropical squall line observed during the COPT 1981 experiment in west Africa. Part I: Kinematic structure inferred from dual-Doppler radar data. Mon. Wea. Rev., 115, 670-694.

Hildebrand, P.H., 1978: Iterative correction for attenuation of 5 cm radar in rain. J. Appl. Meteor., 17, 508-514.

Miller, L.J., C.G. Mohr and A.J. Weinheimer, 1986: The simple rectification to Cartesian space of folded velocities from Doppler radar observations. J. Atmos. Oceanic Tech., 3, 162-174.

Mohr, C.G, L.J. Miller, R.L. Vaughan and H.W. Frank, 1986: The merger of mesoscale data sets into a common Cartesian format for efficient and systematic analyses. J. Atmos. Oceanic Tech., 3, 143-161.

Smull, B.F., and R.A. Houze, 1987: Read inflow in squall lines with trailing stratiform precipitation. Mon. Wea. Rev., 115, 2869-2889.

Srivastava, R.C., T.J. Matejka, and T.J. Lorello, 1986: Doppler radar study of the trailing anvil region associated with a squall line. J. Atmos. Sci., 43, 356-377.

25th International Conference on Radar Meteorology
June 24-28, 1991
Paris, France

KINEMATIC AND PRECIPITATION STRUCTURE OF A SMALL, LONG-LIVED MESOSCALE CONVECTIVE SYSTEM

Kevin R. Knupp
Atmospheric Science and Remote Sensing Laboratory
Johnson Research Center
University of Alabama in Huntsville
Huntsville, AL 35899

1. INTRODUCTION

During the Cooperative Huntsville Meteorological Experiment (*COHMEX* - conducted over northern Alabama and central Tennessee during June and July of 1986) an extensive data set was collected from a variety of observational platforms on an atypical mesoscale convective system. The system was unusual in that it formed near 0900 UTC (~0230 LST) 15 July and dissipated near 2100 UTC (~1430 LST), which is a complete reversal of climatological patterns of deep convection (including systems that exhibit mesoscale organization) for the summer months in the Southeast. Moreover, the system attained an unusually long lifetime of 12 hr despite its small horizontal dimension of ~100 km. At maturity the MCS was quasi-circular in shape, and the stratiform region was located to the left (with respect to system motion) the the convective region. A comprehensive analysis, utilizing conventional single Doppler radar analyses, analysis of multiparameter (CP-2) data, network sounding and surface data and GOES satellite data is presented to characterize the internal kinematic and precipitation structure of this system.

2. ENVIRONMENT AND MCS SYNOPSIS

Analyses of GOES IR and Nashville (BNA) RADAP data indicate that the MCS formed adjacent to a previous MCS which had dissipated over Kentucky at ~0700 UTC. The first echo associated with the MCS of interest was observed at 0900 UTC, and areal expansion of both the low-level radar echo and cold cloud top occurred from 0900 to 1400 UTC (Fig. 1). A representative sounding which characterizes the environment of the developing MCS is shown in Fig. 2. This environment is moist from the surface to above 50 kPa, with integrated precipitable water values of ~51 mm. Although this sounding is moderately unstable as indicated by CAPE values of ~1700 J kg^{-1}, the intensity of convection within the system was generally weak to moderate in intensity. Cloud-to-ground lightning activity was generally low relative to the total precipitation produced (S. Goodman, personal communication). Both the environmental tropospheric winds and the vertical wind shear were generally small with the exception of the region at the top of the nocturnal inversion where a weak jet of 5.5 m s^{-1} is observed. This particular wind profile appears to have played a key role in dictating the relative

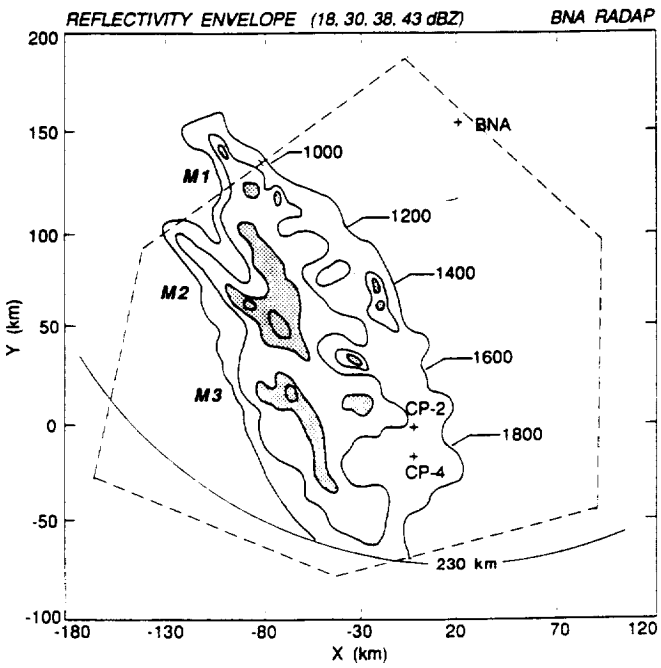

Figure 1. Envelope of reflectivity factor obtained from the 0.5 deg PPI of the Nashville (BNA) RADAP. Values exceeding 38 dBZ are shaded. The approximate system central axis, normal to system motion, is labeled in UTC. First echo was observed at 0900, and the final echo was observed by CP-4 at 2100 UTC, when the system was beyond the maximum range of 232 km.

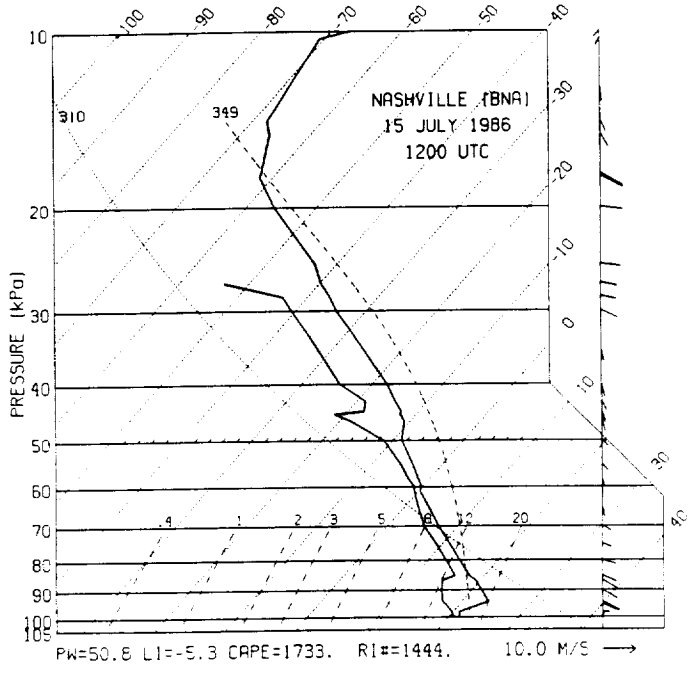

Figure 2. Sounding taken at 1200 UTC from Nashville (BNA), approximately 100 km to the NE of the MCS. See Fig. 1 for location.

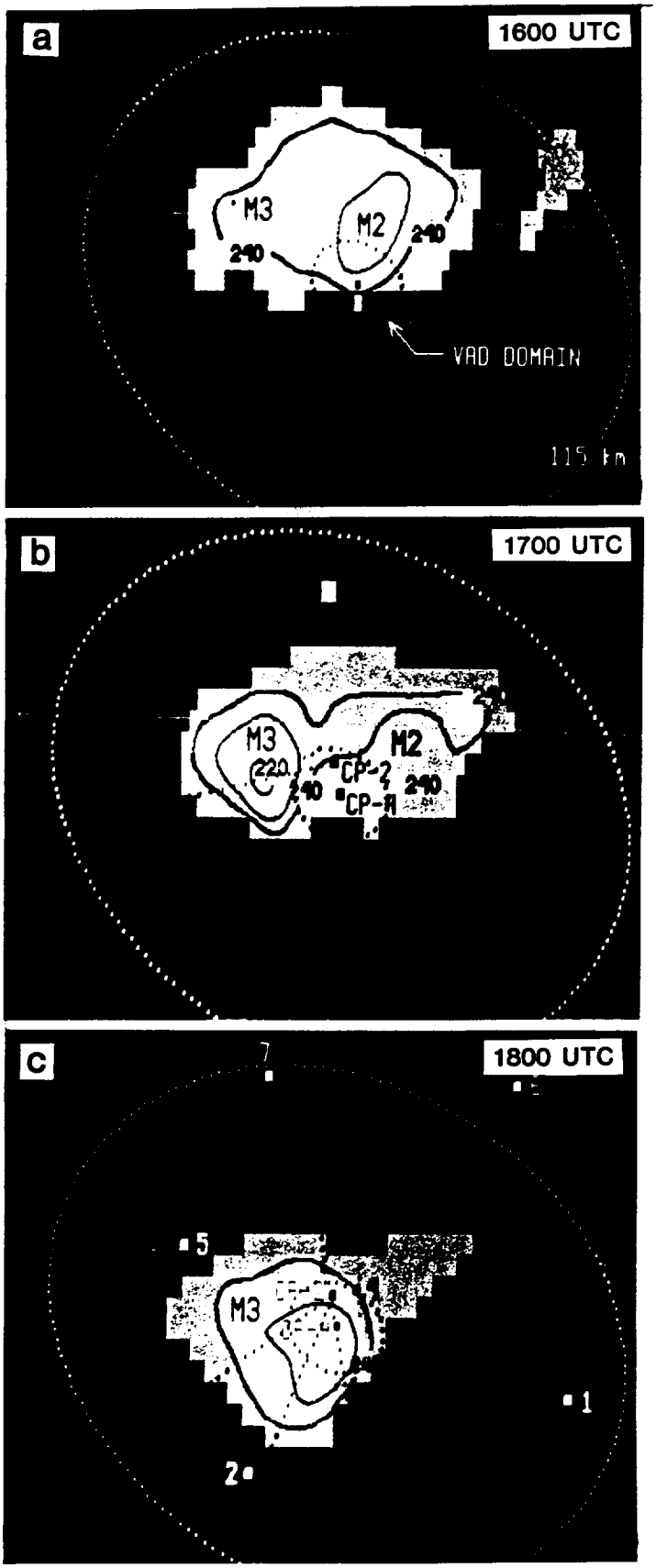

location of deep convection within the system, which occurred primarily along the western flank of the system. Stratiform precipitation was confined primarily to the eastern portion of the MCS. Surface features at 1200 UTC over the COHMEX surface mesonet (20 surface stations distributed within the polygon shown in Fig. 1) display relatively little structure as the surface was largely decoupled from the free atmosphere. The most pronounced signal was weak divergence associated with the area of precipitation. The air mass over the mesonet was nearly saturated at 21 °C.

From the satellite perspective, three major pulsations in deep convective activity were observed at uniform 3 h time intervals between 1000 and 1900 UTC. These pulsations correspond to swaths of enhanced reflectivity, labeled M1, M2 and M3 in Fig. 1, the most substantial of which was M2. These features were first visible in GOES IR imagery (available at 30 min intervals) at 1000, 1300 and 1600 UTC. Each development took place along the MCS western flank and then moved eastward in a system-relative sense as the cloud top pattern warmed. The trajectory of the cold cloud top was directed ~40 deg to the left of the trajectory of high reflectivity (Fig. 1) in response to the increased environmental flow aloft (Fig. 2). This scenario is illustrated in Fig. 3 for the latter two mesoscale features labeled M2 and M3. During this 2 h time sequence M2 is observed to weaken and disappear, while M3 evolves from its initial appearance at 1600 to weakened state at 1800. During the warming phase at cloud top, both M2 (at 1600) and M3 (at 1800) were associated with stratiform precipitation within and below the coldest cloud top region of the system.

The MCS attained a peak areal coverage of cold cloud top temperature (<221 K) of ~1000 km^2 at 1400 UTC. The maximum area occupied by the 241 K (-32 °C) isotherm was ~6700 km^2 at 1500 UTC, less than 10% the area of an MCC as defined by Maddox (1980). The peak area within the 18 dBZ contour at 0.5 deg elevation also occurred at 1500 UTC. Peak reflectivity factor and minimum cloud top temperature measured by RADAP and GOES IR were 50 dBZ and 214 K, respectively. In the next section a detailed examination of the internal system structure associated with M3 at 1800 UTC is presented.

3. INTERNAL STRUCTURE AT 1800 UTC

3.1 General precipitation and kinematic structure

Single Doppler analyses conducted during the mature to dissipating phases (1600 to 1830 UTC) of the system show both similarities and differences to the larger MCC and squall line systems documented in the literature. The intensity of the deep convective components was generally weak, the areal coverage of deep convective components was relatively low at ~20% and the location relative to the stratiform portion, although generally within the western portion of the system, lacked a systematic relative orientation. At times convective cells were located along the far eastern portion of the MCS (Fig. 1). Patterns of reflectivity factor and radial velocity are shown in Fig. 4 at 1810 UTC, which represents a late mature to early dissipating stage of the MCS. At this time relatively weak deep convective elements are confined to the southwest portion of the system. The system is nearly circular in shape and the stratiform region exhibits isolated patches exceeding 35 dBZ. At earlier times patterns were generally similar to those at 1810, with the exception that the deep convective components were weaker at 1810.

Radial velocity patterns (Fig. 4b) show a highly stratified and relatively uniform flow at the 2 km level. At earlier times more structure in velocity was seen in association with the convective region along the western flank. RHI scans show that flows within

Figure 3. GOES IR images at 1600, 1700 and 1800 UTC. CP-4 range markers at 115 km (maximum range) and 20 km (the VAD analysis range) are shown. Other dotted lines drawn in panels *b* and *c* refer to RHI scans from CP-2. Brightness temperature is gray shaded at the following levels (K): white, T<237; light gray, 237<T<250; medium gray, 250<T<260; dark gray, 260<T<270. Additional contours are drawn at 240, 230 and 220 K. In panel *c*, locations of soundings taken between 1715 and 1815 UTC are shown.

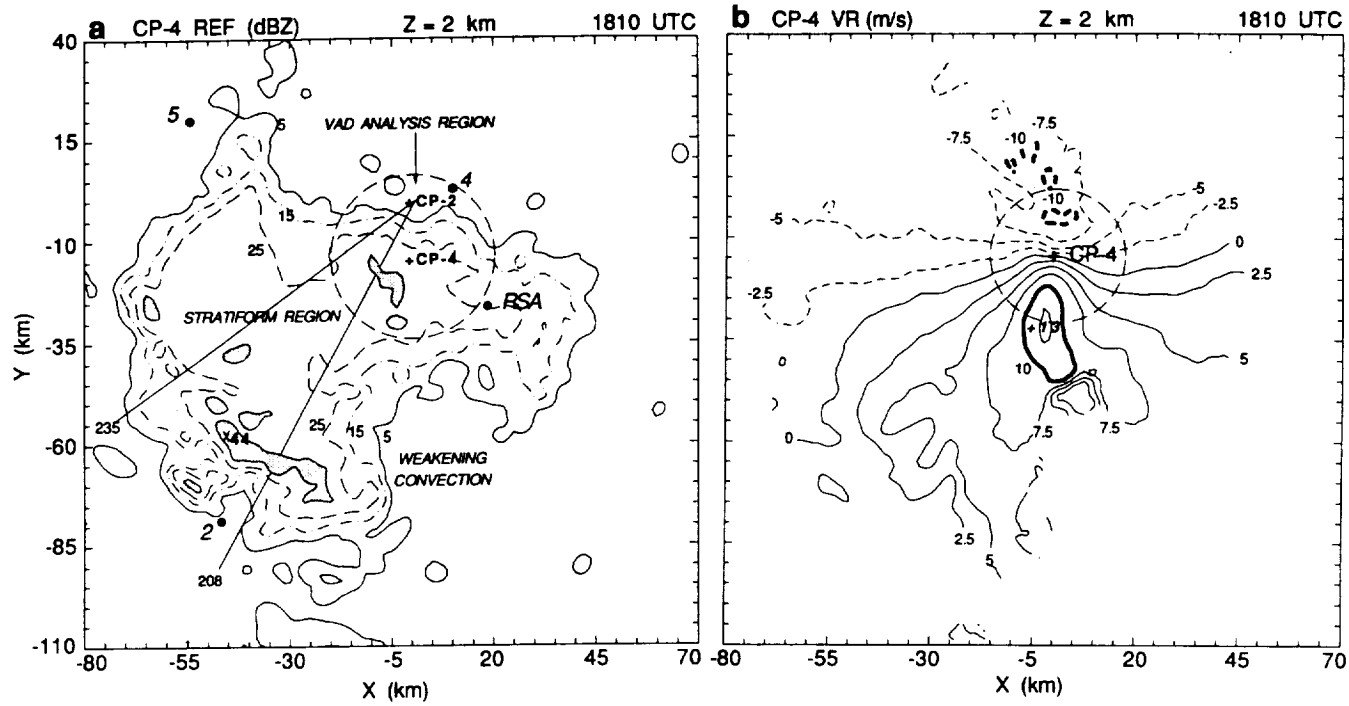

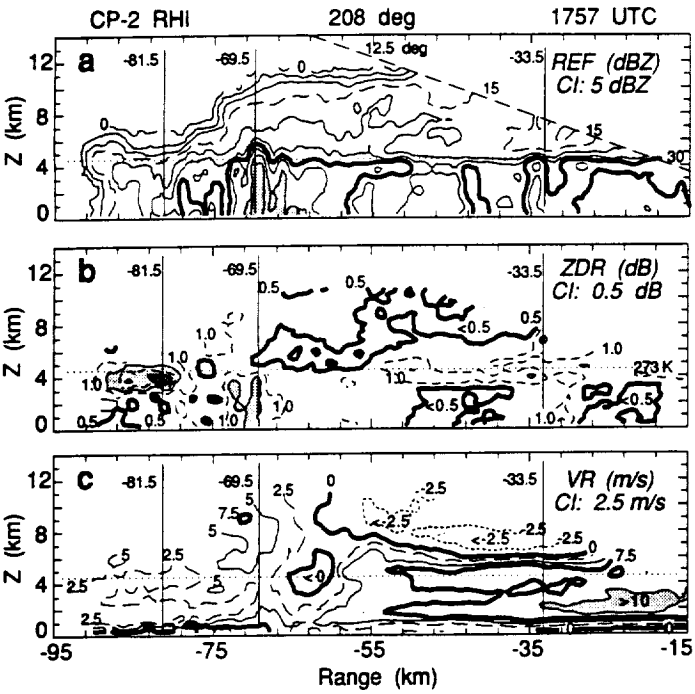

Figure 4 (top). Analysis of CP-4 (a) reflectivity factor and (b) radial velocity at the 2 km level at 1810 UTC. Reflectivity is contoured every 10 dBZ beginning at 5 dBZ, and radial velocity is contoured every 2.5 m s^{-1}. Sounding locations (2, 4, 5 and RSA) and locations of CP-2 RHI scans near 1757 UTC are indicated in panel a. At this time the MCS is in a state of decline.

Figure 5 (left). CP-2 RHI scan at 208 deg azimuth at 1757 UTC. The relative location of this scan is indicated in Figs. 4a and 3c. (a) Reflectivity factor drawn every 5 dBZ, beginning at 0. The thick line is 30 dBZ and shading depicts REF>40 dBZ. (b) Z_{DR} drawn every 0.5 dB, beginning at 0.5 dB. The thick line is 0.5 dB and shading depicts Z_{DR}>1.5. (c) Radial velocity drawn every 2.5 m s^{-1}. The solid lines are drawn at 0 and 7.5 m s^{-1}, values exceeding 10 m s^{-1} are shaded. The dotted horizontal line in each panel indicates the environmental 0 °C level. Vertical solid lines show the location of profiles diplayed in Fig. 6.

Figure 6 (bottom). Vertical profiles of Z, Z_{DR} and VR at ranges of (as shown in Fig. 5) (a) 81.5, (b) 69.5 and (c) 33.5 km from CP-2.

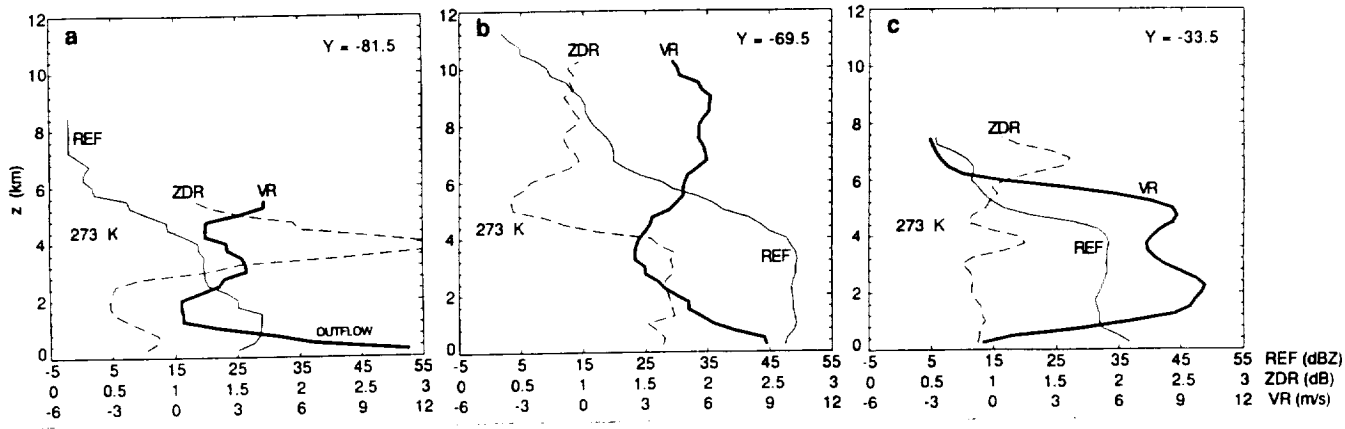

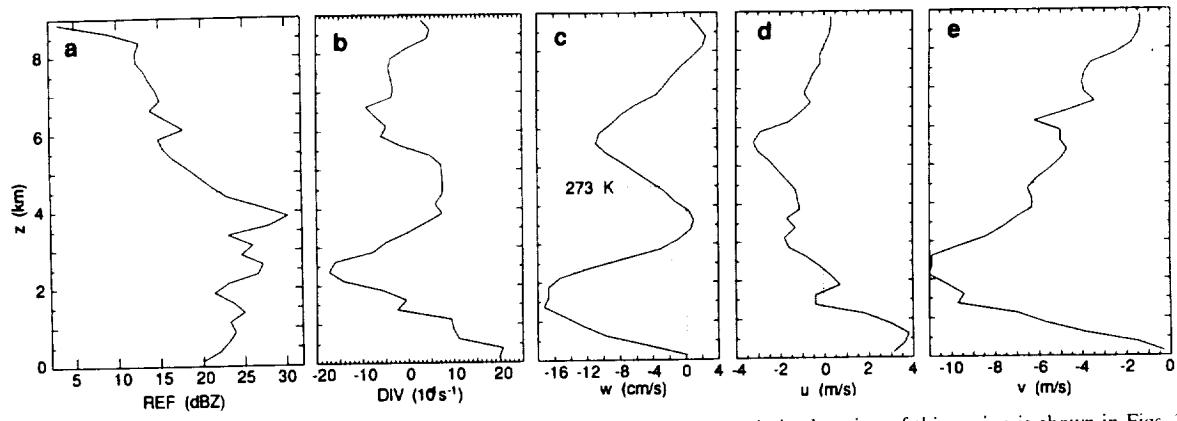

Figure 7. Quantities derived from the CP-4 VAD analysis at 1810 UTC. The relative location of this region is shown in Figs. 3c and 4a. Ranges of 16, 20 and 24 km were used to obtain high vertical resolution.

the stratiform region of this system were highly stratified and laminar in appearance. Such stratification is apparent in the CP-2 RHI scan (Fig. 5c) between ranges of 15 and 55 km. A prominent inflow jet of 12-14 m s^{-1} magnitude, located over CP-4, was observed throughout the period of observations. A component of this jet is also visible in Fig. 5b at 15 to 55 km range near the 2 km level. Unlike the slanted jet structure observed in other MCSs (e.g., Smull and Houze 1987), the jet feature observed here was quasi-horizontal and centered at a height of 2.0-2.5 km, roughly 2 km below the 0 °C level. The perturbation of the wind within this jet feature, assuming that the ambient wind is represented in the 1200 UTC BNA sounding (Fig. 2), is roughly 10 m s^{-1}.

The major MCS pulsations visible in the IR patterns were associated with the development of closely interacting aggregates of convective elements. The aggregates were ~20 km in diameter, attained echo tops of ~13 km, and were dominated by a single relatively intense convective element although additional weaker convective elements of smaller size were generally present. The measured difference in radial velocity across the upper portion of these elements was ~20 m s^{-1} over a distance of 10 km. At 1810, a residual velocity difference of ~10 m s^{-1} over a 20 km horizontal distance is centered at a height of 10 km and a range of 60 km (Fig. 5c).

3.2 CP-2 multiparameter analysis

Multiparameter measurements from CP-2 revealed a highly variable structure in Z_{DR} within both the convective and stratiform regions of the MCS. The RHI analysis presented in Fig. 5 intersects (a) new but weak growth at far range; (b) a weakening major convective element, representing the major component of M3, at intermediate range; and (c) the stratiform region at near range. The stratiform region exhibits a non-uniform structure in both Z and Z_{DR} (Fig. 5a,b). Vertical profiles at 33.5 km range are shown in Fig. 6c. A bright band is located near the 4 km level (the 0° C level is at 4.4 km). Enhanced values of Z_{DR} occur in association with enhanced Z. A secondary peak in Z_{DR} (1.5 dB) is also present near 6.7 km height (T = -14 °C). As shown in Fig. 5b, this region of enhanced Z_{DR} is confined to a region ~10 km wide. Such patches were observed throughout the period of CP-2 measurements and are similar in some respects to Z_{DR} observations made in stratiform clouds (e.g., Bader et al, 1987).

At other locations much different profiles of Z_{DR} are seen in Fig. 6a,b. For example, the profile within the core of an old convective element (Fig. 6b) shows a relative minimum value in Z_{DR} 1 km above the 273 K level, which is capped by nearly uniform values of ~1 dB from 7 to 10 km. The radial velocity patterns in Fig. 5c suggest a pattern of weak updraft (several m s^{-1} or less) within the upper half of this domain, and weak downdraft over the lower portion. Thus, the Z_{DR} profile may suggest a systematic fallout of precipitation from the cloud, with graupel providing the low Z_{DR} values and oriented plate-like crystals producing the higher values above 7 km.

Finally, a region of new precipitation growth within kinematically-weak cumuli (echo top ~6km and updraft on the order of several m s^{-1}, as inferred from the radial velocity patterns in Fig. 5a) is suggested by the measurements at 81.5 km range. This growth is located directly above an outflow boundary as indicated in the profile of radial velocity (Fig. 5a) Here, relatively high Z_{DR} values peaking just above 3 dB are located within relatively weak Z of 15-20 dBZ. Such values are similar to measurements described by Illingworth (1988) and suggest a small number of large raindrops whose growth was accomplished by the collision-coalescence process.

3.3 CP-4 VAD analysis

Characteristics of the stratiform region surrounding the CP-4 radar were determined from VAD analyses during the 1600-1810 time period. In general the stratiform region over the eastern portion of the MCS exhibited downward motion throughout much of the cloud depth, typically from the 6 km level to the surface. Only the uppermost portion exhibited very weak ascent on the order of several cm s^{-1}. The results from the 1810 analysis are shown in Fig. 7. At this time two individual downdraft (and mass convergence) maxima were analyzed, one at low levels near 1.5 km and the other above the 273 K level at 5 km. The low-level feature is associated with the inflow jet, located near 2.5 km, which appears in the v wind profile. Such patterns are substantially different from measurements taken in the stratiform region of larger-scale convective systems (e.g., Rutledge et al, 1988).

Acknowledgments

Programming assistance was provided by Tim Rushing and James Coker. This research was supported by the National Aeronautics and Space Administration under grant NAG8-654.

References

Bader, M.J., S.A. Clough and G.P. Cox, 1987: Aircraft and dual-polarization observations of hydrometeors in light stratiform precipitation. *Quart. J. Roy. Meteor. Soc.*, **113**, 491-515.

Illingworth, A.J., 1988: The formation of rain in convective clouds. *Nature*, **336**, 754-756.

Maddox, R.A., 1980: Mesoscale convective complexes. *Bull. Amer. Meteor. Soc.*, **61**, 1374-1387.

Rutledge, S.A., R.A. Houze, M.I. Biggerstaff and T. Matejka, 1988: The Oklahoma-Kansas mesoscale convective system of 10-11 June 1985: Precipitation structure and singe-Doppler radar analysis. *Mon. Wea. Rev.*, **116**, 1409-1430.

Smull, B.F., and R.A. Houze, 1987: Rear inflow in squall lines with trailing stratiform precipitation. *Mon. Wea. Rev.*, **115**, 2869-2889.